NASA TECHNICAL
MEMORANDUM
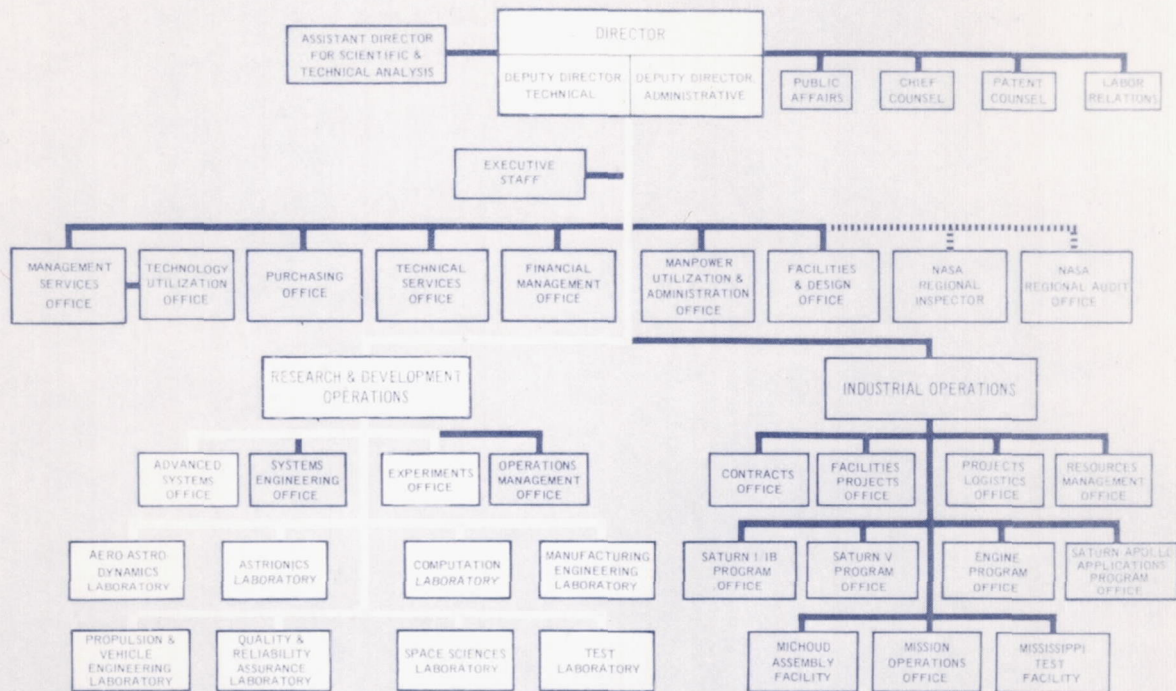
NASA TM X-53799

1968

NASA TM X-53799

AEROPHYSICS RESEARCH AT MSFC

RESEARCH ACHIEVEMENTS REVIEW

VOLUME III   REPORT NO. 4

RESEARCH AND DEVELOPMENT OPERATIONS
GEORGE C. MARSHALL SPACE FLIGHT CENTER
MARSHALL SPACE FLIGHT CENTER, ALABAMA

GEORGE C. MARSHALL SPACE FLIGHT CENTER

RESEARCH ACHIEVEMENTS REVIEWS COVER THE FOLLOWING FIELDS OF RESEARCH

- Radiation Physics
- Thermophysics
- Chemical Propulsion
- Cryogenic Technology
- Electronics
- Control Systems
- Materials
- Manufacturing
- Ground Testing
- Quality Assurance and Checkout
- Terrestrial and Space Environment

- Aerodynamics
- Instrumentation
- Power Systems
- Guidance Concepts
- Astrodynamics
- Advanced Tracking Systems
- Communication Systems
- Structures
- Mathematics and Computation
- Advanced Propulsion
- Lunar and Meteoroid Physics

NATIONAL AERONAUTICS AND SPACE ADMINISTRATION

WASHINGTON, D. C.

RESEARCH ACHIEVEMENTS REVIEW

VOLUME III   REPORT NO. 4

AEROPHYSICS RESEARCH AT MSFC

RESEARCH AND DEVELOPMENT OPERATIONS
GEORGE C. MARSHALL SPACE FLIGHT CENTER
MARSHALL SPACE FLIGHT CENTER, ALABAMA

1968

PREFACE

In February, 1965, Dr. Ernst Stuhlinger, Director, Research Projects Laboratory (now Space Sciences Laboratory), initiated a series of Research Achievements Reviews which set forth those achievements accomplished by the laboratories of the Marshall Space Flight Center. Each review covered one or two fields of research in a form readily usable by specialists, systems engineers and program managers. The review of February 24, 1966, completed this series. Each review was documented in the "Research Achievements Review Series."

In March, 1966, a second series of Research Achievements Reviews was initiated. This second series emphasized research areas of greatest concentration of effort, of most rapid progress, or of most pertinent interest and was published as "Research Achievements Review Reports, Volume II." Volume II covered the reviews from March, 1966, through February, 1968.

This third series of Research Achievements Reviews was begun in March, 1968, and continues the concept introduced in the second series. Reviews of the third series are designated Volume III and will span the period from March, 1968, through February, 1970.

The papers in this report were presented September 26, 1968

William G. Johnson
Director
Research Planning Office

CONTENTS. . .

ROCKETS AT LARGE ANGLES OF ATTACK

Page

by Clayton D. Andrews, James F. Weaver, John D. Warmbrod, and Heinz G. Struck

LIST OF ILLUSTRATIONS

LUDWIEG TUBE PILOT TESTS AND HIGH REYNOLDS NUMBER TEST EQUIPMENT

Page

by John W. Davis

CONTENTS (Continued) . . .

LIST OF ILLUSTRATIONS

THEORETICAL ANALYSIS OF THE STARTING PROCESS IN THE LUDWIEG TUBE

by John D. Warmbrod and Heinz G. Struck

CONTENTS (Continued)...

FLOW CHARACTERISTICS OF ORIFICES USED FOR VENTING LAUNCH VEHICLE COMPARTMENTS

Page

by P. E. Ramsey

CONTENTS (Continued)...

PLUME FLOW FIELD ANALYSIS FOR LIQUID PROPELLANT ROCKET ENGINES

Page

by Joseph L. Sims and Terry Greenwood

LIST OF TABLES

LIST OF ILLUSTRATIONS

CONTENTS (Continued) . . .

TECHNIQUES DEVELOPED TO DETERMINE AERODYNAMIC COEFFICIENTS FOR APOLLO APPLICATIONS PROGRAM VEHICLES IN AN ORBITAL ENVIRONMENT

Page

by Josh D. Johnson

CONTENTS (Continued) . . .

LIST OF ILLUSTRATIONS

ACQUISITION AND REDUCTION OF LARGE VOLUMES OF FLUCTUATING DATA

by Luke A. Schutzenhofer and Paul W. Howard

LIST OF TABLES

CONTENTS (Continued)...

PERCEIVED SOUND

Page

by Jess H. Jones

CONTENTS (Continued) . . .

RADIATIVE HEAT TRANSFER FROM SATURN EXHAUST PLUMES

by Robert M. Huffaker

LIST OF TABLES

LIST OF ILLUSTRATIONS

CONTENTS (Continued) . . .

DEVELOPMENT OF LASER-DOPPLER GAS VELOCITY INSTRUMENTATION

Page

by Robert M. Huffaker

LIST OF ILLUSTRATIONS

CONTENTS (Concluded)...

OPTICAL CROSSED-BEAM INVESTIGATION OF LOCAL SOUND GENERATION IN JETS

LIST OF ILLUSTRATIONS

ROCKETS AT LARGE ANGLES OF ATTACK

By

Clayton D. Andrews, James F. Weaver,
John D. Warmbrod, and Heinz G. Struck

SUMMARY

The prediction of high angle of attack rocket
aerodynamic characteristics represents a special
problem to the aerodynamicist. From the rocket
designer's point of view, no acceptably accurate
method for predicting load distribution exists. An
experimental approach to the problem is inadequate
as a result of the Reynolds number deficiencies of
existing test facilities.

The program currently in progress at MSFC to
better define high angle of attack rocket loadings is
based on a combined experimental-theoretical ap-
proach. Because of the assumptions involved, the
present two-dimensional theoretical tools do not
provide an answer to design problems; however, they
provide a theoretical model to aid in the under-
standing of the significant flow mechanisms involved
and provide a basis for defining the experimental
program.

Currently available experimental and theoretical
results are compared for simple bodies of revolution.
The modified two-dimensional theoretical results com-
pare favorably, trendwise, with the experimental data.
Suggestions are made for improving the modified two-
dimensional theory, based on wake flow studies about
delta wings at high angles of attack.

The combined experimental and theoretical pro-
gram to better define high angle of attack rocket
loadings is approximately 50 percent complete. It is
felt that the end product design "tool" will be an
empirical-theoretical approximation that can be made
with a high degree of confidence.

INTRODUCTION

Accurate prediction of the high angle of attack
stability and loads on rockets is an important consid-
eration in the flight of manned vehicles. Given any
point along the trajectory, knowledge of the magnitude
and distribution of aerodynamic lift is essential for
predicting the angle of attack at which the vehicle
would break apart. This information is needed for
proper astronaut abort decisions. The astronauts
will use any chance of saving the expensive vehicle by
not aborting unnecessarily, but the crew must be
saved sufficiently in advance of structural breakup.

The prediction of loads on rockets at large angles
of attack represents a special problem to the aero-
dynamicist. The lift of rockets is essentially fuselage
lift, controlled at moderate to large angles of attack
($\alpha > 6°$) by the so-called "viscous crossflow," i.e.,
flow separation on the lee side of bodies of revolution
that forms two vortices which are connected by a
feeding sheet to the body boundary layer as shown in
Figure 1. The vortex system and the consequent non-
linear lift are strongly influenced by (1) the axial
position at which an incipient vortex develops suffi-
cient strength to depart from the body and (2) the
position of the boundary layer separation point. Even
with an essentially turbulent boundary layer, this
lift is subject to Reynolds number effects which are
as yet unpredictable. From the designer's point of
view, no acceptable method for predicting the total
lift and moment and the pressure distribution along
bodies of revolution at large angles of attack is pre-
sently available. Wind tunnel data are usually subject
to large Reynolds number deficits. It is not yet pos-
sible to estimate the magnitude or even the trend of
these differences within the critical Reynolds number
range. Wind tunnel data are therefore presently used
for design at face value, and these data contain an un-
known uncertainty.

The approach to better define loading at high an-
gles of attack has been a combined experimental and
theoretical effort. Existing wind tunnel facilities are
being pushed to their limits to extend the Reynolds
number range of data on both simple and Saturn-type
bodies of revolution. Also, existing theories are be-
ing updated empirically, based on the resulting high
Reynolds number experimental results. This paper
describes briefly the experimental-theoretical
approach to the problem and reports on currently
available results. The end product of these studies
will hopefully provide a "tool" for predicting full-
scale high angle of attack rocket load distributions.

Plane Fixed in Fluid
Perpendicular to
Body Axis

Leeward
Vortex Sheets

NACA Vortex Model

Vortex Cores

Separation
Point

U sin α

Simplified Analogy in the
Two-Dimensional Plane
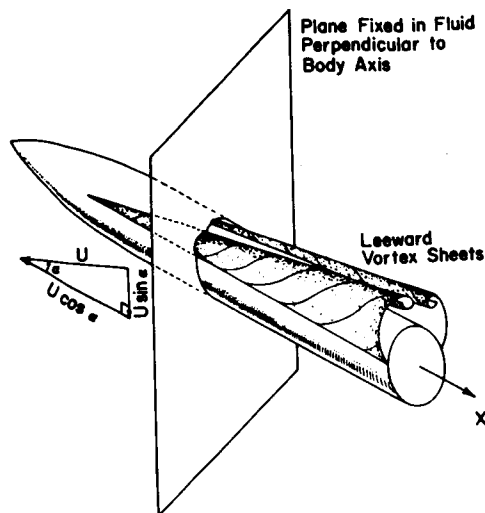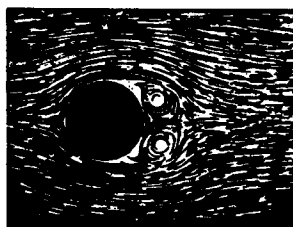
Streamline Picture (Prandtl)
Development of Two
Symmetric Vortices

Ma = 2.87
Re = 3.7x10⁶

Typical Variation of Normal Force
Coefficient With Angle of Attack
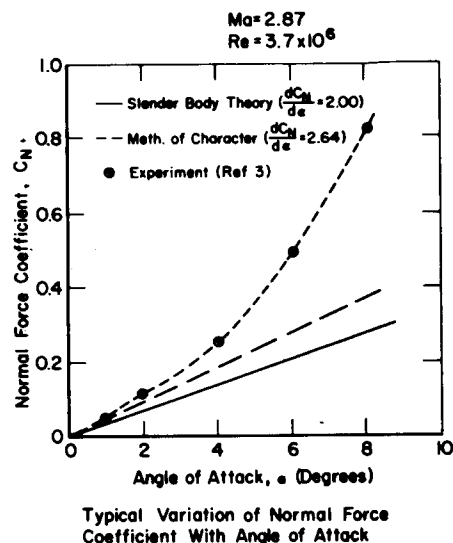
FIGURE 1. EXTERNAL FLOW MECHANISM ABOUT ROCKETS AT HIGH ANGLES OF ATTACK

LIST OF SYMBOLS

Symbol	Definition
c_{D_c}	crossflow drag
$c_{D_c}^{*}$	steady state crossflow drag
c_N	normal force coefficient
$(dc_N/d\alpha)_{\alpha = 0}$	slope of the normal force co-efficient at zero angle of attack
D	diameter of the body

L	length of the body
M_∞	Mach number
R	radius of the body
Re	Reynolds number, based on body length
Re_C	crossflow Reynolds number
Re_D	Reynolds number based on body diameter
U_∞	velocity

2

x, y, z   cartesian coordinates

x, r, Θ   cylindrical coordinates

α angle of attack

Γ vortex strength

δ tangent cone semi-apex angle

$\zeta_1 = x_1 + i z_1$ location of vortex in the physical plane

θ_0 two-dimensional separation angle

APPROACH

Very little information is available that is related to the problem of predicting rocket aerodynamics at high angles of attack. Allen [1] published his viscous crossflow theory in the early fifties. Kelly [2] improved this concept by replacing the steady state crossflow drag coefficient by a more appropriate transient state drag coefficient. Both authors attempted to cover Reynolds number effects by assuming the boundary layer to be identical with the boundary layer on a cylinder in two-dimensional flow at the same crossflow Reynolds number. During the mid-fifties considerable effort was spent on experimental investigations; however, because of facility limitations, these tests covered only a small Mach-Reynolds number range. Since then, little progress has been made on either the experimental or theoretical approach to the problem, except perhaps for the contributions of Hill [3] and Bryson [4] who obtained solutions for the separated crossflow independent of experimental data. Schindel [5] adapted Bryson's theory to a three-dimensional body by specifying the axial circumferential location of the separation line and compared the theoretical results for various body shapes with experimental data.

The current approach to the problem of high angle of attack rocket aerodynamics builds upon these available results, both experimental and theoretical.

EXPERIMENTAL APPROACH

Facilities. In aerodynamic testing it is a common practice to violate the Reynolds similarity law as a result of lacking suitable test facilities. In many cases this violation is permissible; however, in the design and operation of large manned launch vehicles a number of flow problems exist where Reynolds number effects become significant. The high angle of attack load definition problem falls in this category. Consequently, an attempt is made to simulate full scale Reynolds numbers. Available wind tunnel facilities provide Reynolds numbers that are about 1/50 to 1/100 of the Saturn V flight Reynolds numbers in and around the most critical transonic, low supersonic range of Mach numbers. A comparison of existing aerodynamic test facility capabilities is made with a typical Saturn V trajectory in Figure 2. MSFC has proposed to close this Reynolds number gap with a Ludwieg-tube tunnel, i.e., a short duration blowdown tunnel. The Reynolds number capability of this proposed facility is also indicated.

The experimental effort in support of the high angle of attack load definition makes use of the maximum capabilities of existing wind tunnel test facilities as indicated in Figure 2 at selected Mach numbers. Although the test Reynolds numbers are much lower than trajectory values, the test results will be at the highest values currently available and will provide a considerable extension to any existing related information. The test Reynolds number range was achieved by variations in model scale using the MSFC 36-cm (14-in.) trisonic tunnel and the Vought Aeronautics 1.2-m (4-ft.) high speed wind tunnel. The operating characteristics of these facilities are described in References 6 and 7, respectively. Standard testing techniques were used in all phases of the experimental programs.

Body Geometries. The geometric configurations selected for the high angle of attack study are shown in Figure 3. Configuration B (ogive-cylinder) provides a simple shape whose aerodynamic characteristics can be predicted by existing theories, provided enough information is given about the boundary layer. In addition, some test information is available in the literature over a limited Reynolds number range for this shape. Configuration C (ogive-cylinder-frustum-cylinder) was selected to provide information on the effects of changes in body cross section on high-angle-of-attack loads. Configuration A is a simplification of a typical Saturn shape, the geometry of most interest, and yet the most complex shape from the aerodynamic point of view. The data from configuration A will be used as a guideline in the extrapolation versus Reynolds number to full scale values.
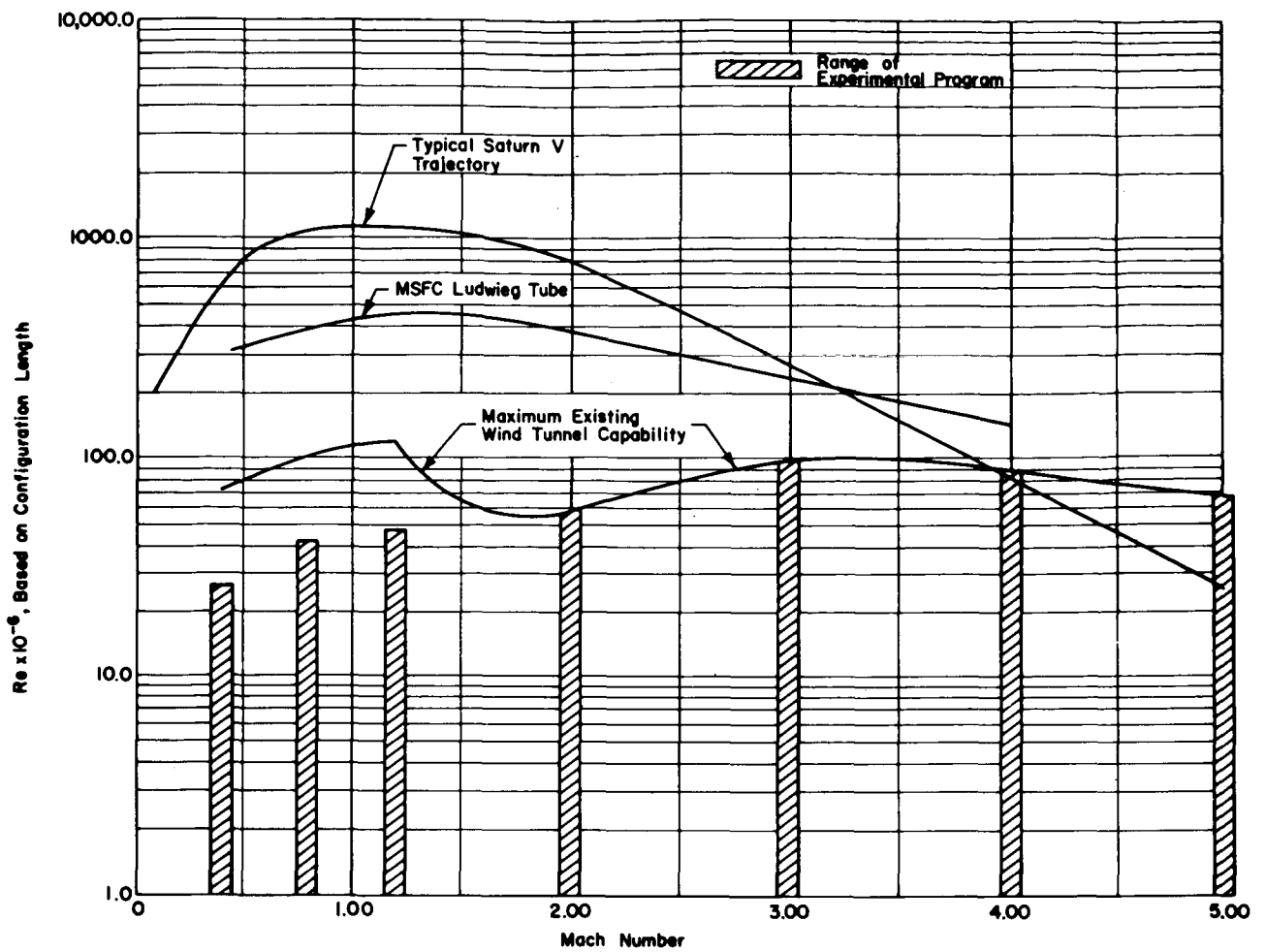
FIGURE 2. EXPERIMENTAL FACILITY REYNOLDS NUMBER SIMULATION CAPABILITIES

Geometry "A"
(Typical SATURN)

Geometry "B"
(Ogive - Cylinder)

Geometry "C"
(Ogive - Cylinder - Frustum - Cylinder)
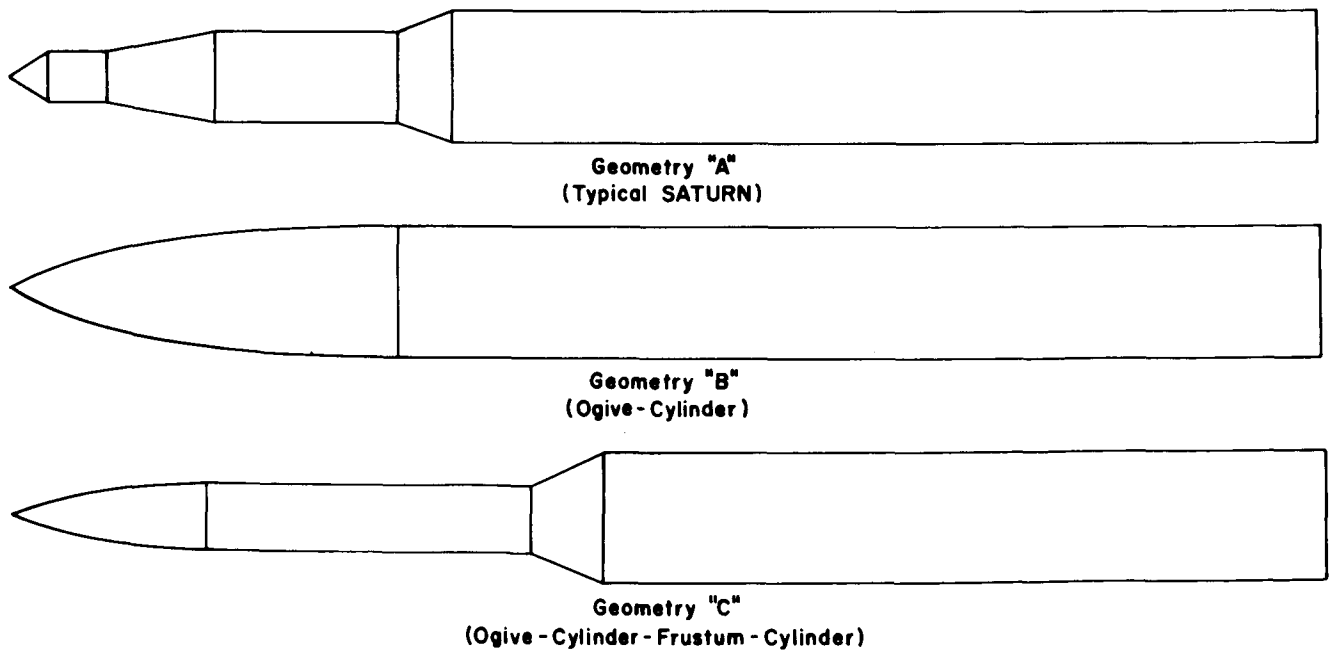
FIGURE 3. EXPERIMENTAL STUDY CONFIGURATIONS

<u>Data Requirements</u>. Because of the complexity of the problem, a great many data must be taken. In addition to the usual force and moment measurements, detailed flow field investigations must be made.

In past programs, total model forces were measured by a three-component strain-gage balance. Normal force, pitching moment, and axial force were measured for each test run as a function of the angle of attack. No boundary layer trips were installed. In additional runs, the models were painted with china clay to investigate the boundary layer separation lines. Furthermore, shadowgraphs and schlieren pictures were made.

In future programs, additional information will be obtained about the local pressure distribution on the surface of the body and in the wake as a function of the Mach and Reynolds number. From the data we are able to determine the location of the vortex and its approximate strength. The results will serve as a check on the accuracy of the two-vortex model and will indicate in which direction improvements should be made.

THEORETICAL APPROACH

To explain the theoretical approach, let us again examine Figure 1, which shows a schematic of a simplified rocket at a high angle of attack flying with a velocity of U_∞. The normal component of the velocity is $U_\infty \sin \alpha$. On the lee side of the body, two symmetric vortices develop on the forward portion as a result of accumulated low energy boundary layer material. New boundary layer material is collected as we pass along the length of the body, and consequently the separated region grows in size; or in other words, the vortex grows and the vortex centerline moves farther from the body's surface. If we imagine a moving plane perpendicular to the axis and we take pictures of the trace of the vortex in that particular plane at equidistant x-stations, we will observe that the series of pictures resembles the two-dimensional development of a flow around a cylinder started impulsively from rest with a velocity of $U_\infty \sin \alpha$. The presence of the vortex pair changes the pressure distribution on the lee side of the body and the total normal force is higher, as we would expect from pure potential flow where there is no separation. If we plot the normal force coefficient over a range of angles of attack, we discover that the normal force coefficient is proportionally higher at higher angles of

attack than at small angles. No classical theory, whether the slender body or the more elaborate method of characteristics, can predict this nonlinear increase in lift. The illustration in the lower right-hand corner represents the normal force coefficient as a function of angle of attack for an ogive cylinder body with a fineness ratio of Length/Diameter = 14 and a nose fineness ratio of 3.5. The lift starts to deviate already at very small angles of attack because of the thickening of the boundary layer on the lee side of the rearward portion of the body.

Our theoretical approach to the problem follows closely the physical picture. In Figure 4 the rather complex three-dimensional mechanism of the flow is idealized by a two-dimensional model. A pair of symmetric vortices of strength Γ is placed at ζ_1 in the physical plane. This vortex is connected with the body by an infinitely thin vortex feeding sheet, and joins the body at the separation point ζ_0 at a meridian angle of θ_0. These free vortices behave in a flow field in a certain manner. Since the feeding sheet and the free vortex cannot sustain any pressure forces, the pressures on either side of the sheet must be balanced. This is one condition; the other condition is that the separation point must be a stagnation point. From these conditions we obtain expressions for determining the vortex strength and the position of the vortex relative to the body. Image vortices are placed inside the body to satisfy the boundary condition on the body surface. This is, in essence, the flow model as Bryson [4] developed it. The free parameter of this problem is the separation angle θ_0 for the two-dimensional problem. The angle is a function of the Reynolds number. The three-dimensional problem has one additional parameter: the axial separation distance from the nose of the body. This parameter is a function of the angle of attack α and will depend on the nose shape. Analytical expressions for these parameters still come from the experiment, as long as the state of the art of calculating three-dimensional boundary layers is still in the beginning stages. From experiment [4] it is found that the boundary layer does not separate until

$$\frac{\tan \alpha}{\tan \delta} = \frac{3}{2} \frac{1}{\sin \theta_\infty} \, ,$$

where α = angle of attack, δ = semi-angle of the tangent cone to the nose shape, and θ_∞ is the meridian angle of the separation point.

Figure 4 also shows some of the two-dimensional theoretical results. The vortex path is plotted for
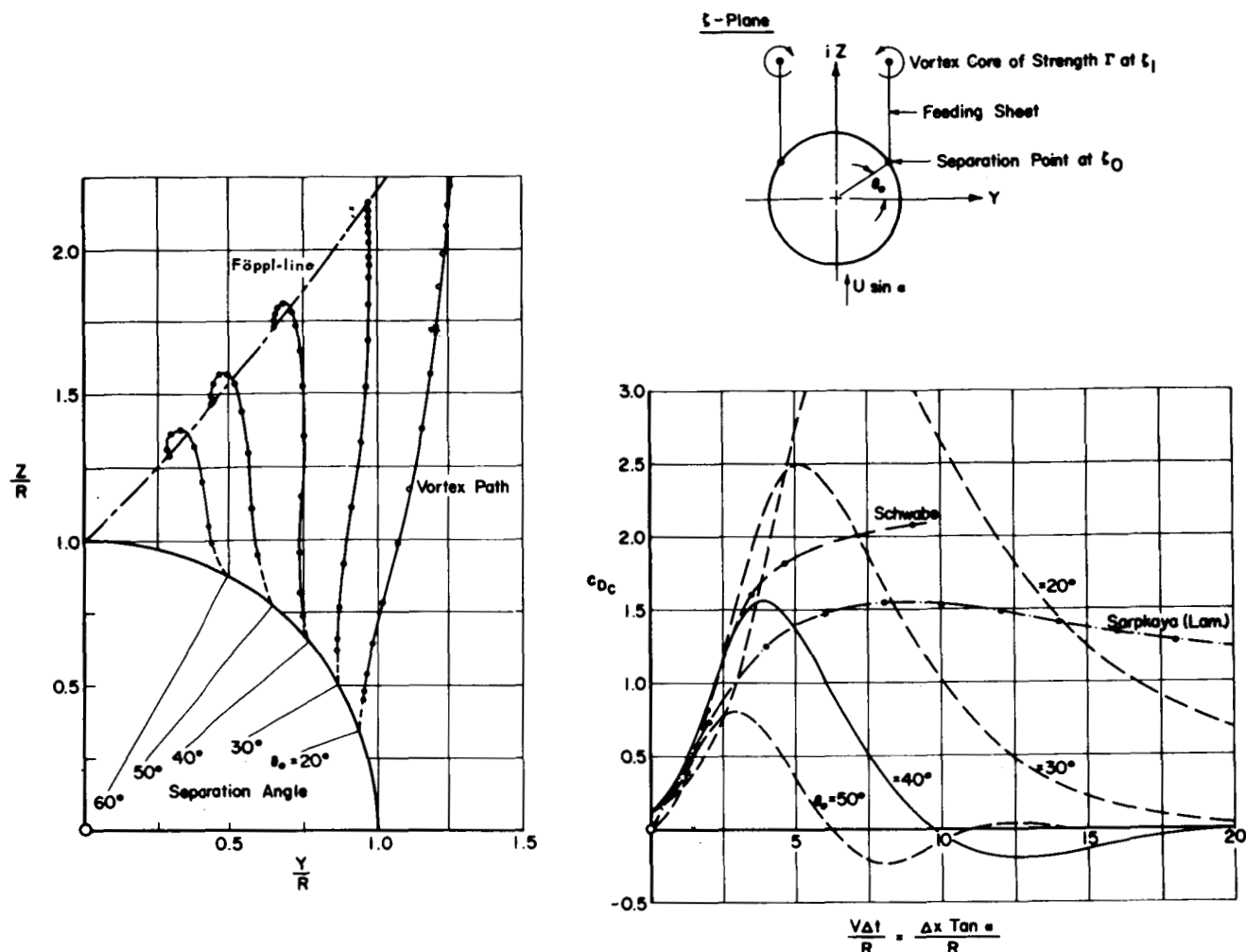
FIGURE 4. ANALYTICAL APPROACH TO HIGH ANGLE OF ATTACK FLOW

different separation angles θ_0, from 20 degrees to 60 degrees. In all cases, the vortex was started off the cylinder surface with a certain strength and a certain direction. With increasing velocity and increasing strength, the vortex leaves the cylinder and approaches the Föppl-line, where the symmetric vortex pair is stable toward symmetric disturbances and their relative velocity to the body decreases and becomes zero after an infinite time. Along the Föppl-line, the vortex pair becomes stationary and does not move with respect to the cylinder. Since their strength is constant, the momentum change of the configuration is zero and no forces develop. The $\theta_0 \leqq 30$ degree-lines approach the equilibrium line asymptotically, whereas the $\theta_0 > 30$ degree-lines overshoot the Föppl-line and return to it in a spiral-like fashion. In terms of the cross flow drag, c_{D_c}, we observe that

with increasing time or distance, the curves pass a maximum c_{D_c} corresponding to the maximum relative velocity and decrease thereafter. The curves for $\theta_0 \leq 30$ degrees approach asymptotically the $c_{D_c} = 0$ abcissa from the positive side only, whereas the curves $\theta_0 > 30$ degrees have temporarily negative drag coefficients corresponding to a feedback of vorticity. Two experimental curves have been drawn for comparison: Schwabe [8] and Sarpkaya's data [9] refer to a cylinder started impulsively from rest in laminar flow. After an early maximum of $c_{D_c} \approx 1.6$ for Sarpkaya's data [9], the crossflow drag curve asymptotically approaches the steady state value of $c_{D_c} \approx 1.1$, corresponding to a Reynolds number range of Re $\propto 10^4$ to 10^5, which places the experiments

into the laminar Reynolds number range. We observe that with increasing separation angle, the wake becomes narrower and the maxima of the crossflow drag curves decrease. This analytical result follows, in principle, the real flow around a cylinder. We observe that the time scale of the abscissa can be converted to a length scale; thus, Δx represents the body station downstream of the axial separation point. Existing theories were conceived along these theoretical lines. Brown and Michael [10] applied this model to the calculation of the nonlinear lift of slender delta wings with conical flow fields. Bryson [4], by improving the earlier model of Hill [3], applied it to cones and simple bodies of revolution. Schindel [11] used the same flow model and by comparison with experimental data fixed the axial starting point of the vortex, its initial strength, and the separation point for the laminar and turbulent case. Difficulties are encountered when applying Schindel's method [11] to calculate the normal force coefficients for long slender bodies, since the theory is not valid beyond

$$\frac{L}{R} \tan \alpha < 8.$$

The body in Figure 4 is an example where the above relation fails near the aft end of the cylinder. Therefore, Schindel's theory was modified, and whenever the crossflow drag curve c_{D_c} passes below the steady state value $c_{D_c}^* = f(Re, M_\infty)$, this value was taken and kept constant over the rest of the body, provided the body diameter is kept constant. The normal force coefficient c_N is a component of the crossflow drag.

The drag coefficient of a circular cylinder is a function of the Reynolds number and the Mach number. Up to the critical Mach number, the $c_{D_c}^*$ (Re, M_∞) curve is mildly dependent on the Mach number. All curves with the Mach number as a parameter show the same behavior in the laminar, transition, and turbulent Reynolds number range. Beyond the critical Mach number of $M_\infty \approx 0.4$ (cylinder normal to the flow), the transition range with low $c_{D_c}^*$ and rearward wandering separation point shifts to higher Reynolds numbers. The crossflow drag curve flattens and becomes almost completely a function of the Mach number [12, 13]. Thus, by the modification of Schindel's [11] or Bryson's [4] theory, another free parameter, which has to come from experiment, has been introduced. For the calculation of the cases represented in the following

figures, we retain the two-dimensional model and apply it to the cylindrical configurations at an angle of attack. In this way, the crossflow Mach number and Reynolds number determine the separation point and the level of the crossflow drag curve. For large angles of attack, $\alpha \rightarrow 90$ degrees, the assumption is justified. For small angles $\alpha \propto 10$ degrees to 30 degrees, however, the assumption is at best only qualitatively correct since the boundary layer of a slanted cylinder is quite different from that of a cylinder in normal flow. In a slanted cylinder the separation points move farther downstream, the wake becomes thinner, and consequently the drag becomes smaller.

In Figure 5 the nonlinear normal force as calculated by the theory is compared with the experimental normal force coefficient of a 10-caliber ogive-cylinder. The curve labeled "turbulent" was obtained by assuming a turbulent separation line on the ogive cylinder surface and a steady state crossflow drag coefficient of $c_{D_c} \approx 0.4$ to 0.7 according to increasing crossflow Reynolds number and crossflow Mach number (which stayed below 0.4). The curve labeled "laminar" overestimates the nonlinear lift. For this case, it was assumed that the boundary layer has a laminar separation along the entire length of the body. Although this is a rather crude and simplified assumption for the boundary layer, this example points out the difficulties we are faced with and the shortcomings of the theory.
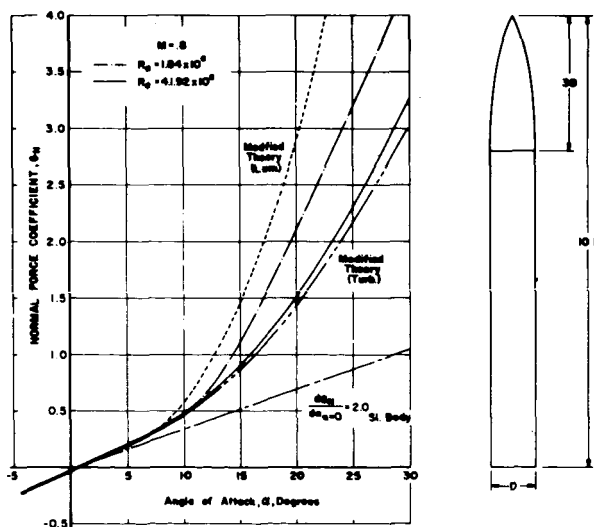
FIGURE 5. VARIATION OF NORMAL FORCE COEFFICIENT WITH ANGLE OF ATTACK FOR CONFIGURATION B

Although no vortex shedding has been observed in the turbulent wake of certain bodies, the model still gives reasonable answers. This occurs because the steady state crossflow drag coefficient, $c_{D_c}{}^*$ is reached much sooner for the turbulent flow than for the laminar flow; therefore, the viscous part of the normal force depends predominantly on the experimentally determined parameter, $c_{D_c}{}^*$.

Figure 6 shows the nonlinear lift of an ogive-cylinder frustum-cylinder body for a Mach number of $M_\infty = 2.0$ and a Reynolds number range of 2.2 to 8.4×10^6. The experiments showed no essential influence of the Reynolds number, at least in this range and for these angles of attack. One possible and logical explanation is that the boundary layer was turbulent over most of the body as a result of secondary shock systems and shock/boundary-layer interaction in front of the frustum. It was therefore attempted to predict the nonlinear normal force coefficient for this configuration. The assumptions were that the laminar-turbulent axial transition point was located at $x \propto 0.20L$ from the nose of the body downstream in front of the frustum, and that the steady state crossflow drag coefficient is a function of the crossflow Mach and Reynolds number and was chosen according to Reference 12. At an angle of attack of
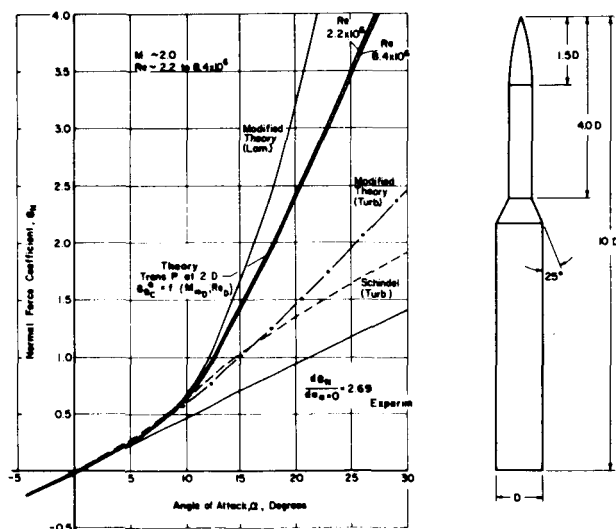
$\alpha \approx 12$ degrees, the critical Mach number based on the normal flow was reached. A very good agreement between theory and experiment is obtained.

Another area of considerable interest is the possibility of vortex bursting on bodies of revolution at high angles of attack analogous to what is observed above delta wings at high angle of attack. This usually happens in an asymmetric fashion producing considerable side forces on the body. Bryson's [4] symmetric two-vortex model is identical with Mangler and Smith's [14] vortex model for delta wings in conical flow. Bryson's [4] model for bodies of revolution could be improved by considering the wake results obtained for delta wings. The vortex-bursting phenomenon might happen above bodies of revolution when a vortex passes a shock front or penetrates a region of an adverse pressure gradient. The supersonic wake flow in front of and above the frustrum of configuration C in Figure 6 will be surveyed to obtain some insight into the flow behavior. Since vortex flows are always connected with high axial velocities in the vortex core, the slender body assumptions are violated. Consequently, we should develop a three-dimensional vortex model.

CONCLUSIONS

We conclude that the approach to better define the high angle of attack rocket aerodynamics depends on a combined experimental and theoretical effort. A pure experimental approach to the problem is inadequate because of the Reynolds number deficiencies of existing test facilities.

The theory, as outlined, depends strongly on the exact location of the vortex separation line, and since the three-dimensional boundary layer theory is not yet in a stage where it can readily be applied, this part must come from the experiment.

Vortex bursting makes the introduction of a three-dimensional model necessary.

The experimental investigation now being conducted will help us to better understand the flow mechanism about bodies so that the theoretical model can be improved.

FIGURE 6. VARIATION OF NORMAL FORCE COEFFICIENT WITH ANGLE OF ATTACK FOR CONFIGURATION C

REFERENCES

1. Allen, H. Julian: Pressure Distribution and some Effects of Viscosity on Slender Inclined Bodies of Revolution. NACA Report No. 2044, 1950.

2. Kelly, Howard, R.: The Estimation of Normal Force and Pitching Movement Coefficient for Blunt-Based Bodies of Revolution at Large Angles of Attack. U. S. Naval Ordnance Test Station, Tech. Memo. 998, July 1953.

3. Hill, J. A. F.: A Nonlinear Theory of the Lift on Slender Bodies of Revolution. Proceedings U. S. Navy Symposium on Aeroballistics, NOVARD Report 5338, October 1954.

4. Bryson, A. E., Jr.: Symmetric Vortex Separation on Circular Cylinders and Cones. Appl. Mech., vol. 26, no. 4, December 1959.

5. Schindel, Leon H.: Effect of Vortex Separation on Lifting Bodies of Elliptic Cross-Section. MIT Aeroph. Lab. Tech. Report 118, September 1965.

6. Simon, E. H.: The George C. Marshall Space Flight Center 14x14 Inch Trisonic Wind Tunnel. Tech. Handbook, NASA TM X-53185, December 1964.

7. Wolf, J. A.: LTV High Speed Wind Tunnel. AER-EIR-13552-A, Undated.

8. Schwabe, M.: Über Druckermittlung in der nicht stationären ebenen Strömung. Ingenieur Archiv, Bd. VI, no. 1, 1935.

9. Sarpkaya, T.: Separated Flow about Lifting Bodies and Impulsive Flow about Cylinders. AIAA J., vol. 4, no. 3, March 1966.

10. Brown, C. E.; and Michael, W. H., Jr.: Effect of Leading Edge Separation on the Lift of a Delta Wing. J. Aero. Sci., vol. 21, no. 10, October 1954.

11. Schindel, Leon H.: Vortex Separation on Slender Bodies of Elliptic Cross-Section. MIT Aeroph. Lab. Tech., Report 138, August 1967.

12. Gowen, Forrest E.; and Perkins, Edward W.: Drag of Circular Cylinders for a Wide Range of Reynolds Numbers and Mach Numbers. NACA Tech. Note 2960, June 1953.

13. Naumann, A.; Morsbach, M.; and Kramer, C.: The Conditions of Separation and Vortex Formation past Cylinders. In "Separated Flows," Part 2, AGARD Conf. Proc. no. 4, May 1966.

14. Mangler, K. W.; and Smith, L. H. B.: Calculation of the Flow Past Slender Delta Wings with Leading Edge Separation. Royal Aircraft Est. Tech. Note Aero. 2593, May 1957.

BIBLIOGRAPHY

Allen, H. J. and Perkins, E. W.: A Study of Effects of Viscosity on Flow over Slender Inclined Bodies of Revolution. NACA Report 1048, 1951.

Batchelor, G. K.: Axial Flow in Trailing Line Vortices. J. Fluid Mech., 1964, vol. 20, Part 4, pp. 645-658.

Buchinskaya, E. K. and Pochkina, K. A.: Investigation of a Vortex Wake behind a Body of Revolution Promyshlennaya Aerodinamika No. 27. pp. 121-144, 1966, or Translation John Hopkins Univ., APL TG 230-T546, February 28, 1968.

BIBLIOGRAPHY (Concluded)

Chang, I. Dee: A Study of Flow Separation Based on a Linearized Model I. Flow Past a Circular Cylinder. Stanford Univ. Report SUDAER No. 199, AD-450809, July 1964.

Crabbe, R. S.: Flow Separation about Elliptic Cylinders. AIAA Paper No. 65-396, AIAA Second Annual Meeting, San Francisco, July 26-29, 1965.

Earnshaw; and Kavforce, J. A.: Low-Speed Wind Tunnel Experiments on a Series of Sharp-Edged Delta Wings. ARC Rpt. and Memo., R & D No. 3424, 1966.

Friberg, Eric G.: Measurement of Vortex Separation, Part 1 and Part 2. MIT Aeroph. Lab. Tech. Report 114 and 115, August 1965.

Hummel, D.: Experimentelle Untersuchungen der Strömung auf der Saugseite eines schlanken Delta-flügels. Zfw. 13 (1965), Heft 7, July 1965, pp. 247-252.

Jorgensen, L. H. and Perkins, E. W.: Investigations of Some Wake Vortex Characteristics of an Inclined Ogive-Cylinder Body at Mach Number 2. NACA Report 1371, 1958.

Küchemann, D.; and Weber, J.: Vortex Motion. ZAMM 45, Heft 7/8 December.

Maltleg, R. L.; and Peckham, D. H.: Low Speed Studies of the Vortex Patterns above Inclined Slender Bodies Using a New Technique. RAE Tech. Note No. Aero. 2482, March 1957.

Maskell, E. C.: Flow Separation in Three-Dimensions. RAE Report No. Aero. 2565, November 1955.

Mello, J. F.: Investigation of Normal Force Distribution and Wake Vortex Characteristics of Bodies of Revolution at Supersonic Speeds. J. Aerosp. Sci., vol. 26, no. 3, March 1959.

Rainbird, William John: Turbulent Boundary Layer Growth and Separation on a Yawed 12 1/2 Degree Cone at Mach Number 1.8 and 4.25. AIAA Paper No. 68-98, AIAA Sixth Aerosp. Sci. Mtg., New York, January 22-24, 1968.

Rainbird, W. J.; Crabbe, R. S.; and Jurewitz, L. S.: A Water Tunnel Investigation of the Flow Separation about Circular Cones at Incidence. Nat. Res. Council of Canada Aero. Report LR-457, July 1966.

Rogers, E. J.: The Flow and Turbulence Effects of a Body of Revolution and its Stabilizing Surfaces when at Small Angle of Attack. ASME Paper No. 65-FE-5.

Schlichting, Hermann: Boundary Layer Theory. Fourth Edition, McGraw-Hill Book Company, Inc. 1960.

Tinling, B. E.; and Allen, C. Q.: An Investigation of the Normal Force and Vortex-Wake Characteristics of an Ogive-Cylinder-Body at Subsonic Speeds. NASA TN D-1297, April 1962.

LUDWIEG TUBE PILOT TEST AND HIGH REYNOLDS NUMBER TEST EQUIPMENT

By

John W. Davis

SUMMARY

To obtain data concerning Reynolds number effects at test conditions considerably higher than now being simulated in existing facilities, MSFC has initiated the development of a relatively simple and inexpensive wind tunnel which will be capable of simulating Reynolds numbers of the order of 400 million (based on vehicle length) over the subsonic, transonic, and supersonic speed ranges. This test equipment and its operating concept are described, along with experimental results obtained in a pilot test program.

INTRODUCTION

Aerodynamic problems associated with large boost vehicles, such as load distribution at high angles of attack, shock-induced boundary layer separation, aerodynamic noise, and certain aspects of base heating, seem to exhibit Reynolds number effects of an unknown character and magnitude, even with a turbulent boundary layer. Figure 1 shows that the capabilities of existing facilities are about one order of magnitude below the simulation requirements for present flight conditions. In light of this, we have conducted pilot tests on an advanced facility concept
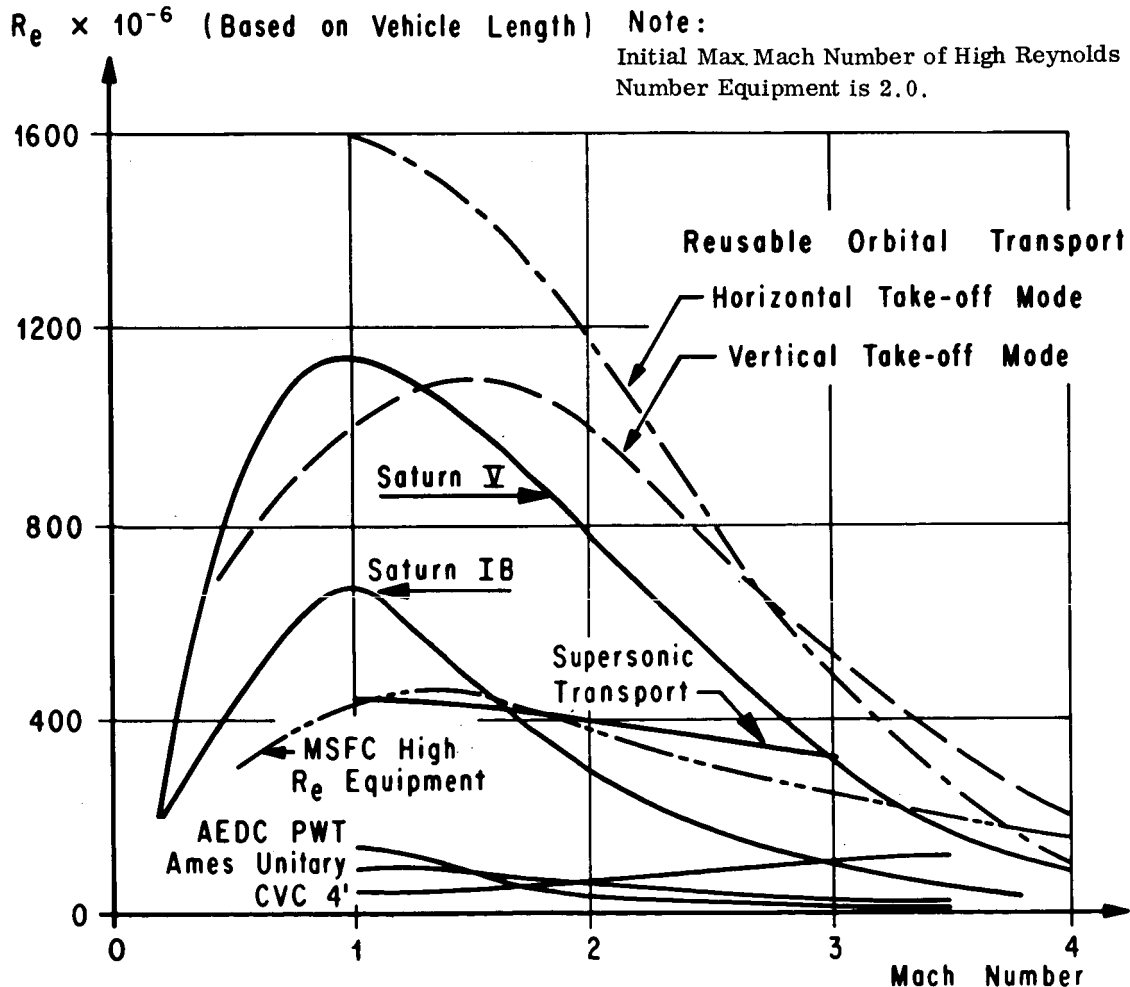
FIGURE 1. REYNOLDS NUMBER SIMULATION REQUIREMENTS

which would be capable of handling these problems, and we have also initiated the development of new test equipment capable of simulating Reynolds numbers of the order of 400×10^6 (based on vehicle length) over the subsonic, transonic, and supersonic speed ranges for test periods in excess of 100 msec. This concept is technically capable of fully simulating the required flight Reynolds numbers in excess of 1000 $\times 10^6$. The Reynolds number level of 400 million was selected on the basis of funding considerations.

OPERATING CONCEPT

The operating principle for the new facility is indicated in Figure 2. The test medium is stored in a supply tube and held there by means of a diaphragm or a quick-acting valve. When the diaphragm is broken, a rearward-facing centered-rarefaction fan propagates throughout the test section and nozzle into the supply tube, setting the gas in motion and somewhat lowering the pressure and temperature. Rarefaction waves may pass through the nozzle into the supply tube only until sonic velocity is reached at the nozzle throat. At this point, a shock wave system forms and gradually moves to the nozzle exit. The remainder of the rarefaction fan weakens the shock system, and the shock eventually is swept through the test section, commencing the period of steady flow. Also, after the rupturing of the diaphragm, a shock wave and contact surface proceed downstream from the diaphragm unit. Between the time when the nozzle starting process has ended and when the head of the reflected rarefaction fan arrives at the nozzle throat, useful testing may be accomplished in the test section under constant reservoir conditions. Subsequent test periods can be obtained at reduced reservoir conditions between re-reflected wave processes in the supply tube. Normally, the test gas would be discharged to the atmosphere after passing through the test section.

PILOT TESTS

The original concept was proposed by Ludwieg [1] in 1955 and was oriented toward supersonic-hypersonic speed ranges. When the need for high Reynolds data in the transonic range was recognized, we became interested in this concept because of its economy and applicability to high pressures and therefore to high Reynolds numbers. However, its
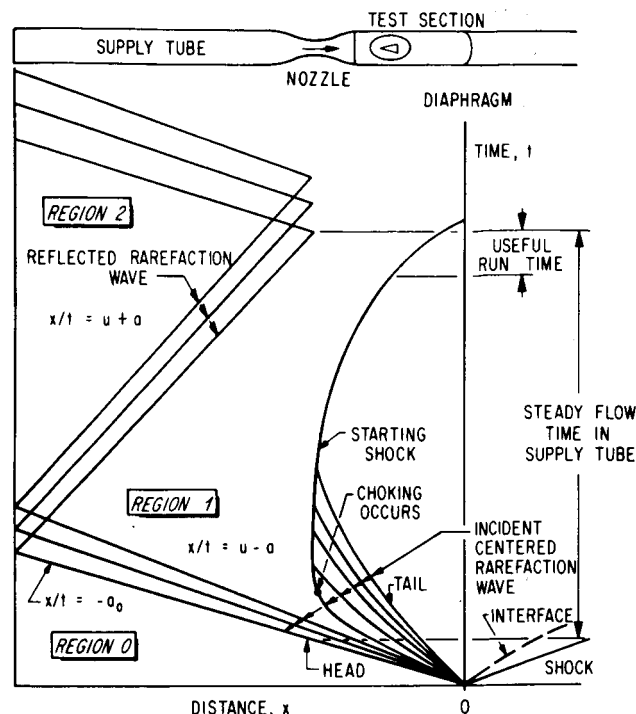
FIGURE 2. WAVE DIAGRAM FOR DOWNSTREAM DIAPHRAGM LOCATION INDICATING BASIC FACILITY CONCEPT

feasibility in the transonic speed range had not been established, and the ability of designing the test equipment to withstand the large starting loads was seriously questioned. Furthermore, no studies had been made which allowed insight into optimizing the geometry. To provide answers to these questions, a series of experimental programs was conducted, the results of which are briefly described in the following paragraphs. A schematic drawing indicating the major components of the supersonic test configuration is shown in Figure 3. The subsonic version of the facility is similar to this supersonic one, except that the converging-diverging nozzle is replaced by a sonic nozzle, and a choking device is installed downstream of the test section. A transonic version, with a perforated wall test section, has also been tested.

Some experimental results [2] are summarized in Figure 4. Test Mach numbers from 0.3 to 3.5 show start times from about 10 to 32 msec, with the largest start times required in the transonic range. A fivefold increase in plenum chamber volume increased the maximum transonic starting time from 32 to about 50 msec. Placing the diaphragm upstream

SUPPLY TUBE
(not shown)

D = 14.63 cm
L = 1118 cm

SUPERSONIC
NOZZLE

D = 2.54 cm
L = 38.1 cm

MODEL
SUPPORT

D = 7.36 cm
L = 13.34 cm

DIAPHRAGM
CUTTER

D = 10.2 cm
L = 15.8 cm

MUFFLER

MODEL

DIAPHRAGM

SETTLING CHAMBER

D_1 = 14.63 cm
D_2 = 20.96 cm
L   = 59.69 cm

TEST SECTION

D = 6.63 cm
L = 26.7 cm

TRANSITION

D_1 = 7.36 cm
D_2 = 10.2 cm
L   = 15.2 cm

TRANSITION

D_1 = 10.2 cm
D_2 = 7.36 cm
L   = 15.2 cm

VACUUM
TANK
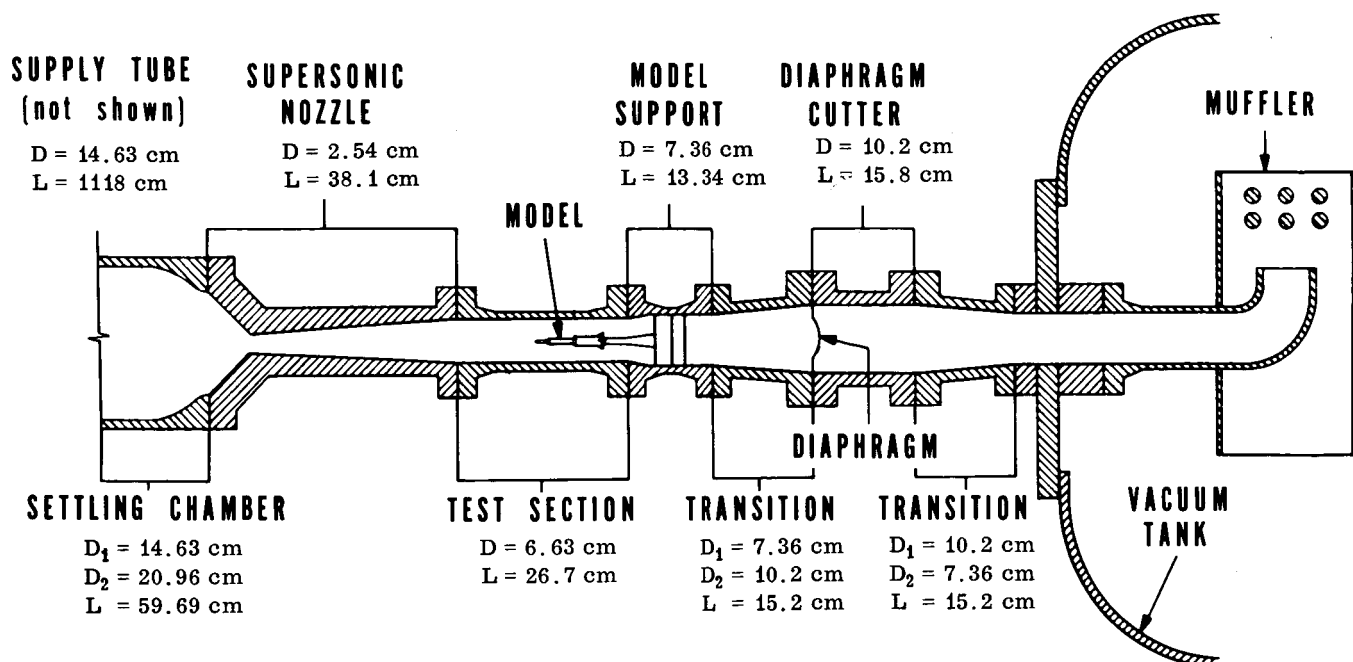
FIGURE 3.   FEASIBILITY MODEL HIGH REYNOLDS NUMBER FACILITY
(Supersonic test section configuration, downstream diaphragm position, settling chamber installed)

SYMBOL	DIAPHRAGM POSITION	TEST SECTION	PLENUM
△	UPSTREAM	SUBSONIC	N. A.
▽	DOWNSTREAM	SUBSONIC	N. A.
▢	UPSTREAM	TRANSONIC	1
○	DOWNSTREAM	TRANSONIC	1
○	UPSTREAM	SUPERSONIC	N. A.
◇	DOWNSTREAM	SUPERSONIC	N. A.

START TIME (millisecond)
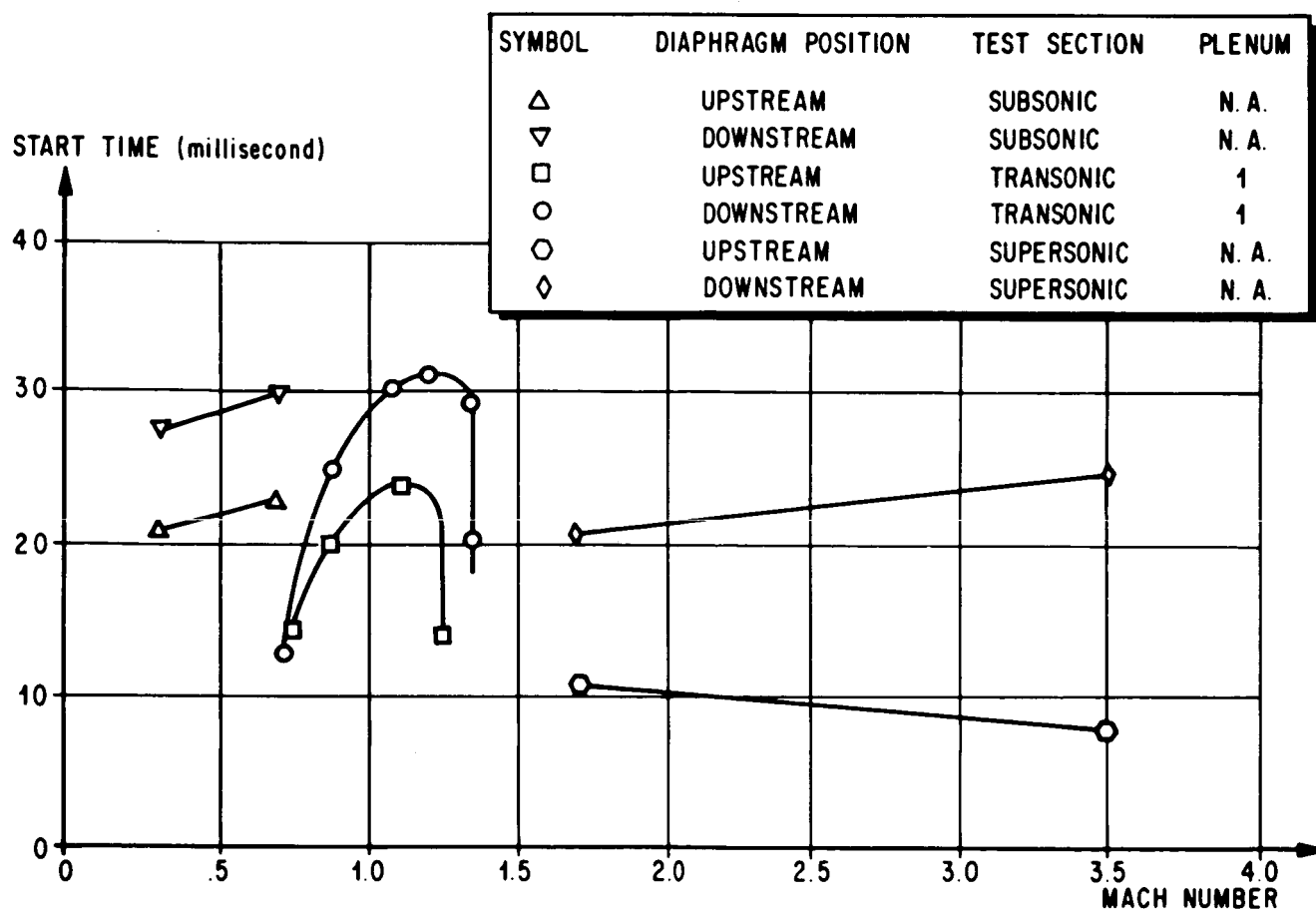
FIGURE 4.   TUBE TUNNEL START TIME CHARACTERISTICS OVER RANGE OF MACH NUMBERS SURVEYED

of the nozzle, with a corresponding simplification of the wave process, gave starting times as much as 55 percent lower than those for a downstream diaphragm. It is apparent in Figure 4 that choking of the perforated walls occurs near Mach 1.3, thus restricting further increase in flow through the wall.

Unsteady expansion theory and experimental measurements show good agreement over the range of contraction ratios studied. Reynolds number effects on the various flow processes were negligible for supply tube pressures from 35 to 700 N/cm² (50 to 1000 psia).

The magnitude of model starting loads perhaps represents the most severe problem in high Reynolds number testing. Because of the small size of the test hardware, the precise measurement of model starting loads was considered impractical. However, it seemed that an assessment of starting load trends could be obtained by measuring the relationship of starting loads during the transient starting process to those loads existing during the period of steady flow. A model typical of the Saturn vehicle, whose static stability characteristics were known, was tested without the benefit of inertial compensation. Some of the results are shown in Figure 5 as a function of Mach number.
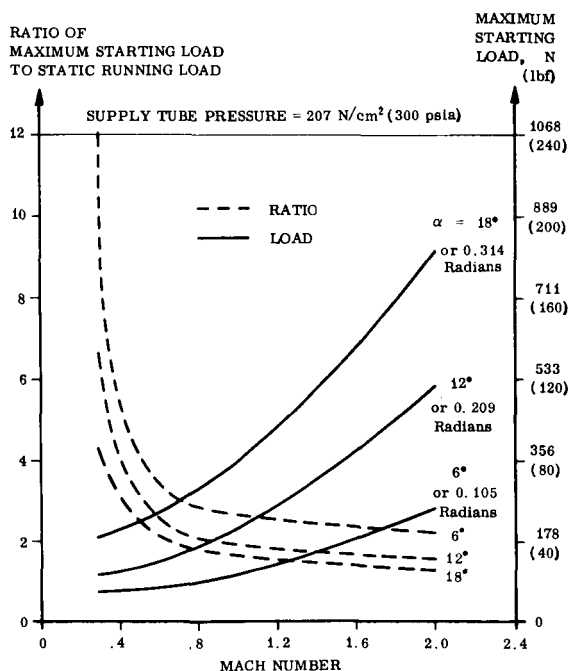
FIGURE 5. VARIATION OF STARTING LOAD TO
RUNNING LOAD RATIO WITH MACH NUMBER

The ratio of starting loads to running loads decreased somewhat with angle of attack, as well as with pressure and Mach number. While the ratio is largest at low subsonic Mach numbers, the worst design condition occurs at higher Mach numbers where the static running load is much larger and hence the starting load, being the product of these values, is larger. Designs using high strength materials to accommodate these starting loads appear to be within the state of the art.

DESCRIPTION OF HIGH REYNOLDS NUMBER TEST EQUIPMENT

The feasibility of this testing technique having been established, the development of a pilot model tunnel has been undertaken at Marshall. This tunnel will be capable of simulating Reynolds numbers as high as 440 x 10⁶, based on vehicle length, for test periods as long as 650 msec. Test Mach numbers will range from 0.2 to 3.5 using dry air, initially stored at pressures as high as 493 N/cm² (715 psia) and at ambient temperature, as the test medium. The expected run rate is 3 to 5 runs per day. The basic configuration is shown in Figure 6.

The supply tube will have an inside diameter of 132 cm (52 in.) and a length of 121.9 m (400 ft.). The recoil force, which ranges to approximately 4 448 222 N (1 000 000 lbf), will be restrained by a thrust anchor located near the downstream end of the supply tube.

The stilling chamber will have a contraction ratio of 6 to 1 and an entrance half-angle of 0.0698 radians (4 degrees). Axisymmetric contoured nozzles will be incorporated to accommodate the high pressure levels. The attendant problems of focusing effects and flow visualization difficulties must, however, be accepted. Initially, nozzles will be available for Mach numbers 1.0, 1.4, 1.7, and 2.0. Ultimately, nozzles will be provided to allow testing to Mach number 3.5. Unless the test gas is heated, testing above Mach number 3.5 will not be possible because of liquefaction.

Two 81.4-cm (32-in.) diameter test sections are to be provided: a 162.5-cm (64-in) long supersonic test section and a 254-cm (100-in.) long transonic test section. Two 25.4-cm (10-in.) diameter windows will be installed in the supersonic test section for flow visualization studies. The transonic section will have walls of 10 percent maximum porosity, with holes inclined 0.524 radians (30 degrees) to the
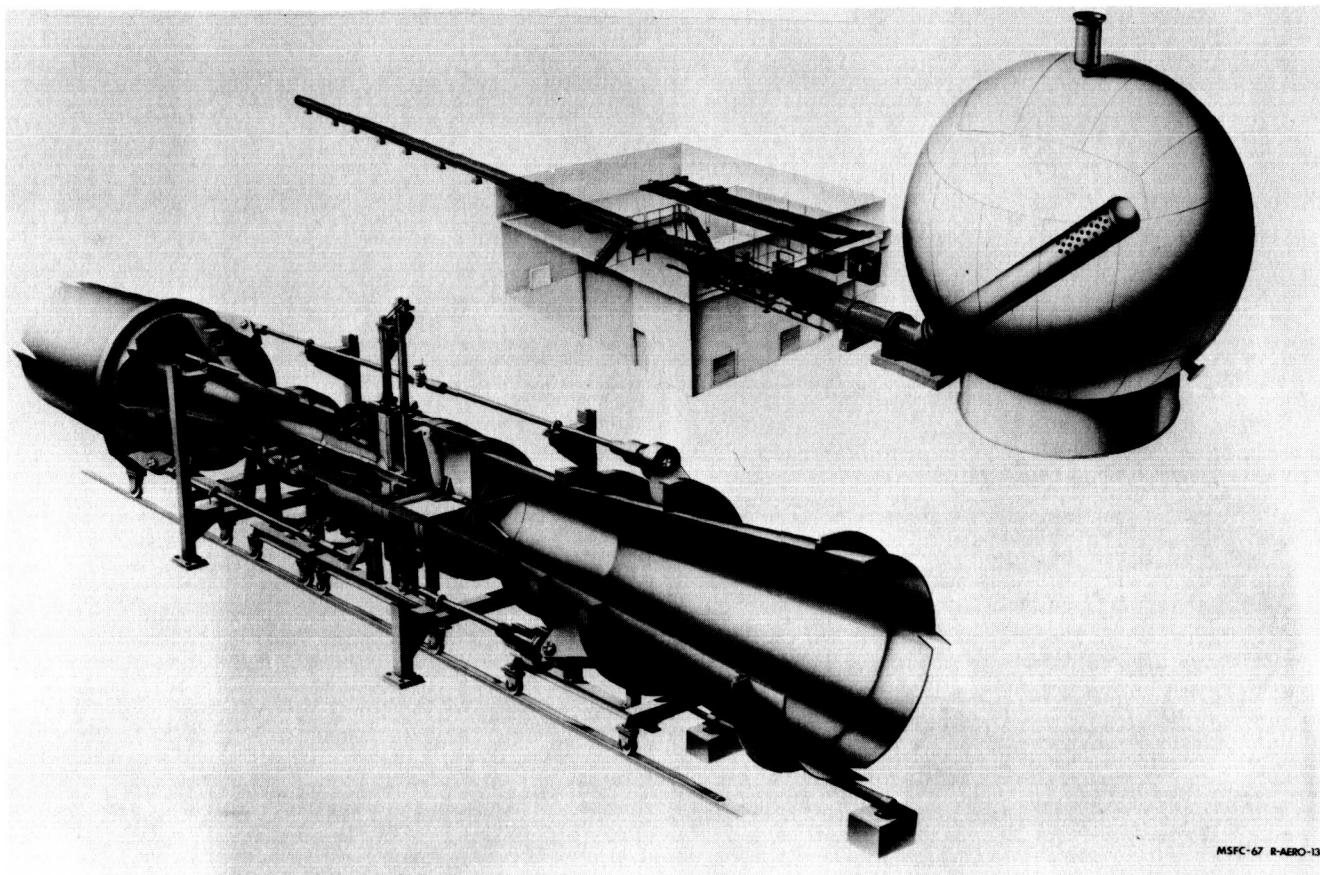
FIGURE 6. HIGH REYNOLDS NUMBER TEST EQUIPMENT

tunnel centerline and with taper strips in the up-stream end. Plenum chamber flow, obtained by ejector pumping action of the primary flow, will be controlled by variable orifices located at the downstream end of the plenum chamber. Subsonic testing will be possible in either test section using the sonic nozzle and choking flaps located within the model support unit. Test articles will be sting-mounted on a conventional model support unit capable of a ±0.314 radians (± 18 degrees) motion in the pitch plane.

The flow initiator will be a 122 cm (48-in.) diameter unit incorporating a diaphragm, consisting of multiple layers of Mylar and bearing on a four-element support. A cutter unit housed within the centerbody will shear the diaphragm into four petals, commencing the flow process. Test gas will then flow through a telescoping diffuser and a 0.785-radian (45-degree) elbow into a 15.24-m (50-ft.) diameter sphere, which will attenuate the sound generated by the exhausting gas.

PRESENT STATUS

The present status of this effort is shown in Figure 7. The building and receiver sphere are complete, and the supply tube, stilling chamber, tension rod system, and telescoping diffuser have been installed. Other components such as nozzles, test section, and model support system should arrive by November 1968. It is expected that this equipment will be operational late this year, and that useful testing can be commenced early in 1969.

15
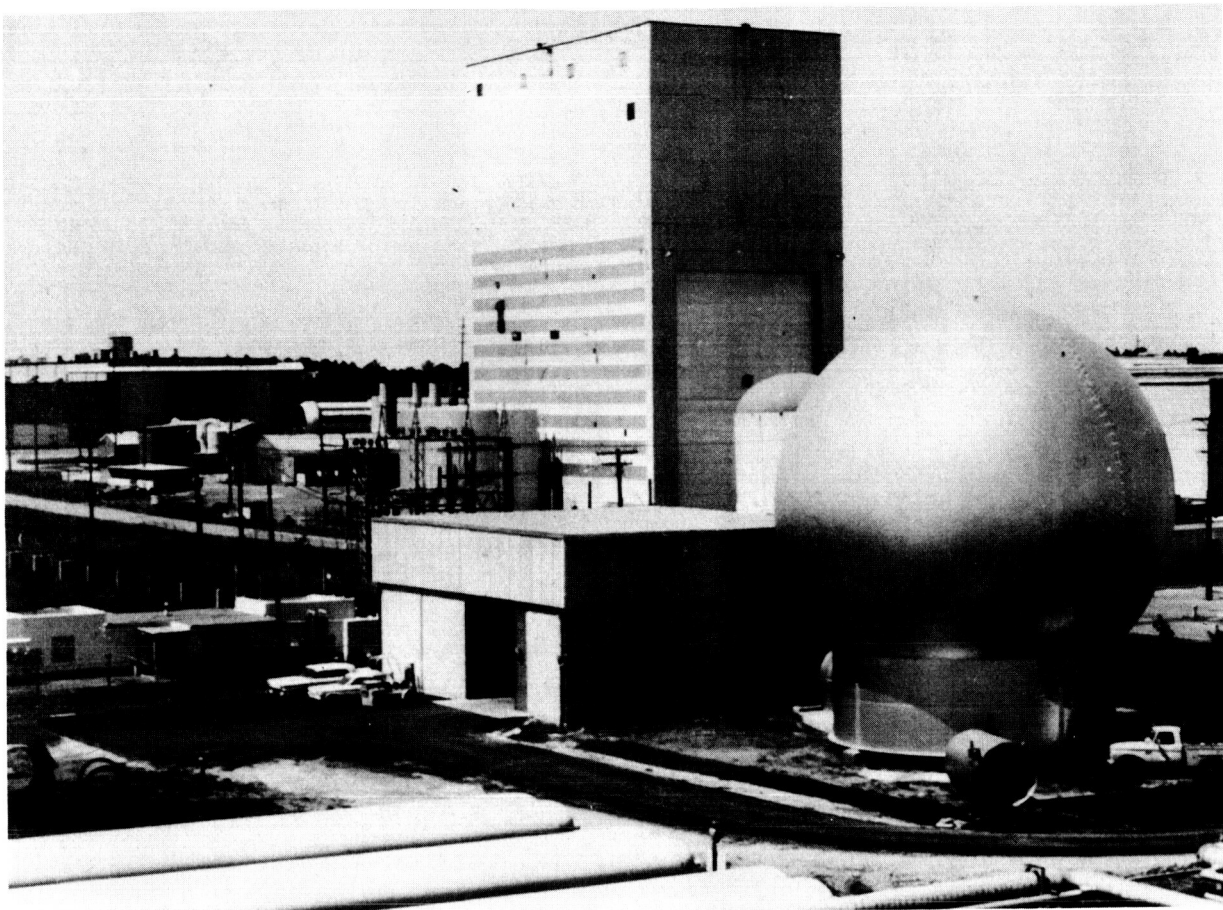
FIGURE 7. CONSTRUCTION OF TEST EQUIPMENT

REFERENCES

1. Ludwieg, H.: Tube Wind Tunnel: A Special Type of Blow-Down Wind Tunnel. July 1957, NATO Advisory Group for Aeronautical Research and Development, Report 143, Unclassified.

2. Davis, John W.; and Gwin, Hal S.: Feasibility Studies of a Short Duration High Reynolds Number Tube Wind Tunnel. NASA TM X-53571, January 3, 1967, Unclassified.

THEORETICAL ANALYSIS OF THE STARTING PROCESS IN THE LUDWIEG TUBE

By

John D. Warmbrod and Heinz G. Struck

SUMMARY

A theoretical analysis assuming quasi-one-dimensional flow through a duct is undertaken to better understand the time-dependent flow phenomenon that takes place in the Ludwieg tube wind tunnel during the early development of the flow. Wave interactions and boundary conditions which can occur in one-dimensional time-dependent flow, such as shock formation, shock-shock interactions, and shock-contact surface interactions are discussed. Theoretical results are compared with experimental data from a pilot model of the large scale Ludwieg tube wind tunnel. Agreement between theory and experiment was good when considering the assumptions made for the theoretical model.

LIST OF SYMBOLS

Symbol	Definition
a	nondimensional speed of sound a^*/a_o^*
A	cross-sectional area
c_p	specific heat at constant pressure
f	nondimensional quantity $\dfrac{f^* L_o}{a_o^{*2}}$ where f^* is the sum of body and dissipative forces per unit mass
L_o	total length of facility (with dimensions)
p	nondimensional static pressure p^*/p_o^*
P	right running characteristic variable
Q	left running characteristic variable
R	gas constant
S	nondimensional specific entropy s/c_p $(\gamma-1)$
t	nondimensional time $a_o^* t^*/L_o$
T	nondimensional temperature T^*/T_o^*
u	nondimensional flow velocity u^*/a_o^*
γ	ratio of specific heats
ρ	nondimensional density
Ψ	nondimensional quantity $\dfrac{L_o a_o^* \Psi^*}{\gamma A p_o^*}$ where Ψ^* represents the mass flow removed through the walls per unit length

Subscripts	Definition
o	reference conditions which for the case at hand were the conditions on the right side of the diaphragm before rupture

Superscripts	
*	dimensional quantities

INTRODUCTION

Davis [1] discussed the geometrical aspects, operating principles, and some pilot test results of a Ludwieg tube wind tunnel capable of simulating Reynolds numbers of the order experienced during the flight of Saturn vehicles. The approval for constructing a wind tunnel of the Ludwieg tube type at MSFC led to the need for a theoretical investigation to better understand the starting processes of the facility.

The complete system of partial differential equations that describe the flow of a compressible fluid through a variable cross-sectional duct are, for all practical purposes, too complicated to solve in their most general form. The usual procedure to obtain

analytical solutions for a particular flow problem is to reduce the general equations to a manageable form. This reduction is ordinarily accomplished by omitting those terms in the equations that are believed to be of small magnitude. For the problem of flow through a duct, the cross-sectional dimensions of the duct are considered to be small compared to the length dimensions. We are thus naturally led to the simplification of assuming the flow in the duct to be quasi-one-dimensional. This simply means that all the flow properties are assumed to be uniform over any cross section of the duct at any time.

For the past 10 to 15 years, many aerospace companies and government agencies have conducted studies which led to the development of computer programs that solved the inviscid supersonic flow field problems by the method of characteristics. With few exceptions, these programs were concerned with solving the steady state flow problems in two or three dimensions. The automated application of the method of characteristics for one-dimensional time-dependent flow has been, however, relatively ignored.

It is also of interest to point out that the method of characteristics can be applied only in the supersonic regime for the steady-state problems, whereas a continuous application of the method through all regimes is possible for the time-dependent problems.

The construction of a computer program for the steady-state flow problems seems to be somewhat less complicated than for the unsteady problems. For the steady state case, the computational philosophy generally involves calculating along characteristic waves which are terminated by known boundaries, such as a shock wave or a body. In the unsteady case, many combinations of time-dependent boundary conditions and discontinuities can occur as a result of the complicated wave interactions that are encountered in time-dependent flows. These boundary conditions or discontinuities consist of such phenomena as shock formation, shock-shock collisions, shocks reflecting off a wall and shock-contact surface interactions. Some of these occurrences will be shown later in a wave diagram.

This paper presents results of a computer program developed by the Fluid Mechanics Research Office for a one-dimensional time-dependent theoretical model of the gas flow through the Ludwieg tube wind tunnel which is presently under construction at MSFC. Details of the theory and computer program have been published in Reference 2.

THEORETICAL MODEL

Equations (1-4) present the Eulerian form of the hyperbolic partial differential equations which describe the time-dependent one-dimensional compressible flow of gas through a duct.

Continuity Equation

$$\frac{\partial(\rho^* A)}{\partial t^*} + \frac{\partial(\rho^* u^* A)}{\partial x^*} + \Psi^* = 0.$$

Momentum Equation

$$\frac{Du^*}{Dt^*} = \frac{\partial u^*}{\partial t^*} + u^* \frac{\partial u^*}{\partial x^*} = -\frac{1}{\rho^*} \frac{\partial p^*}{\partial x^*} + f^*.$$

Equation of State

$$a^{*2} = \gamma \frac{p^*}{\rho^*} = \gamma R T^*.$$

Integrated Form of the First Law of Thermodynamics

$$s^* - s_0^* = c_p \ln \frac{T^*}{T_0^*} - c_p \frac{\gamma - 1}{\gamma} \ln \frac{p^*}{p_0^*}.$$

The subscript o indicates some state from which entropy changes are measured. The star superscript refers to dimensional quantities. For a definition of the symbols, the reader should refer to the LIST OF SYMBOLS. The underlying assumptions in the derivation of the above equations are as follows:

1. All quantities depend on the time t^* and a single coordinate x^*.

2. There is only one velocity component u^* and that is in the x^*-direction.

3. The gas follows the ideal gas laws, and the values of the specific heat are constant.

4. All body and dissipative forces are lumped into a resultant force per unit mass, which is denoted in the momentum equation by f^*.

5. Gas is permitted to leave the duct through the walls and is denoted in the continuity equation by Ψ^*, which is defined as the mass flow through the walls per unit length.

It is customary to solve the above set of equations by a numerical integration procedure along a set of curves in the independent variable (x, t) plane. These curves are usually defined as characteristic curves and particle paths, and the numerical method is referred to as the method of characteristics. Reference 2 presents the derivation of the characteristic equations from the partial differential equations, which are presented here in their final form.

$$\frac{\delta_+ P}{\delta t} = - au \frac{\partial \ln A}{\partial x} - a \frac{\partial \ln A}{\partial t} + a \frac{\delta_+ S}{\delta t}$$
$$+ (\gamma - 1) a \frac{DS}{Dt} + f - \Psi a^{(\gamma-3)/(\gamma-1)} e^{\gamma(S-S_o)} . \tag{5}$$

$$\frac{\delta_- Q}{\delta t} = - au \frac{\partial \ln A}{\partial x} - a \frac{\partial \ln A}{\partial t} + a \frac{\delta_- S}{\delta t}$$
$$+ (\gamma - 1) a \frac{DS}{Dt} - f - \Psi a^{(\gamma-3)/(\gamma-1)} e^{\gamma(S-S_o)} . \tag{6}$$

The entropy condition which must be prescribed for any problem is given in a general form as

$$\frac{DS}{Dt} = F(a, u, S, x, t) . \tag{7}$$

and this completes the system of equations for the three dependent variables, a, u, and S.

The special symbols for the differential operators are defined as

$$\frac{\delta_+}{\delta t} = \frac{\partial}{\partial t} + (u + a) \frac{\partial}{\partial x} . \tag{8}$$

$$\frac{\delta_-}{\delta t} = \frac{\partial}{\partial t} + (u - a) \frac{\partial}{\partial x} . \tag{9}$$

$$\frac{D}{Dt} = \frac{\partial}{\partial t} + u \frac{\partial}{\partial x} . \tag{10}$$

All quantities are nondimensional in the above equations (see LIST OF SYMBOLS). Equations (5) through (7) form a system of three linear first-order equations for three dependent variables, a, u, and S, that will be solved by means of a step-by-step procedure. The parameters P, Q, and S vary along curves in the (x, t)-plane that satisfy

$$\frac{dx}{dt} = u + a \qquad \text{for P,} \tag{11}$$

$$\frac{dx}{dt} = u - a \qquad \text{for Q,} \tag{12}$$

$$\frac{dx}{dt} = u \qquad \text{for S.} \tag{13}$$

The characteristic variables are defined by the relations

$$P = \frac{2}{\gamma - 1} a + u \tag{14}$$

and

$$Q = \frac{2}{\gamma - 1} a - u. \tag{15}$$

The details of the calculation procedure for solving numerically the system of equations (5) through (7) are given in Reference 2. The effects of boundary layer and mass flow through the walls of the duct were not considered for the results presented in this paper.

The prescribed entropy condition for the problem at hand is given by

$$\frac{DS}{Dt} = 0, \tag{16}$$

which characterizes the flow as multi-isentropic. This satisfies the condition that each gas particle maintains a constant value of its entropy, but different gas particles may have different entropies. Flows of this type are encountered when a compression wave develops into a shock wave that is gradually growing stronger. This type of phenomenon arises for the Ludwieg tube problem where the cross-sectional area changes and diaphragm rupture lead to shock development with passage of time.

The characteristic equations (5) and (6), which are derived from the basic differential equations, along with the entropy condition equation (16) are solved by taking small step-by-step increments in time, and the solution for each characteristic and entropy equation proceeds along its respective path. The two characteristics were referred to as P in direction u+a, Q in direction u-a, and the entropy S in direction u. Since the entropy S follows a curve of direction u, which is the particle path, two curves of this family can never cross. Whenever two curves of the same family (either P or Q) meet, a discontinuity in the pressure exists at this point. A boundary in the flow is thus established, and this boundary is defined as a normal shock wave. Two types of shock waves can therefore occur, either a P shock (converging of the P characteristics) or a Q shock

(converging of the Q characteristics). The shock wave path will divide the wave diagram into two parts, and on each side certain conditions must be matched. Since it is assumed that changes of the flow variables across a shock wave take place instantaneously, the steady state relationships between flow variables on each side of the shock can be employed. The equations which relate the flow variables upstream and downstream of a stationary normal shock are generally referred to as the Rankine-Hugoniot equations. The derivation of these equations can be found in many references, and therefore will not be repeated here [3,4]. Since we are dealing with shocks that move with respect to the coordinate system, some modifications to the stationary shock relations are necessary. The relations which satisfy the conditions across both types of shocks for the moving shock system have recently been published in Reference 2, and will therefore not be repeated here. The mathematical process at a shock point is to match the normal shock solution with the characteristic solution.

Another discontinuity that can occur is referred to as a contact surface which is defined as a boundary through which no flux of matter can pass. By nature of its definition, the boundary conditions for a contact surface point are that its velocity must be equal to the flow velocity on either side and also that the pressure must be the same on both sides.

THEORETICAL RESULTS

A computer program was developed by the Fluid Mechanics Research Office at MSFC to solve the time-dependent one-dimensional flow through the Ludwieg tube wind tunnel described in Reference 1. Figure 1 shows a wave diagram of the calculated results for the Ludwieg tube wind tunnel with a Mach 2 nozzle mounted upstream of the test section. When the diaphragm is ruptured, the high pressure gas on the left expands and compresses the low pressure gas on the right creating a P shock wave which travels downstream through the undisturbed gas. Proceeding downstream behind the P shock is a contact surface which is the interface between the gas particles that were initially in contact with each side of the diaphragm. Also created at diaphragm rupture is an expansion fan which is bounded on the left by the headwave and on the right by a tailwave. The waves shown in the expansion fan belong to the family of left-running or Q characteristic waves. In Figure 1 we can

see that part of the fan that travels upstream through the nozzle and into the supply tube before choking at the nozzle throat occurs. After the t·oat chokes, no more expansion or Q characteristic waves can pass through the throat position. Subsequently, sonic flow is established as illustrated by the vertically running Q characteristic wave in Figure 1. A physical picture of local flow regimes is given by the slope of the Q characteristics. In regions where they travel toward the left, the flow is subsonic; running vertically, the flow is sonic, and toward the right the flow is supersonic.

Immediately after choking, a Q shock is formed downstream of the nozzle throat (Fig. 1). This shock wave, which becomes stronger as it travels through the expanding portion of the nozzle, is eventually swept through the test section leaving behind it a period of steady flow. The start time for the supersonic cases is defined as the time when the shock that is formed just downstream of the nozzle throat immediately after choking has passed out of the test section.

For this example there were four Q shocks formed within the duct along with the P shock that is created at diaphragm rupture. One incidence of a collision between two of the Q shocks is also shown in Figure 1.

COMPARISON OF THEORETICAL WITH EXPERIMENTAL RESULTS

Figure 2 compares theoretical with experimental static pressures at a station in a supersonic ($M = 2.0$) test section. Measured data were obtained from an 18.75 percent pilot model of the Ludwieg tube wind tunnel with a Mach 2 nozzle. Figure 2 shows that it took approximately 1 msec for the headwave of the expansion fan to reach the station in the test section where the pressures are being recorded. The gas is set in motion at this time with a subsequent dropping of pressure as the velocity increases. In Figure 2 for the theoretical case, choking occurred at the nozzle throat near the 4 msec time elapse. As shown in Figure 1, a normal shock developed downstream of the throat immediately after choking and was eventually swept through the test section leaving a steady flow behind it. The sudden drop in the theoretical static pressure indicates the time when the shock passes through this measuring station in the test section. The theoretical start time for this case is
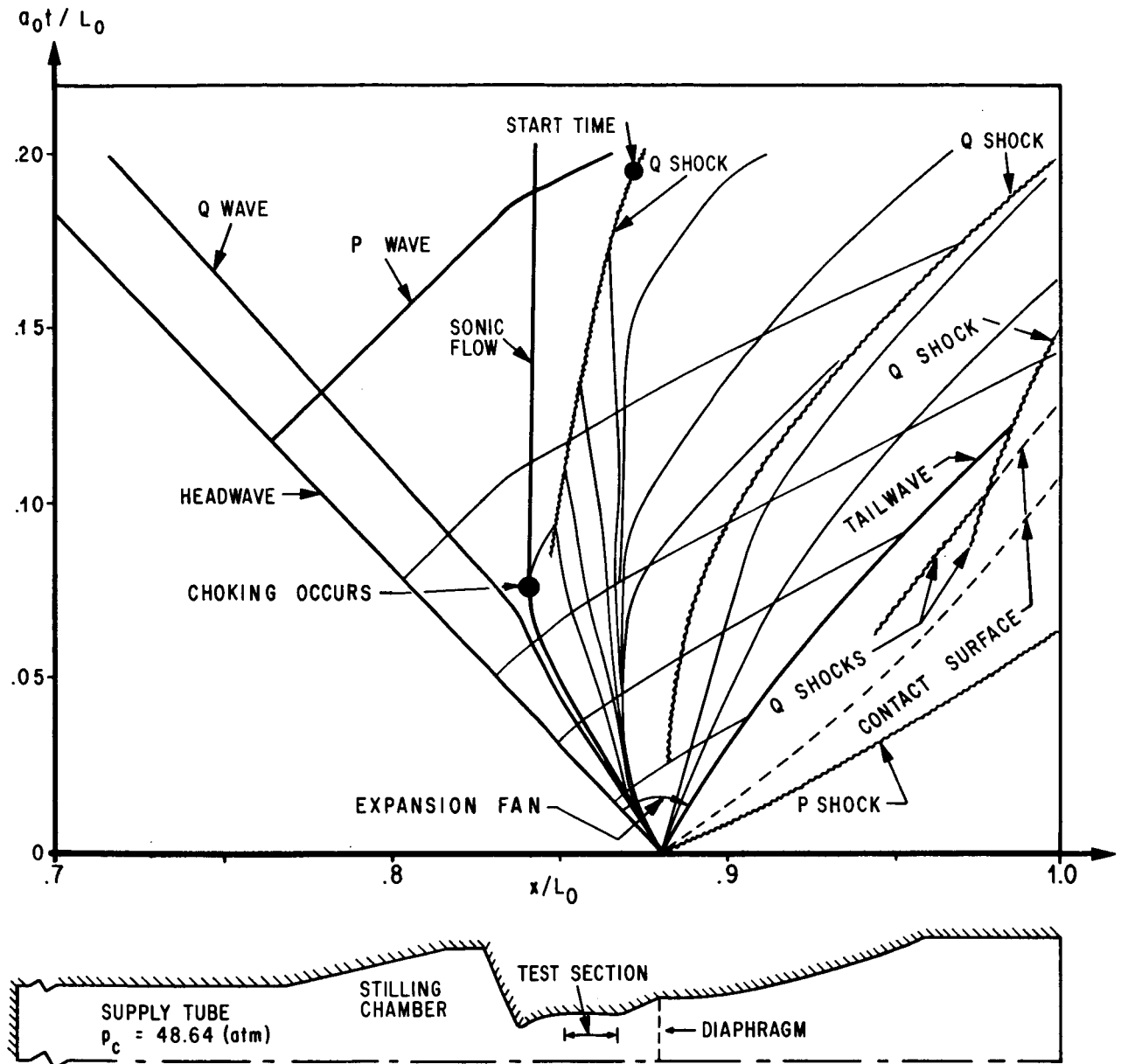
FIGURE 1. WAVE DIAGRAM FOR LUDWIEG TUBE FACILITY WITH A MACH NUMBER 2 NOZZLE

around 10 msec compared with the experimental value of 18 msec.

The difference in theory and experiment can be attributed to the assumption of one-dimensional flow downstream of the nozzle throat for the theoretical model. Bull [5] observed the following sequence of events during the early development of the flow downstream of a Laval nozzle throat:

1. Some form of curved or concaved normal shock formed slightly downstream from the throat just before the throat choking.

2. This curved normal shock then develops into a pair of crossed oblique shocks immediately after choking, and the flow separates from the wall downstream of the shock system.
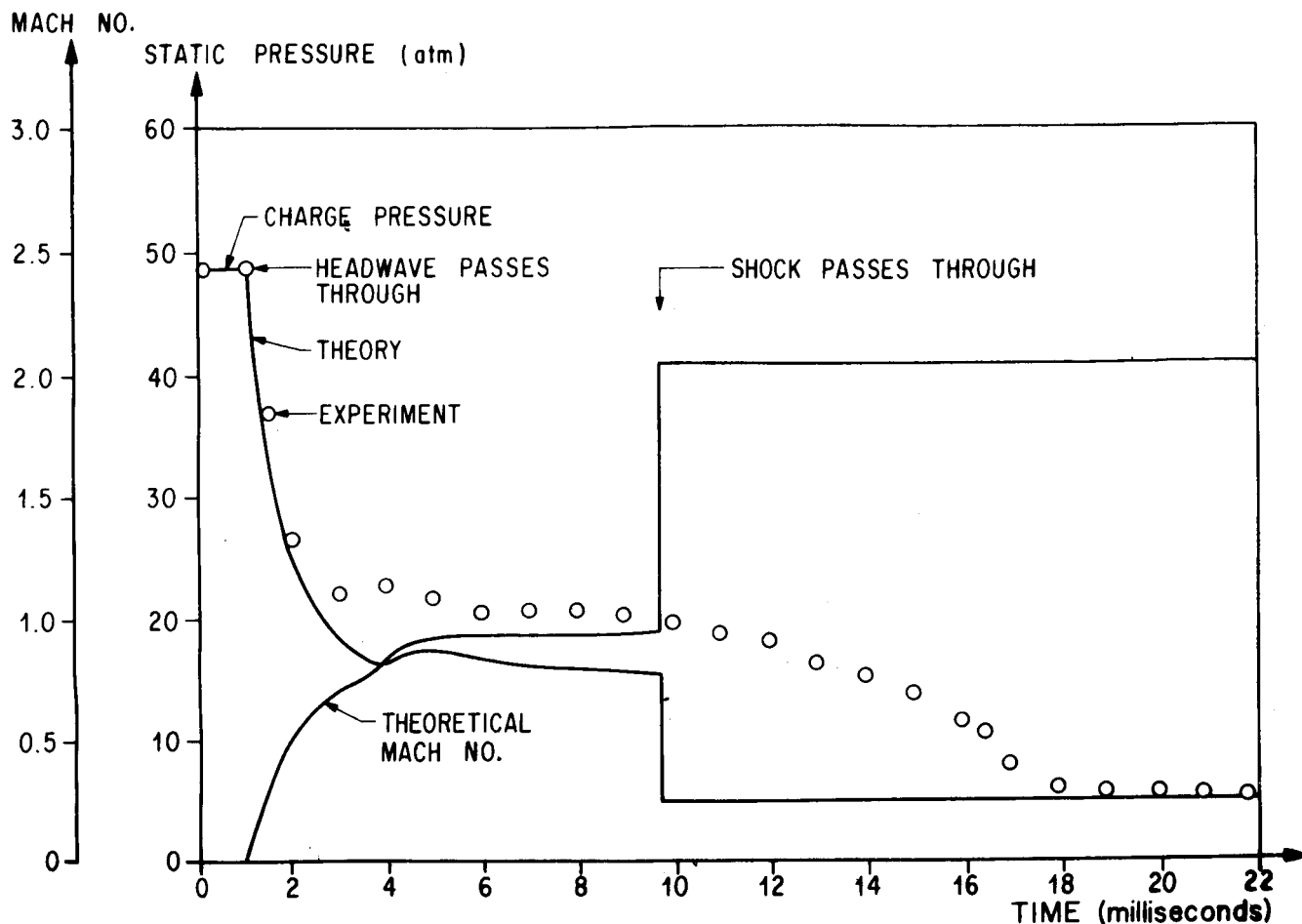
FIGURE 2. TIME DEPENDENCE OF STATIC PRESSURE AND MACH NUMBER IN SUPERSONIC (M = 2.0)
TEST SECTION OF LUDWIEG TUBE PILOT FACILITY

3. The oblique shocks rotate toward the Mach angle as it moves through the nozzle and working section, leaving a uniform flow behind it.

The conclusion that the difference in theory and experiment is caused by the two-dimensional rather than one-dimensional flow phenomenon that occurs downstream of the nozzle throat can be somewhat verified in Figure 3.

Figure 3 shows the experimental and theoretical static pressures as a function of time at a station in a subsonic (M = 0.7) test section. For the subsonic cases, the flow is choked downstream of the test section by choking flaps, and therefore no shocks are formed upstream of this position. For this case, choking at the flap position occurred at approximately 2 msec. Steady flow in the test section is then established when the transient effects of the area changes

on the characteristic waves die out. The starting time for the subsonic test cases is defined as the time when the pressure in the test section becomes invariant with time. A curve which shows the calculated Mach numbers as a function of time for this station in the test section is also shown in Figure 3. Figure 3 shows that the theoretical results agree extremely well with the measured data.

CONCLUSIONS

The results which have been presented indicate that a time-dependent one-dimensional analysis of the starting process for the Ludwieg tube wind tunnel show reasonable agreement with the experimental data. The subsonic cases show much better agreement than the supersonic cases. The divergence of the theoretical
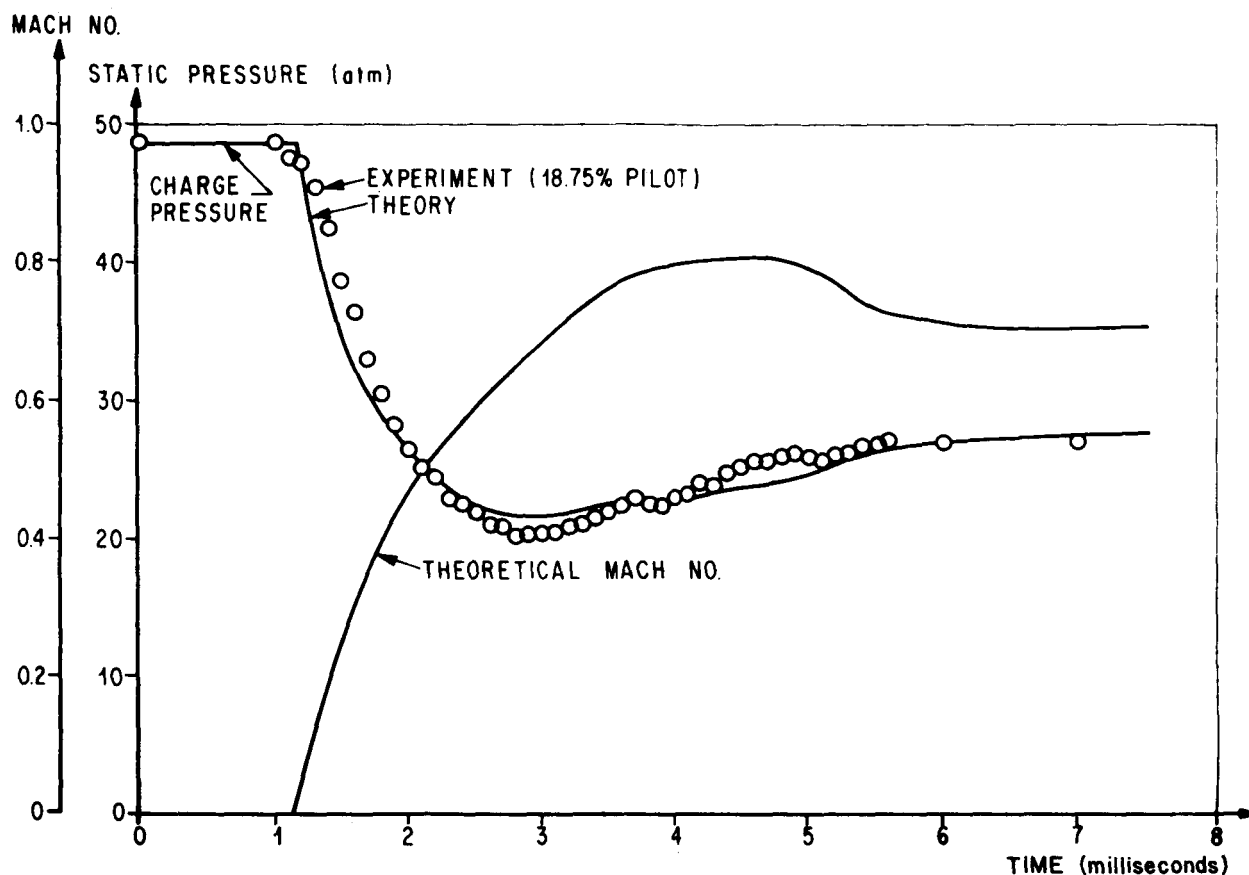
FIGURE 3. TIME DEPENDENCE OF STATIC PRESSURE AND MACH NUMBER IN SUBSONIC (M = 0.7)
TEST SECTION OF LUDWIEG TUBE PILOT FACILITY

results from the experimental data in the supersonic cases is considered to be caused by the two-dimensional shock system that develops downstream of the nozzle throat rather than a simple normal shock which results from the one-dimensional theory.

REFERENCES

1.   Davis, J. W.: Ludwieg Tube Pilot Tests and High Reynolds Number Test Equipment, MSFC Research Achievements Review, Third Series, No. 4, September 1968.

2.   Warmbrod, J. D., and Struck, H. G.: Application of the Characteristic Method in Calculating the Time Dependent, One Dimensional, Compressible Flow in a Tube Wind Tunnel. NASA TM X-53769, August 1968.

3.   Pai, S. P.: Introduction to the Theory of Compressible Flow. D. Van Nostrand Company Inc., New York, 1959.

4.   Shapiro, A. H.: Compressible Fluid Flow, Vol. 1. The Ronald Press Company, New York, 1953.

5.   Bull, G. V.: Starting Processes in an Intermittent Supersonic Wind Tunnel, UTIA Report No. 12, University of Toronto, February 1951.

FLOW CHARACTERISTICS OF ORIFICES FOR VENTING LAUNCH VEHICLE COMPARTMENTS

By

P. E. Ramsey

SUMMARY

Internal compartments of massive modern space boosters have become very large, especially in the booster's base and interstage areas. These compartments experience rapidly decreasing ambient pressure during the ascent portion of flight. Because of the huge volumes involved, a method must be provided to vent the gases in these compartments so that the differential pressure across the vehicle's external skin will not become great enough to cause failure of the vehicle's structure.

A digital computer program has been developed by the Aerophysics Division to predict the compartment's internal pressures during flight. However, because of the lack of knowledge concerning the vent discharge flow coefficients, this program is an approximate solution. An analytical determination of the flow coefficients falters when the jet interaction and the three-dimensional mixing of the jet with the external flow boundary layer are considered.

Available experimental data are limited to ratios of jet-to-external stream mass flow greater than 0.15 and negligible external-flow boundary layers. To obtain the necessary design data applicable to flight conditions, an experimental study was undertaken in the Ames Research Center's 1.8 by 1.8-m (6 by 6-ft.) supersonic wind tunnel for the following parameters:

1. External stream Mach numbers of 0.7 to 1.9.

2. Vent geometry; circular, square, elliptical, rectangular, and slots.

3. Vent orientation; long axis 90 degrees to or aligned with the external flow.

4. Boundary layer thicknesses of 1.0 to 10.2 cm.

5. Jet to external mass flow ratios of 0.05 to 0.9.

The test was run on a large flat plate which could be translated from a position flush with the tunnel wall (maximum boundary layer thickness) to a position outside of the tunnel boundary layer (minimum boundary layer thickness on test plate).

In general, the flow coefficients were nearly the same for circular, square, rectangular, and elliptical vents, with the long axis 90 degrees to the flow. The efficiency of the larger slots oriented 90 degrees to the flow agreed with the other vent data, but very thin slots were more efficient than all other vents. When the major axes of the vents were aligned with the external flow, substantial gains in efficiency were realized. Also, vent efficiencies increased with increased boundary layer thickness. Mach number effects were small for all vents in the subsonic and transonic regions, but became significant for supersonic Mach numbers. Efficiencies of the very narrow slots were not affected by changes in Mach number.

LIST OF SYMBOLS

Symbol	Definition
a	dimension of major axis, centimeters
A	vent area, square centimeters
b	dimension of minor axis, centimeters
K	vent flow coefficient
m	mass flow rate (based on vent area), kilograms/second
M	free stream Mach number
P	Pressure, Newtons/square meter
t	time, seconds
V	velocity, meters/second
δ	external flow boundary layer thickness on flat plate, centimeters
ϕ	vent orientation angle ($\phi = 90$ degrees when major axis is aligned with free stream flow), degrees

ρ mass density, kilograms/cubic meter

Subscripts

Act.   actual condition

c   compartment conditions

e   external free stream flow conditions

eff.   effective condition

j   vent jet conditions

INTRODUCTION

Space launch vehicles must necessarily contain internal spaces or compartments which are bounded by the external skin structure and fuel tank bulkheads. Typical examples are the areas between the fuel tanks and heat shield in the base region and interstage compartments. These internal volumes are indicated by the shaded areas on the Saturn V outline presented in Figure 1.

Before a space vehicle leaves the launch pad, the pressure and temperature within internal compartments are essentially ambient. After lift-off, high altitudes are reached rapidly; consequently, the ambient pressure reaches nearly zero within approximately two minutes depending upon the vehicle and its trajectory. Under these circumstances, if no provision is made for venting the vehicle's compartments, large differential pressures across the vehicle's skin can exceed the vehicle's structual limitations.

Early vehicles such as Redstone and Jupiter did not encounter this problem because the internal compartments were relatively small. The limited amounts of gases involved could vent through inherent seams and cracks in the skin's structure. However, with the advent of space boosters such as Saturn, these compartments have become exceptionally large. One example is the S-IC/S-II interstage compartment which contains a volume of 510 m^3. Because of the size of the compartments and the affected skin areas, a method of disposing of large amounts of air or purge gases must be provided. Present vehicle design practice includes vent holes in the external skin to insure proper venting of each space booster compartment. These vents are shaped, sized, and located in such

a manner that when coupled with the vehicle external pressure during flight, the differential pressure across the skin is kept to a minimum.
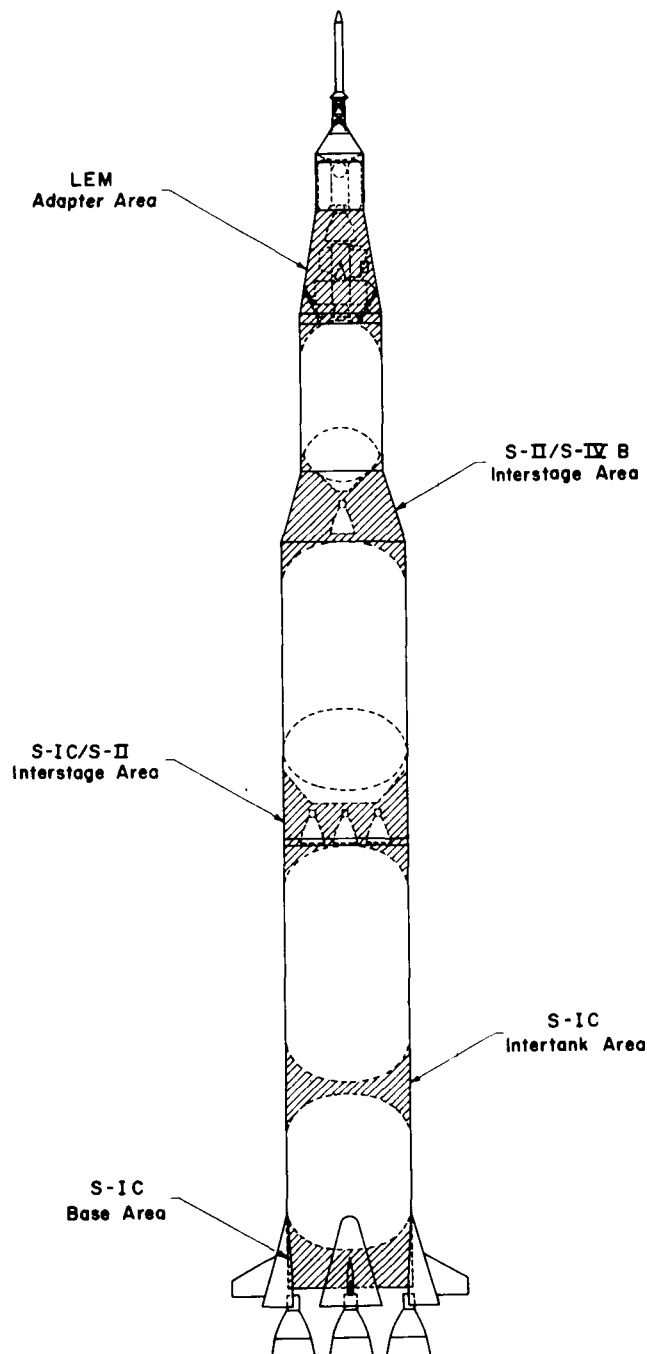
FIGURE 1. TYPICAL SATURN V INTERNAL COMPARTMENTS

COMPUTER PROGRAM

To predict the time history of compartment internal pressures during flight, a digital computer program was developed by the Aerophysics Division. This program provides design data for circular, rectangular, and elliptical vents discharging into either quiescent or moving air. Based on the results of this program, vents can be sized and located to minimize the differential loading of the vehicle's skin during flight.

Unfortunately, the vent discharge coefficients, compartment initial conditions, and structural leakage through seams are not exactly known; therefore, the program gives only approximate design data. Among these sources of inaccuracy, the vent discharge coefficient uncertainty is the major obstacle to an accurate analytical determination of the compartment pressures. The factors which influence flat-plate orifice flow coefficients are (1) ratio of the orifice jet mass flow to the external stream mass flow, (2) vent shape, (3) vent orientation, if not circular or square, (4) vent size, and (5) external environment receiving the vent exhaust. A theoretical approach has been relatively unsuccessful because of the difficulty in defining the lateral jet interaction and three-dimensional mixing of the jet with the external flow boundary layer.

Available experimental data obtained from References 1, 2, and 3, portions of which are presented in Figure 2, were limited to those obtained for very small or negligible external-flow boundary layers and ratios of jet-to-external stream mass flow of 0. 15 or above. However, during flight, mass flow ratios less than 0. 15, as well as greater, are encountered, and vents exhausting into thick turbulent boundary layers are the rule rather than the exception. Since no directly applicable experimental data were available, a method was incorporated into the venting program procedure to provide a "design band" which was conservative enough to cover inherent uncertainties. A more complete description of the assumptions and capabilities of the program is available.[1]
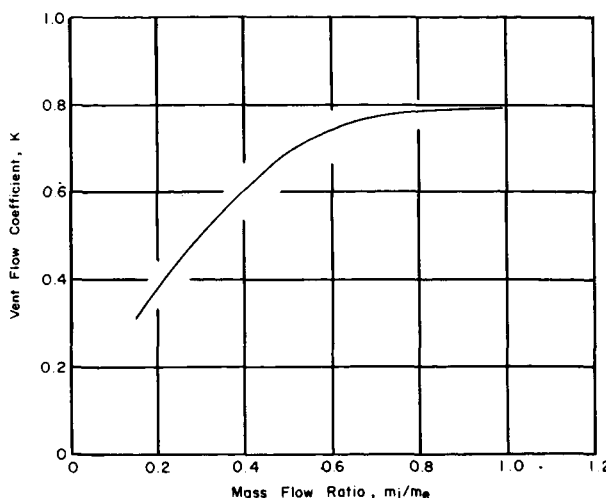
FIGURE 2. VARIATION OF FLOW COEFFICIENTS WITH MASS FLOW RATIO FOR CIRCULAR THIN PLATE ORIFICES DISCHARGING INTO A NEGLIGIBLE BOUNDARY LAYER

EXPERIMENTAL PROGRAM

An experimental wind tunnel program was undertaken to obtain complete flow coefficient data for thin-plate sharp-edged orifices which were applicable to flight venting conditions. This study examined the effects of vent geometry including narrow slots, vent orientation, thick turbulent boundary layers, mass flow ratio, and the external stream Mach number. The program was carried out in the Ames Research Center's 1.8 by 1.8-m (6 by 6 ft.) supersonic wind tunnel. This wind tunnel was chosen because of its low Reynolds number capability which resulted in a 10.2-cm thick tunnel-wall boundary layer. A thickness of this magnitude allowed the use of adequate sized test orifices, which resulted in accurate flow measurements while maintaining a ratio of vent diameter to boundary layer thickness equal to that expected in flight. Also, because the tunnel was a continuous flow type, plenty of time was available to adjust the vent mass flow and to take data. A description of the wind tunnel and its capabilities are presented in Reference 4.

1.   Jump, Rodger A.; and Henson, Victor K.: In-Flight Venting of Launch Vehicle Compartments. NASA-MSFC, R-AERO-IN-30-65, November 29, 1965.

The test model, shown schematically in Figure 3, consisted of a large 121.92-cm square flat plate mounted on four jack screws. This assembly was attached to a support structure containing a drive motor and chains for driving the jack screws. After the glass was removed from a tunnel side window, the entire model setup was then mounted in the window opening. This system allowed the plate to be fully retracted flush with the tunnel side wall or extended into the tunnel flow toward the test section centerline. A maximum boundary layer thickness of approximately 10.2 cm was achieved when the plate was flush with the wall, while a minimum thickness of about 1.0 cm was obtained when the plate was extended approximately 15.2 cm into the tunnel flow beyond the tunnel wall boundary layer. When the flat plate was traversed into the tunnel, a sharp leading edge and two side extensions were bolted to the plate edges. The side extensions extended the plate surface within 2 or 3 cm of the top and bottom of the tunnel, which essentially eliminated tip effects. Also,

auxiliary suction was applied to the cavity under the plate to reduce flow blockage and to minimize spillover at the leading edge.

A circular vent plate, which contained the orifice of interest, was fastened with screws and sealed with neoprene O-rings to the end of a 12.7-cm diameter plenum chamber. The plenum chamber was designed to slip into a hole in the back of the flat plate and to be pulled out of the tunnel through a double-wall door arrangement. This system allowed the vent plate configuration to be changed in a few minutes rather than 1.5 to 2 hours by avoiding the time loss from stopping, starting, and bringing the wind tunnel up to testing speed. The orifice plate was flush with the flat plate surface when the plenum was installed. Figure 4 shows the series of vent geometries which were considered during the study. Except for the slots, the vents contained equal areas for eliminating jet Reynolds number effects and for convenience in computing vent flow parameters.
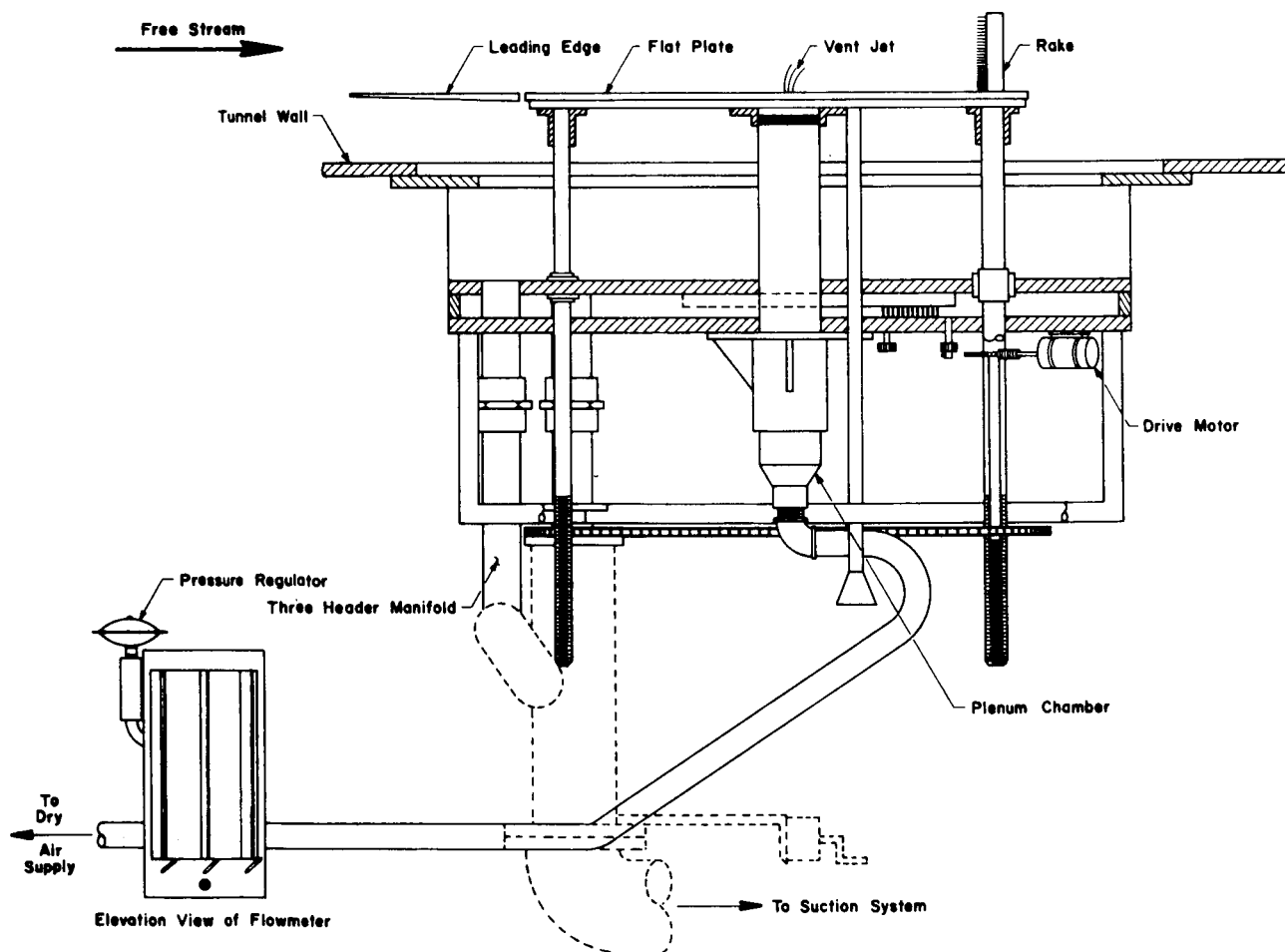
FIGURE 3. DETAILS OF THE TEST MODEL SETUP
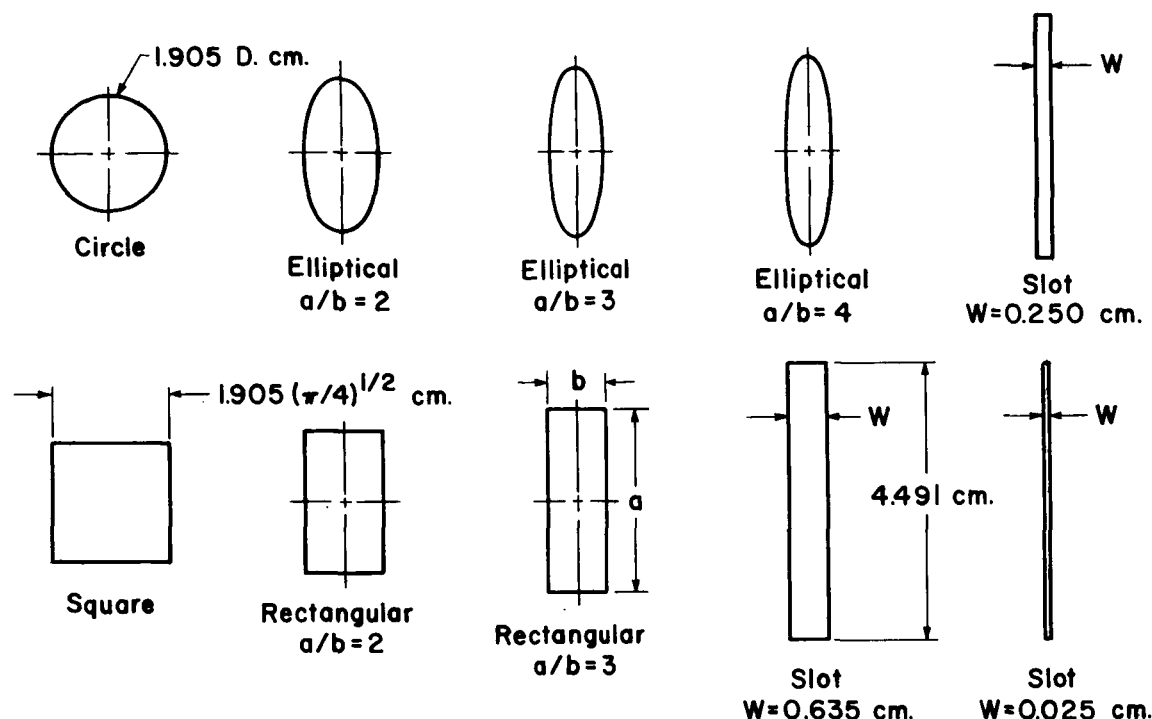
FIGURE 4. VENT CONFIGURATIONS

A Cox rotameter flowmeter, associated pressure regulators, and control valves were used to control and measure the vent jet mass flow. The flowmeter has a nonlinear scale which provided 1 percent of the reading accuracy over the total calibrated range. A more complete description of the model and its installation in the Ames Research Center's 1.8 by 1.8-m (6 by 6-ft.) wind tunnel are presented in Reference 5.

TEST PARAMETERS

One of the most important parameters considered during this investigation was the mass flow ratio, which was defined as the ratio of the vent mass flow to the free stream mass flow through a stream tube of equivalent area as the vent. The range of mass flow ratios, m_j/m_e, considered was 0.05 to 0.90.

Because of the difficulty in measuring the jet static pressure and for convenience in applying the data to the physical problem, the vent flow coefficients presented are computed based on the tunnel free stream static pressure. The vent flow coefficient, K, was defined as the ratio of the actual vent mass flow to the ideal (isentropic) mass flow,

$$K = \frac{(\rho A V)_{meas.}}{(\rho A V)_{ideal}} ,$$

which can be stated as

$$K = \frac{A_{eff.}}{A_{Act}} .$$

The vent flow coefficient is an efficiency factor which accounts for the losses from friction, viscosity, and real gas effects.

Other parameters of importance were Mach number, which ranged from 0.70 to 1.90, and boundary layer thickness, which included three values: approximately 10.2 cm, an intermediate thickness of 2.5 cm, and 1.0 cm. A majority of the data were obtained for the maximum and minimum boundary layers. The tests and the basic data are described in Reference 6.

RESULTS AND DISCUSSION

Typical data are presented in Figures 5-7 as the variation of vent flow coefficient with mass flow ratio for the parameters of interest: vent geometry, vent orientation, external flow boundary layer thickness, and Mach number.

Figure 5 shows that the efficiencies of the circles and squares are essentially the same for the range of parameters investigated. The differences between the circular/square vent flow coefficients and those of the elliptical and rectangular vents at Mach 1.3 with the long axis 90 degrees to the flow ($\phi = 0$) are small, although a slight decreasing trend is evident with an increase in the vent length-to-width ratio. This trend

(a) 10.2 cm. Boundary Layer

(b) 1.0 cm. Boundary Layer
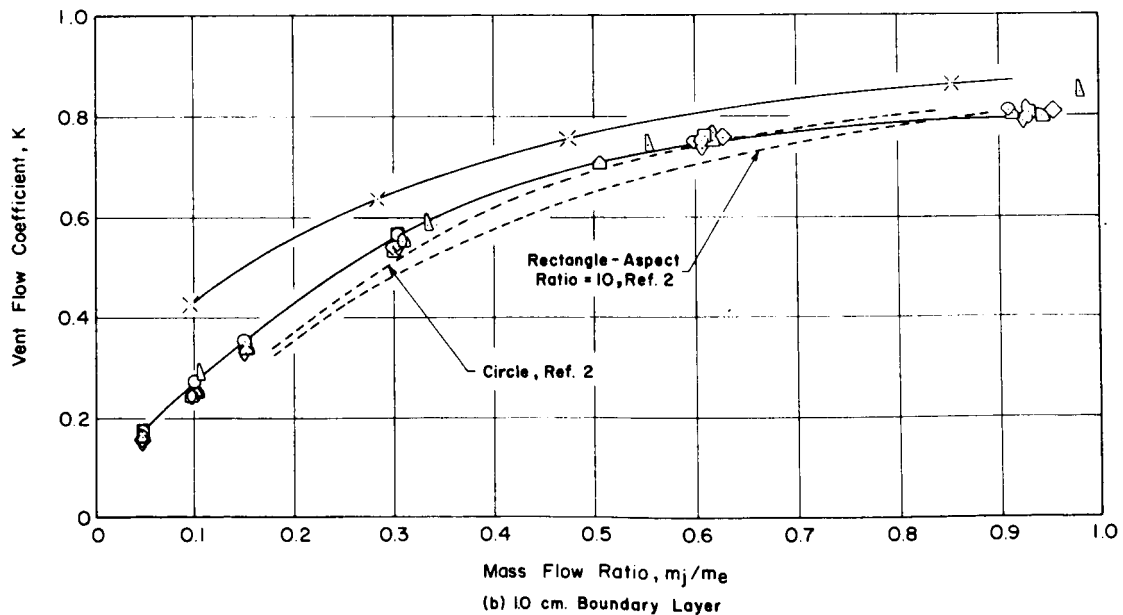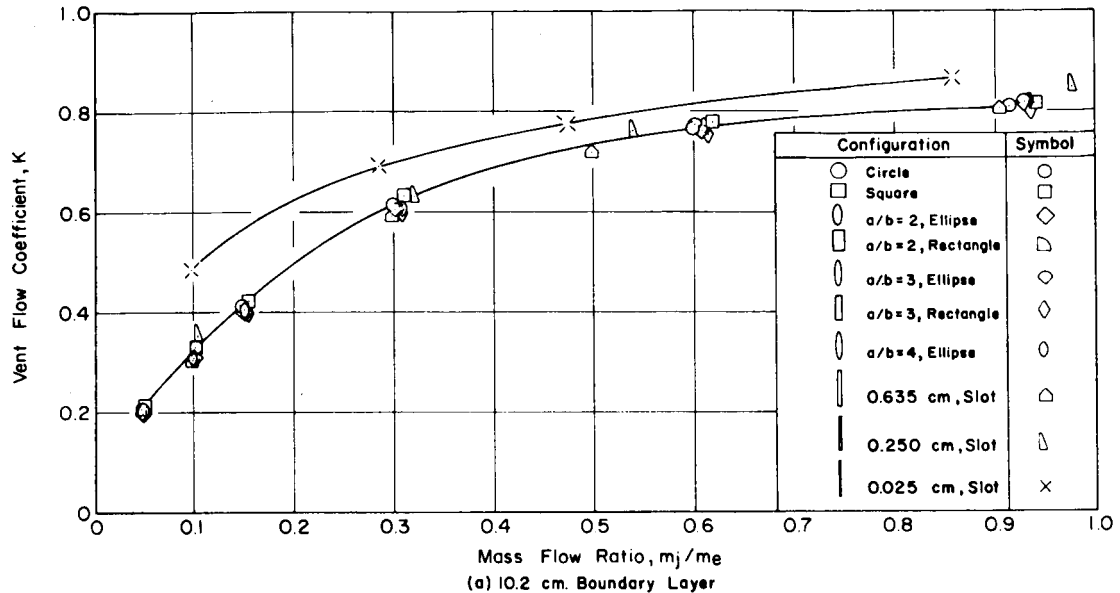
FIGURE 5. EFFECT OF VENT GEOMETRY ON THE FLOW COEFFICIENT FOR A MACH NUMBER OF 1.3

agrees with the two data curves obtained from Reference 2, which are presented for square and rectangular vents. Even though the trends are similar, the absolute values of the Reference 2 data appear to

be slightly lower than the present data. This difference may be caused by scale effects and facility differences of the two investigations.

(a) 10.2 cm. Boundary Layer

(b) 1.0 cm. Boundary Layer
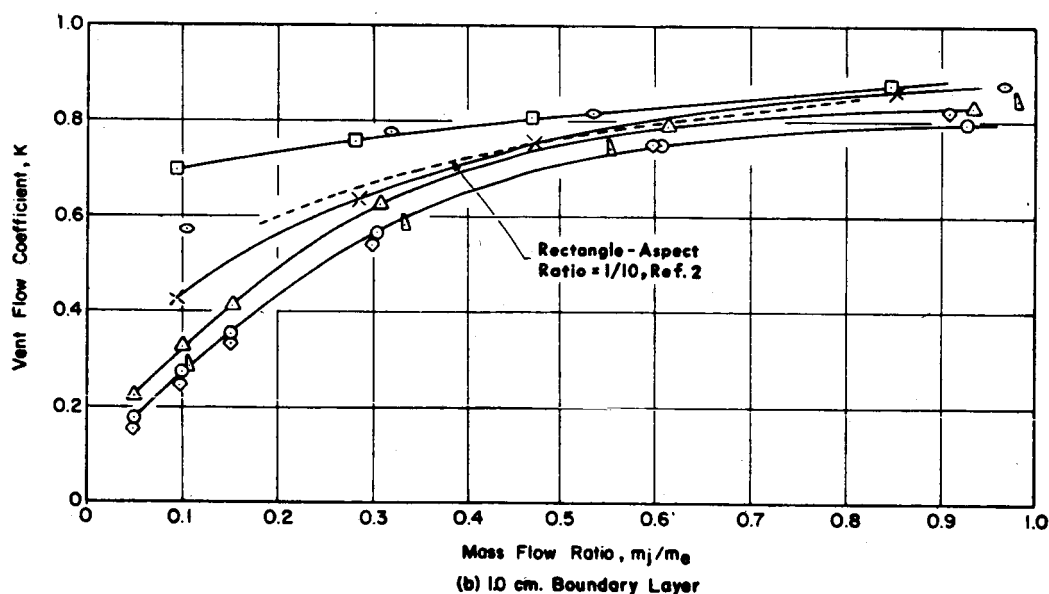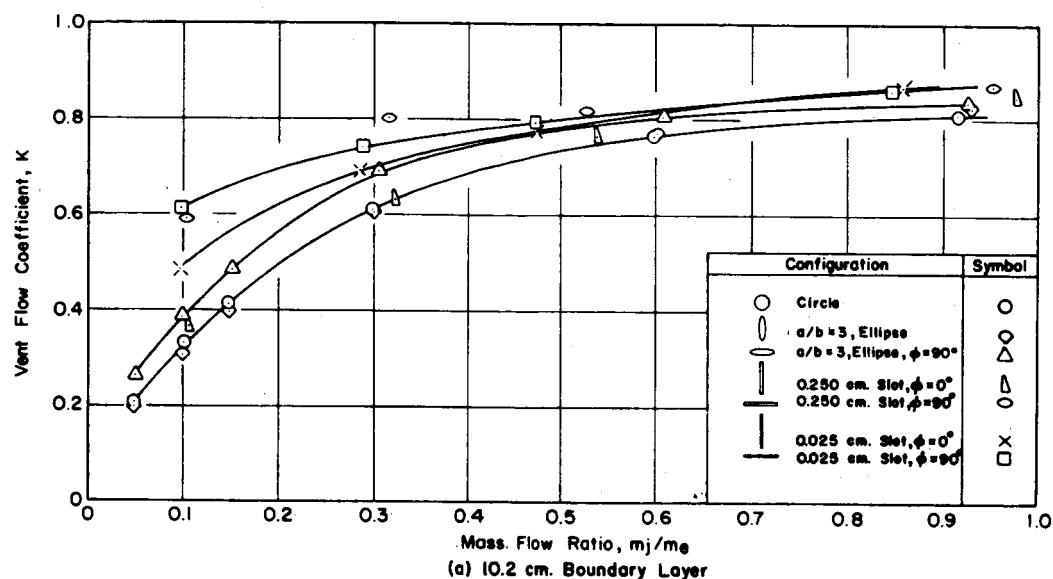
FIGURE 6. EFFECT OF VENT ORIENTATION ON THE FLOW COEFFICIENT FOR A MACH NUMBER OF 1.3
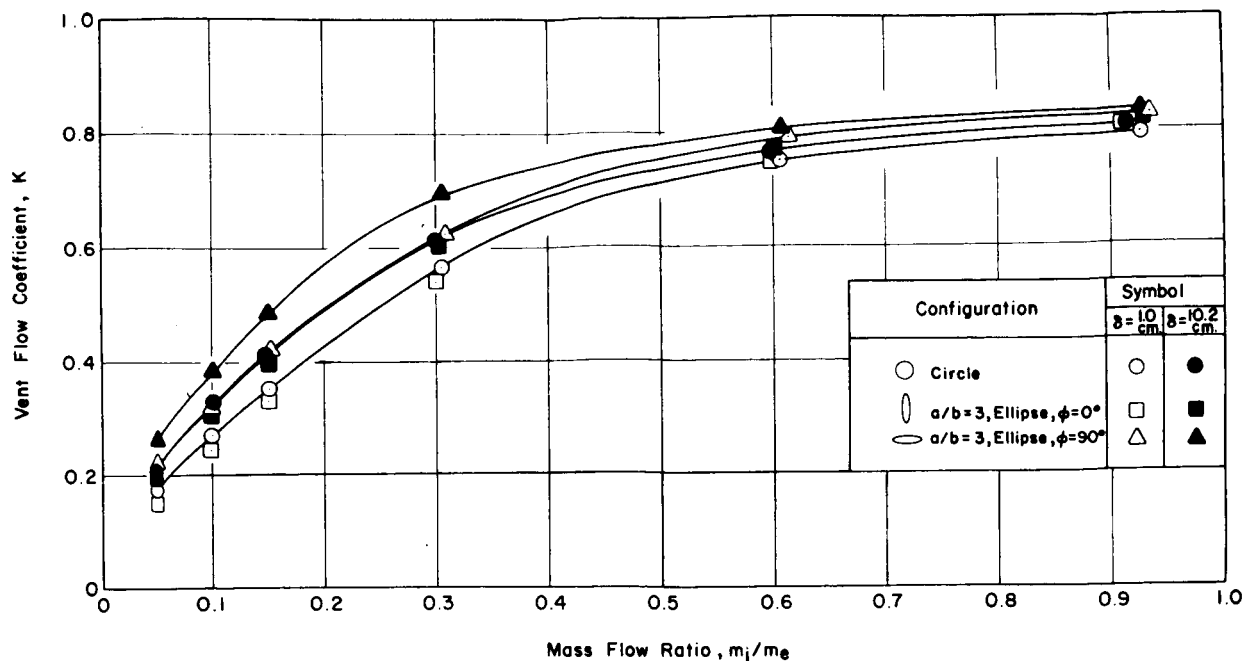
FIGURE 7. EFFECT OF BOUNDARY LAYER THICKNESS ON THE FLOW COEFFICIENT FOR A MACH
NUMBER OF 1.3

The efficiency of the large slots followed the same trends as the other vents, but as the width of the slots decreased, the coefficients began to increase. Finally, as the flow in the smallest slots became more two-dimensional, a point was reached where the slot efficiency became greater than that of the circular vents. This phenomenon agrees with the free-jet results obtained in Reference 2. This effect did not appear for external flow during the Reference 2 investigation because the slot length-to-width ratios studied were limited to 10 or less. The smallest slot (0.025-cm wide) reached efficiencies significantly larger than the other vent shapes, particularly in the low end of the mass flow ratio regime. Comparison of Figures 5a and 5b indicates that these trends are not appreciably affected by the boundary layer thickness.

Figure 6 compares vent flow coefficients for the circular vents and several vents oriented 0 degrees and 90 degrees to the external flow. Obviously, vents with the long axis aligned with the flow are more efficient than those placed 90 degrees to the flow. This effect appears to be greatest at the lower mass flow ratios. Data obtained from Reference 2 for a rectangular vent with a 1/10 aspect ratio indicates a

similar effect (Fig. 6). The superior efficiency of the aligned vents increases with a decrease in the slot width to a point at which no further gain is realized with decreasing width. This effect, which seems to occur at approximatley 0.25-cm slot width, is consistent for all mass flow ratios for the 10.2-cm boundary layer. However, for the 1.0-cm boundary layer, the data still indicated an increase in the flow coefficient for mass flow ratio values less than 0.3. From this discussion, it is clear that a long narrow vent with the long axis aligned with the external flow results in the optimum venting efficiency.

Increasing the boundary layer thickness from 1.0 to 10.2-cm caused the vent efficiency to increase, as indicated in Figure 7, probably because the interaction losses were less in a thick boundary layer where the relative external flow energy level near the vent is lower than for a small or nonexistent boundary layer. This effect appears to be greatest in the low mass flow ratio region and appears to be approximately equal for all vents.

The vent flow coefficient is cross-plotted and presented in Figure 8 as a function of the external flow Mach number for a constant mass flow ratio of 0.3
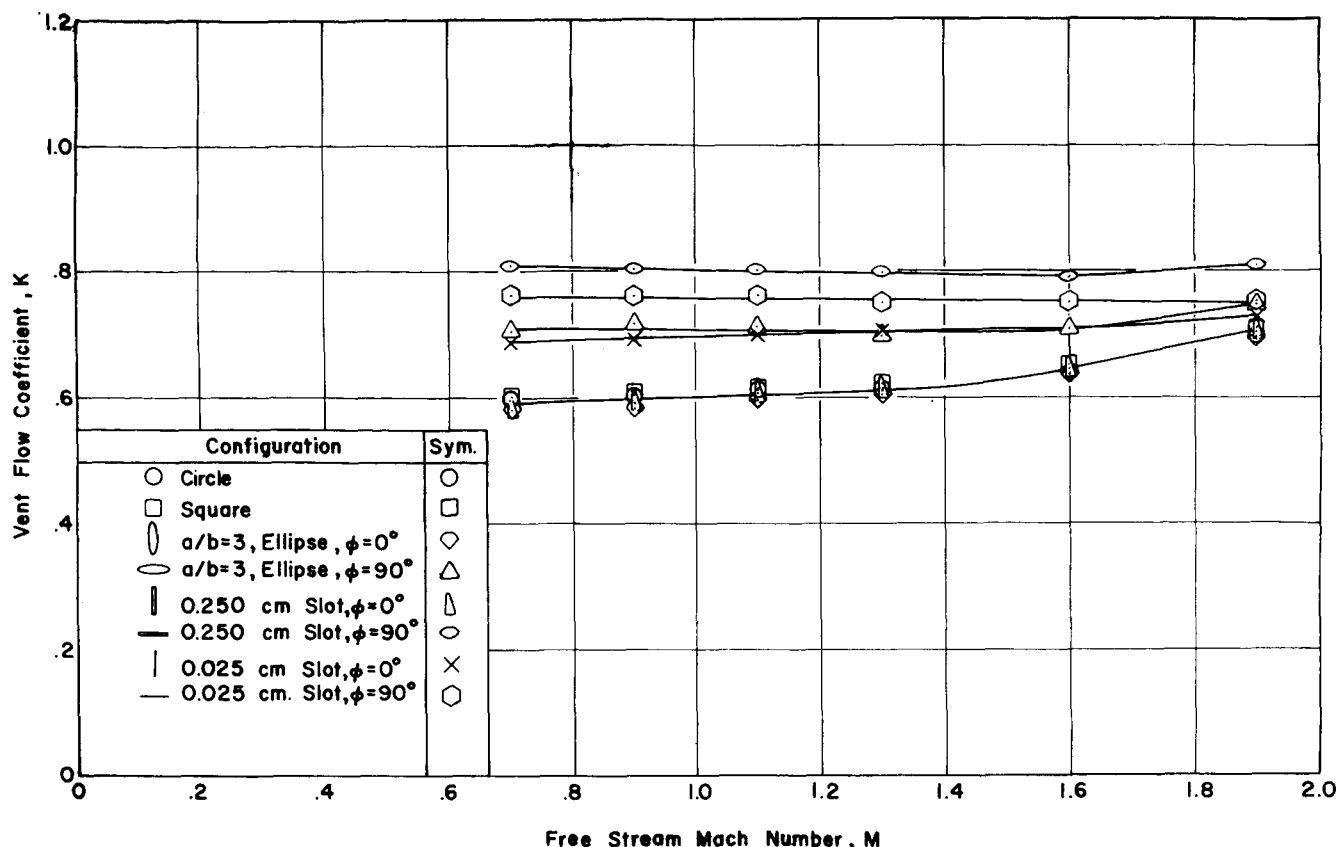
FIGURE 8. VARIATION OF VENT FLOW COEFFICIENT AS A FUNCTION OF FREE STREAM MACH NUMBER
FOR A MASS FLOW RATIO OF 0.3 AND A BOUNDARY LAYER THICKNESS OF 10.2 cm

and several vent configurations. This set of curves indicates that, subsonically and transonically, the vent efficiencies are nearly constant for all vent shapes and orientations, although there appears to be a very slight increasing trend as Mach number increases for vents at $\phi = 0$, while a slight decrease is evident for vents aligned with the flow. In the supersonic regime, the vent efficiency increased for all vents and orientations except for the 0.025-cm wide slot at $\phi - 90$ degrees data, which remained constant throughout the Mach number range investigated. The supersonic region vent efficiency increase was greatest for the circular, square, elliptical and rectangular vents at $\phi = 0$, plus slots at $\phi = 0$ up to 0.25 cm in width. The vents which were aligned with the flow seemed to maintain the subsonic values farther into the supersonic region (up to approximately $M = 1.6$) than $\phi = 0$ vents.

Figure 9 shows the internal/external differential pressure for a typical launch vehicle compartment as a function of flight time using rectangular vents with

rounded ends. The large cross-hatched area indicates the maximum and minimum pressures constituting the "design band" which was obtained from the earlier mentioned computer program. Flight data from AS-204 are presented as a comparison and fall within the "design band". Efforts are being made to incorporate the vent flow coefficients, which resulted from this investigation, into the computer program to improve the accuracy of the absolute pressure computations and to reduce the present "design band" for Saturn vehicles. The expected new "design band" is approximately 50 percent less than the original and is represented by the smaller shaded area.

Hopefully, a means of data correlation will be found which will lead to empirical methods for determining vent efficiencies for future Saturn vehicles. Also, the data will be used as a guide and a point of comparison for developing analytical methods which may eventually replace an extensive experimental program such as the present one.
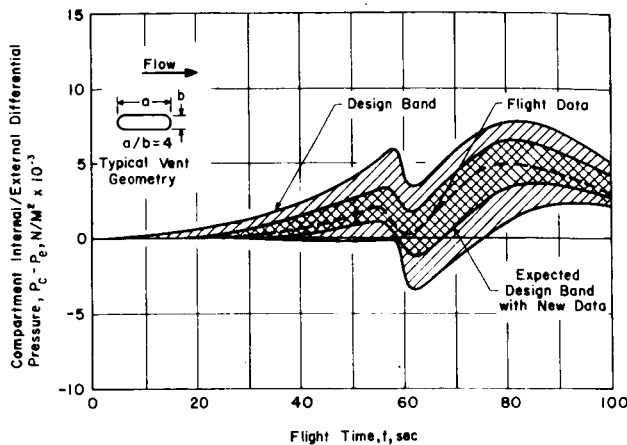
FIGURE 9. SPACECRAFT COMPARTMENT
PRESSURE HISTORY FOR AS-204

CONCLUDING REMARKS

Based on the results of the present investigation, several observations can be made.

1. There is practically no difference in the vent efficiencies of circles and squares of equal areas.

2. The differences between the coefficients of circular vents and vents with length-to-width ratios greater than one and with the long axis 90 degrees to the external flow is relatively small.

3. A very narrow slot maintains an efficiency greater than that of a circular or square orifice.

4. Vents which have the long axis aligned with the external flow were substantially more efficient than the 90 degree oriented vents, with the narrow slots being the most efficient of all.

5. Mach number effects appear to be small for $\phi = 0$ vents until supersonic Mach numbers are reached. Mach number effects are small for all aligned vents for the ranges investigated.

6. Increasing the boundary layer thickness caused the vent efficiencies to increase.

Apparently, the optimum vent shape for venting flight vehicle compartments would be a narrow slot aligned with the external flow around a flight vehicle. However, since incorporating a long narrow slot into the vehicle skin and substructure may be impractical, a compromise vent shape may be needed. A good compromise would be a slot with a length-to-width ratio less than the very narrow test slots but greater than the four to one vents now used. The addition of round ends to reduce stress concentrations in the skin would be desirable.

Because of the complexity of the Saturn shape, the probability of vents being located in adverse flow fields is substantial. Consequently, future experimental work is contemplated for vents located on frustums, behind frustum/cylinder shoulders, and beside or behind typical protuberances. Should it be discovered that the vent efficiencies under these flow conditions are destroyed, the emphasis would then be placed on determination of the minimum distance which could be tolerated between a vent and a flow-disturbance generator.

REFERENCES

1. Callaghan, E.; and Bowlen, D.: Investigation of flow Coefficient of Circular, Square, and Elliptical Orifices at High Pressure Ratios. NACA TN-1947, September 1949.

2. Dewey, P.; and Allen, R.: An Investigation of the Discharge and Drag Characteristics of Auxiliary Air Outlets Discharging Into a Transonic Stream. NACA TN-3466, July 1955.

3. Nelson, W.; and Dewey, P.: A Transonic Investigation of the Aerodynamic Characteristics of Plate and Bell-Type Outlets for Auxiliary Air. NACA RM-L52H20, September 3, 1952.

4. Staff, Ames Research Center: Characteristics of Six Research Wind Tunnels of the Ames Aeronautical Laboratory. 1967.

5. Rader, R.: Pre-Test Report for Experimentally Determining Generalized Venting Characteristics. Northrop/Huntsville Technical Report No. 316 TR-793-7-157, April 1967.

6. Walters. W. P.; Glasgow, R.M.; and Baker, J. M.: Experimental Determination of Generalized Venting Characteristics. Nortronics/Huntsville, Technical Report No. 388 TR-792-8-368, July 1968.

PLUME FLOW FIELD ANALYSIS FOR LIQUID PROPELLANT ROCKET ENGINES

By

Joseph L. Sims and Terry Greenwood

LIST OF SYMBOLS

Symbol	Definition
M	Mach number
n	percent mass flow of foreign nuclei
N_d	number flux of foreign nuclei through the nozzle, particles/sec
O/F	ratio of oxidizer to fuel
P	static pressure, Newtons per square meter
r	radius in spherical coordinate system
r_d'	radius of foreign nuclei, meter
S_d	surface area flux of foreign nuclei
u	velocity, meter/sec
X, R	axial and radial coordinates of a cylindrical coordinate system

Subscripts

CHAMBER	combustion chamber conditions
EXIT	exit plane
j	jet
S	stagnation
THROAT	nozzle throat
∞	free stream

Superscripts

*	sonic conditions

INTRODUCTION

Rocket plume flow fields have created problems for the design and operation of both ascent stages and orbital vehicles. Some of the problems caused by the plumes are listed in Table I. A solution to these problems requires an analysis of all regions of the plume flow field which encompasses many complex physical phenomena.

TABLE I. PROBLEMS CREATED BY ROCKET PLUMES

A. Ascent stage problems

    1. Base Convective Heat Transfer

    2. Base Radiative Heat Transfer

    3. RF Signal Attenuation

    4. Free Stream Separation Caused By Plume Billowing

    5. Impingement Loads And Heat Fluxes Caused By Firing Of Retro and Ullage Rockets

B. Orbital Vehicle Operations Problems (Created By Reaction Control Rocket Plumes)

    1. Interaction Forces and Moments

    2. Thermal and Surface Erosion Environment In Impingement Regions

    3. Vehicle Surface And Near Space Contamination By Plume Gases And Condensates

Rocket plumes are characteristically high-energy multicomponent flow fields which expand into the

surrounding environment. The basic flow field is supersonic, but there are subsonic portions which must be treated. A representation of the basic plume model is shown in Figure 1 for flow into an external supersonic flow field. For flow into a vacuum, the internal shock pattern and the free shear layer no longer exist, but now we have transition from continuum to free molecular flow in the plume flow field. The flow fields are ultimately dissipated by viscous and eddy mixing, by shock waves, and/or by dilution into a space environment to a static condition.

The source for the plume field is the flow field created by the rocket nozzle and its associated injector. In general, a rather complex analysis of the nozzle flow is required to obtain satisfactory initial conditions for the plume analysis. The phenomena that need to be analyzed occur in the rocket nozzle and are listed in Table II.

TABLE II. NOZZLE AND CHAMBER PHENOMENA

| 1. Radial O/F Gradient Caused By Injector Hydraulic Design |
| 2. Freezing of Thermochemical Reactions |
| 3. Shock Waves Caused By Nozzle Geometrical Design |
| 4. Mass Addition (Turbine Exhaust Dump) To The Nozzle Boundary Layer |

Generally, for the high temperature and enthalpy associated with rocket gases, the thermochemical reactions will be significant. Finite rate chemical reaction effects are not included in the basic flow field calculation. Initially the flow field is computed for instantaneous chemical equilibrium, and then a one-dimensional finite rate program is used to find the point of departure from equilibrium. At this point all chemical reactions are considered to be stopped, and the flow field calculation is restarted as a frozen thermochemical calculation.

All of the foregoing considerations apply to a single engine which produces an axisymmetric plume. For this case, relatively straightforward analysis techniques are available to attack most of the problems outlined above. The plumes from the engines of a vehicle with multiple nozzles will interact with

each other once a certain environmental pressure level is reached. From this point on, the plume structure changes into a very complex three-dimensional flow field. Plume flow field structure in the interaction regions may be computed for certain highly restricted cases. However, the general three-dimensional plume flow field cannot be solved at the present time.

ANALYSIS

At the present time, a number of computer programs have been developed and can be used to solve technical problems in all areas of the overall analysis of the plume flow fields emanating from liquid propellant rocket engines. Depending upon the operating characteristics of the particular engine being analyzed and the degree of sophistication desired in the final results, the individual computer programs may be combined in a variety of ways. It is beyond the scope of this paper to give a complete technical analysis of all the programs; however, a short description of the various solutions is presented in the following individual sections.

COMBUSTION CHAMBER ANALYSIS

No complete characterization of the combustion chamber is possible at present. However, various combustion models can be applied to the combustion chamber to obtain useful solutions for this flow regime. The NASA/Lewis Thermochemical Program provides a one-dimensional adiabatic combustion chamber analysis with equilibrium products of combustion, and the analysis is straightforward and easy to use. This closed system analysis implicitly assumes that the combustor cross section is infinitely larger than the nozzle cross section. This restriction to the physical problem can be deleted by using the NASA/Lewis Program in connection with another one-dimensional analysis which calculates the total pressure loss the gas undergoes in passing from the injector to the throat, based on a choked flow condition at the throat. Using this technique gives good agreement with observed wall static pressure data, but does not agree with measured mass flow rates. One further modification to this basic one-dimensional analysis is possible. A portion of the fuel passing through the chamber can be assumed inert, and by choosing the correct portion, both wall
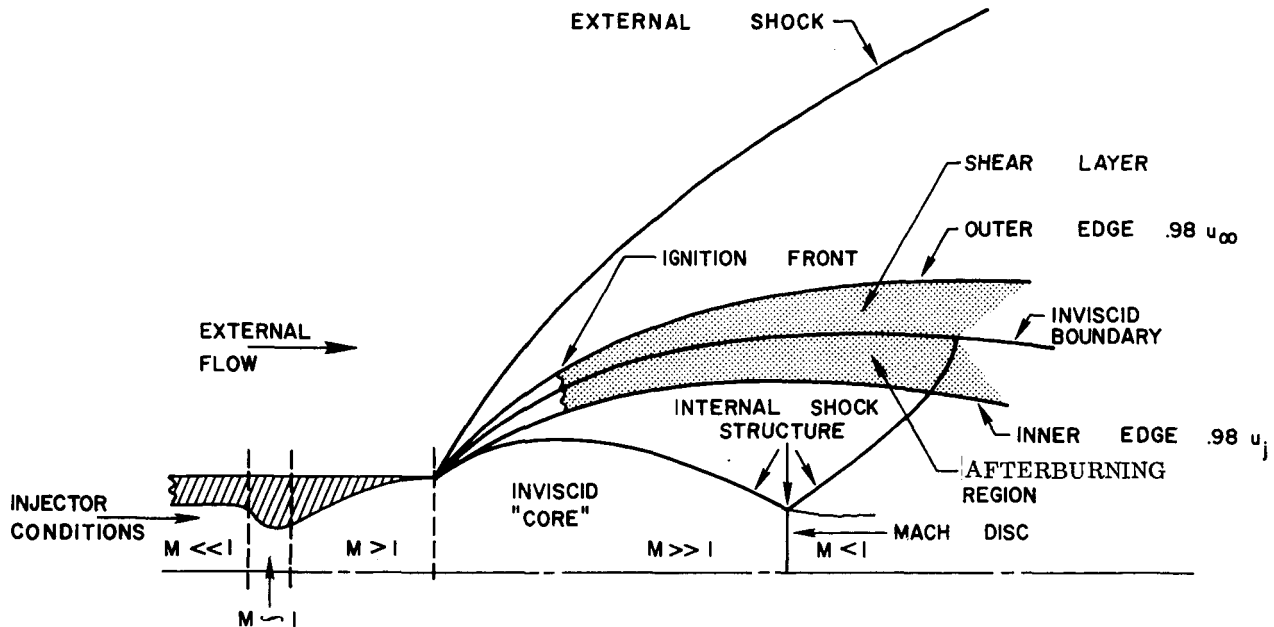
FIGURE 1. BASIC STRUCTURE OF LOW ALTITUDE, AFTERBURNING, JET

pressure data and mass flow data can be matched. This approach is severely dependent upon having experimental data and certainly does not give a great deal of physical understanding to the problem.

A more accurate analysis can be obtained by using a program that solves the two-dimensional turbulent boundary layer equations with wall boundary conditions, diffusion, finite rate chemistry effects, and arbitrary initial conditions. This program accounts for the initial nonuniform oxidizer/fuel (O/F) ratio existing in most large liquid rocket motors. The results from this analysis can be used as an input to the transonic nozzle throat solution, and consequently the effect of initial O/F variation can be traced through the throat and nozzle. This program does not account for droplet breakup, vaporization, or two-phase flow. In addition, the program is difficult to use and requires large amounts of computer time. Further work is needed to fully integrate this combustion chamber model to the transonic and the nozzle programs and to make the program faster and easier to use. The velocity profiles resulting from this type of analysis for a typical case are given in Figure 2.

STATION NUMBER	DISTANCE INJECTOR	FROM FACE
1	0.0254	METERS
2	0.0508	"
3	0.1016	"
4	0.1524	"
5	0.1778	"
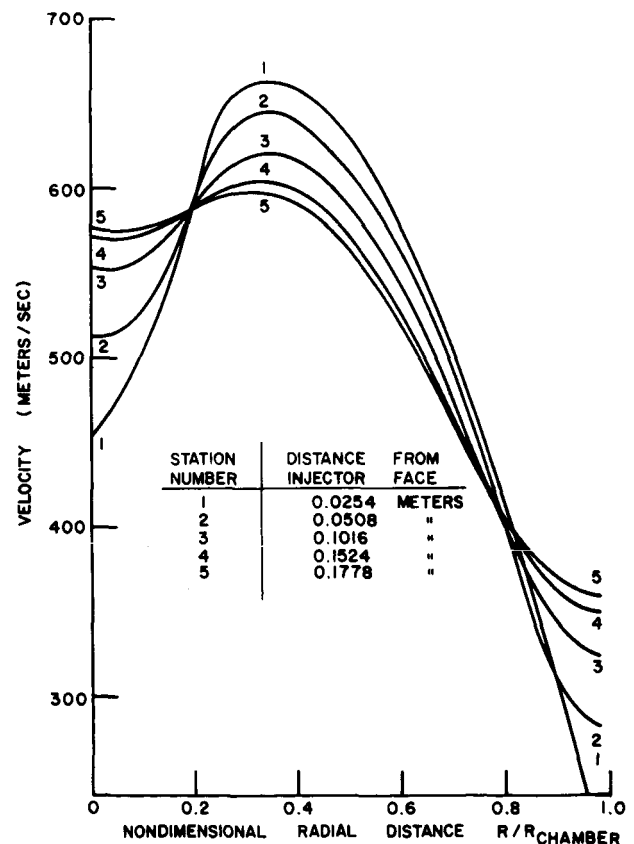
FIGURE 2. RADIAL PROFILES OF VELOCITY AT VARIOUS AXIAL STATIONS THROUGH THE COMBUSTION CHAMBER

INVISCID TRANSONIC THROAT FLOW FIELD ANALYSIS

The flow in the throat region of the nozzle is a mixed subsonic-supersonic flow which can be described by partial differential equations that are elliptic, parabolic, and hyperbolic. By writing the equations of motion in a time-dependent form, the equations of motion are hyperbolic for all velocity ranges, and solutions can be found by using numerical analysis techniques. If no time-dependent forcing function is used and arbitrary initial conditions are given, the desired steady state solution is found as the asymptotic time-dependent solution. The present solution is an explicit finite difference solution of the full Euler equations of motion for axisymmetric flow. In this type of solution, the spatial partial differentials are replaced by finite differences, and the time dependent terms are expanded in a Taylor's series to compute the next time step. This procedure is only conditionally stable, and the time step size is governed by the Courant-Freidrichs-Lewy stability criteria. The final results from this program give an initial data line for the method-of-characteristics program and input data for the nozzle boundary layer program.

A time-dependent solution is a long and tedious calculation, but it does solve the complete equations of motion for any required thermochemical model. It is the only known type of transonic solution which can account for the variable O/F ratio in the radial direction. The results of an ideal gas calculation for air and corresponding experimental data are shown in Figure 3. The absolute necessity for dealing with the O/F gradient problem will be shown in later results.

INVISCID SUPERSONIC NOZZLE AND PLUME FLOW FIELD

The inviscid portion of the nozzle and plume flow field located downstream of the nozzle throat is computed with a method-of-characteristics program. The method of characteristics is a numerical method for the solution of hyperbolic partial differential equations that traces the physical characteristic lines through the flow field. For this solution the differential equations are converted to finite-difference equations, which are solved by an iteration technique. With proper attention to grid size, solu-

tions with an arbitrarily high degree of numerical accuracy may be achieved.

The present program can compute flow fields for gas flow with equilibrium, frozen, or ideal gas thermochemical models. Also, flow fields that contain shock waves generated by geometric or flow phenomena are computed, and by using restart techniques, any number of shock waves may be computed. In conjunction with the equilibrium or frozen thermochemical models, it is possible to solve flow fields with arbitrary O/F gradients. Nozzle and plume flow fields are computed with the same computer program by using different boundary conditions. Plume flow fields may be computed with constant or variable pressure along the plume boundary depending upon the surrounding environment.

In Figure 4 typical results of an inviscid, ideal gas solution for air flowing through a small nozzle are superimposed on a schlieren picture of the flow field. Down to the location of the first Riemann wave, prediction of the flow field details is excellent, even though an approximate starting line was used at the throat and the nozzle boundary layer was not computed. The exit plane temperature distribution for a small lox-alcohol engine is presented in Figure 5, where the experimental data are compared with two theoretical calculations. The variable O/F distribution solution has the same average O/F ratio as the constant O/F solution. An example of F-1 engine and plume flow field at sea level, computed with multiple runs of the characteristics program, is shown in Figure 6. This figure gives an indication of the complexity of the flow fields that can be generated using this program.

NOZZLE BOUNDARY LAYER

For propulsion nozzles the usual thin boundary layer assumptions concerning the interaction with the inviscid flow field are applied. Quite often the turbine exhaust from the gas generator is dumped into the nozzle boundary layer. Within the limitations of an oversimplified chemistry model, these flows may be represented by a boundary layer solution with pressure gradient and mass injection.

A computer program to solve the boundary layer equations for these conditions has been prepared. This program solves the integral boundary layer momentum equation with a stepwise numerical integration along
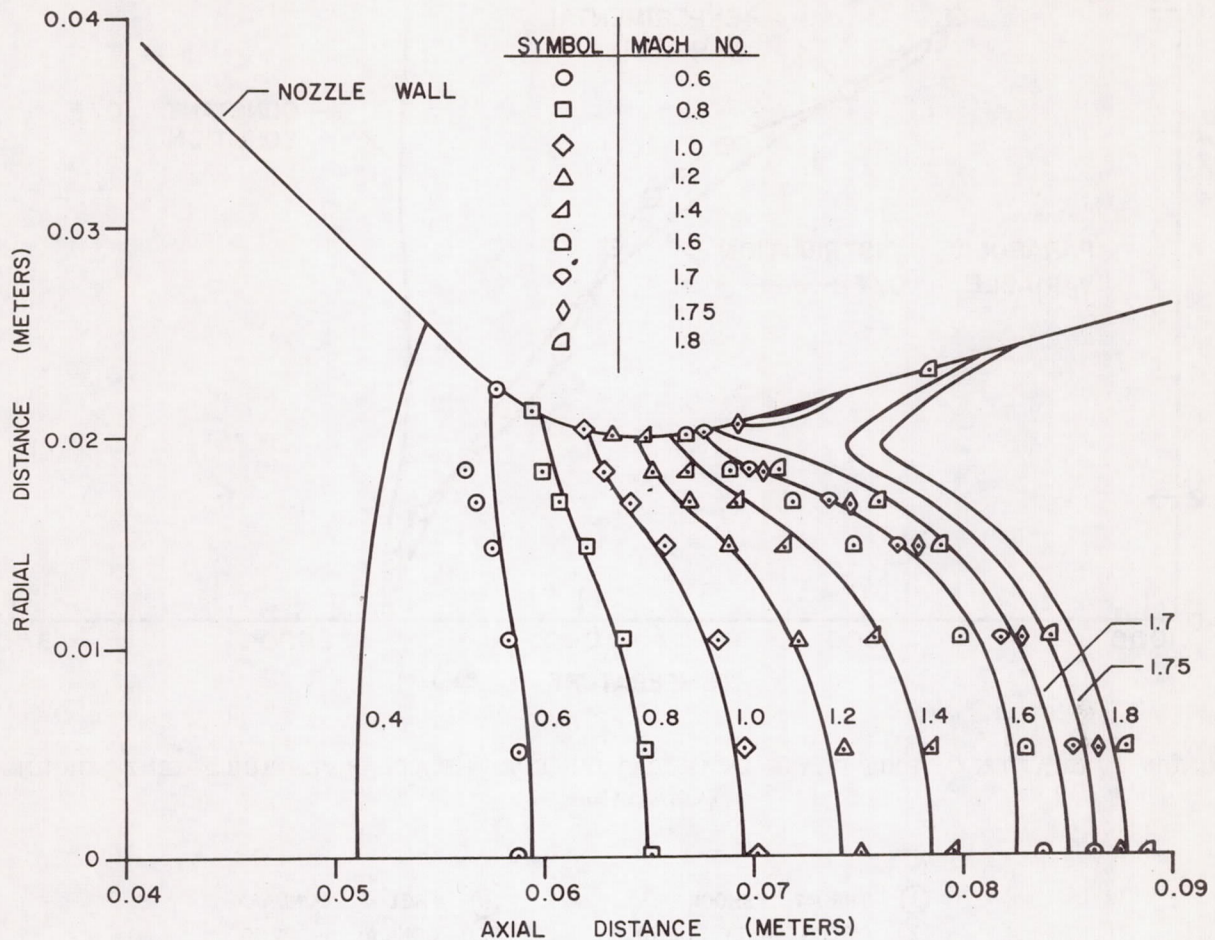
FIGURE 3. COMPARISON OF MEASURED AND COMPUTED MACH CONTOURS IN TRANSONIC FLOW REGION
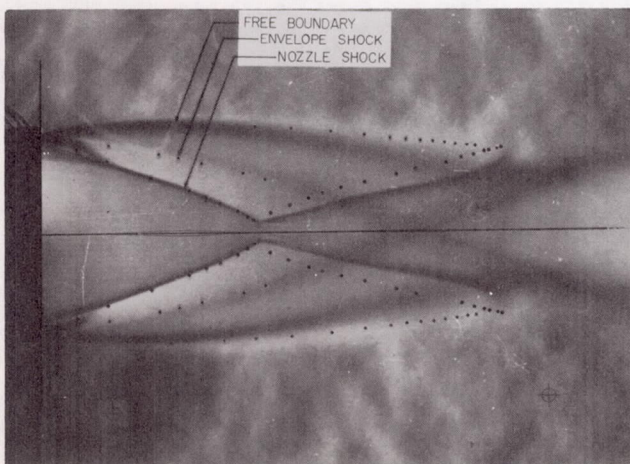
FIGURE 4. COMPARISON OF THEORETICAL AND EXPERIMENTAL RESULTS FOR A SMALL SCALE NOZZLE FLOWING AIR

the nozzle wall. The velocity profile and skin friction formula used in this program are based on Clauser's work, which has been modified for compressibility. A Crocco type density and temperature variation through the boundary layer as a function of velocity is used. The mass injection scheme of Spalding is used; this scheme is capable of calculating the boundary layer characteristics along a nozzle wall which has a distributed mass injection of arbitrary gas. The injected gas does not necessarily have to be the same as the gas in the boundary layer. However, if equilibrium chemistry is to be used, the boundary layer subroutines must be combined with an equilibrium real gas method-of-characteristics program. Either laminar or turbulent boundary layers may be considered, and when appropriate, the program will switch from the laminar mode to the turbulent mode

39
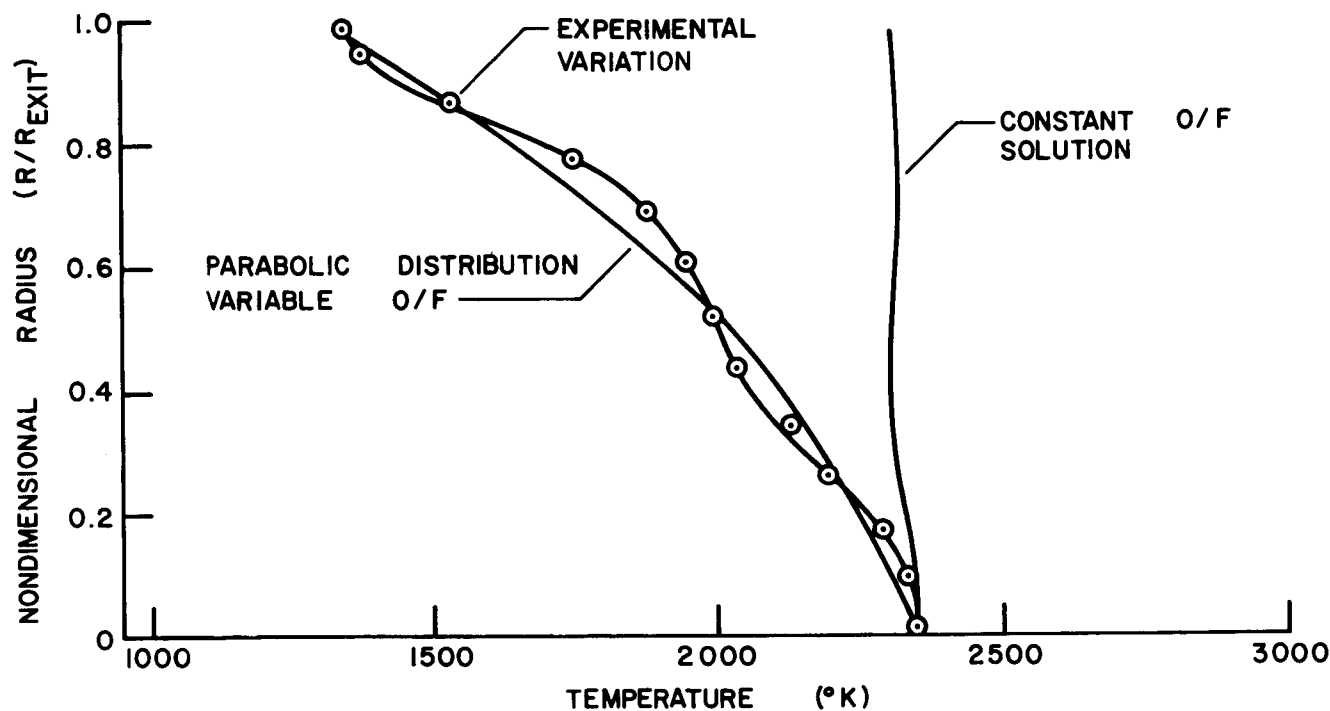
FIGURE 5. VARIATION OF EXIT PLANE TEMPERATURE FOR THE ATLAS VERNIER ENGINE BURNING LOX/ALCOHOL

① THROAT SHOCK   ⑥ FREE BOUNDARY
② DISCONTINUITY SHOCK   ⑦ CONICAL "PLUG"
③ INCIDENT SHOCK   ⑧ AXIS OF SYMMETRY
④ REFLECTED SHOCK   ⑨ EXIT PLANE
⑤ NOZZLE   ⑩ MACH DISC
    ⑪ WEAK REFLECTED SHOCK
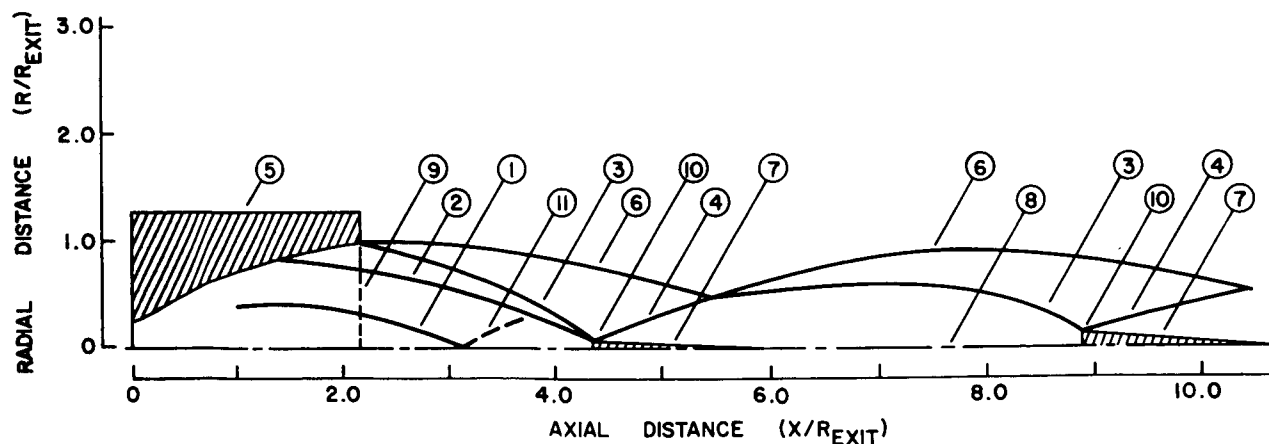
FIGURE 6. PLUME AND SHOCK STRUCTURE FOR AN F-1 ENGINE AT SEA LEVEL CONDITIONS

during a computer run. In addition, this program has the capability of calculating boundary layer expansion around a sharp corner.

Interaction effects of the viscous and inviscid solution, along with experimental data for an F-1 engine, are shown in Figure 7. The coupled solution obviously agrees with the experimental data better than the inviscid solution alone. An increase of momentum and displacement thicknesses along with a reduction of skin friction and heat transfer are the major effects of mass injection. Figure 8 shows the displacement thickness growth along the nozzle wall, plotted both with and without turbine exhaust gas injection. In this case the mass injection increases the displacement thickness by a factor of three.

FREE SHEAR LAYER

To describe a rocket engine exhaust plume at low or medium altitudes, the free shear layer regime must be considered in detail. Free shear layer dissipation results from the turbulent mixing of the plume with the external air flow and proceeds until the supersonic portion of the plume is consumed and finally the flow completely stops. At the present time, there is no general solution that is completely satisfactory for the entire viscous shear layer. However, by using the turbulent boundary layer equations with special boundary conditions and including the effects of chemistry, a reasonable approximation to portions of this region can be obtained. There are basically three programs that can be used for this analysis. One is a finite-difference finite-chemical reaction rate analysis and the other two are similarity-chemical equilibrium-type solutions. All three of these analyses are strongly dependent on empirical viscosity models; consequently, experimental confirmation is necessary to establish their validity. A brief description of the three basic programs follows.

1. Program one solves the boundary layer equations with an explicit finite-difference technique. As the solution proceeds downstream, the chemical composition is updated by the solution of a set of linearized finite rate chemistry equations. The program used to calculate the bottom curve shown in Figure 9 employed basically the parabolic boundary layer equations with no lateral pressure gradients. However, since this curve was generated, program one has been modified to account for lateral pressure gradients and now can be used for unbalanced (under-expanded) jet plumes as well as for the balanced (exact expansion) case. This program is the most realistic representation of the physical situation, but it is quite slow and cumbersome to use.

2. Program two solves only the momentum boundary layer equation with an explicit finite-difference technique. The velocity profile is non-dimensionalized with respect to the jet center line velocity, and the distribution of oxidizer and fuel mixture (fuel percentage) is assumed to be similar to the velocity profile. Based on the assumption of constant pressure and chemical equilibrium, a table containing fuel percentages from 0 to 100 versus temperature and concentration is constructed. As the momentum equation solution proceeds downstream, the temperature and concentration profiles are updated by interpolation from the isobaric equilibrium table.

3. Program three is similar to program number two. The difference is in the numerical technique employed to solve the momentum equation. This program does not calculate concentration profiles.

To illustrate the results of these three programs, an F-1 engine operating at sea level was analyzed. In Figure 9, in which maximum temperature is plotted as a function of axial position, the equilibrium solutions predict somewhat higher temperatures than the finite rate solution.

The delayed onset of afterburning can be predicted only by the use of finite rate chemistry models and even then only if all major reaction rates are known. In this calculation, some of this afterburning delay is evident, but, in general, agreement with experimental data has not been satisfactory. Further examination of this phenomenon is certainly warranted.

For calculations of this kind, the choice of the turbulent eddy viscosity model is of the utmost importance. For programs one and three, the Schetz-Favin eddy viscosity model is used, and for program two the Klunstein formula is used. The effect of the different formulations for the turbulent eddy viscosity models can be pronounced, especially concerning temperature and velocity decay along the streamline. Because of a lack of appropriate experimental information on reacting jet mixing, the most realistic eddy viscosity model cannot be determined at this time.
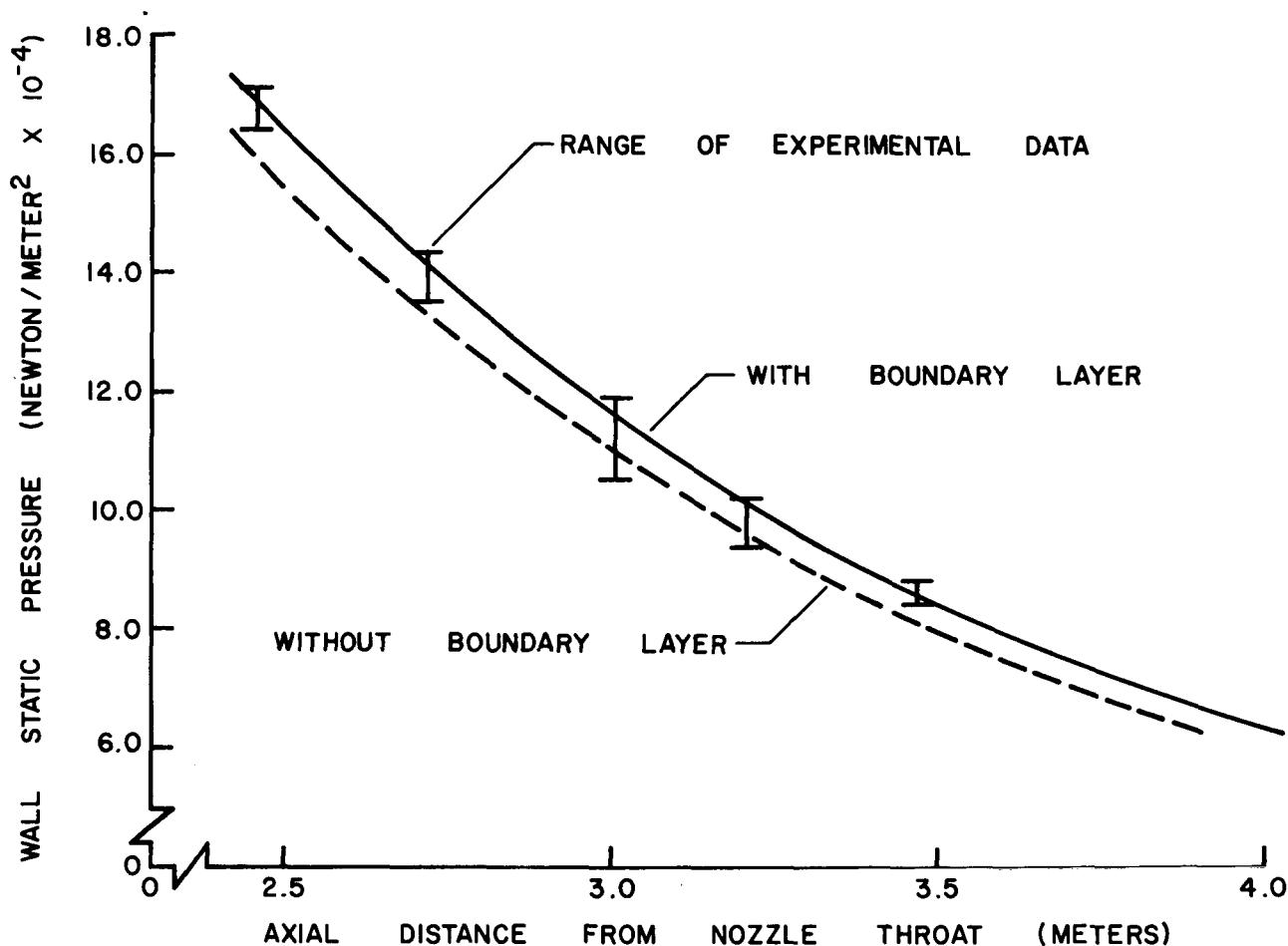
FIGURE 7. COMPARISON OF EXPERIMENTAL AND CALCULATED WALL PRESSURE ON F-1 COOLED NOZZLE EXTENSION, WITH AND WITHOUT BOUNDARY LAYER DISPLACEMENT THICKNESS EFFECTS

CONDENSATION

Most propellant combinations produce significant fractions of species, such as water vapor and carbon dioxide, that are easily condensed at relatively high temperatures. The condensation is homogeneous if no foreign particles are present; however, when foreign particles are present, the condensation may be homogeneous, heterogeneous, or a combination of both. Homogeneous condensation is controlled by the nuclei formation rate, which is obtained by solving the kinetic equation of condensation using the concept of a critical drop size. Drop growth rates are governed by the same condensation rate equations for both heterogeneous and homogeneous condensation.

The condensation process is controlled by physical and thermodynamic data that can best be derived from experimental data. For many of the species occurring in exhaust gases, very few data are available at the pressures and temperatures where condensation occurs. Also, surface tension data for small drops are not available, and values are usually extrapolated from plane surface values. This means that any condensation calculations made at the present time may be seriously in error.

Typical condensation calculation results for a one-dimensional nitrogen flow, taken from Reference 1, are presented in Figure 10. Obviously, the condensation process produces large changes in the physical properties of the gas phase compared to an isentropic expansion. This phenomenon needs to be considered if far-field regions of high altitude plumes must be analyzed.
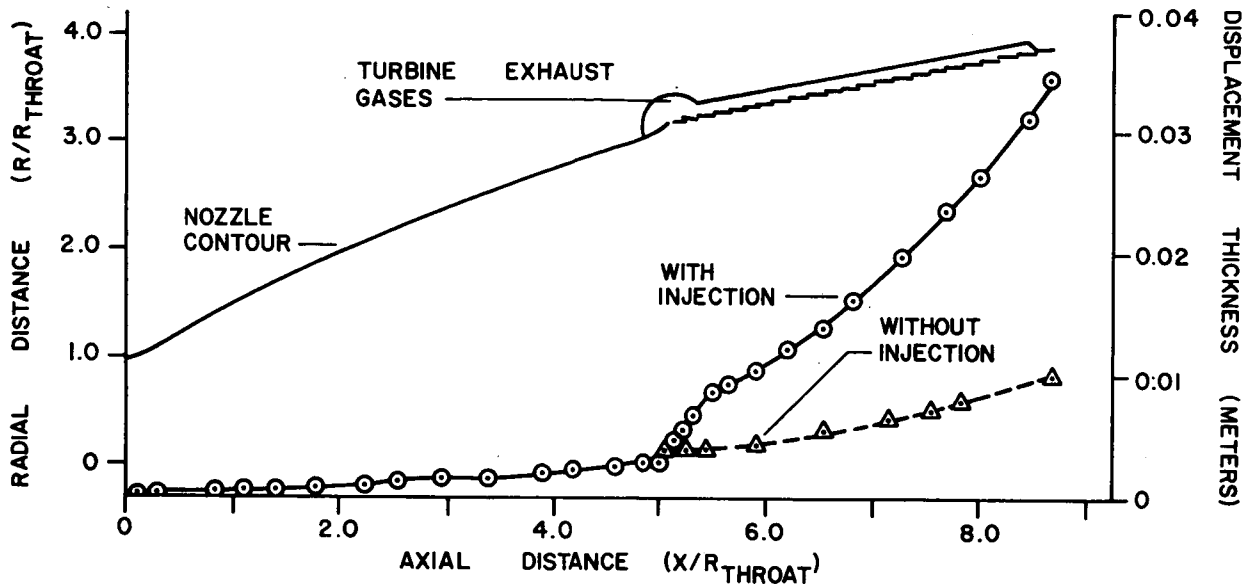
FIGURE 8. EFFECT OF TURBINE EXHAUST GAS INJECTION ON BOUNDARY LAYER DISPLACEMENT THICKNESS IN F-1 NOZZLE
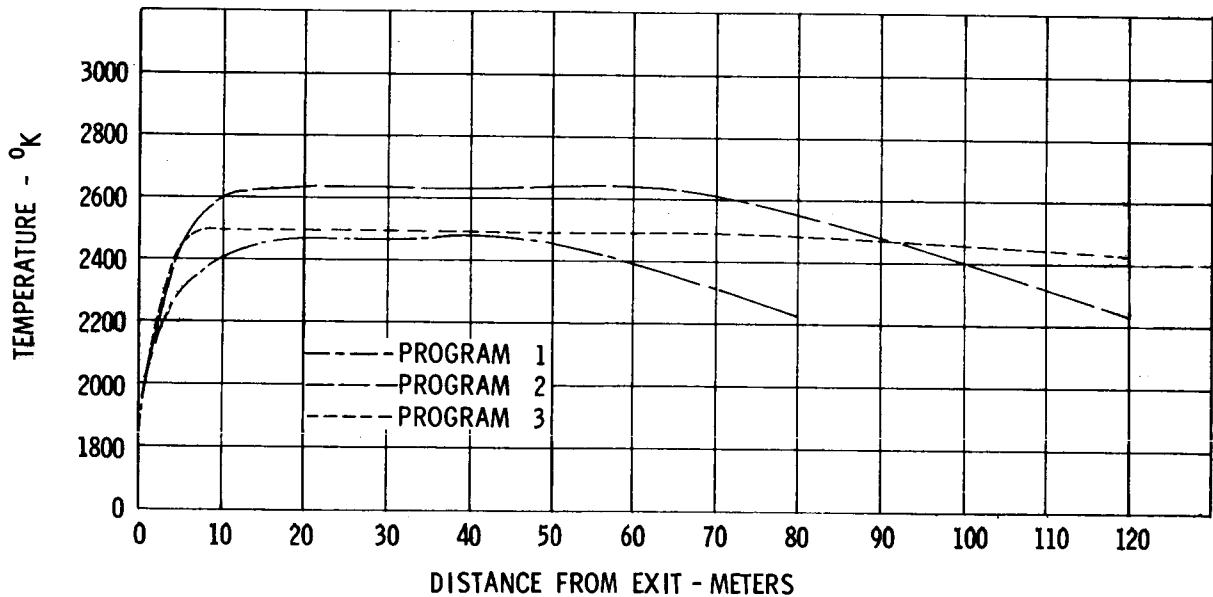
FIGURE 9. LONGITUDINAL VARIATION OF FREE SHEAR LAYER MAXIMUM TEMPERATURE

n,%	r_d,cm	N_d, $\frac{drops}{sec}$	S_d, $\frac{cm^2}{sec}$	Remarks
1 — 0	—	—	—	"Clean" case No effect
2 — .01	5×10^{-7}	2.6×10^{15}	0.82×10^4	
3 — .01	5×10^{-8}	2.6×10^{18}	0.82×10^5	
4 — 1.0	5×10^{-6}	2.6×10^{14}	0.82×10^5	Affected by
5 — 1.0	5×10^{-7}	2.6×10^{17}	0.82×10^6	foreign nuclei
6 — 1.0	5×10^{-8}	2.6×10^{20}	0.82×10^7	
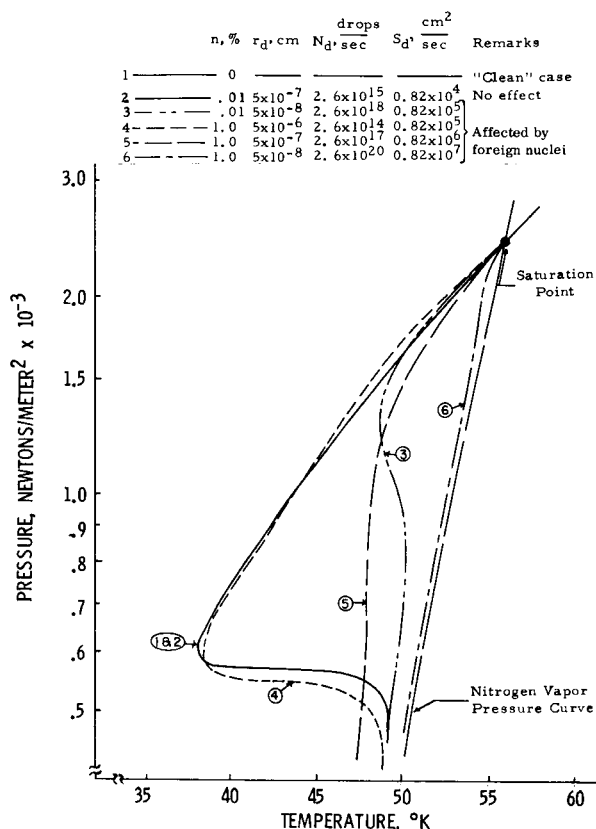
FIGURE 10. HETEROGENEOUS CONDENSATION: EFFECT OF FOREIGN NUCLEI ON CONDENSATION HISTORY

TRANSITION TO FREE MOLECULAR FLOW

On some surface in the flow field, the density of the gas becomes low enough so that it no longer obeys the laws of a continuum fluid. From this point on, a rigorous solution would require a general solution to the Boltzmann equation. Since this is not generally possible, an engineering approach to obtain numerical results was selected. The method of approach is based on the "freezing" of the various energy modes of the gas molecules. Since a large number of intermolecular collisions are necessary to maintain vibrational equilibrium and because the number of collisions steadily decreases with increasing rarefaction, vibrational equilibrium eventually can no longer be maintained. In a similar manner the rotational, and eventually, the translational energy modes also "freeze," and at that time the flow is considered to be free molecular. The calculations are then continued along streamlines (considered straight because of the source-like nature of the flow at high altitude) with the temperature and velocity held constant. The density of the flow field in the free molecular region is allowed to vary inversely as the cross-sectional area of the streamtubes formed by the adjacent streamlines. A local Knudsen number, which is defined as the ratio of the gas mean free path to a characteristic streamline length, is used as the freeze criterion.

The results computed by this method and the solution of Hamel and Willis of the Boltzmann equation for spherical source flow are compared in Figure 11. The overall agreement of these two results is quite good, although, as to be expected, there are significant differences at the freeze point. Figures 12 and 13 present the results of the calculation of a typical space plume computed by the methods described herein.

THREE-DIMENSIONAL PLUME REGIONS

For vehicles with multiple nozzles, the plumes interact and form a three-dimensional flow field when a certain environmental pressure level is reached. For certain parametric conditions, the entire three-dimensional flow field is supersonic, and it is theoretically possible to compute this flow with a three-dimensional method-of-characteristics procedure or with a finite-difference technique. At low environmental pressures, the plumes intersect at large angles, and strong shock waves with subsonic flow regions occur. At the present time, there is no solution available for this three-dimensional fixed-flow problem.

Even the simplest of these three-dimensional flow field problems is extremely complex. Finite-difference techniques for the calculation of the two-plume and five-plume interaction problems are available. This is not a time-dependent solution; therefore, all velocities must be supersonic for the procedure to be stable. Shock waves are computed as steep gradients over two or three mesh lengths. Overall, this represents a good first approximation, but is certainly far from the final desired result. The three-dimensional method-of-characteristics program for the two-plume interaction case is nearly complete. This solution uses a complex computer code which contains theoretical flow models for all physical phenomena found in the inviscid three-dimensional flow field.
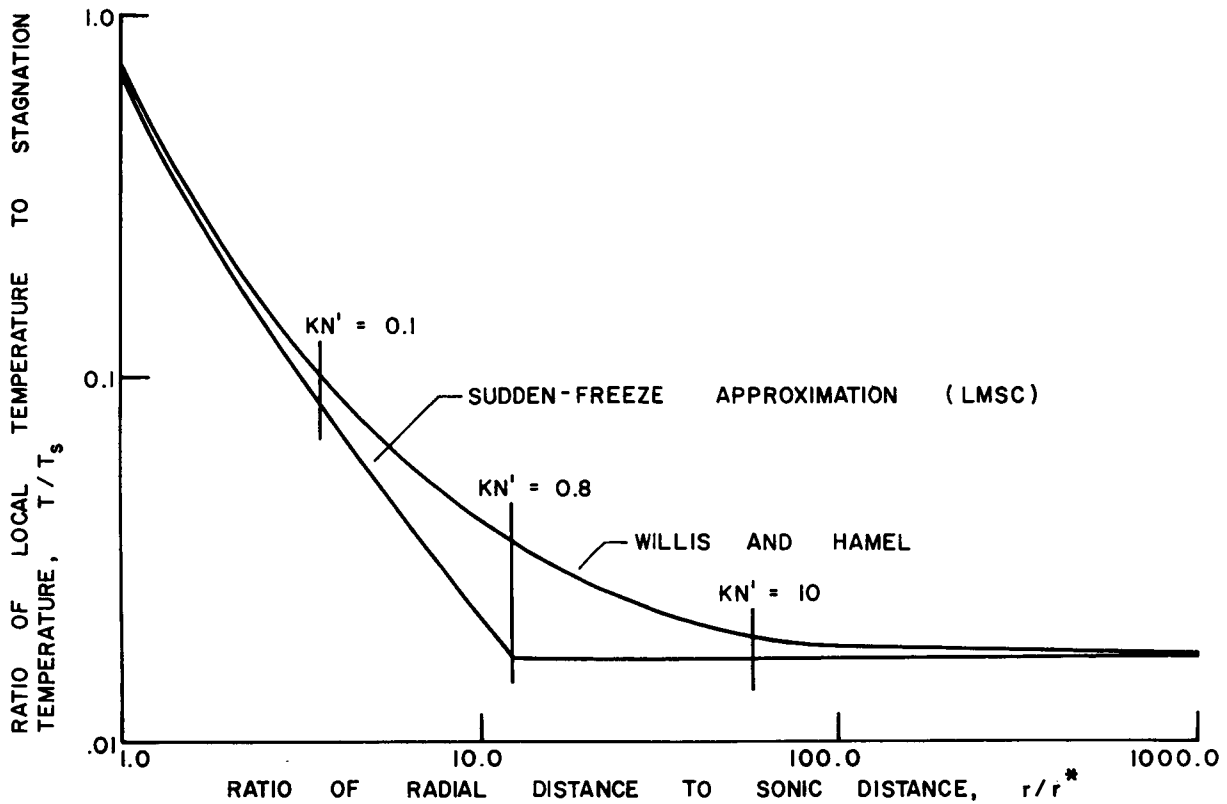
FIGURE 11. VARIATION IN TEMPERATURE WITH RADIAL DISTANCE FOR A SPHERICAL SOURCE FLOW EXPANSION

CONCLUSIONS

A number of computer programs have been developed for the solution of various technical aspects of the overall plume analysis problem. Depending upon the particular problem under consideration and the degree of sophistication desired in the final results, the individual computer programs may be coupled in a variety of ways. Some of these coupled modes of equation are shown in Figure 14.

When the somewhat sparse, detailed, experimental data for liquid fuel rocket engines are examined and compared with theoretical calculations, some of the conclusions that can be drawn are as follows:

1. Mixing and non-adiabatic combustion adjacent to the injector face cannot, at the present time, be adequately treated by purely theoretical analyses.

2. For nozzles operating with variable O/F ratio in the radial direction, the flow from the injector face to the throat entrance should be computed with programs that contain the diffusion-mixing terms.

3. A transonic solution which can handle equilibrium thermochemical properties and variable O/F ratios is required. Since the convective velocity is large compared with diffusion velocity in this region of the nozzle, an inviscid flow field solution may be adequate.

4. The point switch from equilibrium to frozen thermochemical models apparently yields excellent results in the inviscid flow field calculations. However, for many fuel/oxidizer combinations, the chemical reaction rates are not known sufficiently accurate to yield good freeze point locations.

45
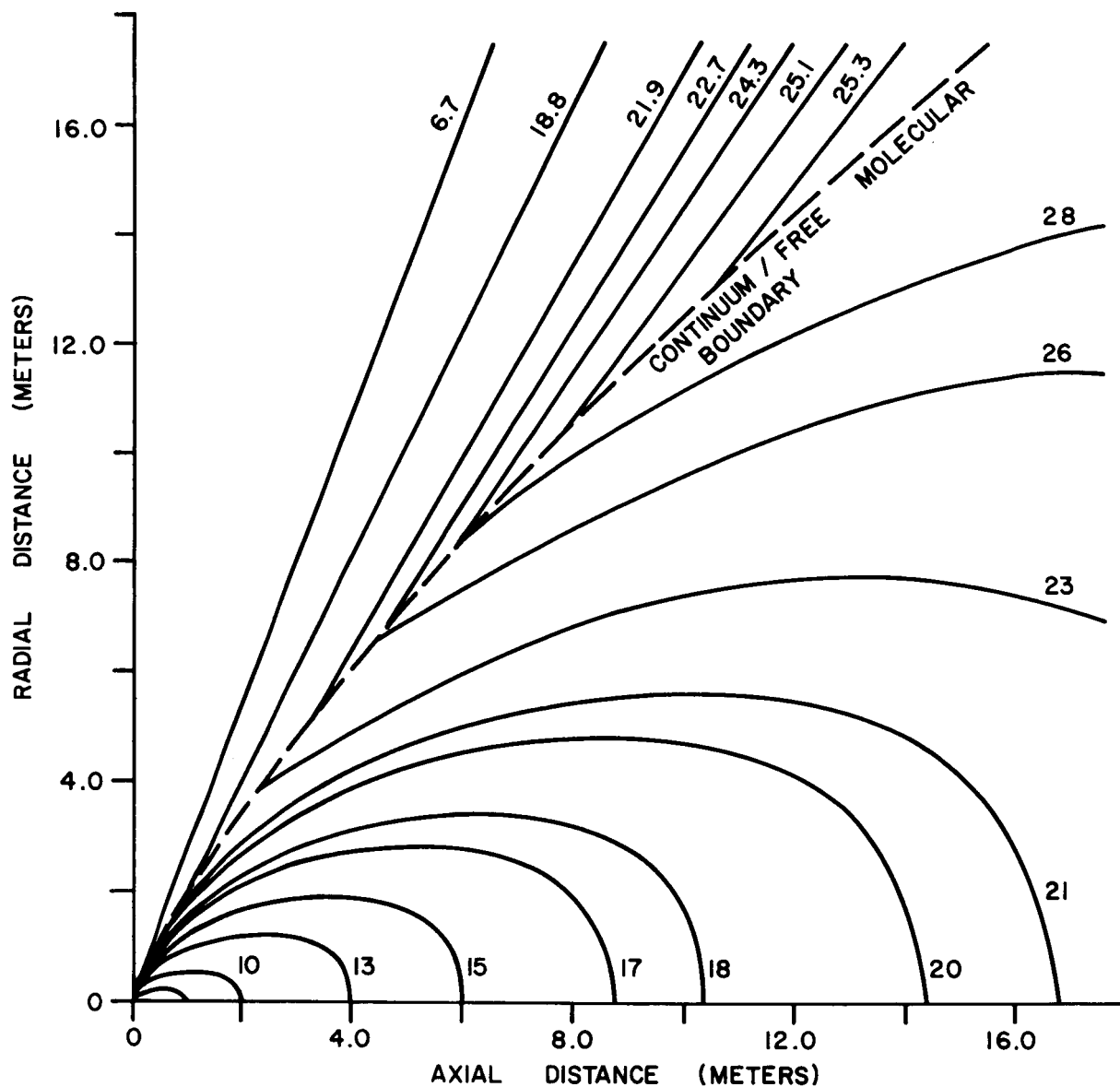
FIGURE 12. MACH NUMBER CONTOURS IN A TYPICAL SPACE PLUME

5. For afterburning in the free shock layer, it appears that chemical reaction times and flow times are comparable, and therefore are of equal importance in describing this portion of the plume.

6. Condensation phenomena and transition to free molecular flow are being considered in an elementary manner and much work remains to be done in these areas.
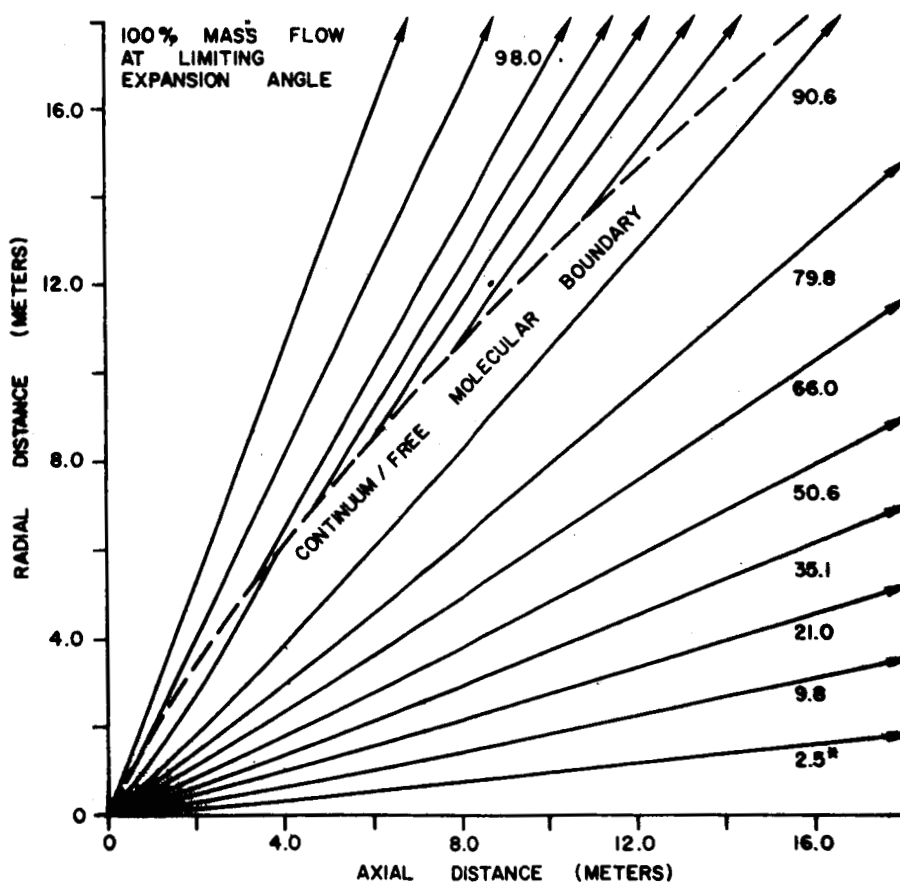
FIGURE 13. STREAMLINES AND MASSFLOW (2.5*) DISTRIBUTION IN TYPICAL SPACE PLUME
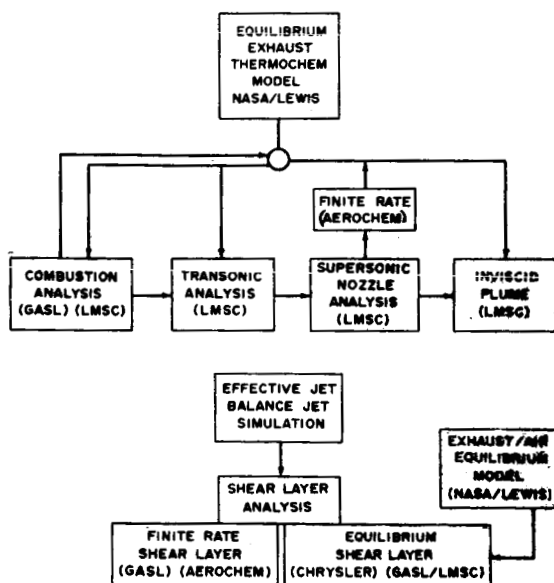
FIGURE 14. CALCULATIONAL PROCEDURES AND
FLOW REGIMES CONSIDERED IN STATE-OF-THE-
ART SHEAR LAYER ANALYSIS

47

REFERENCE

Sivier, Kenneth R.: Digital Computer Studies of Condensation in Expanding One-Component Flows. ARL 65-234, University of Michigan, November 1965.

BIBLIOGRAPHY

Audeh, B. J.: Equilibrium Shear Layer Program. Report No. A-784899, Lockheed Missiles and Space Co., LMSC/HREC, December 1967.

Butler, H.: Theoretical Analysis of an F-1 Engine Plume at Sea Level Design Conditions. Report No. A-784260, Lockheed Missiles and Space Co., LMSC/HREC.

Choudary, B. R.: Viscous Plume of the H-1 Engine at Sea Level. Report No. A-784263, Lockheed Missiles and Space Co., LMSC/HREC, May 1967.

Choudary, B. R.: Viscous Plumes of Saturn V Solid Propellant Engines at Sea Level. Report No. A-784302, Lockheed Missiles and Space Co., LMSC/HREC, May 1967.

D'Attorre, L.; and Thommen, H. V.: Base Flow Field Investigation on the S-II Stage. GDC DBE 67-013, Convair Division of General Dynamics, March 1967.

Edelman, R.; and Fortune, O.: A Preliminary Analysis of Mixing and Combustion of Ducted Flows with Application to Ejector Ramjet Technology. Job. No. 8876, General Applied Science Laboratories, Inc., Westbury, L. I., New York, May 1967.

Edelman, R.; and Weilerstein, G.: Multi-Component Multi-Phase Viscous Flow with Chemical Reactions. GASL Technical Report No. 508, General Applied Science Laboratories, Inc., Westbury, L.,I., New York, March 1965.

Edelman, R. and Fortune, O.: Mixing and Combustion in the Exhaust Plumes of Rocket Engines Burning RP-1 and Liquid Oxygen. GASL Report No. 631, General Applied Science Laboratories, Inc., Westbury, L. I., New York, November 1966.

Edelman, R.; and DeGroat: Mixing and Combustion in Supersonic Flow with Lateral Pressure Gradient Effects. GASL TR 636, General Applied Science Laboratories, Inc., Westbury, L. I. New York, August 1968.

Farmer, R. C.; Prozan, R. J.; McGimsey, L. R.; and Ratliff, A. W.: Verification of a Mathematical Model which Represents Large, Liquid Rocket-Engine Exhaust Plumes. AIAA Paper No. 66-650, Presented at the AIAA Second Propulsion Joint Specialist Conference, Colorado Springs, Colorado, June 13-17, 1966.

Fortune, O.; and Edelman, R.: The Effect of Mixing, Radiation and Finite-Rate Combustion upon the Flow Field and Surroundings of the Exhaust Plumes of Rocket Engines Burning RP-1 (Kerosene) and Liquid Oxygen. GASL TR No. 681, General Applied Science Laboratories, Inc., December 1967.

Hale, D. V.: A Turbulent Distributed Injection Boundary Layer Computer Program. Report No. A-183452, Contract NAS 8-20052, Lockheed Missiles and Space Company, LMSC/HREC, November 1966.

Hoenig, R. J.: LMSC/HREC Boundary Layer Computer Program-Theory. Report No. A-782405, Lockheed Missiles and Space Co., LMSC/HREC, March 1967.

BIBLIOGRAPHY (Concluded)

Jensen, D. E.; and Kurzius, S. C.: Rate Constants for Calculations on Nozzle and Rocket Exhaust Flow Fields. TP-149, Aero-Chemical Research Laboratories, Inc., March 1967.

Komianos, S. A.; Bleich, G. D.; and Pergament, H. S.: The Aero-Chem Non-Equilibrium Streamline Program. Aero-Chem TN 103, Aero-Chem Research Laboratories, Inc., May 1967.

McGimsey, L. R.: Viscous Plume of F-1 Engine at Sea Level. Report No. A-784075, Lockheed Missiles and Space Co., LMSC/HREC, March 1967.

Powers, S. A.; and Ziegler, H.: Determination of the Aerodynamic Properties of Engine Exhaust Plumes. Progress Reports on NAS 8-11260, in progress.

Prozan, R. J.; and Audeh, B. J.: Prediction of Electron Density in Rocket Exhaust Plumes. Report No. A-784870, Lockheed Missiles and Space Co., LMSC/HREC, October 1967.

Prozan, R. J.: Development of a Method of Characteristics Solution for Supersonic Flow of an Ideal, Frozen, or Equilibrium Reacting Gas Mixture. Report No. A-782535, Lockheed Missiles and Space Co., LMSC/HREC, April 1966.

Ratliff, A. W.; Blackledge, M. L.; Butler, H. W.; and Kooker, D. E.: Analysis of Heating Rates and Forces on Bodies Subject to Rocket Exhaust Plume Impingement. Report No. A-791230, Lockheed Missiles and Space Company, LMSC/HREC, March 1968.

Rochell, W. C.;: Review of Thermal Radiation from Liquid and Solid Propellant Rocket Exhaust. NASA TM X-53579, February 1967.

Rochell, W. C.: Theoretical and Experimental Investigation of Heating from Saturn Solid Propellant Rocket Plumes. AIAA Paper No. 66-653, Presented at AIAA Second Propulsion Joint Specialist Conference, Colorado Springs, Colorado, June 13-17, 1966.

Slutsky, S.: Stable Computation Techniques of Coupled Diffusion and Chemical Reaction in Shear Flows. Technical Memo No. 101, General Applied Science Laboratories, December 1963.

Smoot, L. D. and Farmer, R. C.: Rocket Plume Technology. Preprint 13A, Presented at the Symposium on Rocket Exhaust Plume Phenomena, Second Joint AICHE-IIQPR Meeting, Tampa, Florida, May 1968.

Spalding, Audender; and Sundaram: The Calculation of Heat and Mass Transfer through the Turbulent Boundary Layer on a Flat Plate at High Mach Numbers, with and without Chemical Reaction. Supersonic Flow, Chemical and Radiative Transfer, edited by Olfe Zakkay, 1964, pp. 211-276.

Stephens, J. T.: Analytical Results for Transonic Flow Fields in Rocket Motors. Report No. A-784847, Lockheed Missiles and Space Co., LMSC/HREC, October 1967.

Tamagno, J.; and Trentacoste, N.: An Experimental and Analytical Investigation of Ignition and Axisymmetric Turbulent Flame Propagation in Hydrogen-Air Mixture at Supersonic Speeds. GASL Tech Report 445, General Applied Sciences Laboratories, Inc., Westbury, L. I., New York, July 1964.

Zelezink, F. J.; and Gordon, S.: A General IBM 704 or 7090 Computer Program for Computation of Chemical Equilibrium Compositions, Rocket Performance and Chapman-Jouquet Detonations. NASA TN D-1454, October 1962.

TECHNIQUES DEVELOPED TO DETERMINE AERODYNAMIC COEFFICIENTS FOR APOLLO APPLICATIONS PROGRAM VEHICLES IN AN ORBITAL ENVIRONMENT

By

Josh D. Johnson

SUMMARY

This paper describes two methods that were developed to determine the aerodynamic forces acting on artificial earth satellites with complex external shapes. One method, a numerical solution based on well-established free molecule flow theory, has the capability to determine areas on a vehicle that are shaded from the flow. This method, which is applicable for speed ratios equal to or greater than two, requires large amounts of computer time. The second method is an approximation technique that uses the projected frontal area as a basis for computing aerodynamic forces. This method, applicable for speed ratios greater than seven, is particularly useful when large amounts of data are required for several similar configuration geometries. Projected areas for use in this method are determined with a machine developed by the Aerophysics Division of the Aero-Astrodynamics Laboratory.

LIST OF SYMBOLS

Symbol	Definition
A	surface area
A_{ref}	reference area
C_A	axial force coefficient, $\dfrac{\text{Axial Force}}{qA_{ref}}$
C_D	drag coefficient, $\dfrac{\text{Drag}}{qA_{ref}}$
C_{D_o}	drag coefficient based on projected frontal area, $\dfrac{\text{Drag}}{q\times(\text{projected frontal area})}$
C_L	lift coefficient, $\dfrac{\text{Lift}}{qA_{ref}}$
C_{L_o}	lift coefficient based on projected frontal area, $\dfrac{\text{Lift}}{q\times(\text{projected frontal area})}$
C_M	pitching moment coefficient, $\dfrac{\text{Pitching Moment}}{qA_{ref}}$
C_N	normal force coefficient, $\dfrac{\text{Normal Force}}{qA_{ref}}$
dE_i	energy flux incident on an elemental surface per unit time
dE_r	energy flux re-emitted from an elemental surface element per unit time
dE_w	energy flux that would be carried away from an elemental surface per unit time if incident molecules were re-emitted with a Maxwellian distribution corresponding to the surface temperature.
erf	error function
k, ℓ, t	direction cosines between local coordinates on an elemental surface and the desired force direction
q	dynamic pressure
S	molecule speed ratio
T_i	incident molecule (atmospheric) temperature
T_r	reflected molecule temperature
T_w	vehicle wall temperature
$\vec{V}$	velocity vector
α	angle of attack
α'	energy accommodation coefficient

ϵ, ξ, η direction cosines between local coordinates on an elemental surface and the velocity vector

INTRODUCTION

Acquiring and maintaining a satellite orbit and orientation, or predicting the long and short term motion of an orbiting body, requires a commanding knowledge of the forces perturbing the body's motion. For example, Apollo Applications experiments require a detailed knowledge of the inertial forces, gravity gradient torques, and aerodynamic forces so that prescribed vehicle attitudes can be maintained during orbital operations. This paper describes two methods that have been developed to calculate the aerodynamic forces, which are some of the more important perturbing forces that influence satellite attitudes and orbital lifetimes for vehicles in low earth orbits.

The first method developed to calculate aerodynamic forces is a numerical solution based on free molecule flow theory. This solution has been incorporated in a computer program that can be used to analyze vehicles such as the S-IVB Orbital Workshop with the docked Command and Service Module and Lunar Module/Apollo Telescope Mount. The second method is based on a simplified analysis, and can be used to produce numbers fairly rapidly. This method, called the "shadow method," uses the projected frontal area as a basis for calculating aerodynamic force coefficients. Both of these methods can be used to calculate aerodynamic forces on satellites that have complex external shapes. Before the development of these two methods, free molecule aerodynamic forces were calculated with a computer program capable of handling only simple external shapes.

NUMERICAL SOLUTION

In a highly rarefied flow, the mean free path of molecules is much greater than the dimensions of bodies immersed in the flow. We are thus led to the assumption that incident-molecule/surface collisions are much more numerous than incident-molecule/incident-molecule and incident-molecule/reflected-molecule collisions. This assumption means that the incident flow can be assumed to be undisturbed by the

presence of a body in the flow [1]. For this type of flow, which is called "free molecule" flow, Sentman [1] has used Maxwell's velocity distribution function to derive aerodynamic force coefficient equations for flat plates, spherical sections, cylinders, and conic sections. Sentman assumed completely diffuse reflection to derive force coefficient equations. He derived the following free molecule force coefficient equation for an arbitrary body shape:

$$
\frac{dC}{dA} = \frac{1}{A_{ref}} \left\{ [\epsilon k + \xi \ell + \eta t] \left[\xi(1 + erf \xi S) + \frac{e^{-\xi^2 S^2}}{S \sqrt{\pi}} \right] \right.
$$
$$
+ \frac{\ell}{2S^2} [1 + erf \xi S] + \frac{\ell}{2} \sqrt{\frac{T_r}{T_i}} \left[\frac{\xi \sqrt{\pi}}{S} (1 + erf \xi S) \right.
$$
$$
\left. \left. + \frac{e^{-\xi^2 S^2}}{S^2} \right] \right\} \quad (1)
$$

In this equation, S is the molecular speed ratio which, for a satellite, is defined as the ratio of the speed of the satellite relative to the surrounding atmosphere to the most probable random speed of the molecules in the surrounding atmosphere.

Equation (1) is the equation for the total force coefficient acting in a particular direction on an elemental area of a body immersed in free molecule flow, assuming diffuse reflection. This equation is exact within the physical assumptions of kinetic theory, free molecule flow, and diffuse reflection [1].

Davis, Lake, and Breckenridge [2] have used equation (1) to formulate a numerical solution. This solution has been incorporated in a computer that can be used to calculate free molecule aerodynamic force coefficients on bodies having complex external shapes. In order to use equation (1), the authors listed above made three assumptions, in addition to those already stated:

1. Incident molecules are assumed to be fully accommodated to the body wall temperature before they are reflected; i.e., $T_r = T_w$.

2. Elemental surface areas that are located on the leeward side of a body so that they are shielded from the flow are assumed to experience no molecule collisions. This type of shielding is indicated on Figure 1 as Type I shading. This is a good assumption for bodies traveling at high velocities because the number of molecules colliding on the back side of the body will be considerably less than the number colliding on

Body C

Body B

Type II Shading:
Body B and Part of
Body C Shielded from
the Flow by Body A

Type I Shading: Leeward Side of
Body A does not
"see" the Flow

Body A
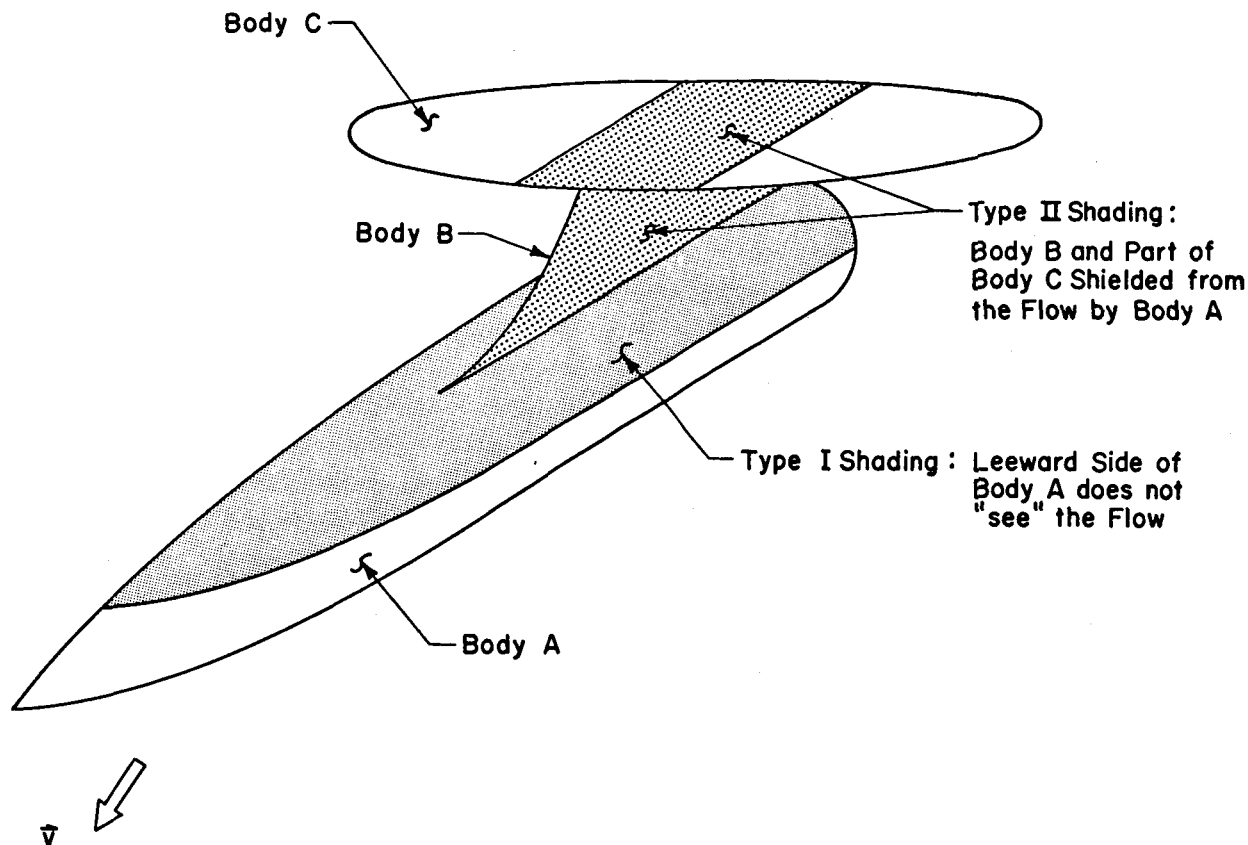
FIGURE 1. CONFIGURATION DRAWING ILLUSTRATING THE TWO TYPES OF SHADING

the front side. For instance, for a flat plate moving broadside through a rarefied gas with the relatively low speed ratio of 2, the ratio of the number of collisions on the front side of the plate to the number of collisions on the rear side is approximately 10^3.

3. Parts of a body that are shielded from the flow by other parts of the body are assumed to experience no molecule collisions.[1] This type of shielding is indicated as Type II shading in Figure 1. This assumption will not introduce large errors into computed aerodynamic coefficients as long as the speed ratio is high and the distance between the shaded and shading parts is short.

The second and third assumptions limit the use of the numerical solution at low speed ratios. Since speed ratios range from approximately six to ten for typical Apollo Applications missions, detailed studies

have not been conducted to determine the effects of these assumptions at low speed ratios. However, it is suggested that caution certainly should be used when the numerical solution is used at speed ratios of less than 2. Although a detailed description of the numerical solution is beyond the scope of this paper, such a description, including program listings and flow charts, is available in Reference 2.

THE SHADOW METHOD

The use of numerical techniques to analyze complex satellite shapes is time-consuming even on fast electronic computers. Also, the subroutines necessary to determine shaded portions of a satellite are time-consuming. Because the numerical solution must, of necessity, use these time-consuming techniques, a large amount of computer time is required

---

1. When compared to other existing computer solutions, the things that make this numerical solution unique are its ability to handle complex shapes and the subroutines that can determine the two types of shaded areas.

to examine a satellite such as the S-IVB Orbital Workshop for a large number of angles of attack and roll angles. It is desirable, then, to have a simplified method that can produce numbers rapidly. This is particularly desirable during the preliminary design stages when a quick answer based on a simplified analysis will suffice. With these requirements in mind, the shadow method, described below, was developed by the Aerophysics Division of the Aero-Astrodynamics Laboratory.

Consider free molecule flow past a flat plate at some angle of attack, α, as shown in Figure 2. The lift and drag coefficients, derived from equation (1), are as follows:

$$C_L = \frac{A}{A_{ref}} \left\{ \frac{\cos\alpha}{S^2} \operatorname{erf}(S\sin\alpha) \right.$$

$$\left. + \sqrt{\frac{T_r}{T_i}} \frac{\sqrt{\pi}}{S} \sin\alpha \cos\alpha \right\} \qquad (2)$$

$$C_D = \frac{A}{A_{ref}} \left\{ \left[2 + \frac{1}{S^2}\right] \sin\alpha \operatorname{erf}(S\sin\alpha) \right.$$

$$\left. + \frac{2e^{-S^2\sin^2\alpha}}{S\sqrt{\pi}} + \sqrt{\frac{T_r}{T_i}} \frac{\sqrt{\pi}}{S} \sin^2\alpha \right\} . \qquad (3)$$

If the projected frontal area is used as the reference area, then these equations reduce to

$$C_{L_o} = \frac{\operatorname{erf}(S\sin\alpha)}{S^2 \tan\alpha} + \sqrt{\frac{T_r}{T_i}} \frac{\sqrt{\pi}}{S} \cos\alpha \qquad (4)$$

and

$$C_{D_o} = \left[2 + \frac{1}{S^2}\right] \operatorname{erf}(S\sin\alpha) + \frac{2e^{-S^2\sin^2\alpha}}{S\sqrt{\pi}\sin\alpha}$$

$$+ \sqrt{\frac{T_r}{T_i}} \frac{\sqrt{\pi}}{S} \sin\alpha . \qquad (5)$$
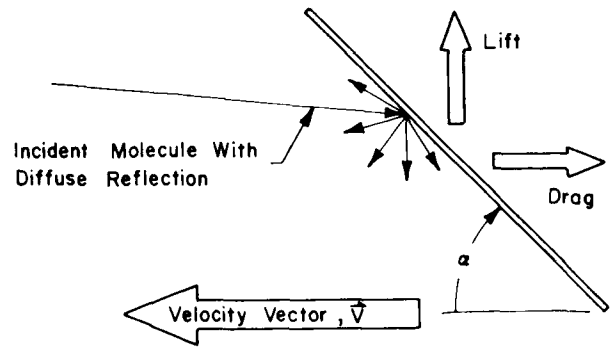
FIGURE 2. FREE MOLECULE FLOW OVER A FLAT PLATE

An examination of these two equations shows that as S approaches infinity, C_{L_o} approaches zero and C_{D_o} approaches 2. Moreover, at low speed ratios, C_{L_o} and C_{D_o} approach these limits quite rapidly (Fig. 3) because incident molecules are assumed to be completely absorbed on the flat plate surface and then re-emitted diffusely with a Maxwellian velocity distribution corresponding to the temperature of the plate;[2] therefore, incident molecules create a force on the plate at high speed ratios that is directed almost entirely in the drag direction, while lift is created primarily by the diffusely reflected molecules that are re-emitted at an energy level much lower than the energy level of incident molecules. From these observations, we conclude that, for a first order approximation, the drag may be assumed to be the total force acting on the plate when the speed ratio is large (greater than 7 or 8). Furthermore, the drag coefficient can be assumed to have a value only slightly larger than 2.0.

The analysis presented above for a flat plate may also be applied to other body shapes, such as cones, cylinders, and spheres; that is, for these body shapes, C_{D_o} approaches 2, and C_{L_o} approaches zero as the speed ratio increases. Therefore, we may conclude that, for any vehicle moving in free molecule flow with

---

2. As indicated in Figure 2, incident molecules are not necessarily moving in a direction parallel to the plate velocity vector. The velocity of impinging molecules is composed of a component created by random thermal motion of the molecules and a component created by the motion of the plate through the atmosphere. The component created by random thermal motion remains constant as the plate velocity increases; therefore, as the speed ratio increases, it has a decreasing effect so that, at high speed ratios, most molecules are moving in a direction almost parallel to the plate velocity vector when they strike the plate.
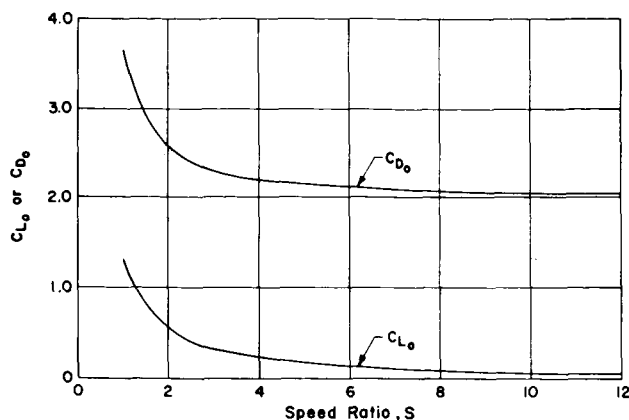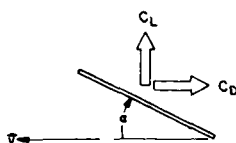
FIGURE 3. LIFT AND DRAG COEFFICIENTS FOR A FLAT PLATE ($\alpha = 45°$, $T_w/T_i = 0.25$)

a high speed ratio, drag may be assumed to be the only aerodynamic force acting on the body, and C_{D_o} can be assigned a value near 2. Furthermore, since C_{D_o} is based on a reference area equal to the projected frontal area, the aerodynamic force acting on a vehicle of any shape can be determined if the projected frontal area is known. Also, aerodynamic moments can be determined if the centroid of the projected area is known, because the drag vector calculated by this method passes through the centroid of the projected area.

The projected frontal area of a vehicle is equal to the area of the shadow that would be cast on a screen if the vehicle is placed between a parallel light source and the screen. This fact has been used as the foundation for the design of a machine that uses a shadow cast on a screen to measure projected frontal areas of scaled satellite models. This machine, called the "shadow scanner," (sketched in Figure 4) uses a scaled model which is suspended between a parallel light source and a screen. A column of 70 photocells scan behind the 44.450 cm by 44.450 cm screen and record the size and position of the shadow cast on the screen. The model is placed so that the model body axes are at a known position relative to the screen; therefore, the

information from the photocells can be used to determine both the area and the centroid of the model shadow relative to the model axes. Photographs of the shadow scanner are shown in Figure 5.

A detailed analysis presented in Reference 3 describes the equations that are necessary to convert areas and centroids determined with the shadow scanner to full-scale aerodynamic force and moment coefficients. Although a detailed discussion of these equations is beyond the scope of this paper, a brief description of the method used to determine C_{D_o} is in order.

As shown earlier in the text and as shown in Figure 3 for a flat plate, C_{D_o} approaches 2 as S approaches infinity. However, typical Apollo Application satellites orbit the earth with speed ratios in the range from 6 to 10. To offset some of the error that would be introduced by using a value of 2 for C_{D_o}, the following procedure is used to determine the value of C_{D_o} that should be used with the areas calculated from the shadow scanner output. The speed ratio, S, and the temperature ratio, T_r/T_i, are calculated for the orbital mission being investigated. Then a value of C_{D_o} is selected that corresponds to the value of C_{D_o} for a flat plate moving broadside through the atmosphere with a speed ratio and temperature ratio equal to these calculated values. Typical curves of C_{D_o} vs. S, shown in Figure 6 for a flat plate, are presented for temperature ratios of 0, 0.25, and 1.00. The ratio $T_r/T_i = 0.25$ was selected for one of the curves since calculated values for AAP missions are near this number.

COMPARISON OF TECHNIQUES

Comparisons are presented in Figures 7 and 8 for aerodynamic coefficients calculated with the numerical solution and the shadow method. Data for a cone-cylinder model are presented in Figure 7, and data for the Apollo Application Orbital Workshop configuration are presented in Figure 8. The data presented in these figures for the shadow method were
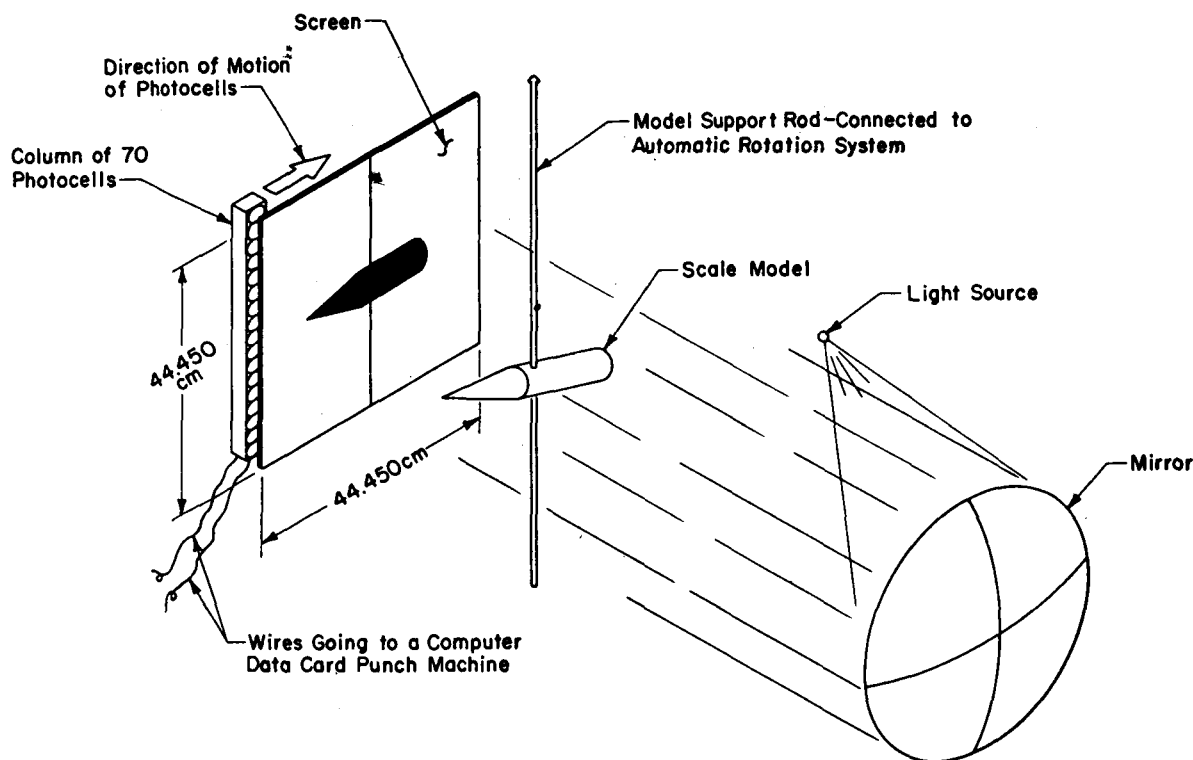
FIGURE 4. SCHEMATIC DIAGRAM OF THE SHADOW SCANNER

determined from projected areas that were measured with models in the shadow scanner. The cone-cylinder model had the dimensions that are shown in Figure 7, and the Orbital Workshop model was a one percent scale model.

The comparison of the data for the cone-cylinder model shows excellent agreement between the two methods. The comparison for the Orbital Workshop shows excellent agreement for C_D, and the pitching moment coefficient, C_m, shows fair agreement with a maximum difference of approximately 7 percent at an angle of attack of 90 degrees. These comparisons indicate that the shadow method is a perfectly acceptable method for calculating free molecule aerodynamic coefficients for vehicles moving at high speed ratios. However, some degree of caution should be exercised when the shadow method is used to calculate aerodynamic coefficients for vehicles moving at low angles of attack. This is apparent in part in Figures 7 and 8 where we see that, for $\alpha = 0$ degrees, the value of C_A (Fig. 7) and the value of C_D (Fig. 8) calculated with the shadow method are lower than the

values calculated with the numerical solution. This point is clearly visible in Figure 9.

In Figure 9, curves for a cylinder show the variation of C_{D_o} and C_{L_o} as a function of the length-to-diameter ratio of the cylinder for a speed ratio of 10 and a temperature ratio of 0.25. Curves for angles of attack of 45 and 90 degrees show values of C_{D_o} near 2, as would be expected from the discussion presented earlier in this paper. However, the curve for zero degrees angle of attack shows that the value of C_{D_o} increases linearly with increasing length. This increase is caused by the shear forces on the cylinder that are directly proportional to the surface area of the cylinder. Since, for $\alpha = 0$ degrees, the projected frontal area of the cylinder does not increase as the length increases, the shadow method cannot be used for this particular orientation of a long cylinder. Thus, we conclude that the shadow method cannot be used to calculate free molecule aerodynamic coefficients for long slender bodies at low angles of attack.
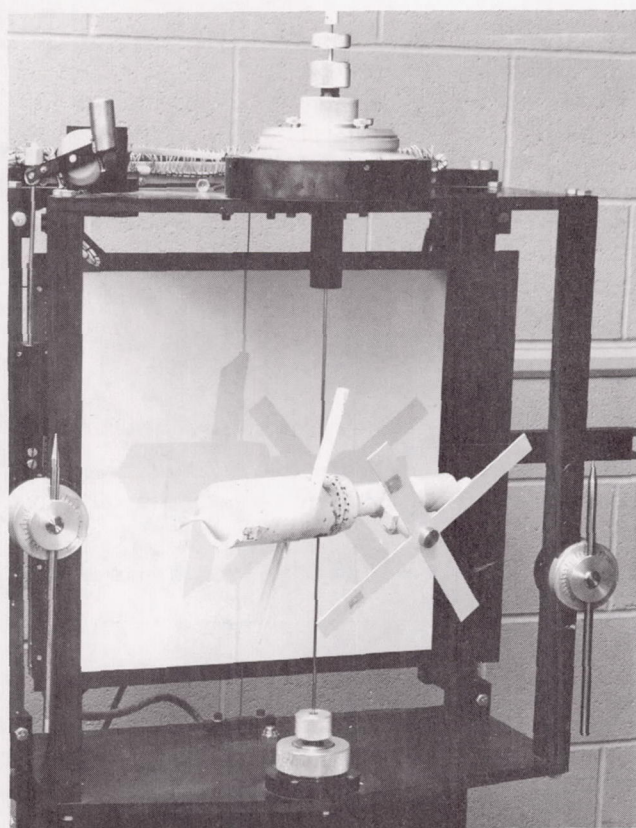
(a)

Lights on so That Details of
the Shadow Scanner are Visible
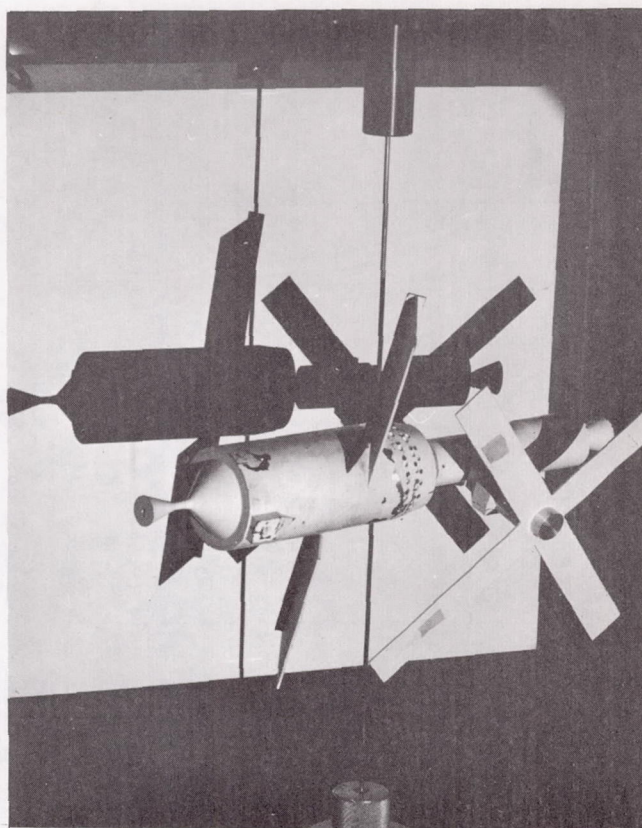
(b)

Lights out Showing the Model Shadow
on the Shadow Scanner Screen

FIGURE 5. PHOTOGRAPHS OF A SCALED AAP CLUSTER MODEL MOUNTED IN THE SHADOW SCANNER

CONCLUDING REMARKS

Both the numerical solution and the shadow method are suitable techniques that are being used to determine aerodynamic coefficients for orbital missions such as those in the Apollo Applications program. The numerical solution is a state-of-the-art technique for vehicles that have complex external shapes. It can be used over a wide range of speed ratios ($S \geqq 2$), but it may require large amounts of computer time.

The shadow method is a simplified technique that is used to produce numbers rapidly. The shadow method is limited to high speed ratios ($S \geqq 6$ or 7). Also, use of the shadow method requires that a model

be fabricated for use in determining projected areas. This limits the shadow method to use in cases where large amounts of data are required or to situations in which minor model modifications can make one model adaptable to a large number of cases.

The shadow method is used primarily during early design stages, and the numerical solution is used for final design confirmation.

FUTURE PLANS

One of the assumptions listed in the description of the numerical solution is that incident molecules
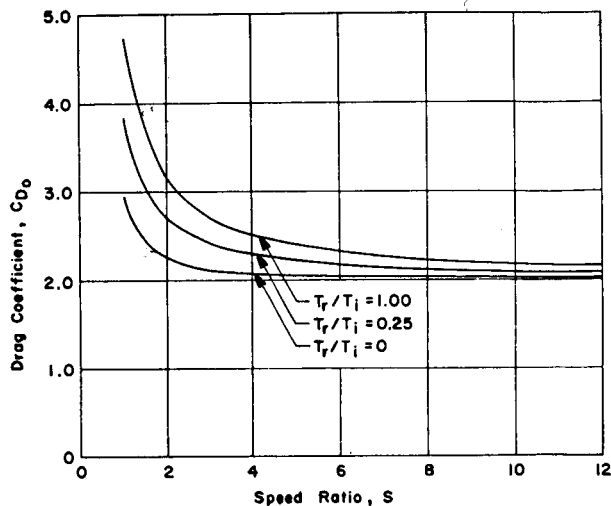
FIGURE 6. DRAG COEFFICIENT FOR A FLAT PLATE IN FREE MOLECULE FLOW ($\alpha = 90°$)
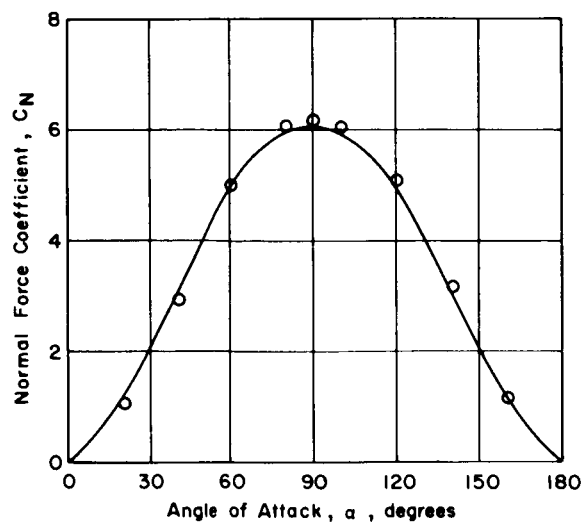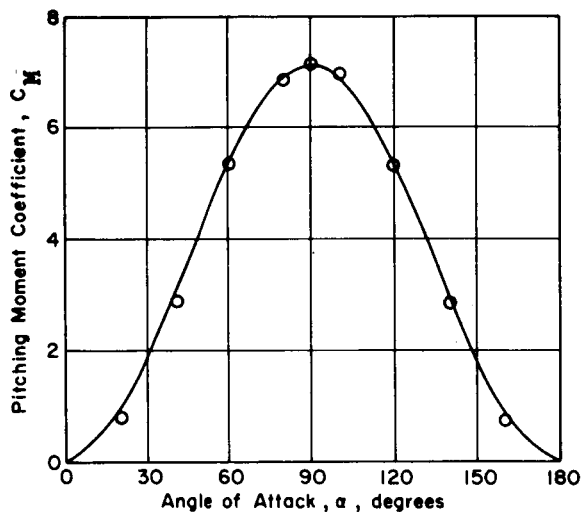
are fully accommodated to satellite surface temperatures before they are reflected. However, experimental evidence indicates that accommodation is not complete [4]. The parameter used to define the degree of equilibrium attained between the molecule and the surface before the molecule is re-emitted is measured by the energy accommodation coefficient, α', which is defined by

$$\alpha' = \frac{dE_i - dE_r}{dE_i - dE_w} \quad , \qquad (6)$$

where dE_i and dE_r, are, respectively, the energy fluxes incident on and re-emitted from a differential surface element per unit time. The quantity dE_w is the energy flux that would be carried away if all incident molecules were re-emitted with a Maxwellian
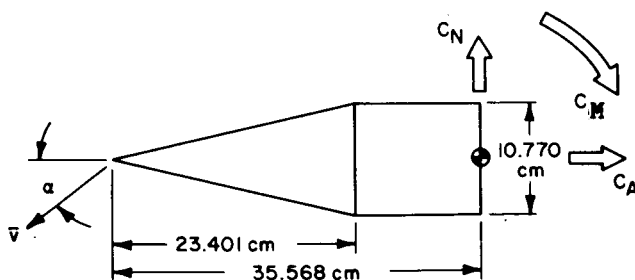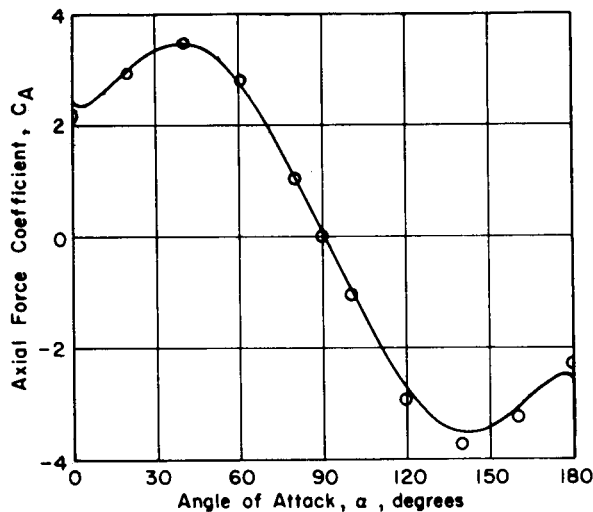
$D_{ref} = 10.770$ cm $A_{ref} = 1/4 \pi$ D_{ref}^2
$S = 8.0$, $T_r / T_i = 0.25$

METHOD:
— Numerical Solution
O Shadow Method

FIGURE 7. COMPARISON OF NUMERICAL SOLUTION AND SHADOW METHOD FOR A CONE-CYLINDER MODEL
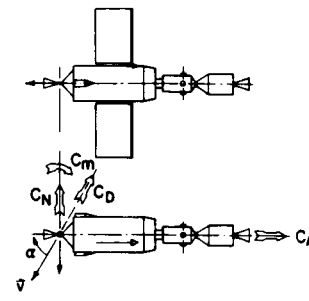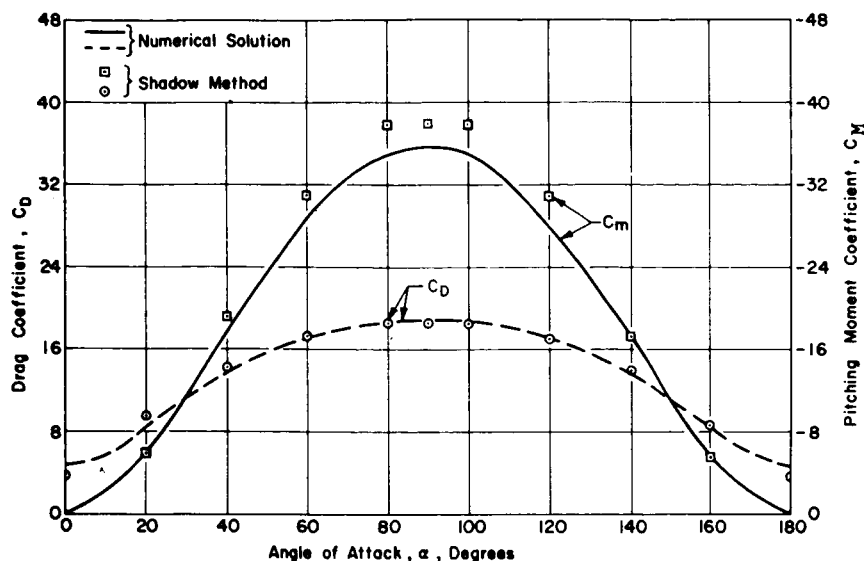
FIGURE 8. COMPARISON OF FREE MOLECULE AERODYNAMIC COEFFICIENTS CALCULATED WITH THE NUMERICAL SOLUTION AND WITH THE SHADOW METHOD FOR THE ORBITAL WORKSHOP

distribution corresponding to the surface temperature T_w. For perfect accommodation, $\alpha' = 1.0$; while for the case of vanishing energy exchange with the surface, $dE_i = dE_r$, and hence $\alpha' = 0$ [4]. Experimental values of α' range from 0.87 to 0.97 for air impinging on typical engineering surfaces [4]. In the future, we plan to modify the numerical solution so that the accommodation coefficient can be varied from zero to 1.0.

Future plans also include writing a computer program that will duplicate the shadow method. This program will use the same input data format that the numerical solution uses, but it will simply determine the projected area and aerodynamic coefficients based on the project areas rather than performing a detailed analysis based on free molecule flow theory. This computer program will require much less time than the numerical solution, and it will eliminate the necessity to build a model in order to use the shadow method.
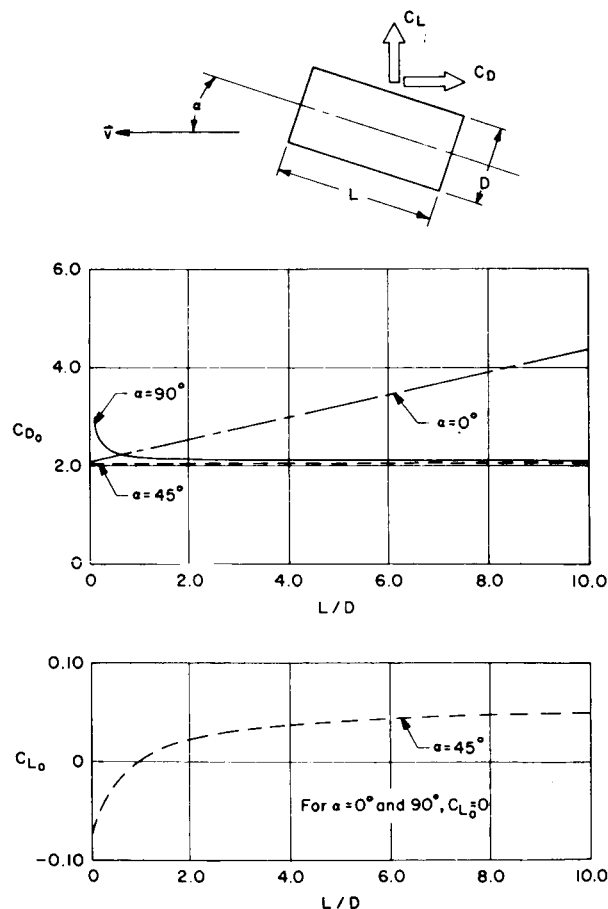
FIGURE 9. LIFT AND DRAG COEFFICIENTS FOR A CLOSED-END CYLINDER (S = 10, $T_r/T_i = 0.25$)

REFERENCES

1. Sentman, Lee H.: Free Molecule Flow Theory and its Application to the Determination of Aerodynamic Forces. Report 448514, Lockheed Missiles and Space Company, Sunnyvale, California, October, 1961.

2. Davis, T. C.; Lake, A. R.; and Breckenridge, R. R.: A Computer Program to Calculate Force and Moment Coefficients on Complex Bodies Formed From Combinations of Simple Subshapes. Report A784522, Lockheed Missiles and Space Company, Huntsville Research and Engineering Center, August, 1967.

3. Buxbaum, J. G.; Lake, A. R.; and Robertson, S. J.: Orbital Aerodynamic Data for the OWS-CSM with Solar Panels Aligned Parallel to the OWS Axis (Revision A). Report A791483-A, Lockheed Missiles and Space Company, Huntsville Research and Engineering Center, August, 1968.

4. Schaaf, S. A.; and Chambre, P. L.: Flow of Rarefied Gases. Fundamentals of Gas Dynamics, Sect. H, H. W. Emmons, ed., Princeton University Press, Princeton, New Jersy, 1958, pp. 687-739.

ACQUISITION AND REDUCTION OF LARGE VOLUMES OF FLUCTUATING DATA

By

Luke A. Schutzenhofer and Paul W. Howard

SUMMARY

The definition of the spatial and spectral decomposition of unsteady physical phenomena is commanding a new role in space vehicle development. For example, unsteady pressure fluctuations on the surface of a launch vehicle induce vehicle buffeting, local shell and panel vibrations, and internal noise. Presently, a description of these unsteady phenomena is derived from model testing where sophisticated data acquisition and reduction techniques are required. This paper describes an experimental program in which large volumes of random (in space and time) data were generated and provides some of the details of the overall requirements, the data acquisition system, amplitude and phase calibration techniques, static and dynamic operating characteristics of the data acquisition system, component qualification testing, model vibration testing, and the data reduction technique.

LIST OF SYMBOLS

Symbol	Definition
A	amplitude of a sinusoidal wave
B	amplitude of a sinusoidal wave
f	variable frequency
f_o	fixed frequency
G(f)	cross-spectral density or power spectral density function defined for non-negative frequencies
H(f)	frequency response function
i	$\sqrt{-1}$
j	index
k	index
K	constant value of a white noise spectrum
M_∞	free stream Mach number
P	pressure
Rn/ft	Reynolds number per foot
S	cross-spectral density for positive and negative frequencies
t	time variable
T	averaging time
X	time-dependent variable (input)
Y	time-dependent variable (output)
z_k	variable space coordinate vector in index notation
z_j	variable space coordinate vector in index notation
z'_k	particular (fixed) space coordinate vector in index notation
z'_j	particular (fixed) space coordinate vector in index notation
α	angle of attack
δ	dirac function
χ	roll angle
τ	delayed time
ϕ	phase angle

Subscripts

1 and 2 indices	denotes different systems, phase angles, or frequencies

∞   infinity

Superscripts

*   denotes complex conjugate.

INTRODUCTION

The spatial and temporal definition of design environments pertaining to unsteady physical phenomena is commanding a new and important role in space vehicle development. This is particularly true in the cases of rocket exhaust noise, ground winds, and inflight fluctuating pressure fields. The acute impact of possible adverse effects of these physical phenomena demands that a meaningful (however complex) engineering description of them be provided at the earliest possible time during the vehicle's research, development, and operational phase. Realistic vehicle design criteria cannot be formulated until a meaningful engineering description of the space-time fluctuating environment is achieved.

In each of these cases, best engineering estimates for vehicle design are derived primarily from model testing, and in each case, astronomically large volumes of space-and-time-dependent data are generated. To provide the minimum (even this is a tremendous volume) amount of data needed for a foundation upon which realistic design criteria are to be based, the data must be computer-analyzed, scaled, and organized into meaningful engineering terms. The engineering terms for all of these design environments are statistical quantities, i.e., root-mean-square values, power-spectral density, and cross-spectral density functions, because the time-dependent physical processes creating the environments are random processes. Previously, data acquisition and reduction systems were not capable of measuring the most important parameter, the cross spectral density, because they could not retain phase with sufficient accuracy. Therefore, earlier wind tunnel programs were concentrated on obtaining overall mean-square values and power-spectral densities for engineering application. Realistic environmental design criteria cannot be derived without knowing the cross-power spectral density.

To gain an appreciation of the large volume of data and the experimental detail required to successfully estimate design environments caused by time-dependent random physical processes, this paper describes an experimental program and its associated data acquisition and reduction requirements to determine the inflight fluctuating pressure (inflight acoustics) design environment for the Saturn V.

ENGINEERING APPLICATION OF RANDOM PRESSURE DATA

To determine the inflight fluctuating pressure field design environment for the Saturn V vehicle, it was necessary to fabricate a four percent model of the vehicle and conduct a series of tests in the largest wind tunnels available: the AEDC 4.9-m (16-ft.) transonic and supersonic tunnels. Once the unsteady surface pressures are measured and properly recorded, it is necessary to reduce them to statistical quantities including overall root-mean-square values, power-spectral densities, and the "pressure cross-spectral density function" for engineering application. Then we can (1) delineate buffet loads for estimating vehicle body bending response computations, (2) determine local fluctuating pressure loads for input to local panel and shell mode structural response calculations, and (3) define the inflight external acoustic environment to determine vehicle internal noise levels. These applications are necessary to assess vehicle integrity, determine realistic margins of safety, and insure mission success.

REQUIREMENTS

Before a complex test program can be conducted successfully to measure unsteady surface pressure fluctuations, guidelines for the following six items must be specified: (a) instrumentation and aerodynamic requirements, (b) qualification tests for the data acquisition systems to establish their performance characteristics in the field environment, (c) a meaningful amplitude and phase calibration scheme for use at the field test site, (d) a plan to define the static and dynamic characteristics of the data acquisition and reduction system, (e) a data acquisition system to measure the dynamic vibration response of the model-sting configuration and other components, and (f) a data reduction procedure that is technically adequate and economically practical.

The objective of this paper, to reveal the complexities associated with the data acquisition and reduction, can now be achieved by considering in detail each of these requirements.

INSTRUMENTATION AND AERODYNAMIC REQUIREMENTS

To insure the correct measurement of the primary fluctuating physical process, that is, the unsteady surface pressure fluctuation on the four percent Saturn V model, instrumentation specifications called for flush-mounted microphone measurements of noise levels, internal microphones to assess the effect of model vibration on the unsteady data, accelerometers to measure model-sting accelerations, static pressure transducers to measure surface static pressures, pressure rakes to measure total pressures, and internal thermocouples to measure internal temperature. The additional measurements, i. e., internal microphones, accelerometers, thermocouples, etc., were required for interpreting and establishing the utility of the unsteady pressure data. Table I shows the measurement plan by number and type.

TABLE I. NUMBER AND TYPE OF MEASUREMENT

Number	Type of Measurement
140	Surface dynamic pressure
5	Internal dynamic pressure
10	Model-sting acceleration
320	Surface static pressure
5	Pressure rake, 9 to 15 probes
10	Internal thermocouple

Since the buffet loads, local shell and panel unsteady loads, and external sources of internal noise require the determination of the "pressure cross-spectral density," a constraint that is not found in conventional aerodynamic engineering tests existed in this test. This constraint is phase retention. For example, given a surface being acted upon by an unsteady pressure field which has statistical characteristics that are independent of time translations, the pressure cross-spectral density is defined as

$$S(z_k, z_j, f) = \int_{-\infty}^{\infty} \left[\lim_{T \to \infty} \frac{1}{2T} \int_{-T}^{T} P(z_k, t) P(z_j, t+\tau) \right] e^{-i2\pi f\tau} d\tau. \quad (1)$$

If the pressure fluctuations at z_k and z_j are given, respectively, as

$$P(z_k, t) = A\delta(z_k - z'_k) \sin(2\pi f_0 t + \phi_1)$$

$$P(z_j, t) = B\delta(z_j - z'_j) \sin(2\pi f_0 t + \phi_2), \quad (2)$$

then, the cross-spectral density of the fluctuating pressure field for positive frequencies is

$$G(z_k, z_j, f) = \frac{AB}{2} \delta(z_k - z'_k) \delta(z_j - z'_j) \delta(f - f_0)$$
$$\left\{ \cos(\phi_2 - \phi_1) + i \sin(\phi_2 - \phi_1) \right\}. \quad (3)$$
$$0 \le f < \infty, \text{ otherwise zero}$$

From equation (3), it can be seen that phase retention is required in cross-spectral density estimates. As a result of this requirement, a data acquisition and reduction system was required that would resolve phase within $\pm$ 5 degrees at 20 kHz. This system was also required to be capable of measuring mean-square amplitudes in the range of 135 to 173 dB within 10 percent. It was necessary to design, build, and test a totally new (multiplexing) data acquistion system for this purpose, since conventional systems could not even come close to those stringent requirements. This represented a major advance in acquiring phase-related information in large quantities over a relatively large frequency range, i.e., 20 Hz to 20 kHz.

It is worth noting that the pressure cross-spectral density is a cross product and a function of frequency. If all necessary combinations of cross products were computed at one test condition for 100 possible pressure transducers for 27 one-third octave bands, the resulting number of data points would be equivalent to the number of data points generated from 1500 static tests. Thus, it is easy to understand how large volumes of data are generated from one model test, considering that the above crude analogy was for one test condition and that many test conditions must be covered.

To meet these requirements, the general specifications and the multiplex concept were initiated and resulted in the data acquisition system shown in Figure 1. This system was designed and built by and under the supervision of the Experimental Aerophysics Branch of the Aerophysics Division, Aero-Astrodynamics Laboratory. A thorough laboratory test of the equipment was also conducted by this organization.

The microphones, Kistler model 601L, have their first resonant frequency at 130 kHz and an output of 6.89×10^{-9} C/N/m².

Diagram

MICRO-DOT LOW NOISE CABLE

KISTLER 601L — MICROPHONE

KISTLER 553A — CHARGE AMP.

SELF TEST CALIBRATION INPUT

AEDC HARDLINE SYSTEM

C.E.C. VOLTAGE CONTROL OSCILLATOR — VCO

ELECTRICAL CALIBRATION INPUT

C.E.C. VR-3600 — MULTIPLEX TAPE RECORDER

AMPEX CP-100 — AUXILIARY TAPE RECORDER
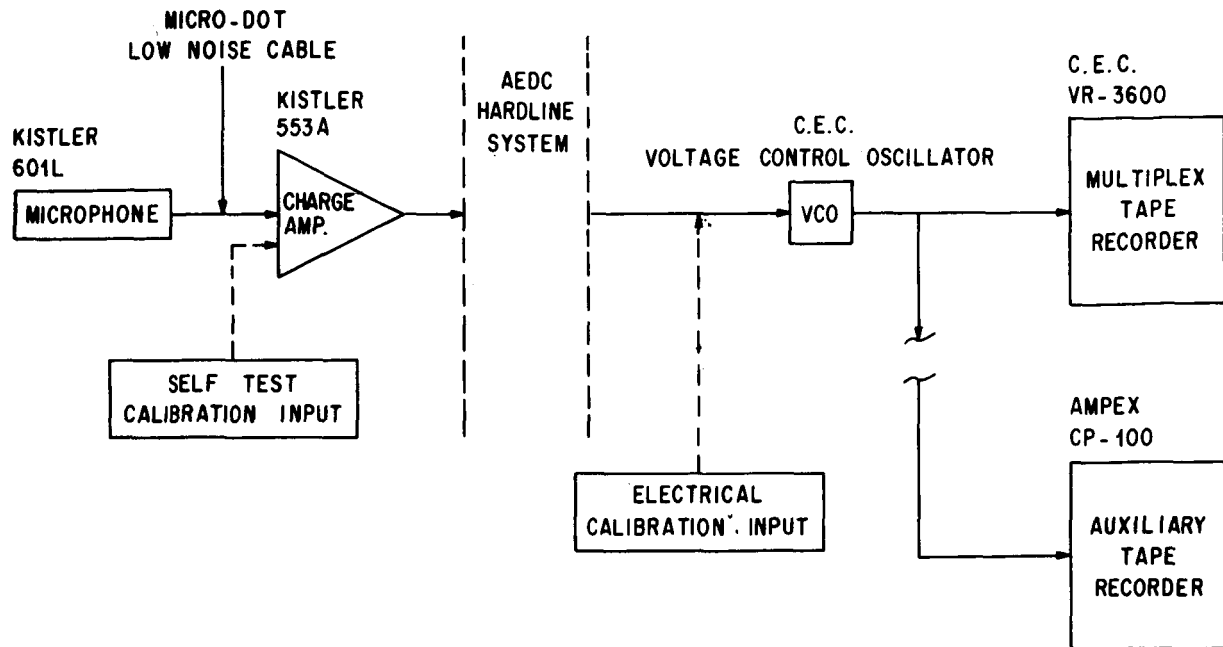
FIGURE 1. FLUCTUATING PRESSURE DATA ACQUISITION SYSTEM

The amplifiers, modified Kistler model 553A, are a constant-phase type and have a flat frequency response range from 20 Hz to 80 kHz.

The main recorder, a C.E.C. VR-3600, can record frequencies of 1.5 MHz on each of 14 tape channels. On each of the fourteen tape channels, nine multiplex signals were recorded, each with a 20 Hz to 20 kHz flat frequency response. This particular arrangement, with a modulation index 2, limited the upper usable data bandwidth to 20 kHz. A larger number of measurements with a lower upper-frequency limit is also possible. Some data were recorded on an Ampex CP-100; these data were not multiplex.

A typical microphone installation is shown on Figure 2. Also shown in this figure are some pressure rakes, protuberances, and static pressure orifices.

To measure the static and total pressures, pressure scanners made by Scanivalve of San Diego, California, were used in conjunction with a Statham model PM 131TC pressure transducer.

The model-sting vibrations were measured with C.E.C. model 4-203-0001 accelerometers along with Endero model 4402 signal conditioners.

The model internal temperature was obtained with a thermocouple.

This test program was conducted in two phases at the Arnold Engineering Development Center's Propulsion 4.9-m (16-ft.) transonic and supersonic wind tunnels. Phase I testing was transonic and was conducted in tunnel 16-T; phase II testing was supersonic and was conducted in tunnel 16-S.
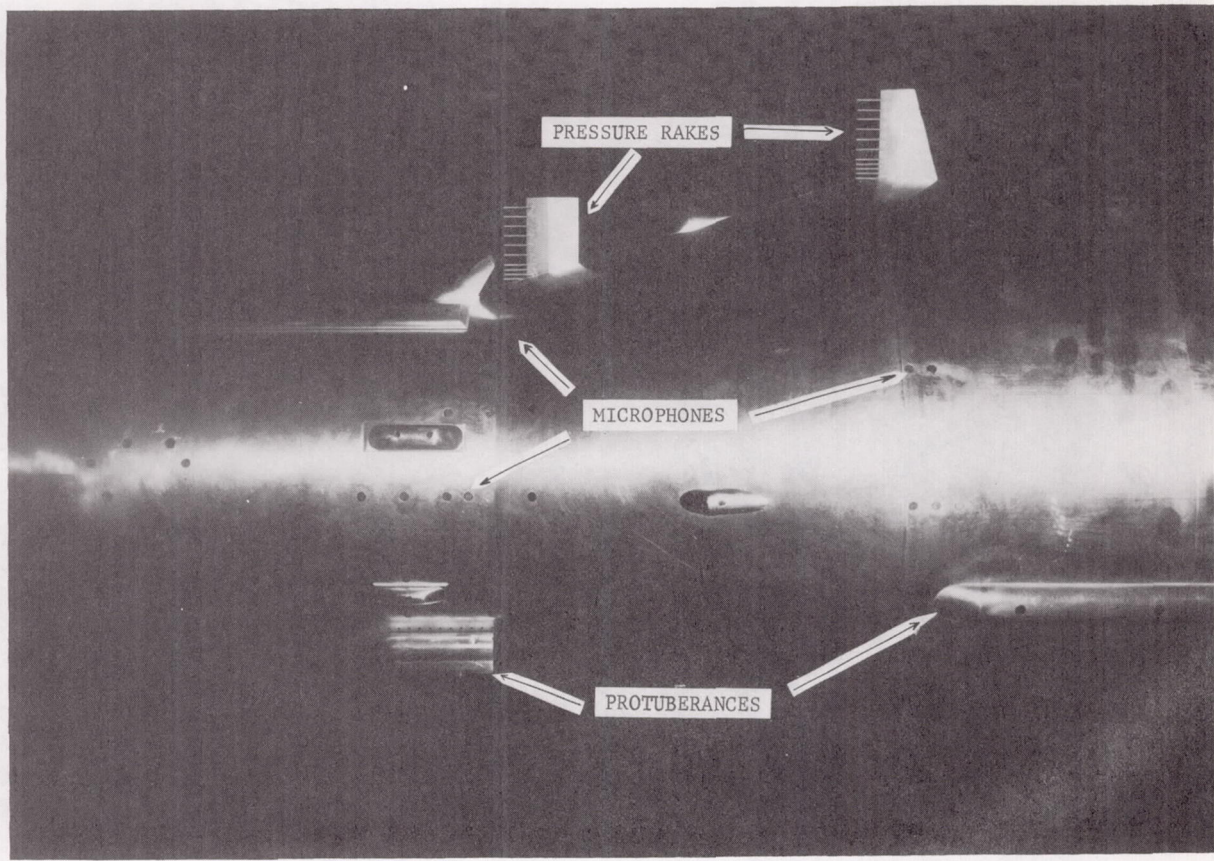
FIGURE 2. TRANSDUCERS, RAKES AND STATIC PRESSURE ORIFICES

During phase I testing, the range of parameters was as follows:

$$0.6 \leq M_\infty \leq 1.4, \ -10° \leq \alpha \leq 10°, \ 0 \leq \chi \leq 60°, \ \text{and}$$

$$4.2 \leq Rn/ft \times 10^{-6} \leq 4.9.$$

A Mach number sweep (at a slow rate) was executed because the locations of some violent unsteady phenomena are extremely Mach number sensitive, and since transducer locations are fixed, then discrete incremental Mach number testing may or may not produce the maximum environment at the transducer.

During phase II testing, the range of parameters was as follows:

$$1.6 \leq M_\infty \leq 3.0, \ -4 \leq \alpha \leq 4°, \ 0 \leq \chi \leq 60°, \ \text{and}$$

$$1.0 \leq Rn/ft \times 10^{-6} \leq 2.0.$$

In both phases of this test, two model configurations were used. Figure 3 shows configuration I with protuberances, and Figure 4 shows configuration II without protuberances.

QUALIFICATION TESTS FOR THE DATA ACQUISITION SYSTEM

After the data acquisition system was designed and the aerodynamic objectives delineated, qualification tests were conducted to determine if the components of the system exposed to the wind tunnel environment could survive and perform within specifications. The dynamic pressure transducer, amplifiers, and cabling were qualification tested at the facilities of Ling-Temco-Vought, Inc. These systems were subjected to and passed a variety of tests including vibration, high-temperature environments, etc. [1].
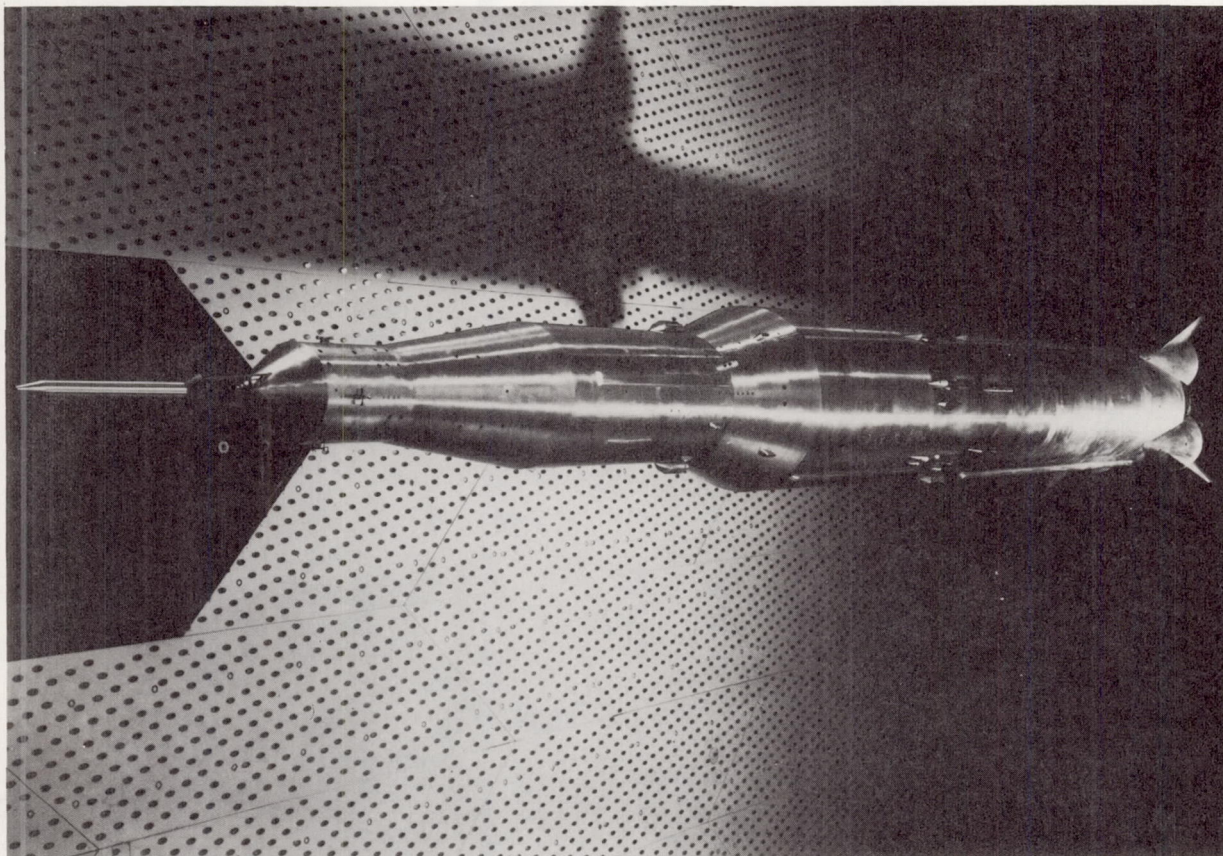
FIGURE 3. CONFIGURATION I

AMPLITUDE AND PHASE CALIBRATION PROCEDURES

To amplitude calibrate the flush-mounted microphones, a Photocon PC-125 acoustical calibrator that had a known output of 160 dB (0.00002 N/m^2 at 1 kHz) was used as a source. This source was applied to the microphone systems to determine their amplitude sensitivity. This procedure was done three times for each transducer for each phase of the testing, and an average amplitude sensitivity was computed from the three results for each test phase. The deviation from the average was small (on the order of 4 percent). As an additional system check, an electrical signal of 1 kHz was input (inserted) at the voltage control oscillator. The system output generated by this inserted electrical signal was recorded on every tape.

Because of the large volume of data to be recorded and the complexities of the data acquisition system, an absolute phase calibration would have been extremely time consuming, if it could be done at all. However, since the primary concern is "cross-spectral" density computations, relative phase is more important than absolute phase. It was assumed that the data acquisition system, the dubbing (copying on other tapes) process, and the data reduction system could be treated as lumped constant-parameter linear systems. With statistically stationary random inputs, the cross-spectral density of the two outputs of any two of the lumped systems in terms of the cross-spectral density of the inputs and the systems frequency response functions can be shown to be

$$G_{y_1y_2}(f) = H_1^*(f) \, H_2(f) \, G_{x_1x_2}(f), \qquad (4)$$

$$0 \leq f < \infty \text{ , otherwise zero}$$

where $G_{x_1x_2}(f)$ is the cross-spectral density data
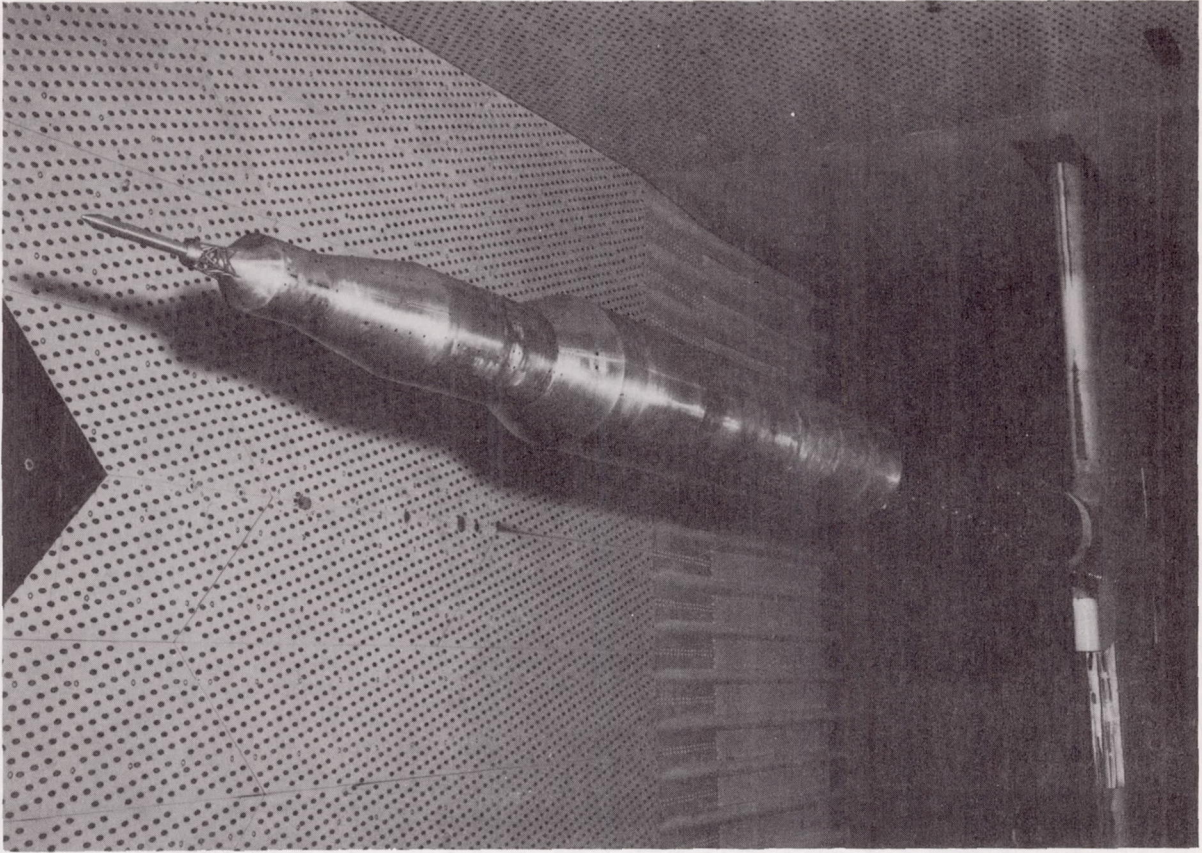
FIGURE 4. CONFIGURATION II

that we are attempting to obtain, and H_1^* (f) H_2 (f) are the system's lumped constant distortions. Now H_1^* (f) H_2 (f) is the product of two transfer functions (each characterizing a given system), is independent of the input, and needs to be determined only once. This product then characterizes the two systems, and thus the amplitude and phase distortions will be known between two acquisition-to-reduction channels. It was decided to input a common single-source band-limited white noise at the self-test circuit of all the Kistler charge amplifiers. The cross-spectral density then becomes

$$G_{x_1 x_2} (f) = G_{x_1 x_1} (f) = K, \qquad f_1 \leq f \leq f_2 \qquad (5)$$
$$\text{otherwise zero}$$

where $f_2 - f_1$ determines the limiting bandwidth. Therefore,

$$H_1^* (f) H_2 (f) = \frac{G_{y_1 y_2}}{K} (f). \qquad f_1 \leq f \leq f_2 \qquad (6)$$
$$\text{otherwise zero}$$

Consequently, the entire lumped system relative characteristics for the $f_2 - f_1$ frequency bandwidth are determined from the white-noise test. This recorded information is used in the data processing to estimate and correct for phase distortions.

EXPERIMENTAL PROGRAM TO DETERMINE SYSTEM STATIC AND DYNAMIC CHARACTERISTICS

In addition to the field calibration procedures, field instrumentation tests were performed by Measurement Analysis Corporation to determine the data acquisition system's noise floor, frequency response, amplitude linearity, and intermodulation distortion. In other words, experimental test of a complex instrumentation system's total characteristics was conducted at the field site for comparison against conventional laboratory tests to accomplish this task. Detailed analyses are now underway but are not yet completed; however, cursory analyses indicate no major problems.

67

VIBRATION TEST OF THE INSTALLED FOUR PERCENT SATURN V MODEL TO MEASURE MODEL-STING RESPONSE.

During the week of the Phase I testing, Lockheed Missiles and Space Corporation, Huntsville, Alabama, performed a vibration test on the model-sting configuration with all model data acquisition systems active. Figure 5 shows the vibration test set up. The intention here was to determine (1) model-sting mode shapes and frequency response and (2) the sensitivity of all the model data acquisition systems to a vibration input only.
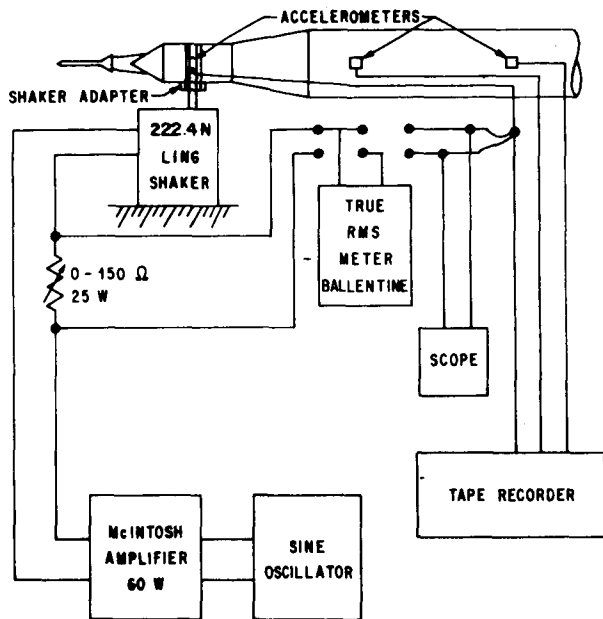
FIGURE 5. VIBRATION TEST OF A FOUR PERCENT SATURN V MODEL

The vibration test was conducted for the first four pitch modes. The fundamental resonant frequency of the system was about 5.76 Hz. Analyses of these data are in progress; however, the large amount of fluctuating pressure data already analyzed does not seem to be seriously affected by model vibrations.

DATA REDUCTION PROCEDURE

The data reduction, i.e., the analyzed cross-spectral density data resulting from the experiment

is being performed by Baganoff and Associates. The analyses are being performed in one-third octave bands.

The mean square spectral density in a one-third octave band, using an ideal unit rectangular filter, corresponds to the average over a one-third octave bandwidth of the mean square value per bandwidth. If the cross-spectral density is a monotonically varying function in a bandwidth and if the slopes of the modulus and phase angle are not steep, the one-third octave band value is a good approximation to the point function. For example, calculations [2] using triple-tuned filters indicate that for a worse case, the modulus (amplitude) could be in error at most by 5 percent and the phase could be biased by 5 degrees. In the general applications intended, the bulk of the data are smooth and continuous; therfore, the one-third octave band analysis was used because it is an excellent compromise between application of the data, the time required to reduce the data, and the cost of reduction.

The one-third octave band cross-spectral densities are being obtained by analog techniques. The system being used to analyze the four percent Saturn V model data is shown in Figure 6. The averaging time, or the time required to compute the cross-spectral density for one pair of measurements is approximately $7\frac{1}{2}$ minutes for a 30-second sample.

With averaging times of 30 to 45 seconds, phase-angle deviations of $\pm$ 5 degree peak-to-peak at 20 kHz have been achieved in 92 percent of the white-noise calibration test cases. This phase accuracy of the total system, i.e., data acquisition, dubbing, and reduction chain, at such high frequencies is unprecedented for this type of testing and represents a significant advance over conventional systems. Before this system was developed, it was impossible to produce cross-correlation data for engineering applications by wind tunnel model testing of a given vehicle configuration.

CONCLUSIONS

In the acquisition and reduction of large volumes of fluctuating data pertaining to the four percent Saturn V model experiment, we can make the following conclusions:

1. Mean square amplitudes have been resolved within a 10 percent scatter band.
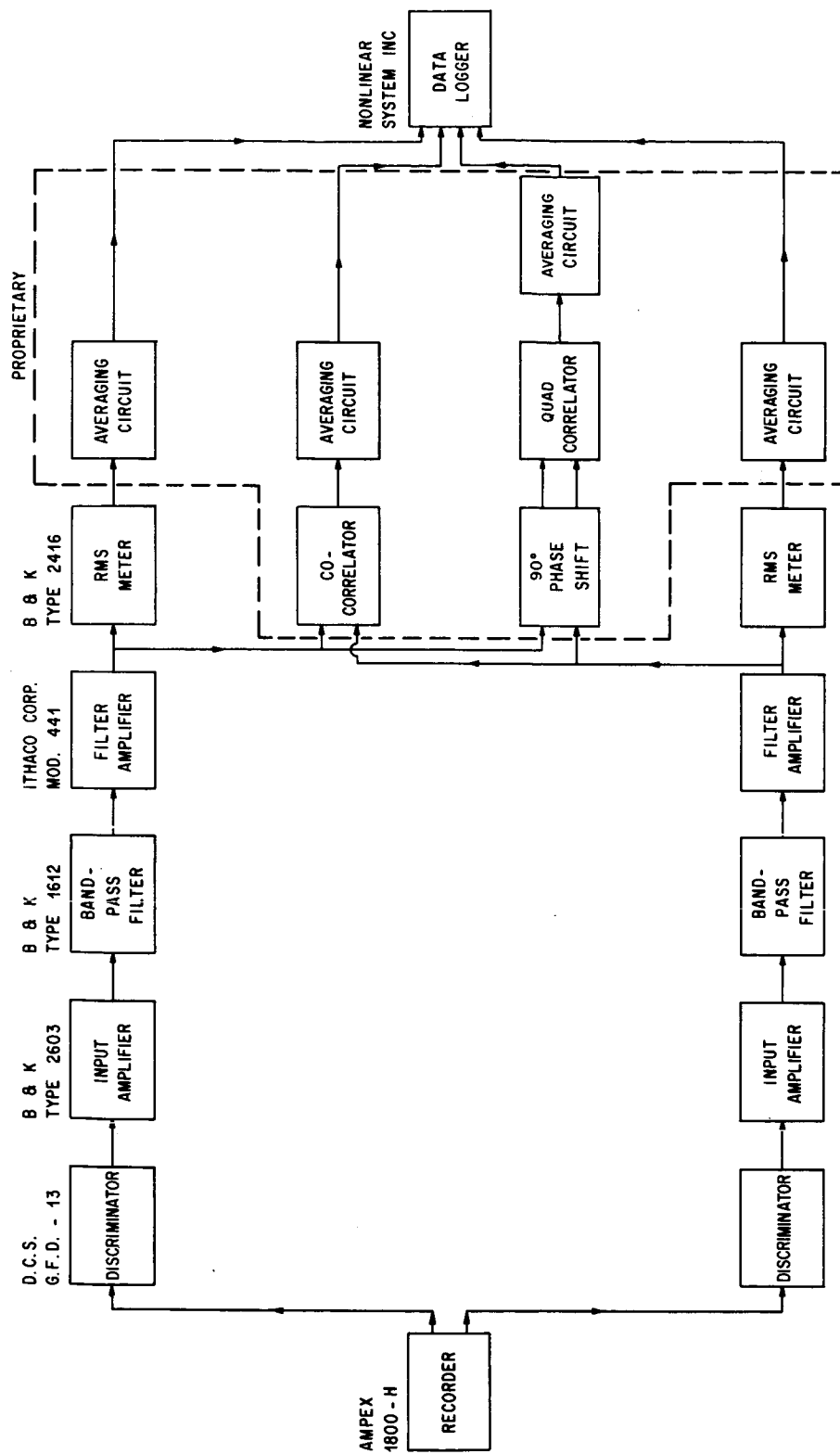
FIGURE 6. DATA REDUCTION SYSTEM

2. The data acquisition system successfully passed all environmental qualification tests.

3. Field instrumentation tests were performed and the results are being analyzed to determine the data acquisition system's static and dynamic characteristics under field conditions as compared to laboratory-controlled conditions.

4. Mode shapes, frequency response, and vibration sensitivity are being determined from model-sting vibration tests.

5. The data acquisition system's vibration sensitivity is being established with the field data acquired from the internal acoustic and vibration measurements.

6. This is the first time that 122 channels of phase-related random data with ± 5 degrees (at 20 kHz) phase distortions have been recorded successfully. This represents a major advance over the conventional approach to this problem and therefore allows the generation of cross correlation information for engineering purposes for the first time. Before this, such information was so limited that it was used primarily for research purposes only.

7. One-third octave band spectrum analyses are technically adequate and economically practical in these types of large-volume data analyses.

8. Comparisons are being made between the model data and Saturn flight data.

9. This has been the first successful attempt in using band-limited white noise to establish relative phase distortions.

10. This data acquisition system, calibration scheme, and data reduction system combination is unique and represents a significant advance in the state of the art. Additionally, this system is versatile, and its use is not limited to fluctuating pressure tests.

REFERENCES

1. Dahlke, Hugo E.: Calibration and Laboratory Evaluation of Kistler Pressure Transducer Model 601 L and Change Amplifier 553A. LTVR Project No. 60500, July 25, 1967.

2. Kelly, R. D.; and Mauner, J. R.: Filter Mismatching Errors in Cross-Spectral Density Analysis. Measurement Analysis Corporation Report MAC 703-06, January 1968.

PERCEIVED SOUND

By

Jess H. Jones

SUMMARY

The human auditory system can be represented as a simple input/output system. When presented in this manner, the magnitude of an auditory sensation, or more specifically, the perceived sound can be obtained by multiplying the input acoustic stimulus by the square of the complex frequency response function of the human auditory system. The results obtained through the use of this simple model agree with the results of judgment test as well or better than the presently accepted methods.

INTRODUCTION

When an auditory system is exposed to an acoustic stimulus, the resultant quantity is normally referred to as the perceived sound. Qualitatively, perceived sound can be described in many different ways: by the characteristics of loudness, noisiness, annoyance, or any other desired quality. Past studies concerning the subjective response of humans to an acoustic stimulus have been performed mainly from a loudness or noisiness point of view. These studies have revealed that subjects responded differently when asked to judge sounds of equal loudness as compared to sounds of equal noisiness. Individuals, therefore, seemed to respond differently to the various qualities which can be ascribed to the perceived sound. This difference may be that the individuals are not sure just what they are trying to judge, or the differences may, in fact, be real. At any rate, loudness (or noisiness, etc.) is then a psychological term which is used to describe the magnitude of an auditory sensation.

There have been many tests devised to measure loudness, loudness growth, and loudness calculation, and in reality, much of the present day efforts owe their origin to the early studies of Fletcher and Munson [1]. Since that time (1961), numerous proposals have been made to predict the total loudness associated with any given complex acoustic pressure spectrum. Gates [2] proposed that the total loudness of a complex spectrum could be calculated by a direct summation of the individual loudness units of the spectrum: $s_T = \Sigma s_i$. Beranek, et. al. [3] and Minty and Tyzzer [4] later elaborated upon a method developed by Gates. Stevens [5,6], however, discovered that if the total loudness was obtained through a direct summation of the loudness units, this indicated loudness would exceed the actual loudness of the total noise by a factor of more than two. Consequently, from a series of tests, Stevens devised an empirical summation procedure, which tended to weight the total loudness of a complex noise spectrum to the maximum loudness unit of that noise spectrum; i.e., $s_T = s_M + K(\Sigma s_i - s_M)$, where s_M is the maximum loudness unit of the complex spectrum, s_i is the individual loudness units of the spectrum, and K is the empirically determined "bandwidth" constant. This technique, which appeared to be successful in predicting the results of judgment tests, is in the form of a numerical calculation scheme. The unit of loudness used by Stevens is called "sones," and its logarithmic equivalent is the loudness level in "phons." Zwicker and Feldtkeller [7] devised a procedure similar to that used by Stevens and it is in the form of a graphical calculation scheme. Kryter [8] devised a procedure almost exactly paralleling that of Stevens; the only exception is that this technique was derived for noisiness, whereas Stevens' approach was intended to be used for a loudness evaluation. The procedure by Kryter and Pearsons [9] uses the same summation procedure, i.e., $N_T = N_m + K(\Sigma N_i - N_m)$, and it is also in the form of a numerical calculation scheme. The unit of noisiness is called "noy" and its logarithmic equivalent is the perceived noise level (PNL) given in PNdB. Use of these latter techniques is very tedious and extremely time-consuming. With present-day computers this may not seem like too much of a problem, but these approaches severely restrict the direct "on-line" measure of the magnitude of the total loudness (or noisiness) of a complex spectrum, and they also complicate the physical interpretation of the auditory system.

Of all the procedures or techniques which have been proposed to date, the approach by Kryter seems to have gained the most general acceptance. The

results predicted by this approach also seem to compare favorably with the results of judgment tests. Kryter and Pearsons [9] have subsequently modified their approach so that it will adequately take into account complex noise spectra with strong pure tone or high level narrow band energy components.

The crucial element in·any scheme developed to determine the noisiness (or loudness) of a complex noise spectrum is the proper definition of the equal loudness function for the typical, or average, human auditory system. The equal noisiness function, which was used in the development of the proposed model, was adapted from Kryter and Pearsons [10] (Fig. 1). This equal noisiness function implies that all bands of noise which lie on this curve sound as noisy as all other bands of noise; in other words, they´are equally noisy. Equal noisiness (or loudness) functions are normally determined by averaging the individual results from a large number of subjects which have been asked to perform one of several standard judgment tests; the two most generally accepted tests are the method of paired comparison

and the method of individual adjustment. The equal noisiness curve presented in Figure 1 was obtained by averaging the subjective results of 20 different subjects using the method of individual adjustment. In performing this type of test, each individual was asked to listen to a standard noise and then to a comparison noise. They were then asked to adjust the level of the comparison noise until it sounds as noisy as the standard. The frequency band of the comparison noise was changed (the standard being held constant) until the total frequency range of interest was covered.

As stated previously, equal noisiness implies constant noisiness, and it therefore represents a definite unit of noisiness. In the framework of the Kryter technique [10], the unit of noisiness is called a "noy"; therefore, the equal noisiness contour in Figure 1 is associated with a certain noy value (the 40 noy contour in this case). In brief, by combining the equal noisiness contour with the so-called "loudness (or noisiness) growth" functions, a series of equal noisiness curves can be generated for various
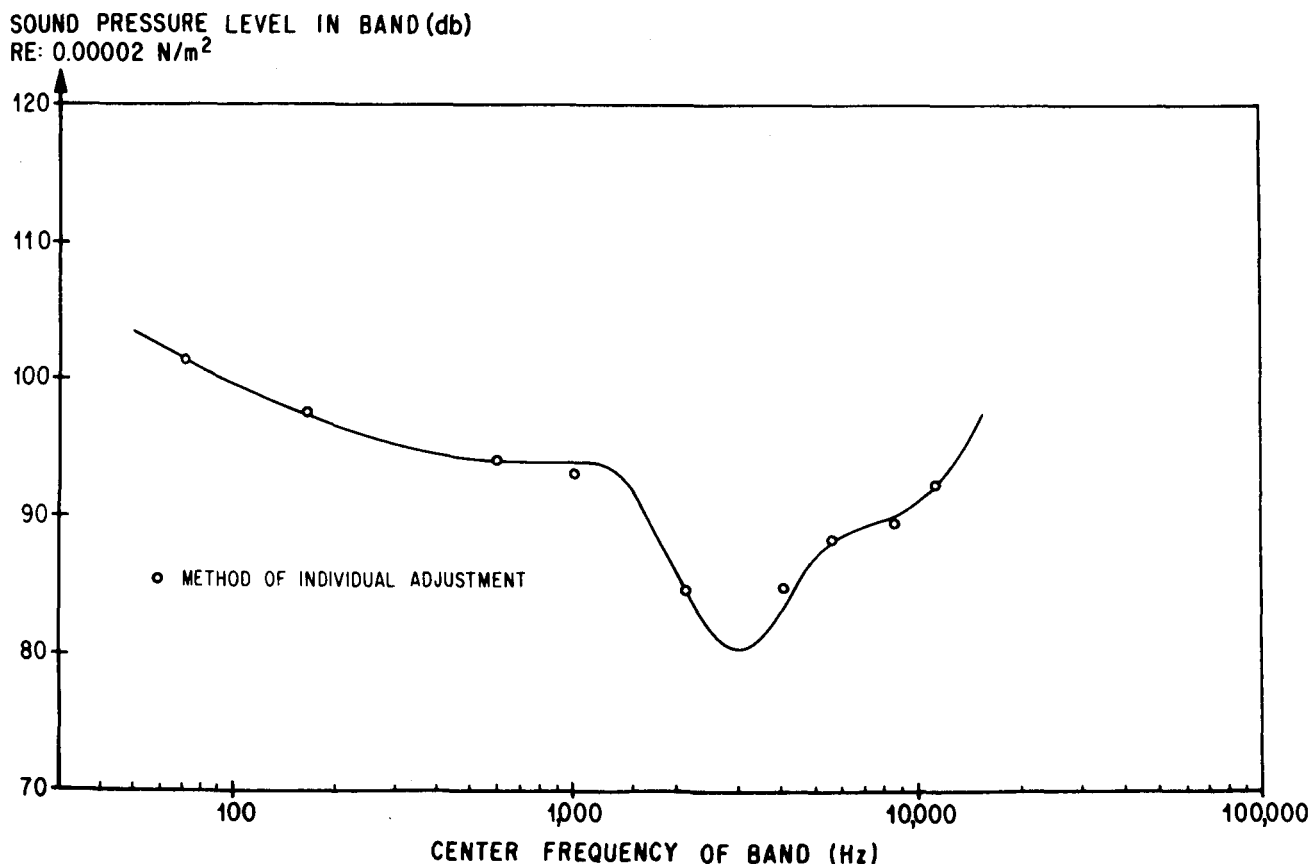
FIGURE 1. EQUAL NOISINESS CONTOURS (from Kryter and Pearsons [10])

noy values (References 5, 6, 8, and 11 give a complete description of this process). Therefore, these noy values (the unit of noisiness, Fig. 2) are a function of the amplitude and frequency of the input acoustic stimuli. By applying the summation procedure given earlier to the individual noy values associated with a given acoustic stimulus, the total noisiness of a complex spectrum can be obtained. From this total noy value and the definition of the perceived noise level [8], the perceived noise level in PNdB's can be determined. This is the approach which is presently in use.

Band Sound Pressure Level (dB)
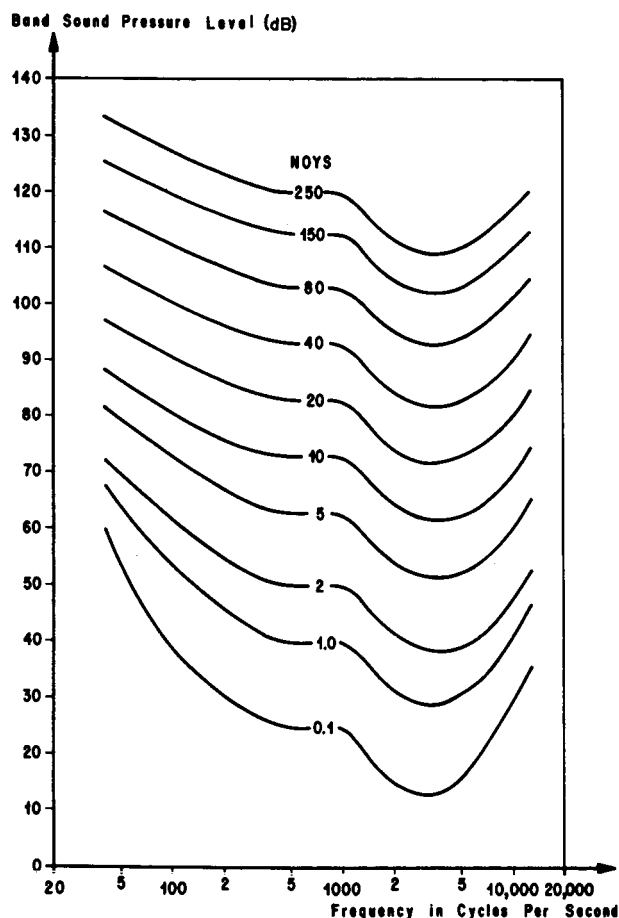
FIGURE 2. NOISINESS OF BANDS OF SOUND

PROPOSED MODEL

The discussion thus far has been totally related to the presently accepted methods of providing estimates of the magnitude of the perceived sound in terms of noisiness or loudness. What follows is yet another approach to the very real and urgent problem of providing realistic estimates of the magnitude of perceived sound. With every passing day, people are becoming more concerned with such problems as noise abatement, aircraft noise control, air traffic control, and other associated noise problems. The general public is, in effect, becoming more noise conscious. What is ideally desired to provide genuine assistance to this very urgent problem is the development of a method and/or device which will accurately, efficiently, and directly predict the magnitude of the subjective reaction of an average individual to any given acoustic stimulus. It may be argued that the presently accepted techniques will perform this objective, and this is indeed true to a certain degree. Present techniques can adequately predict the magnitude of perceived sound, but without the aid of graphs and a computer the task becomes very tedious, cumbersome, and extremely inefficient. The method being proposed here will eliminate these shortcomings and, at the same time, simplify the physical interpretation of the response of the human auditory system to a given acoustic stimulus.

The proposed method is to consider the human auditory system from a dynamic response viewpoint (Fig. 3).

FIGURE 3. INPUT/OUTPUT RELATIONSHIP FOR THE HUMAN AUDITORY SYSTEM

When this is done, the input and output (for a constant parameter linear system) can be related as follows [12],

$$S_I(f) \left| H(f) \right|^2 = S_p(f) \quad ; \quad 0 \leq f < \infty \qquad (1)$$

where
S_I = power spectral density of the input acoustic stimulus

$H(f)$ = the frequency response function

$S_p(f)$ = perceived spectral density of the output.

73

The input (Fig. 3) in this case implies any given acoustic stimulus, and therefore the input/output relationship applies equally as well to pure tones or bands of noise. To apply this relationship to combinations of pure tones and/or bands of noise, it is necessary to assume that the tones and bands of noise are statistically independent; when this is done, the mean squared values add directly.

The human auditory system (Fig. 3) consists of the ear and its associated physical hearing mechanisms, the nerve system, the brain, and any other elements, both psychological and physical, which would have any possible effect upon the total hearing process. The auditory system can be represented by a transfer function which will in turn operate in a systematic manner upon the input to transform it into the perceived sound. The auditory system is by its very nature a dynamic system, and because of this, it will have definite frequency response characteristics. These response characteristics will vary from individual to individual; therefore, if we are to predict the perceived sound that is representative of an average or typical individual, the response characteristics of the typical or average human auditory system will have to be used.

The output is then the perceived sound. The perceived output integrated over all frequencies; i.e.,

$\int_0^\infty S_p(f)\, df$ is then the magnitude of the perceived sound and is analogous to the total noisiness discussed earlier (N_T). To avoid confusion with presently accepted methods, it is necessary to introduce additional descriptive terms: The output of the auditory system will be called "perceived sound" (instead of noisiness, loudness, etc.), the unit of perceived sound will be called "perceived pressure" (instead of noy, sone, etc.), and its logarithmic equivalent is then the "perceived sound level" (instead of perceived noise level, etc.), which is given in dB (J) (instead of PNdB, etc.). The dB (J) is written in this manner in order to indicate that the output was obtained with a (J) weighting function. This is analogous to the notation used when presenting results obtained with the A, B or C weighting scales presently in use on sound level meters.

Representing the human auditory system in this manner may be considered as radical or reverting to concepts which have long been abandoned, but in any case, it is believed that this type of representation is warranted in considering the results, the simplicity,

and the physical insight which can be achieved by the use of this very basic and simple model.

It might be argued that the human auditory system cannot be considered as a linear system, and in view of the present interpretation, this appears to be the case. However, consider for the moment that the functional form of the equal noisiness curves presently in use are essentially independent of input amplitude (SPL), at least for input levels greater than about 60 dB (RE: 0.00002 N/m²) (Fig. 2). It is clearly seen that the equal noisiness curves are no longer invariant with amplitude for input levels below 60 dB. Also, it is well known that for a 10 dB change in a given input spectrum, the perceived noise level (the Kryter approach [10]) changes by 10 PNdB. This in itself implies some sort of linear or one-to-one correspondence. Accepting the linear assumption for the moment, equation (1) for a constant value of Perceived Sound (assuming $H(f_c)$ is constant over the frequency band of interest) can be expressed in decibel form as follows:

$$BSPL(f_c) + 10\log_{10}\left\{\left|H(f_c)\right|^2\right\} = K, \qquad (2)$$

where

$BSPL(f_c)$ = the input band sound pressure level (BSPL) in dB

$10\log_{10}\left\{\left|H(f_c)\right|^2\right\}$ = the frequency response function of the human auditory system in dB

k = perceived constant

In effect, the above equation states that as we proceed from one band to the next throughout the complete audio range, the sound pressure level in each band must change in such a fashion that K remains constant. This is, by definition, the concept of equal noisiness (or loudness) which was discussed earlier. It is apparent, therefore, that the equal noisiness curves presently in use can be used to determine the frequency response function of the human auditory system. By defining a relative frequency response function such that $H(f_c)^2$ is unity when the sound pressure level of a band of noise or pure tone centered at 1000 Hz equals the value K, equation (2) becomes

$$10\log_{10}\left\{\left|H(f_c)\right|^2\right\} = BSPL(f_c = 1000\ Hz) - BSPL(f_c). \qquad (3)$$

This equation can be used to obtain the relative frequency response function for the human auditory system. As noted earlier, since the equal noisiness curves above 60 dB input are essentially invariant with input amplitude, equation (3) is considered to be valid above this level. This linearity only above 60 dB is not a very severe limitation because in actual practice the only noise levels of concern are those levels which are well in excess of 60 dB. The result, using the equal noisiness curves and judgments test results of Kryter and Pearsons [10] along with the expression in equation (3), is presented in Figure 4. The calculation of the perceived sound now becomes an extremely simple matter of adjusting the input spectrum by the appropriate response values of Figure 4 to obtain the "perceived spectrum." The total energy associated with the perceived spectrum is then the magnitude of the auditory sensation and is called the "perceived sound." This greatly simplifies the calculation procedure presently in use. Also, the results can be presented in terms of a perceived spectrum which can be interpreted in terms of what an individual thinks he is hearing.

RESULTS

To test the validity of this model, the frequency response function of Figure 4 has been applied to predict the results from a wide variety of judgment tests which have been reported in the open literature. Probably the most revealing and stringent tests to which the proposed model has been applied are those judgment results of Kryter and Pearsons [10].

These tests covered a wide variety of spectra (wide band, narrow band and pure tone), and therefore should provide a very strong test of the validity of the proposed model. The point to be emphasized now is that of the predicted results computed thus far, the estimates from this simple model compare as well or better with the results of judgment tests than the presently accepted methods.

Expressing equations (1) in terms of a relative response function in decibel form yields
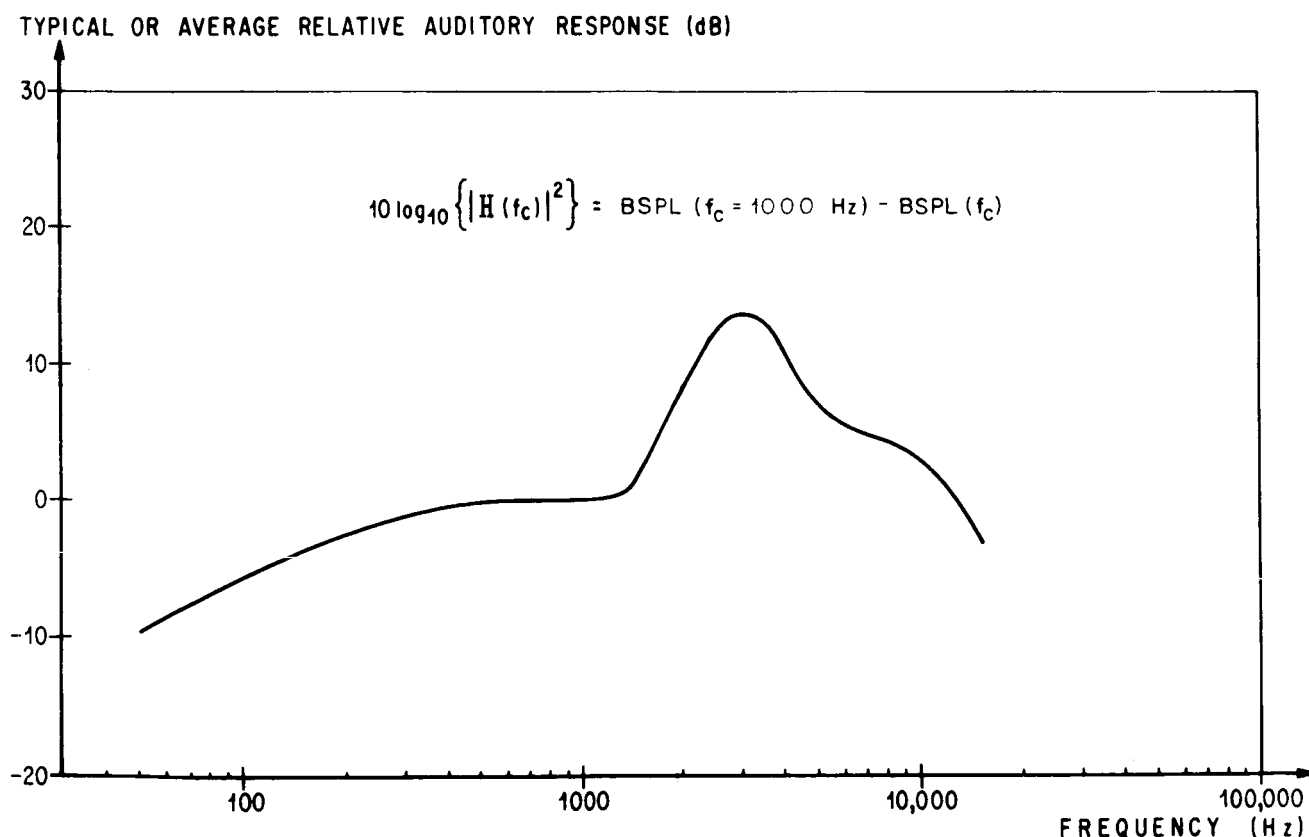
TYPICAL OR AVERAGE RELATIVE AUDITORY RESPONSE (dB)

$$10 \log_{10}\left\{|H(f_c)|^2\right\} = BSPL\ (f_c = 1000\ Hz) - BSPL\ (f_c)$$

FIGURE 4. FREQUENCY RESPONSE FUNCTION FOR A TYPICAL OR AVERAGE HUMAN AUDITORY SYSTEM

$$OB \ PSL \ (f_c) = OBSPL \ (f_c) + 10\log_{10} \left\{ \left| H(f_c) \right|^2 \right\},$$
(4)

where

$10 \log_{10} \left\{ \left| H(f_c) \right|^2 \right\}$ = is the relative frequency response function in dB

OB SPL (f_c) = is the curve band sound pressure level (OB SPL) of the input in dB

OB PSL (f_c) = is the octave band perceived sound level (OB PSL) in dB (J).

The perceived sound level (PSL) is obtained by combining, in the usual manner, all OB PSL (f_c)'s within the audio range. This approach is not restricted to only octave band analyses; in fact, the frequency response function is independent of bandwidth and can, therefore, be used in any desired form.

Equation (4) and the frequency response function presented in Figure 4 were applied to the judgment test of Kryter and Pearson [10]; the results are presented in Tables I, II and III. In these tables, the results of the proposed method are compared to the predicted results of Kryter (using the modified noy table of Reference 13). It is somewhat misleading to compare absolute values of the two methods. This is caused, in part, by the different weighting characteristics associated with each method and also by the way in which the reference level for each method was established. To avoid this problem, the absolute magnitudes will not be directly compared, but instead, each will be compared to its own standard (difference from the standard); then these differences will be compared.

Table I compares the absolute magnitudes of the predictions of the proposed method with the Kryter approach [10]. The spectra presented in Table I were all judged to be equally noisy; therefore, an ideal assessment method should indicate the same value for each spectrum. In this case, the average difference from the standard should be zero. As can be seen, the average difference is small; i.e., Kryter's approach is -0.6 and the proposed method is -1.0. For these types of spectra, these small differences are considered to be very good.

Table II presents the individual differences from the standard. Table III presents the rank, in the order of noisiness, of each of the input spectra given

in Table I. The purpose of this exercise is to verify the capability of the prediction technique to select the spectrum that would be perceived to be the noisiest from a variety of input stimuli, all of which have the same total energy content (i.e., the physical overall mean squared pressure being constant for all input spectra). The rank was determined as follows: The individual overall sound pressure level values (OASPL) of the input spectra given in Table I were all readjusted to a constant OASPL value. The spectrum which had to be increased the most to obtain the selected overall value would be judged the noisiest, and that spectrum which was changed by the smallest amount would be judged the least noisy. This then provides valid results based on judgment tests from which the predictions, determined from the readjusted values, can be compared. The results of this operation are presented in Table III. The numbers refer to the numbered spectra in Table I, and the order of the numbers indicates the order of noisiness from the noisiest to the least noisy. It can be seen that the proposed method was successful in selecting the noisiest spectrum, whereas the Kryter approach ranked the noisiest spectrum (the number 3 spectrum) fourth in the order of noisiness. The other spectra, with the exception of number six, appear to be ranked in their approximate order.

As previously indicated, the proposed model has been applied to other judgment tests, and the comparison between the predicted and measured results was about the same as that presented in this paper. These comparisons were made with acoustic stimuli consisting of pure tone and high level narrow band energy components. The results will be reported at a later date.

CONCLUDING REMARKS

A model of the human auditory system has been proposed to function as a simple input/output system. For a system of this type, the output (defined as the perceived sound) can be determined by multiplying the input acoustic stimulus by the square of the complex frequency response function of the human auditory system. The results obtained through the use of this model are in agreement with results obtained in recent judgment tests. The small variability in the predicted results [approximately 5 dB (J)] is considered to be insignificant in view of the extremely large variability which is inherent in most judgment test results (usually 10 to 20 dB's).

TABLE I

COMPARISON OF ASSESSMENT METHODS FOR NOISES JUDGED TO BE EQUALLY NOISY (ACCEPTABLE). (AN IDEAL ASSESSMENT METHOD SHOULD INDICATE THE SAME VALUE FOR EACH OF THE INDICATED SPECTRA. FROM KRYTER AND PEARSONS [10] 1963.) (AVERAGE TEST VALUES WERE OBTAINED THROUGH THE AVERAGE OF THE MEAN SQUARED PRESSURES.)

ASSESSMENT METHOD	(1) NOISE 150-300 Hz	(2) STANDARD NOISE 600-1200 Hz	(3) NOISE 2400-4800 Hz	(4) NOISE 4800-10,000 Hz	(5) NOISE 150-4800 Hz "FLAT"	(6) NOISE 150-4800 Hz +6 dB/OCT SLOPE	(7) NOISE 150-4800 Hz +12 dB/OCT SLOPE	(8) DIESEL ENGINE	(9) 707-120B LANDING TURBO FAN WITH HUSH KIT	RANGE	AVERAGE DIFFERENCE FROM STANDARD
KRYTER * (PNdB)	94.3	94.3	92.7	92.8	93.3	97.2	91.3	92.7	95.7	4.5	-0.6
JONES (dB(J))	91.0	90.1	89.5	87.7	88.9	93.5	85.0	87.0	91.3	8.5	-0.9

* AVERAGE OF THE OCTAVE AND 1/3 OCTAVE VALUES

TABLE II

DIFFERENCE FROM THE STANDARD (COMPARISON MINUS STANDARD). (PLUS IS OVERESTIMATION AND MINUS IS UNDERESTIMATION.)

SPECTRA (FROM TABLE I)	PREDICTION METHOD	
	KRYTER (PNdB)	JONES (dB(J))
1	0.0	+0.9
2	0.0 (94.3)*	0.0 (90.1)*
3	-1.6	-0.6
4	-1.5	-2.4
5	-1.0	-1.2
6	+2.9	+3.4
7	-3.0	-5.1
8	-1.6	-3.1
9	+1.4	+1.2
AVERAGE DIFFERENCE FROM STANDARD	-0.6	-0.9

* LEVEL OF STANDARD

TABLE III

RANK - ORDER OF NOISINESS OF PERCEIVED SPECTRA. (INPUT SPECTRA READJUSTED TO A CONSTANT OA SPL VALUE.)

RANK OF PERCEIVED SPECTRA	PREDICTION METHOD		RANK FROM JUDGMENT TEST
	KRYTER	JONES	
NOISIEST	9*	3	3
	6	6	5
	5	9	9
	3	5	4
	4	4	6
	7	2	7
	2	7	8
	8	8	2
LEAST NOISY	1	1	1

* NUMBERS REFER TO SPECTRA IN TABLE I

Considering the human auditory system as a simple input/output system implies, by necessity, that the auditory system functions as a linear system. When input sound pressure levels are in excess of approximately 60 dB, a linear or one-to-one correspondence can be inferred since (1) the equal noisiness curves have the same functional form and (2) for a 10 dB increase in input sound pressure level, the perceived noise level increases by 10 PNdB's. Because of this, the results obtained through the use of this proposed model should provide reliable results for input sound pressure levels in excess of 60 dB. For levels lower than this, the equal noisiness curves become radically different, and therefore the results obtained with the response curve given herein would not be expected to compare with judgment tests. However, a separate response function could be obtained for use exclusively with these lower levels.

The simplicity of providing estimates of the magnitude of an auditory stimulation with the proposed method as compared to the presently accepted methods is obvious. Consideration of the auditory system as a simple input/output system places the calculation procedure on an energy basis and thereby simplifies the physical interpretation of the hearing process. A direct "on-line" measure of the perceived sound can be easily obtained with the aid of a simple electronic filter network with the response characteristics indicated in Figure 4. A device of this kind could have far-reaching benefit, in air transportation, aircraft noise control, and other commercial or industrial noise control problems. There have been many appeals in the past to use a simple weighting network for estimating noisiness, loudness, etc. The results presented indicate that the use of simple weighting can provide valid estimates of the noisiness or loudness of a complex acoustic stimulus.

REFERENCES

1. Fletcher, F.; and Munson,W. A.: Loudness, Its Definition, Measurement and Calculation. Journal Acoustical Society of America, vol. 33, no. 5, 1961, pp. 82-108.

2. Churcher, B. G.; and King, A. J.: Journal Institute of Electrical Engineering, (London), vol. 81, 1937, discussion by B. G. Gates, pp. 57-90.

3. Beranek, L. L., et al.: Calculation and Measurement of the Loudness of Sounds. Journal Acoustical Society of America, vol. 23, no. 3, 1951, pp. 261-269.

4. Minty, F.; and Tyzzer, F. G. : A Loudness Chart for Octave-Band Data on Complex Sounds. Journal Acoustical Society of America, vol. 24, no. 1, 1952, pp. 80-82.

5. Stevens, S. S.: Calculation of the Loudness of Complex Noise. Journal Acoustical Society of America, vol. 28, no. 5, 1956, pp. 807-832.

6. Stevens, S. S.: Procedure for Calculating Loudness: Mark VI. Journal Acoustical Society of America. vol. 33, no. 11, 1961.

7. Zwicker, E.; and Feldtkeller, R.: Acoustica, vol. 5, 1955, pp. 303-316.

8. Kryter, Karl D.: Scaling Human Reactions to the Sound from Aircraft. Journal Acoustical Society of America, vol. 31, no. 11, 1959, pp. 1415-1429.

9. Kryter, K. D.; and Pearsons, K. S.: Judged Noisiness of a Band of Random Noise Containing an Audible Pure Tone. Journal Acoustical Society of America, vol. 38, 1965, pp. 106-112.

10. Kryter, K. D.; and Pearsons, K. S.: Some Effects of Spectral Content and Duration on Perceived Noise Level. NASA Technical Note, TN D-1873, 1963.

11. Stevens, S. S.: The Measurement of Loudness. Journal Acoustical Society of America, vol. 27, no. 5, 1955, pp. 815-829.

REFERENCES (Concluded)

12. Crandall, Stephan, ed.: Random Vibrations. Chapter 4 by Stephan Crandal, Statistical Properties of Response to Random Vibration, 1958.

13. Kryter, K. D.; and Pearsons, K. S.: Modification of Noy Tables. Journal of Acoustical Society of America, vol. 36, 1964, pp. 394–397.

RADIATIVE HEAT TRANSFER FROM
SATURN EXHAUST PLUMES

By

Robert M. Huffaker

LIST OF SYMBOLS

Symbol	Definition
$A(\bar{\nu})$	absorptance, Fraction of incident intensity absorbed by the gas at a given wave number.
$B^0_{\bar{\nu}}(T)$	blackbody function
C	mole fraction of absorbing gas.
d	spacing between the spectral lines.
$\bar{d}(T)$	average line spacing over a finite wave number increment, cm^{-1}.
$D_c(j)$	ratio of average equivalent line width to average line spacing for collision broadened lines.
$D_D(j)$	ratio of average equivalent line width to average line spacing for Doppler broadened lines.
$f(X)$	Ladenberg–Reiche function.
$I(\bar{\nu})$	spectral radiance.
$k(\bar{\nu})$	spectral absorption coefficient; this quantity is the fractional change in intensity per unit length of absorbing (or emitting) path. Units may be cm^{-1} $-cm^2/g$, (molecule), $cm^{-1}-atm^{-1}$.
l	path length of absorbing gas, cm.
l	hypothetical path through an inhomogeneous gas.
L	total path length from radiating region to point of interest.
P	pressure of gas, atm.
P(S)	intensity distribution function of a band.

Symbol	Definition
p^h_a	pressure of absorbing gas in the (homogeneous) h-th zone.
p^h_b	pressure of foreign gas broadener in the (inhomogeneous) h-th zone.
S	spectral line intensity.
S	hypothetical intensity from an inhomogeneous gas for spectral lines.
$\bar{S}$	average line intensity over a finite wave number increment.
S^0	intensity per unit pressure.
S_0	normalizing intensity used in the intensity distribution function P(S) for spectral lines.
T	temperature in degrees Kelvin.
U	optical path, equal to pressure × path length.
W	the equivalent width, in the integral of the absorptance over a wave number interval.
$\overline{W}$	average equivalent width with respect to intensity.
Y_c	carbon mass fraction
γ	half-width of the spectral line. Generally expressed in wave numbers (cm^{-1}).
γ_a	half-width of absorbing gas (self-broadening).
γ_b	half-width due to foreign gas broadening.
$(\gamma/d)'_i$	equivalent (γ/d) up to and including the i-th cell for an inhomogeneous path.

$\epsilon(\bar{\nu})$ spectral emissivity; ratio of the spectral radiance of a body to that of a blackbody at the same temperature.

$\kappa_{\lambda, C}$ carbon spectral absorption coefficient.

$\bar{\nu}$ wave number, i.e., reciprocal of the wavelength.

τ transmittance through a homogeneous gas.

τ' transmittance through an inhomogeneous gas.

INTRODUCTION

Heat transfer to the base of a launch vehicle can occur through two modes: convection and radiation. On large vehicles which burn RP-1 (kerosene) and oxygen, these two modes are both important. Convection to the base region depends upon the properties of the gas flow close to the surface being heated. Simple models of the flow, together with boundary-layer correlations for the heat transfer coefficient, have been used in the past to arrive at local heating rates on the heat shield. Radiation, on the other hand, is sensitive to the entire flow field not occluded by the vehicle's structure. Here, predictions have been made either by representing the exhaust plume as a surface with a given emissivity, temperature, and configuration, or by assuming a simple geometrical configuration for the hot gas, which is presumed to be uniform, and integrating the equation of transfer with a simplified absorption coefficient.

The exhaust plume from a multiple-engine configuration like the Saturn V is an extraordinarily complex gas-dynamical structure. The exhaust jets from the different engines interact with the atmosphere and with each other through an intricate series of shock waves and turbulent mixing layers (Fig. 1). At altitude, on a multiengined vehicle, the high-temperature, high-pressure collision zones between engines is the strongest source of radiation (Fig. 2).

For the radiating species of interest in the Saturn exhaust plumes, H_2O, CO_2, and CO, the only emission data available were those of Hottel which were obtained in the 1930's. These data were extrapolated to higher temperatures and lower pressures and were total emissivities. For second stage vehicles where there are impingement regions, ground measurements could not be performed. Also, the radiation data obtained from model engine data could not be scaled to give the full-scale radiation heat transfer design information.
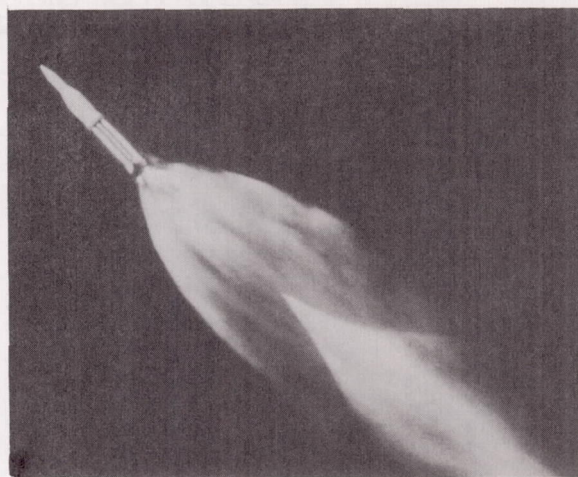
FIGURE 1.   SATURN I AT 38.1 km ALTITUDE
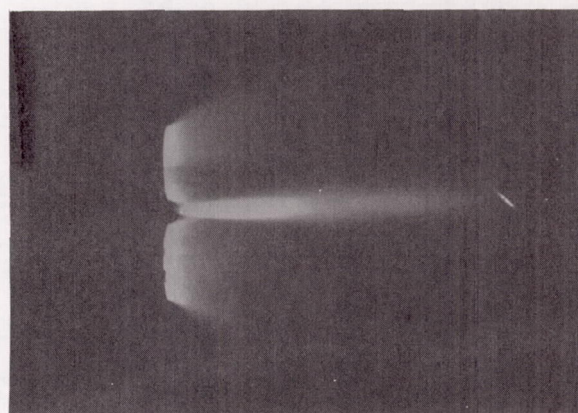
36.6 km Altitude P_c = 760 N/cm^2
Oxygen/Ethylene (O_2/C_2H_4)   O/F = 2.25

FIGURE 2.   1/45 SCALE MODEL F-1 ENGINES

OUTLINE OF THE RADIATION PROGRAM

For first stage vehicles, the heating environment is determined from total and spectral radiation measurements in single engine exhaust plumes. An empirical model is developed by using a total

emissivity along with a form factor program to calculate the radiation to the base. This calculated heat flux, because of the contribution of the after-burning layers, is a maximum at sea level. This maximum value is used in the design of the heat shield. The plume radiation decreases as altitude increases, and the plume spreads, thus becoming cooler and less dense.

The upper stages of the Saturn V are powered by LH$_2$-LOX engines, the Rocketdyne 0.89 MN (200 000-lb.) thrust J-2. The S-II stage has a cluster of five J-2's, while the S-IVB has only one J-2. The radiation from the first stage's engines is principally carbon, which produces a continuum radiation. The principal radiator in the upper stages is water vapor, which forms a band spectrum. The first stage design information obtained from experimental data on single engines is a relatively simple problem, but the design information on the upper stages must be entirely theoretical since scaling laws for model engine data are not yet known.

BAND MODELS

In a specific wavelength region, if the physical state of an absorbing or emitting gas is known as well as the locations, intensities and shapes of the lines, it is possible to calculate the radiation emitted by a specific sample of the gas. However, for the gases of interest in Saturn-type exhaust plumes, the absorption coefficient varies extremely rapidly with wavelength. Consequently, an exact calculation of the radiant heat transfer would be a formidable task even with modern computers. By using band-models, it is possible to replace this detailed calculation over frequency by an average over selected frequency intervals. Another objective of the use of a band model concept is to permit the interchange, in the heat transfer equation, of the order of integration over spatial and frequency variables.

A spectral line is described by the absorption coefficient $k(\bar{\nu})$ so that at frequency $\bar{\nu}$ the emissivity is given by

$$\epsilon(\bar{\nu}) = 1 - \exp[-k(\bar{\nu})U] \qquad (1)$$

where U is the optical depth. The line intensity S is related to $k(\bar{\nu})$ by the equation

$$S = \int k(\bar{\nu}) d(\bar{\nu}) . \qquad (2)$$

The equivalent width W of an isolated spectral line is given by the expression

$$W = \int \{1 - \exp[-k(\bar{\nu})U]\} d\bar{\nu}. \qquad (3)$$

The equivalent width represents the effective spectral interval over which the line is black.

For a Lorentz (pressure-broadened) line shape, W is given by the Ladenberg-Reiche function, which for the limiting case of a weak line gives $W = SU$, and for a strong line gives $W = \sqrt{4S\gamma U}$ where γ is the half-width. In the intermediate transitional region, W varies smoothly with U, and is smaller than the value given by either of the asymptotic expressions.

A band model is used to relate the properties of a group of lines in the spectrum to the properties of the individual lines. Band models may be said to have their origin in the theory advanced by Elsasser in 1938, and his particular treatment is known as the Elsasser Model. Elsasser assumed a particular shape for a single line and a distribution of line intensities. He assumed that all the lines were equally spaced and of equal intensity. The solution for W has been given by Elsasser for an infinite sequence of equally spaced, equally intense lines. Another model advanced by Mayer and Goody assumed that the lines in a band are completely random. For this model, it has been shown that the emissivity is not strongly dependent on the particular intensity distribution chosen, and furthermore that the emissivity can be expressed in terms of the properties of a single line. In this case, the absorptance is

$$A = 1 - e^{-\overline{W}/d}, \qquad (4)$$

where $\overline{W}$ is the equivalent width of a single line averaged over the intensity; that is,

$$\overline{W} = \int_0^\infty W_{single\ line} P(S)\ dS, \qquad (5)$$

where

$$W_{single\ line} = \int_0^\infty \{1 - \exp[-k(\bar{\nu})U]\} d\bar{\nu} \qquad (6)$$

and P(S) dS is the probability that a line has an intensity between S and S + dS. Then we can write

$$\frac{\overline{W}}{d} = \int_0^\infty \frac{2\pi\gamma}{d} f(X) P(S)\ dS, \qquad (7)$$

where f (X) is the Ladenberg-Reiche function; i.e.,

$$f(X) = Xe^{-X} [I_0(X) + I_1(X)]$$

and

$$X = \frac{SU}{2\pi\gamma} . \tag{7}$$

This equation is then evaluated for particular distributions, for example, $P(S) \propto \frac{1}{S}$ or $P(S) \propto e^{-S/S_0}$.

For the random model, if the lines are weak, we have

$$\bar{\epsilon} = 1 - \exp\left(-\frac{SU}{d}\right), \tag{8}$$

which gives $\bar{\epsilon}$ as a function of one parameter S/d, and U. For the strong line limit, we have

$$\bar{\epsilon} = 1 - \exp\left[-2\frac{(S\gamma^0)^{1/2}}{d}(PU)^{1/2}\right], \tag{9}$$

which expresses $\bar{\epsilon}$ as a function of one parameter, $(S\gamma^0)^{1/2}/d$, and one variable, $(PU)^{1/2}$.

If, however, we want to represent $\bar{\epsilon}$ over the entire range of P and U, we have

$$\bar{\epsilon} = 1 - \exp\left[-\frac{2\pi\gamma^0}{d} Pf\left(\frac{S}{2\pi\gamma^0} \frac{U}{P}\right)\right], \tag{10}$$

where f is the Ladenberg-Reiche function. With this expression, we are considering the actual transition region between "weak" and "strong" lines, but are implicitly assuming that all lines are simultaneously in the same part of this transition region. Almost any real spectrum would be expected to contain lines of widely varying intensities, some of which may be in the "weak" region, some in the "strong" region and others at various intermediate stages.

A band model which is frequently used because it is more realistic and also yields simple results is the random model with an exponential intensity distribution. It is assumed that a given number of Lorentz-shaped lines exist in a certain spectral interval and that their intensities are given by an exponential probability distribution function. For this model, we have

$$\bar{\epsilon} = 1 - \exp\left[-\frac{\frac{S_0}{d}U}{\sqrt{1 + \frac{S_0 U}{\pi\gamma}}}\right] . \tag{11}$$

This is a more convenient form to use than equation (10) since it does not involve f, which is defined in terms of exponential and Bessel functions.

THE MODIFIED CURTIS-GODSON APPROXIMATION

To calculate the radiant heating from rocket exhaust plumes, we must know the spectral transmittances of the exhaust plume radiating gases. Exhaust plumes are strongly inhomogeneous. There-, fore, we must determine the spectral transmittances of inhomogeneous gases in order to develop a calculation method. Under MSFC contract, a general method has now been developed to calculate spectral transmittances of inhomogeneous gases from the properties of homogeneous gases. Thus, spectral transmittance for a particular inhomogeneous gas path can be calculated by properly combining known data on gases at constant temperature, pressure, and concentration [1].

The method developed is based principally on two special spectroscopic concepts: the molecular band model and the Curtis-Godson approximation. The band model yields an explicit, closed formula for the molecular radiation within each selected spectral region of interest which uses as input data the averaged line strength, the averaged line spacing, and the averaged line half-width. An average of 25 wave numbers is considered sufficient. The use of a band model is critically important for practical calculations of gas radiation. The Curtis-Godson approximation is a method of combining the parameters that appear in the band model formulas in such a way that the parameters needed for an inhomogeneous gas calculation are obtained solely from homogeneous gas data. This is a critical factor, because the necessary parameters need be calculated or measured in the laboratory only for uniform gas samples. Without the Curtis-Godson or some equally good approximation, we would have to treat each inhomogeneous gas path as a special case. The band model used was the random model with equal line intensities and equal line widths. In terms of the spectral transmittance τ at wave number $\bar{\nu}$

$$\ln \frac{1}{\tau} = 2\pi \frac{\gamma}{d} f(X) \qquad (12)$$

where

$$X = \frac{\left(\frac{S}{d}\right) U}{2\pi (\gamma/d)} . \qquad (13)$$

Since the Curtis-Godson method is based on the premise that we can substitute a hypothetical homogeneous path for an inhomogeneous path, this hypothetical path will have the same spectral transmittance as an inhomogeneous path if the parameters $(\gamma/d)'$ and X' as defined below are used in the band model formulas for the transmittance of a homogeneous gas.

If an inhomogeneous gas has a transmittance of τ', then some hypothetical homogeneous sample has the same transmittance if it has certain values of $(\gamma/d)'$ and $(X)'$. The Curtis-Godson approximation gives us

$$\frac{S'}{d} \ell' = \sum_i \frac{S_i}{d} \ell_i = \sum_i X_i \frac{-\ln \tau_i}{f(X_i)} \qquad (14)$$

and

$$\frac{S'}{d} \ell' \frac{\gamma'}{d} = \sum_i \frac{S_i}{d} \ell_i \frac{\gamma_i}{d} = \frac{1}{2\pi} \sum_i X_i$$

$$\left[\frac{-\ln \tau_i}{f(X_i)}\right]^2 \qquad (15)$$

which define the band model parameters of this particular homogeneous sample. This definition is given in terms of the band model parameters of the individual homogeneous zones comprising the inhomogeneous path being studied, and these zones are labeled with the subscript h.

$(\gamma/d)'$ is obtained by dividing equation (15) by equation (14); X' can then be determined by dividing equation (14) by $2\pi(\gamma'/d)$:

$$\left(\frac{\gamma}{d}\right)'_i = \frac{\sum\limits_{h=1}^{i} P^h_a \left(\frac{S^o}{d}\right)_h \ell_h \left[\left(\frac{\gamma^o_a}{d}\right)_h P^h_a + \left(\frac{\gamma^o_b}{d}\right)_h P^h_b\right]}{\sum\limits_{h=1}^{i} \left(\frac{S^o}{d}\right)_h P^h_a \ell_h} , \qquad (16)$$

$$X'_i = \frac{\left\{\sum\limits_{h=1}^{i} \left(\frac{S^o}{d}\right)_h P^h_a \ell_h\right\}^2}{2\pi \sum\limits_{h=1}^{i} \left(\frac{S^o}{d}\right)_h P^h_a \ell_h \left[\left(\frac{\gamma^o_a}{d}\right)_h P^h_a + \left(\frac{\gamma^o_b}{d}\right)_h P^h_b\right]} . \qquad (17)$$

Substituting these values of $(\gamma/d)'_i$, $(X)'_i$ into equation (12) yields an expression for the transmittance of the inhomogeneous path in terms of zonal transmittances and zonal X's,

$$-\ln \tau' = \frac{\sum\limits_i X_i \left[\frac{-\ln \tau_i}{f(X_i)}\right]^2}{\sum\limits_i X_i \frac{-\ln \tau_i}{f(X_i)}} f\left[\frac{\left[\sum\limits_i X_i \frac{-\ln \tau_i}{f(X_i)}\right]^2}{\sum\limits_i X_i \left[\frac{-\ln \tau_i}{f(X_i)}\right]^2}\right] . \qquad (18)$$

Generally, transmittances calculated with equation (18) are not very sensitive to errors in X_i. Therefore, with moderately accurate values of X_i, the accuracy with which τ' can be calculated is limited by the accuracy of the transmittance measurements and the suitability of the theory. This is particularly true in the high and low X regions where equation (18) reduces to a form in which τ' is independent of X_i. Thus, if all the X values are low (less than 0.2), $f(X) \approx X$, and equation (18) reduces to

$$-\ln \tau' \approx \left\{\sum_i (-\ln \tau_i)\right\} . \qquad (19)$$

If all the X_i's are high (greater than 2.0), and $f(X) \approx (2X/\pi)^{1/2}$, equation (18) reduces to

$$-\ln \tau' \approx \left\{\sum_i (-\ln \tau_i)^2\right\}^{1/2} . \qquad (20)$$

Equation (18) is the general expression and can be used for any X values. Equations (19) and (20) are good in the low and high X regions, respectively. Experiments were carried out to test the Curtis-Godson theory for temperatures and pressures typical of rocket exhaust plumes. Band model parameters were measured for isothermal gases at various temperatures, the results were used to predict transmittances of known inhomogeneous paths, and the inhomogeneous path transmittances were compared to the theoretical prediction. Using a furnace-gas cell arrangement, numerous transmittances of water vapor inhomogenous paths were

measured and compared with transmittances calculated by the Curtis–Godson combination method in conjunction with the statistical band model. An example of the results is shown in Table I.

mean deviation of the $\bar{S}/d$ $(T, \bar{\nu})$ values is within ± 20 percent (Fig. 3). The value of $\frac{\gamma}{d}$ $(T, \bar{\nu}, P_{\text{foreign gas}})$ was experimentally measured using a

TABLE I. TWO-ZONE WATER VAPOR TRANSMITTANCE AT 3990 cm^{-1}
(Optical Path: 0.61 m (24 in.) per zone; $T_1 = T_2 = 1273°$ K; $x_1 = x_2 = 3.49$)

		Measured Transmittance			Calculated $\bar{\tau}$	
p_1 (mm)	p_2 (mm)	τ_1	τ_2	$\bar{\tau}$	From Eq. (18)	From Eq. (20)
53	53	0.720	0.729	0.621	0.628	0.634
102	105	0.571	0.566	0.425	0.443	0.450
150	153	0.438	0.443	0.284	0.306	0.314
51	104	0.743	0.571	0.515	0.524	0.530
56	146	0.724	0.464	0.419	0.428	0.435

DETERMINATION OF THE BAND MODEL PARAMETERS

H$_2$O

From the band model formulas, we can see that if values of $\bar{S}/d$ $(T, \bar{\nu})$ and $\bar{\gamma}/d$ $(T, \bar{\nu}, P_{\text{foreign gas}})$ can be determined, then the absorptance can be calculated for any PL. For thin-gas spectra where $(\bar{S}U/d) / (4\gamma/d) \ll 1$, $\bar{S}/d$ can be determined directly. A large number of water vapor spectra, over the wavelength range from 1 to 22μ, have been published in recent years. These spectra cover the temperature range from 300° to 2700°K. The optical depths range between 0.2 and 100 cm-atm., and total pressures between 0.67 to 101 N/cm^2 (50 mm Hg and 10 atm). If sufficient thin-gas spectra at all temperatures were available, a set of $\frac{\bar{S}}{d}$ $(T, \bar{\nu})$ values could be derived directly. To obtain $\frac{\bar{S}}{d}$ (T, ν) values from measured spectra in which the gas was not thin, the functional relationship between emissivity and optical depth must be known. The curve of growth given by the statistical band model has been used to determine the mean spectral absorption coefficients from thin and nonthin spectra by adjusting the fine structure term in such a way that the integral of the absorption coefficients over a given vibration rotation band results in the known value of the band intensity. Their values have been tabulated [2]. In general, the

long H$_2$–O$_2$ burner and are tabulated in Reference [2]. Measurements were made over path lengths ranging from 0.31 to 6.1 m (1 to 20 ft.).
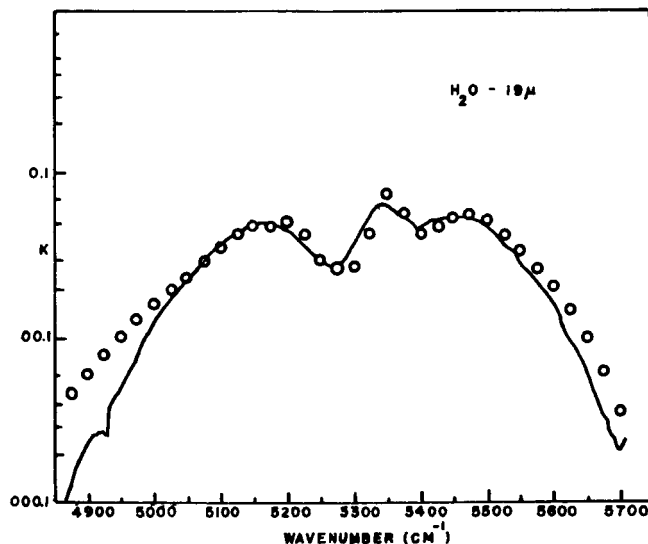

FIGURE 3. COMPARISON OF ABSORPTION COEFFICIENTS OBTAINED BY GOLDSTEIN (SOLID LINE) WITH PRESENT VALUES (POINTS) FOR THE 1.9-μ BAND AT 873° K

Using these experimentally determined band model parameters in a radiation heat transfer computer

program which uses both band model parameters and the Curtis-Godson approximation, we made calculations of the radiation from H_2O at particular temperatures and pressures and compared them with measurements made by other investigators [3]. The results are shown in Figure 4.
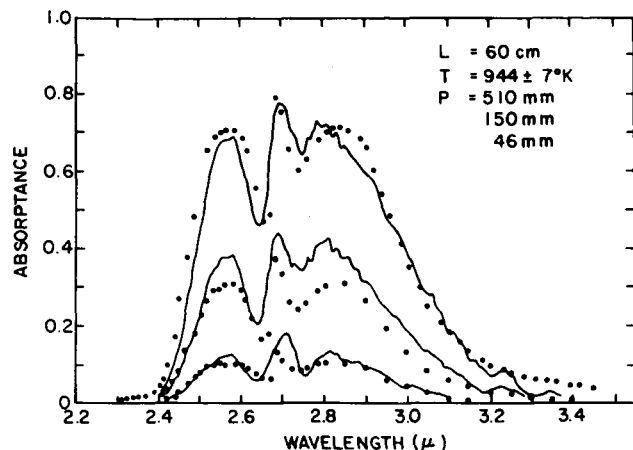

FIGURE 4. COMPARISON OF MEASURED AND CALCULATED EMISSIVITY OF THE 2.7-μ BAND. (Solid lines are the measured spectra taken from Reference 3; points are the present values.)

CO AND CO_2

The emissivity of these two molecules at high temperature have been theoretically calculated by Malkmus [4,5] and by Thomson [2]. For CO_2, many of these results have been verified by experiment [6,7]. It is believed that for exhaust plume application, these calculations are an adequate representation of the spectral properties of CO and CO_2. The results have been described in detail in the original papers and are presented in tabular form in Reference 2.

CARBON PARTICLES

The emissivities of clouds of very small carbon particles have been measured at the exit planes of small rocket motors. The rocket motor for this study used Foelsch-type nozzles for producing an approximately constant temperature and velocity across the exit plane. The product of the carbon mass fraction, Y_c, and the carbon cloud's spectral absorption coefficient, $\kappa_{\lambda, C}$, has been determined for wavelengths between 1 and 4μ, and for temperatures between 300°

and 2600°K. The carbon has been sampled in a full size F-1 engine. The results indicate an approximate particle size of 400 Å. This is in good agreement with the measurements using a small perfectly balanced jet. Therefore, in any calculation of radiant heat transfer from rocket exhaust plumes using hydrocarbon as a fuel, the scattering can be neglected because the size of the particles is too small to absorb much radiant energy in the wavelength where peak heating occurs.

BAND MODEL PREDICTION METHOD

The general method of analysis, referred to here as the band model prediction method, uses absorption coefficients corresponding to the thin-gas values. These absorption coefficients are used with a random or statistical band-model representation of the curve of growth in which the effective fine structure parameters for both Doppler and collision-broadening are evaluated using a modified Curtis-Godson approximation.

The coordinate system used for the heat transfer calculations is shown in Figure 5. The exhaust plume properties are specified in a Cartesian coordinate system, which normally has its origin at the center of the nozzle exit plane. Spatial relationship of the point of interest to the exhaust plume is specified by relating the U, V, W axes at the point of interest to the plume coordinate system. This is done in the general case by specifying the coordinates of the point and the nine direction cosines which fix the U, V, and W axes with respect to the X, Y, and Z axes.

The radiant flux is calculated using a spherical coordinate system centered at the point of interest. In this system, the inclination of a line of sight, s, to the surface normal, W, is the angle, θ, while the angle between the projection of s in the U-V plane and the U axis is ϕ. This procedure is summarized in detail in Reference 8.

The heat transfer equation used to predict the radiation from a spherical segment over a spectral region between wave numbers $\bar{\nu}_i$ and $\bar{\nu}_f$ is

$$\dot{q}/A = \int_{\theta_i}^{\theta_f} \int_{\phi_i}^{\phi_f} \int_{\bar{\nu}_i}^{\bar{\nu}_f} \int_0^{L_{max}}$$

$$- B_{\bar{\nu}}^0 \left(\frac{df}{dL} \right) dL \, d\bar{\nu} \, d\phi \, \cos\theta \, \sin\theta \, d\theta,$$
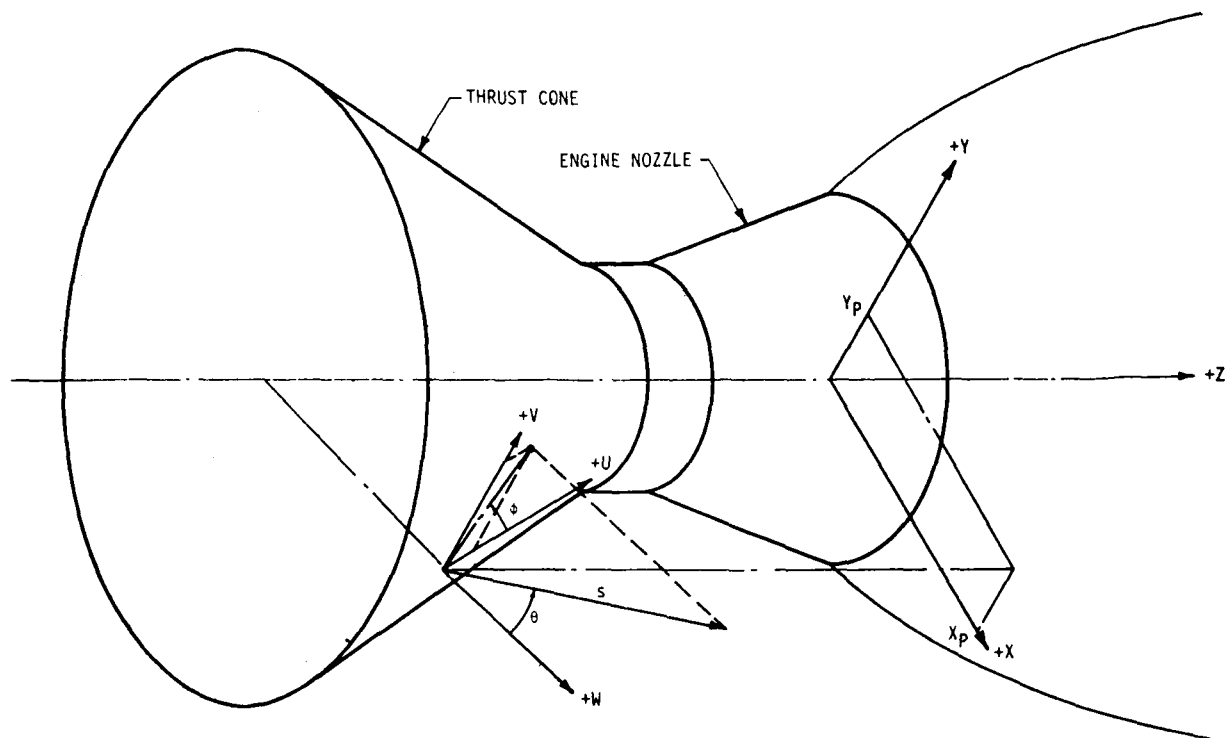
FIGURE 5. ILLUSTRATION OF COORDINATE LOCATIONS

where f is the transmissivity of the gas and B_{ν}^{o} is Planck's function. When this equation is put in numerical form, it becomes

$$\dot{q}/A = \sum_{\theta_i}^{\theta_f} \sum_{\phi_i}^{\phi_f} \sum_{\bar{\nu}_i}^{\bar{\nu}_f} \sum_{0}^{L_{max}}$$

$$- B_{\nu}^{o} \, [f(L,\bar{\nu}) - f(L - \Delta L, \bar{\nu})] \cos\theta \, \sin\theta \, \Delta\theta \, \Delta\phi \, \Delta\bar{\nu}.$$

APPLICATION TO SATURN EXHAUST PLUMES

Using these equations and band model parameters, the radiation has been calculated from the exhaust gases for the S-II vehicle. The radiation to the S-II stage was calculated before launch for several points of interest in the base region. The experimental calorimeter measurements on board the S-II agreed well with the calculations made before launch.

The radiative heat transfer from a 1/45 scale model F-1 engine was measured at Cornell Aeronautical Laboratory using a short-duration technique which produces a steady gas flow out of the engines for approximately 5 msec. The propellants used were gaseous ethylene and oxygen, and the nozzle stagnation pressure was approximately 690 N/cm² (1000 psia). Simulated altitude during the short test period was approximately 36.6 km (120,000 ft).

Radiation measurements were made using a fast-scanning spectrometer, which was set up to scan from 1.6 to 5μ in 1 msec with a 0.25 msec interval between scans.

No comparisons of these tests have yet been made for the impingement region between plumes. The radiation prediction is compared with measured values in Figure 6. The levels of the measurements agree well with the predictions, but there appears to be a slight discrepancy in the wavelength. This discrepancy is attributed to uncertainties in the data reduction. It was necessary to assign a wavelength to some spectral feature in the data to obtain absolute wavelength values.

CONCLUSIONS

1. An improved method has been developed for calculating radiative heat transfer through

inhomogeneous, Saturn-type exhaust plumes. This calculation method uses a band model approach in representing the absorption and emission characteristics of the exhaust gases. A modified Curtis-Godson approximation is used in the radiative heat transfer calculations and effectively averages the band model parameters over the inhomogeneous path. This technique has been shown to be accurate for strong gradients in temperature and concentration. The difference between the measured inhomogeneous transmittance and that calculated by the modified Curtis-Godson approximation was within the experimental error and was not greater than 0.02. Under MSFC contract, these band model parameters have been completely determined.

2. Studies that use these calculation methods are in progress to define radiation scaling relationships between model and full scale engines and stages.

3. A symposium was held at MSFC in October 1967, which primarily reviewed these programs [7].

4. A textbook and design handbook on gaseous radiative heat transfer is being prepared and should be completed by April 1969.

5. Although developed for the Saturn V heating problems, these radiation heat transfer programs have spin-offs for use in other applications. For example, these programs are applicable to almost all flame problems involving radiative heat transfer.
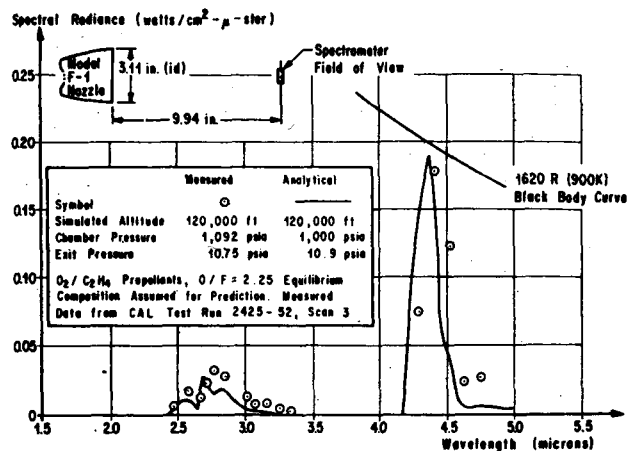
FIGURE 6. COMPARISON OF MEASURED AND PREDICTED RADIATION 25.2 cm AFT OF THE EXIT OF A 1/45 SCALE MODEL F-1 ENGINE

REFERENCES

1. Warner and Swasey: Use of Curtis-Godson Approximation in Calculation of Radiant Heating by Inhomogeneous Hot Gases. NASA TM X-53411, March 15, 1966.

2. Study on Exhaust Plume Radiation Predictions. NASA CR-61233, July 1968.

3. Goody, R. M.: Atmospheric Radiation I. Theoretical Basis, Oxford, 1964.

4. Malkmus, W.; and Thomson, J. A. L.: J. Quant. Spect. Radiant Transfer, vol. 2, no. 17, 1962.

5. Malkmus, W.: Infrared Emissivity of CO_2 (4.3 μ band). GD/A AE 62-0204, 1962.

6. Ferriso, C. C.; Ludwig, C. B.; and Action, L.: Spectral Emissivity Measurements of the 4.3 μ CO_2 Band Between 2650 and 3000°K. GD/C-DBE 65-017, August 1965.

7. Tourin, R. H.: Spectral Emissivities of hot CO_2 - H_2O Mixtures in the 2.7 μ Region. J. Opt. Soc. Am., vol. 51, 1961, p. 799.

8. Specialist Conference on Molecular Radiation and Its Application to Diagnostic Techniques. NASA TM X-53711, October 5-6, 1967.

BIBLIOGRAPHY

Benedict, W. S.; and Kaplan, L. D.: J. Chem. Phys., vol. 30, 1959, p. 391.

Benedict, W. S.; Herman, R.; Moore, G. E.; and Silverman, S.: Astrophys. J., vol. 435, 1962, p. 277.

Benedict, W. S.; et al.: National Bureau of Standards Monograph No. 71, NBS, Washington, D. C.

Dahm, W. K.: Present Techniques and Problems in the Determination of the Base Heating Environment of Propelled Boost and Space Vehicles. International Symposium on Space Technology and Science, 5th, Tokyo, Japan, A65-14290 05-31, September 2-7, 1963.

Ferriso, C. C.; and Ludwig, C. B.: Spectral Emissivities and Integrated Intensities of the 1.87, 1.38, and 1.14 μ H_2O Bands Between 1000 and 2200°K. J. Chem. Phys., vol. 41, 1964, p. 1668.

Goody, R. M.: A Statistical Model for Water Vapor Absorption. Quart. J. Roy. Met. Soc., vol. 78, 1952, p. 165.

Malkmus, W.: Infrared Emissivity of Carbon Dioxide (2.7 μ Band). J. Opt. Soc. Am., vol. 54, 1964, p. 751.

Oppenheim U. P.; and Ben-Aryeh, Y.: Statistical Model Applied to the Region of the 1/3 Fundamental of CO_2 and 1200°K. J. Opt. Soc. Am., vol. 53, 1963, p. 344.

Oppenheim, U. P.; and Goldman, A.: Spectral Emissivity of Water Vapor at 1200°K. Tenth Symposium (International) on Combustion, The Combustion Institute, vol. 10, 1965, p. 185.

Penzias, G. J.; and Maclay, G. J.: Analysis of High Temperature Gases in Situ by Means of Infrared Band Models. NASA CR-54002.

Plass, G. N.: Models for Spectral Band Absorption. J. Opt. Soc. Am., vol. 48, 1958, p. 690.

Plass, G. N.: Useful Representations for Measurements of Spectral Band Absorption. J. Opt. Soc. Am., vol. 50, 1960, p. 868.

Plass, G. N.: Spectral Emissivity of CO_2 from 1800-2500 cm^{-1}. J. Opt. Soc. Am., vol. 49, 1959, p. 821.

Plass, G. N.: Spectral Band Absorptance of Radiation Traversing Two or More Cells in Series. Appl. Opt., vol. 4, 1965, p. 69.

Plass, G. N.: The Theory of the Absorption of Flame Radiation by Molecular Bands. Appl. Opt., vol. 4, 1965, p. 161.

Plass, G. N.: The Theory of the Absorption of Flame Radiation by Molecular Bands. Appl. Opt., vol. 4, 1965, p. 161.

Simmons, F. S.; Arnold, C. B.; and Kent, N. F.: Studies of Infrared Radiative Transfer in Hot Gases Nonisothermal Radiance Measurements in the 2.7 μ H_2O Bands. BAMIRAC 4613-93-T, December 1965.

Stull, V. R.; Wyatt, P. J.; and Plass, G. N.: The Infrared Transmittance of CO_2. Appl. Opt., vol. 3, 1964, p. 243.

Wyatt, P. J.; Stull, Robert, V.; and Plass, G. N.: The Infrared Transmittance of Water Vapor. Appl. Opt., vol. 3, 1964, p. 229.

DEVELOPMENT OF LASER-DOPPLER GAS VELOCITY INSTRUMENTATION

By

Robert M. Huffaker

INTRODUCTION

Approximately four years ago, the Aero-Astro-dynamics Laboratory initiated a program to develop a laser-Doppler heterodyne technique for measuring both the local mean and the fluctuating gas velocity with high spatial and temporal resolution. Optical instrumentation was needed because measuring the velocity and turbulence in supersonic jets and wind tunnel flows by using other physical probes such as the hot wire anemometer will disturb the flow. Optical heterodyning of a portion of the incident laser beam with the laser light that is scattered from the flowing gas will produce a beat signal at the frequency of the Doppler shift as a result of the motion of the particles in the gas. Either natural or artificial tracers are required for this technique.

In optical heterodyning, two coherent, mono-chromatic light beams with different frequencies are directed simultaneously onto the photosensitive surface of a photodetector such as a photomultiplier tube. The intrinsic square-law response of the photodetector leads to an electrical output signal with a frequency equal to the frequency difference between the two incident light beams. Optical heterodyning thus allows a direct measurement of the frequency difference between two coherent, mono-chromatic light beams from a few Hertz to giga-Hertz corresponding to almost zero velocity to very high Mach numbers. The measurement of this beat signal frequency, together with the geometry of the optical system, determines the flow velocity of the gas.

The laser-Doppler instrumentation was also needed for the measurement of atmospheric wind velocity and turbulence that create the Saturn V ground wind problems. The development of laser-Doppler instrumentation for use in both the wind tunnel and atmospheric applications will be reviewed.

WIND TUNNEL AND JET PROGRAM

The measurement of the Doppler shift of a laser beam that is produced by the motion of a volume of gas yields a value for the one-dimensional velocity of that volume of gas, provided the velocity direction is known. Three measurements of the Doppler shifts are required to completely define the point velocity. The technique in Figure 1 is for the case where the velocity direction is known and is in the plane of the laser and receiver beams.
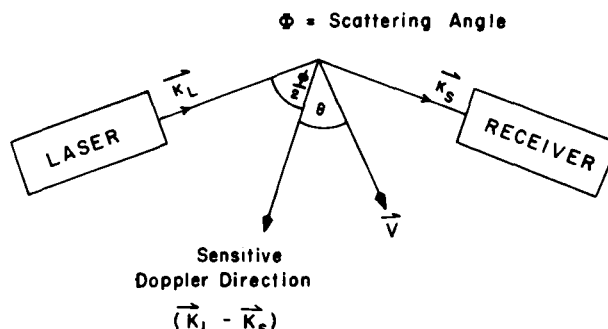
FIGURE 1. SCHEMATIC OF THE LASER-DOPPLER HETERODYNE TECHNIQUE

Consider the scattering geometry in the diagram where $\vec{K}_L$ and $\vec{K}_S$ are vectors of magnitude $\frac{2\pi}{\lambda}$ (λ = laser wavelength) in the direction of the laser and scattered beams, respectively. The angular Doppler frequency shift $\Delta\omega$ is given in general by $\Delta\omega = (\vec{K}_S - \vec{K}_L) \cdot \vec{V}$, which reduces to

$$\Delta\omega = \frac{2\pi}{\lambda} \left| \vec{V} \right| \sqrt{2 - 2\cos\phi} \ \cos\phi$$

for the above geometry. The sensitive direction of the instrument is then $(\vec{K}_S - \vec{K}_L)$, and the Doppler shift is determined by the component of the velocity in this direction.

Using this one–dimensional system, Doppler shift measurements to determine gas velocity were performed initially in the 18–cm (7–in.) wind tunnel at MSFC and compared with a pitot gas velocity measurement system [1]. The results are shown in Figure 2. Measurements have also been made on supersonic jets with gas velocities to Mach 2.5.
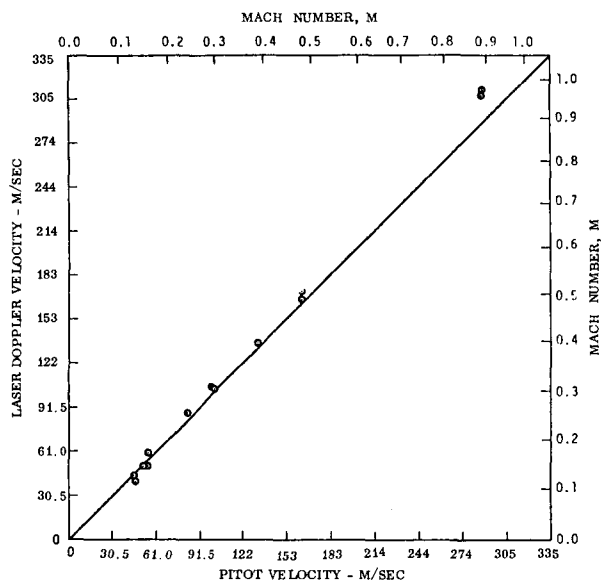
FIGURE 2. HIGH VELOCITY WIND TUNNEL
TEST RESULTS

Figure 3 illustrates the optical arrangement used in the one–dimensional gas velocity measurements. This same optical design has been applied to the three–dimensional instrument (Fig. 4) which has been designed in two parts: an optical receiver system and a movable mount. The mount has adjustments which insure that the laser beam is focused at all times on the same scattering volume viewed by the receiving 3-D optics. This instrument is presently being used for velocity measurements on subsonic and supersonic jet flows. It is important to note that the light scattered from the particle is predominantly Mie scattering since the particles are large (approximately 1 micron in diameter). Thus, since temperature effects are negligible, the instrument measures a true velocity.

The nature of the Doppler shift signal provided by a turbulent flow is a rapidly varying frequency centered about a mean frequency. An example of a turbulent flow signal as seen on a spectrum analyzer which displays amplitude versus frequency (or velocity) is shown in Figure 5. The turbulence level increases with increasing distance downstream from the jet. However, this type of spectrum analyzer display is not the correct way to study the turbulence, or even a mean velocity, in the flow. The nature of the signal from a Doppler shift in a turbulent flow therefore precludes the use of a sequential type of spectrum analyzer for turbulence studies, and a frequency tracking capability is desired. Such a capability is provided by a conventional FM discriminator, which has been used with some success, but the discriminator ceases to operate satisfactorily when the signal-to-noise ratio of the input FM signal deteriorates to below 10 dB. To overcome this limitation, a frequency compressive feedback loop has been incorporated in the output of the phase modulation (PM) tube. The output of the PM tube is fed into a mixer with the output of a voltage controlled oscillator (VCO). A signal at the difference frequency appears at the mixer output, is amplified, and afterwards becomes the input of a discriminator whose center frequency is f_c. The voltage output of the discriminator is zero at f_c; frequencies greater or less than f_c show up as the positive and negative dc levels. The integrated output of the discriminator is used to frequency modulate the VCO, and thereby maintain the output of the mixer at the discriminator center frequency. The instantaneous correction voltage required to produce a discriminator null appears at the input of the VCO as a dc level proportional to the instantaneous PM tube output frequency. The theory of such a feedback loop indicates that considerably improved threshold operation is achieved and that the bandwidth of the feedback loop need be only a fraction of the bandwidth of the input signal. In the operational circuit, a limiter and a provision for overcoming signal fade-outs have been incorporated. Considerable success has been achieved with this tracking device [2]. Gas velocity measurements were performed downstream in a subsonic jet with the laser-Doppler discriminator system and with the hot-wire anemometer. A comparison of one turbulence parameter (rms power spectral density) at one point in the flow is shown in Figure 6.

CONCLUSIONS

A three–dimensional laser-Doppler instrument was developed for the measurement of gas velocity
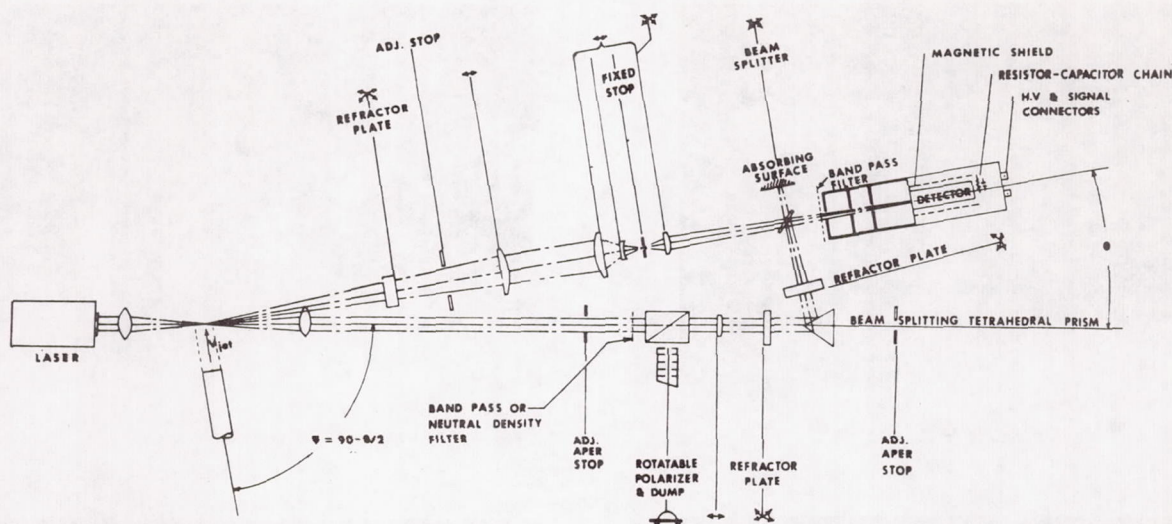
FIGURE 3. SCHEMATIC OF TYPICAL LASER-DOPPLER VELOCIMETER
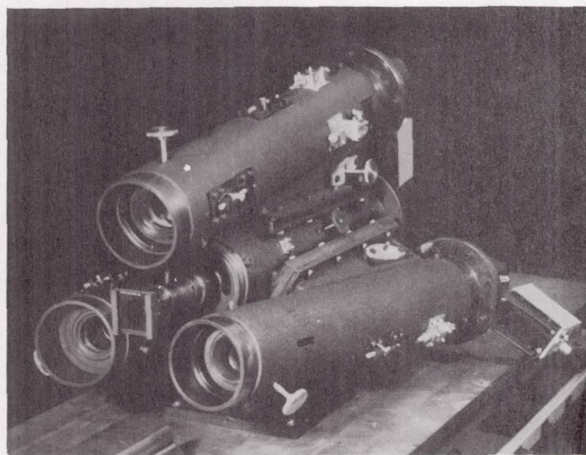
FIGURE 4. ASSEMBLED OPTICAL REVIEW
SYSTEM OF THE 3-D INSTRUMENT

and turbulence. Data from this type of instrumentation agree with results from other velocity measuring instrumentation over a wide range of velocities; for example, measurements of the turbulence properties of a small subsonic jet using the laser-Doppler instrument agree well with measurements using the hot-wire anemometer. Further measurements of turbulence in subsonic and supersonic jets using the

laser-Doppler instrument are in progress. Some other particular conclusions are as follows:

1. The laser Doppler instrument measures near-instantaneous velocities.

2. Natural or artificial tracers are required in the flow.

3. The laser-Doppler instrument does not disturb the flow in any way.

4. The laser-Doppler instrument can measure both subsonic and supersonic velocities.

5. The resolution is very high since the scattering volume can be made very small.

6. The measured velocity is completely independent of gas temperature.

ATMOSPHERIC PROGRAM

The goal of the present atmospheric program is the development of laser-Doppler instrumentation for the measurement of atmospheric wind velocity and turbulence. The present programs involve both analytical studies and experimentation. The analytical studies are necessary to define the optimum

150   200
Velocity - ft/sec
X = 0.25 in.

150   200
Velocity - ft/sec
X = 1.0 in.

150   200
Velocity - ft/sec
X = 1.5 in.

150   200
Velocity - ft/sec
X = 2.0 in.
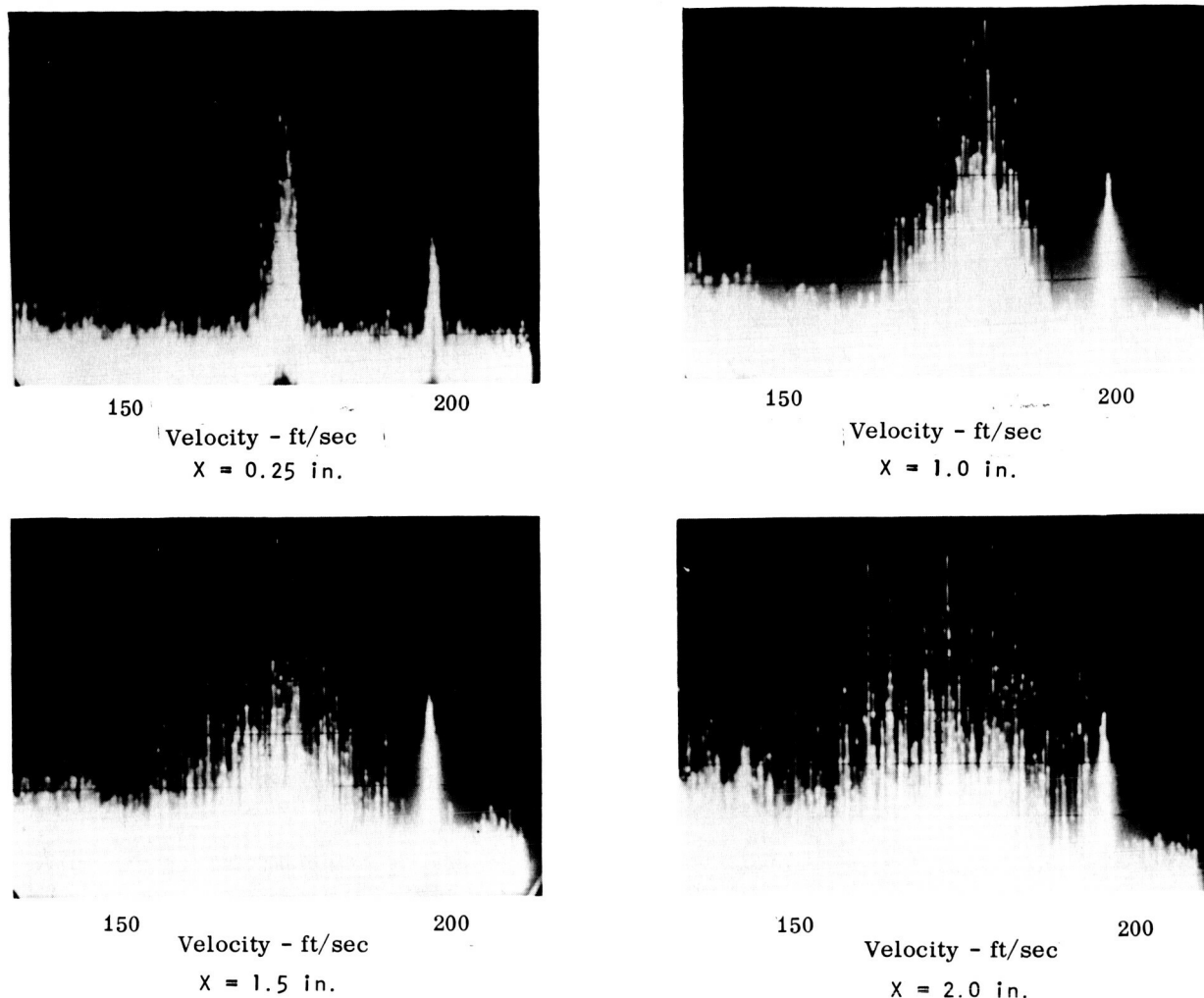
X = DISTANCE DOWNSTREAM OF 0.5 IN. NOZZLE OUTLET ON NOZZLE CENTERLINE.

MARKER FREQUENCY IS AT 26 MHz, AND THE PORTION OF THE SPECTRUM DISPLAYED
IS APPROXIMATELY 10 MHz WIDE.

FIGURE 5. TYPICAL DOPPLER SIGNALS DISPLAYED ON A SPECTRUM ANALYZER

configuration and components for particular applications. The experimental effort consists of actual measurements of atmospheric wind velocity and the parameters which affect the wind velocity measurement.

As a result of analytical studies, a CO_2 gas laser operating at 10.6 microns wavelength is being used. The reasons for this choice are as follows:

1. The CO_2 laser takes maximum advantage of the signal to noise (S/N) dependence on λ^3.

2. The laser is efficient in the use of prime power ($\sim$ 10 percent).

3. Alignment is not critical because of the long wavelength.
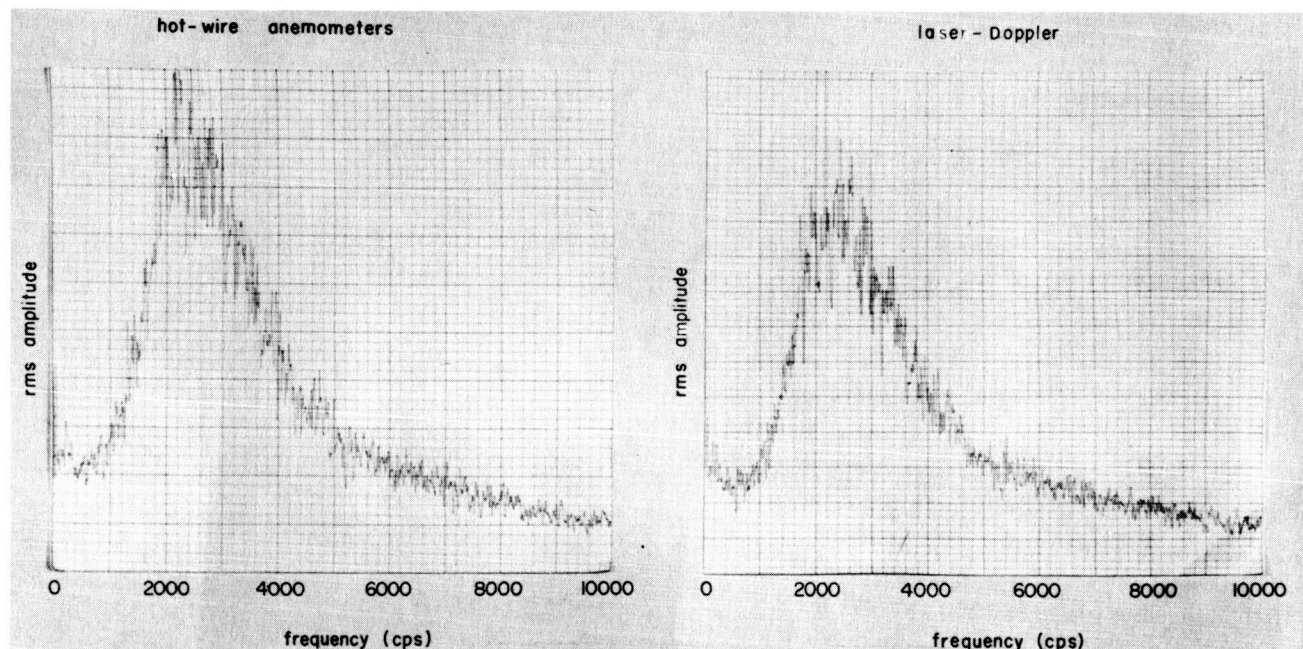
FIGURE 6. TURBULENCE SPECTRA IN A JET

4. The CO_2 laser has the highest CW output power available, and substantial power increases are predicted in the near future.

5. Less bandwidth is required to cover the same range of velocities.

The feasibility of an optical Doppler system to remotely measure the return signal from atmospheric particles centers around the S/N equation. The S/N power at the output of the receiver for a monochromatic source is

$$S/N = \frac{Q\,P_R\,P_{L.O.}}{B\,h\,f\,P_{L.O.} + P_N + P_{AMP}} \, ,$$

where

B   = electronic bandwidth

f   = transmission frequency

h   = Planck's constant

P_{AMP} = equivalent noise figure power of post detection amplifier

$P_{L.O.}$ = local oscillator signal power

P_N = equivalent optical noise power

P_R = received signal power

Q   = detector quantum efficiency .

Typically, in a coherent detection process, we may increase the local oscillator power to outweigh the effects of the additional noise contributing term. As a result of this, the S/N equation becomes equal to the product of the detector quantum efficiency and the received signal power, and is inversely related to the electronic bandwidth, transmission frequency, and Planck's constant.

Replacing the received signal power expression (P_R) with its equivalent expression for an extended target, we may observe the S/N equation to be a function of

$$S/N = \frac{Q\,P_T\,D^2_R\,x\beta_\rho\,x\,L}{16\,h\,f\,R^2\,B} \, ,$$

where

B   = electronic bandwidth

D_R = receiver optics diameter

95

f   = transmission frequency

h   = Planck's constant

L   = length of scattering volume

P_T = transmitter power

Q   = quantum efficiency

R   = system range

β_ρ = aerosol scattering coefficient

Of particular note are four parameters: (1) transmitter power, P_T, (2) electronic bandwidth, B, (3) the aerosol scattering coefficient, β, and (4) the length of the scattering volume, L. Typical system analyses usually revolve around determining the amount of transmitter energy required to perform a chosen task. However, for remote wind measurements at large distances, typically we are transmitter power limited [3].

In most ordinary Doppler systems, the bandwidth of the returned Doppler spectrum is relatively small compared with that required in a pulse system using ideal matched filter concepts. Significant power savings may be obtained by narrow banding to the narrow Doppler spectrum.

The Doppler bandwidth requirement for a differential wind velocity of 1 m/sec is of the order of 200 KHz, which is identical to that required for a matched filter where the pulse width is 5 msec. For the situation discussed, we must therefore conclude that the average power required for a CW system would be substantially greater than the average required in a pulsed system. The use of a CW Doppler technique, therefore, seems to be inefficient for use in a long range system.

Because of the spectrum-broadening caused by the turbulent wind velocity, a pulse-type laser technique is indicated for a long range system having sufficient Doppler shift to make suitable measurements.

EXPERIMENTAL MEASUREMENTS

A block diagram of the experimental system which was used in the first measurements of simulated wind velocities and actual wind velocities is shown in Figure 7. In these measurements, only the natural tracers in the atmosphere were used in the Doppler system wind velocity measurements.
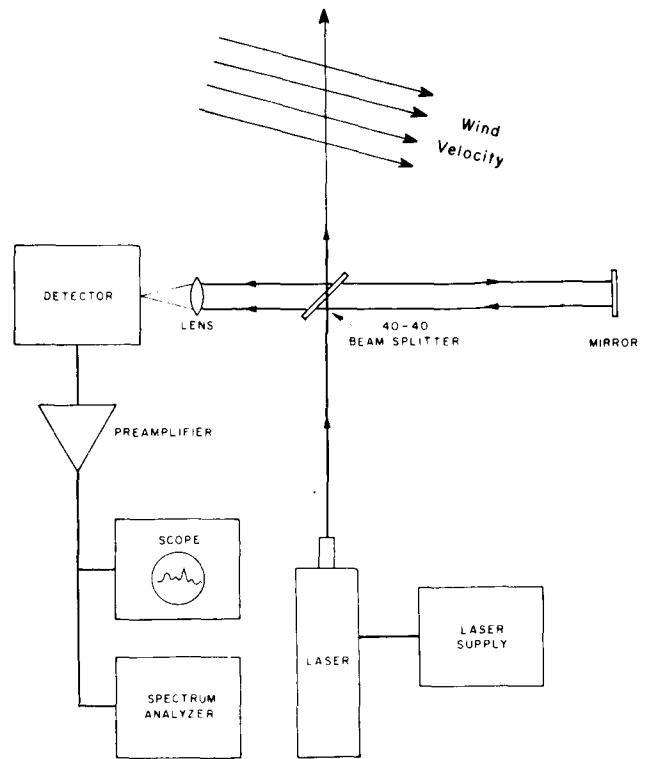
FIGURE 7. BLOCK DIAGRAM OF CO_2 WIND SENSOR SYSTEM

The first experiment perfomed was to use a small fan to generate a turbulent air stream across the laser beam. Figure 8 shows the Doppler velocity distribution as displayed on a spectrum analyzer. The baseline is with the scattered light coming from the volume of interest blocked and represents the noise in the system. The top line of Figure 8 shows the Doppler velocity returns from the turbulent air moving in front of the fan. This Doppler velocity spectrum agreed with an anemometer placed at the same location. Similar spectra have been obtained from Doppler shift measurements of atmospheric winds. These data have been correlated with the general wind velocity prevalent at the time of measurement. These Doppler measurements have been made in the atmosphere over a wide variety of atmospheric conditions ranging from very clear air to heavy smog [3].
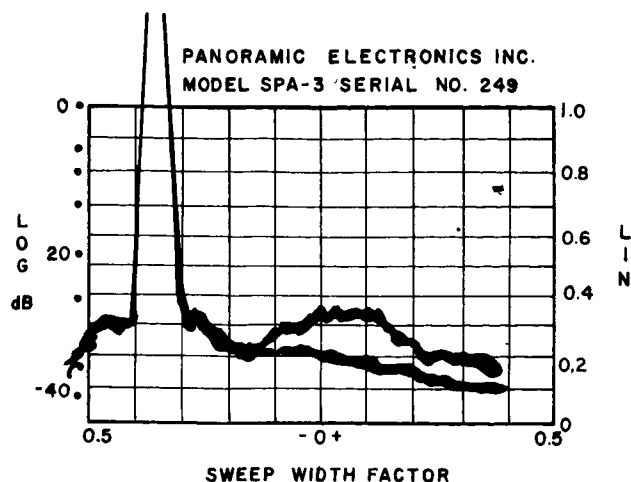
FIGURE 8. VELOCITY DISTRIBUTION WITH
NATURAL CONTAMINANTS ONLY

CONCLUSIONS

The feasibility of using a laser Doppler technique for the measurement of atmospheric wind velocity and turbulence has been established. The atmospheric wind velocity and turbulence have been measured using only the natural contaminants in the atmosphere. Experiments are in progress comparing the laser-Doppler wind velocity instrument with other wind velocity instrumentation. A three-dimensional wind velocity system which will have a 2-m resolution at 300 m altitude is currently under development. Studies are also in progress to determine the feasibility of using this laser-Doppler type of instrumentation for the detection and study of clear air turbulence to act as an on-board warning system for airliners.

REFERENCES

1. Gas Velocity Measurement Using Scattering Techniques. Final Report on Contract No. NAS8-20145, January 1966.

2. Aero-Astrodynamics Research Review No. 3. NASA TM X-53389, October 1965.

3. Wind Velocity Measurements. Final Report on Contract No. NAS8-20413, December 1967.

BIBLIOGRAPHY

Atmospheric Aerosol Properties and Estimates of Volume Scatter Functions. LMSC/HREC A784261 Contract NAS8-20082, July 1967.

Computation of Mie Scattering Coefficients of Absorbing Spherical Particles: A General Computer Program. LMSC/HREC A784513, Contract NAS8-20082, September 1967.

Contributions of System Parameters in the Doppler Method of Fluid Velocity Determination. Interim Report on Research Grant SC-NGR-04-001-015, 1968.

Doppler Velocity Instrument. NASA CR-1199, December 1967.

Feasibility Study of Laser Doppler Measurements of Wind Velocities. LMSC/HREC A784081, Contract NAS8-20082, June 1967.

Measurement of the Intensity of Turbulence. Interim Report on NASA Research Grant SC-NGR-04-001-015, 1967.

Specialist Conference on Molecular Radiation and its Application to Diagnostic Techniques. NASA TM X-53711, October 1967.

BIBLIOGRAPHY (Concluded)

Test Details of Velocity and Turbulence Measurements in a Supersonic Cold Flow Jet. Contract NAS8-20082, August 1968.

Turbulent Jet Studies Using the Laser-Doppler Instrument. Final Report on Contract No. NAS8-21072, July 1967.

Wind Velocity Measurements. Final Report on Contract NAS8-20413, November 1967.

Wind Velocity Measurements. LMSC/HREC A784082, Contract No. NAS8-20082, March 1967.

OPTICAL CROSSED-BEAM INVESTIGATION OF LOCAL SOUND GENERATION IN JETS

By

F. R. Krause

SUMMARY

Optical cross-correlation techniques are being developed to provide many of the experimental inputs which semi-empirical models need for prediction of noise generation at the source.

The location of sound source intensities in jet shear layers requires area integrals of correlated density fluctuations. Two narrow light beams are set to detect sound sources in the flow by triangulation. A digital cross-correlation of the optical signals from the two beams is then used to approximate the desired area integration of correlated disturbances. This optical integration over correlation areas is confirmed experimentally by verifying the radial resolution and spectra that are expected for point area product mean values. The determination of noise sources in jet shear layers will be started as soon as a new infrared crossed-beam system, which should give density-related local beam modulations, is finished.

The measurement of streamwise velocity variations in supersonic jets is required to apply present models of noise generation in turbulence-shock wave interaction zones. Mean velocity profiles have already been measured in supersonic flows by using a statistical cross-correlation between streamwise separated and delayed beams. The measurement of root-mean-square (rms) velocity fluctuations will be started as soon as the appropriate sample reduction and digital filtering techniques are completed.

LIST OF SYMBOLS

Symbols	Definition
a	speed of sound
D	nozzle exit diameter
G	normalized two-beam product mean value, defined by equation (24)
I	detected radiative power (watts)
$i = I - <I>$	beam modulation
$K' = K - <K>$	fluctuation of extinction coefficient
P	probability distribution
P_{ij}	stress tensor
p	pressure
S	turbulence spectrum
T	integration (averaging) time
T_{ij}	turbulent stress tensor
$\vec{U} \equiv (U, V, W)$	velocity components in earth-fixed frame
U_c	group velocity (convection speed of turbulence)
x	longitudinal coordinate along jet axis
y	lateral coordinate in microphone plane
z	lateral coordinate normal to microphone plane
ξ	minimum beam separation distance (space lag)
η	length coordinate along beam B
ζ	length coordinate along beam A
$\vec{\xi} = (\xi, \eta, \zeta)$	point vector in beam oriented frame
ρ	density
λ	optical wavelength
$\Delta\lambda$	optical bandpass

τ	time lag

Superscripts

$\rightarrow$	vector
'	fluctuation
$< >$	time average

Subscripts

XB	crossed-beam spectrum
A	beam A
B	beam B
f	far field

INTRODUCTION

To predict jet noise intensities and spectra, in many instances we must find the source of the noise. Present theoretical studies indicate that the shear layer and the turbulence in the jet are significant generators of noise. The problem is thus to formulate present mathematical noise prediction models in terms of experimentally accessible shear layer and turbulence parameters and to develop probes which could measure these parameters in the jet. This problem was recognized early while trying to predict and to suppress the extreme jet noise levels that are produced during the firing of large rocket motors. One possible set of experimentally accessible shear layer and turbulence parameters is provided by the point area correlation of density fluctuations and by the statistical distribution of streamwise velocity variations. Both of these parameters can conceivably be measured in remote or inaccessible flow regions through the digital correlation of the photometer outputs from two narrow light beams. The progress in developing this crossed-beam concept and the experimental technique is reported in this paper, which includes many unpublished analytical and experimental results. The details of the mathematical derivations will be covered in a future NASA publication.

The data on pitot tube traverses and microphone noise levels were provided by D. Barnett, Nortronics, Huntsville, Alabama. All experimental results with the laser system have been contributed by B. H. Funk,

MSFC, and all spectra have been calculated and evaluated by K. D. Johnston, MSFC. The evaluations of streamwise velocity fluctuations are being conducted by M. Y. Su, Nortronics, Huntsville, Alabama. The experiments with ultraviolet beams in supersonic jets were performed by M. J. Fisher and R. Damkevala, IIT Research Institute [1].

EXPERIMENTAL INPUTS FOR MATHEMATICAL NOISE PREDICTION MODELS

The noise generation of rocket engines is often so intense that individual sound waves become visible on shadowgraphs. Figure 1 illustrates such sound emanation from a cold model air jet.
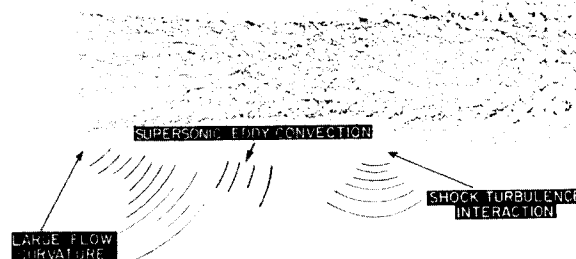
FIGURE 1. LOCATIONS OF JET NOISE SOURCES (M = 3.4)

Three distinct sets of sound waves are clearly recognizable outside the jet and have been enhanced by white lines for projection purposes. The origin of these sound waves may be found by tracing the wave normals back to the jet. The sound sources are apparently located at the nozzle lip, in the jet shear layer, and in the turbulence-shock interaction zone. We therefore hope that the mathematical jet noise prediction models which have been developed for shear layers and turbulence in aircraft engine jets may also be applied to supersonic rocket exhausts. Experimental input parameters which could be used in both subsonic and supersonic jets are sought. Such parameters would allow us to base the noise investigations in rocket engines on the large body of experience that has been accumulated for present aircraft engines. Using such parameters to design experiments on sound generation at the source would result in instrumentation and data reduction systems that could be applied to both aircraft and rocket engines, as well as to supersonic transports.

The main results of our literature search for suitable experimental inputs are illustrated in Figure 2.

FIGURE 2. EXPERIMENTAL INPUTS TO JET
NOISE PREDICTION MODELS

Sound generation in subsonic and supersonic shear layers is predicted as a consequence of vortices that are not aligned in the flow direction. The main experimental input that could be used to stud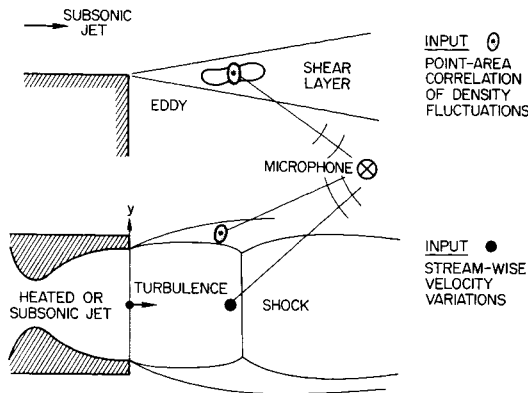y the sound generation by such vortices is a point area correlation of density fluctuations, equations (5) and (12). In supersonic jets additional noise is predicted for streamwise velocity variations upstream of shocks. Such velocity variations produce a shock wave oscillation which will in turn generate sound even if no vortices are present. The main experimental input that could be used to study sound generation by turbulence-shock interaction is thus the probability, $P(U)$, of streamwise velocity fluctuations, equation (14).

SOUND GENERATION STUDIES IN JET SHEAR LAYERS

The theory of sound generation in subsonic jet shear layers was formulated by M. J. Lighthill in 1952 and 1954 [2,3]. His quadrupole sources are physically identical with the deformation of vortex rings of Allan Powell [4]. Any vortex which is not aligned to the local flow direction will exert a force on the surrounding fluid particles and thereby slightly change the local pressure. This pressure change will in turn slightly change the local gas density in an almost isentropic fashion. We can consider many different realizations of a vortex that is traversing

the nozzle-fixed point $\vec{x}$ during the moment, t, of the realization. The deformation of this vortex could be recognized by the temporal variations of the density, $\partial\rho/\partial t$, in a vortex cross section. The size of the deformed cross section will then depend upon the area within which the density changes are correlated. The expected jet noise contribution per cross section of a moving vortex may thus be expressed by the following average, E, over all realizations:

$$F_{supersonic} (\vec{x}, \ldots)$$

$$= \int E \left[\frac{\partial}{\partial t} \rho(\vec{\xi}^* = 0, t) \frac{\partial}{\partial t} (\vec{\xi}^*, t) \right] d\eta^* \, d\zeta^*.$$

vortex-fixed frame $\qquad$ (1)

The integrand represents a correlation between the traveling vortex center, $\vec{\xi}^* = 0$, and the vortex cross section, $\xi^* = $ constant. It can be related to a similar correlation in a nozzle-fixed frame through the following translation of the separation coordinates:

$$\xi = \xi^* + U_c \tau_1$$

$$\eta = \eta^*$$

$$\zeta = \zeta^*. \qquad (2)$$

Lighthill further assumes that the density time derivative in the nozzle-fixed spot, $\vec{x} + \vec{\xi}$, may be represented by a statistically stationary time series [2,3]. In this event, the ensemble average over realizations, E, may be replaced with a time average, < >, and the correlation of the time derivative may be replaced with the time-lag derivative of the temporal fluctuations:

$$\rho' = \rho - < \rho > . \qquad (3)$$

As a result of the translation and time-averaging procedures, the noise contributions from a deforming vortex cross section might be expressed by an experimentally accessible point-area correlation of density variations:

$$F(\vec{x}, \xi) = \lim_{\tau_1 \to 0} \frac{\partial^2}{\partial \tau_1^2}$$

$$\int < \rho'(0;t) \, \rho'(\vec{\xi}^*; t+\tau_1) > d\eta^* \, d\zeta^* \qquad (4)$$

moving vortex
cross section

$$= \lim_{\tau_1 \to 0} \frac{\partial^2}{\partial \tau_1}$$

$$\int_{\text{nozzle-fixed frame}} < \rho'(x;y;z;t) \quad \rho'(x+\xi+U_c\tau_1; y+\eta; z+\zeta; t+\tau_1)> d\eta\, d\zeta. \tag{4}$$

(Continued)

The integrand represents one special case of the following point-area product mean value:

$$G_\rho(\vec{x},\xi,\tau) = \int_{\substack{\text{nozzle-fixed} \\ \text{flow cross} \\ \text{section}}} < \rho'(\vec{x}; t)\, \rho'(\vec{x+\xi}; t+\tau)> d\eta\, d\zeta. \tag{5}$$

The desired relation between such correlation measurements in the flow and the associated mean square pressure fluctuations in the far field follows by substituting equations (1), (4) and (5) into the mathematical model of quadrupole sound. The result is a fourth-order integral that accounts for all jet locations, $\vec{x}$, and all cross sections, ξ.

$$< \rho'^2(x_f) >_{\text{subsonic shear layer}}$$

$$= \frac{1}{16\pi^2} \int_{\text{jet}} \frac{x_f^2\, y_f^2}{\rho_o a_o\, (|\vec{x_f}| - M_C x)^6}\, (\partial\bar{U}/\partial y)^2$$

$$\left(\int_{\substack{\text{vortex} \\ \text{length}}} \frac{\partial^2}{\partial \tau_1^2}\, G_\rho\, [\vec{x};\xi(\tau_1 \to 0); \tau = \tau_1 \to 0]\, d\xi \right) dx\, dy\, dz. \tag{6}$$

Vortices generate very intense and directional sound waves outside the jet as soon as their speed exceeds the speed of sound at the microphone $(U_c/a_o > 1)$. Such vortex speeds will occur both in hot subsonic jets and in cold or hot supersonic jets, and the associated "Mach wave sound emission" may be of primary importance for rocket engines and the supersonic transport. Ffowcs-Williams [5] predicted this type of sound radiation from a theoretical study of the singularity that arises in equation (6) along the particular direction:

$$\theta = \cos^{-1} \frac{a_o}{\bar{U}_c}. \tag{7}$$

His mathematical model can also be represented in terms of point-area correlation of density fluctuations, except that the area deformation must be applied to a nozzle fixed-flow cross section instead of a

drifting cross section [6]. To a nozzle-fixed observer, the cross section of a passing vortex will change because of the variation of the vortex shape. Sound is thus generated even if the vortex is not deformed. The sound waves which emanate from the traveling vortex are very similar to the Mach waves which a bullet traveling along the same streamline would generate.

The desired relation between density correlation measurements in heated subsonic or any supersonic shear layers and the associated mean square pressure fluctuations at the microphone follows by substituting equations (4) and (5) into the mathematical model of Mach wave sound emission. This gives

$$< \rho'^2(\vec{x_f}) >_{\text{supersonic or heated shear layer}}$$

$$= \frac{1}{16\pi^2} \int_{\text{jet}} \frac{x_f^2\, y_f^2}{a_o \rho_o\, |\vec{x_f}|^6}\, (\partial\bar{U}/\partial y)^2$$

$$\left(\int_{\substack{\text{nozzle-} \\ \text{fixed frame}}} \frac{\partial^2}{\partial \tau^2}\, G_\rho(x,\xi;0)\, d\xi \right) dx\, dy\, dz. \tag{8}$$

The integral of equation (8) resembles very much the integral of equation (6). The main difference between the associated density correlation measurements in subsonic and supersonic shear layers is in the interpretation of the temporal correlation function. Equation (8) requires the curvature $\partial^2 G/\partial \tau^2$ of the temporal correlation between a point and an area at a fixed separation, ξ. Equation (7) requires the curvature $\partial^2 G/\partial \tau_1^2$ of the envelope to all time correlation curves $G(\tau)_\xi$ that have been obtained for different point-area separations.

SOUND GENERATION STUDIES IN TURBULENCE-SHOCK INTERACTION ZONES

Streamwise velocity fluctuations upstream of a shock will create a nonuniform pressure jump across the shock. The shock starts oscillations which in turn will propagate pressure waves into the downstream flow. In 1967, H. S. Ribner [7] established a mathematical relation between axial acoustical flux I_{ac} downstream of the shock $(x \to \infty)$ and the

mean square velocity variation $< U'^2 >$ upstream of the shock $(x \rightarrow -0)$.

$$I_{ac}(x \rightarrow \infty) = \frac{3}{2} \frac{\bar{P}}{\rho a} \quad (\vec{x} \rightarrow \infty; \ldots)$$

$$\frac{< U'^2 (x \rightarrow -0) >}{a^{*2}}$$

$$\times \int_{\theta=\theta_{crit}(M;\gamma)}^{\theta=\pi/2} |P(\theta)|^2 \cos^3\theta [1+M \sin \theta_2(\theta;M;\gamma)]$$
$$(1 + \sin \theta_2) \, d\theta. \qquad (9)$$

In this relation, M is the Mach number upstream of the shock, γ denotes the ratio of specific heats, and a* is the critical speed of sound. The functions a* and θ_{crit} can be obtained from isentropic flow and oblique shock tables. The functions θ_2 and $P(\theta)$ were tabulated by Ribner in 1955 [8].

The flux of acoustic energy is steady across the jet boundaries. Just outside the jet, we should therefore have almost the same acoustic flux that was calculated inside the jet. This allows us to estimate the mean square pressure fluctuation, just outside the jet, which turbulence-shock interaction will generate far downstream of the shock.

$$< \rho'^2 (\vec{x_f}) >_{shock-turbulence} = \rho_o a_o I_{ac}. \qquad (10)$$

In this equation, the acoustic flux may be calculated numerically for any given Mach number from equation (9). In fact, a similar integral applicable to oblique shocks can be obtained. Thus, there is a direct relationship between the mean square pressure fluctuation at the downstream microphone and the longitudinal rms velocity. This model is still idealized since the finite extent of the potential core and the interaction between the shear layer and the shock root are not yet included. However, Ribner's formulation could be extended to these more realistic flow fields [8]. Within this model, or any of its future extensions, the measurement of the streamwise velocity variations upstream of shocks seems to be the most important input that would be required in future investigations of jet noise at the source.

CROSSED-BEAM MEASUREMENT OF POINT AREA CORRELATIONS

Two narrow light beams are set to select by triangulation a point in the jet, as shown in Figure 3. Each of these beams is then collected by photo-detectors, A and B. Consider now the passage of vortices, which are slightly more opaque or transparent than the surrounding gas.
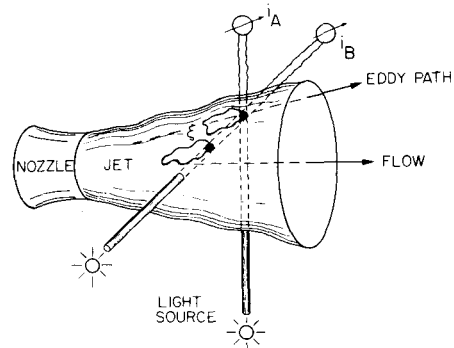

FIGURE 3. SOUND SOURCE IDENTIFICATION IN SUPERSONIC JETS

The passage of such a vortex will slightly change the received radiative power. The fluctuations of the photodetector output signals therefore contain information on the vortices that traverse the beams. These fluctuations, i_A and i_B, are recorded by using ac coupled amplifiers. Each recorded signal will account for any vortex that is traversing the line of sight, whereas we seek information on only those vortices that pass the beam intersection. These "common" signal components can now be retrieved by a digital cross-correlation computation. During such calculation, all radiative power modulations which occur only in one beam without affecting the other beam are cancelled. The cancellation of "noise" components depends upon the number of oscillations in the record and will be very complete if the digital cross-correlation computations are applied to a very long record. Noise components may thus be suppressed to the level of the temporal variations of the boundary conditions by integrating over a long record. All of our crossed-beam data have been reduced with a special digital computer program which provides for a time integration of any desired length by accumulating the time integral in a recursion formula In this recursion, only one short data piece at a time

is used on the computer memory. The associated "piecewise" correlation computations have successfully retrieved common signal components, which have been an order of magnitude smaller than the rms values of the recorded signals, i_A and i_B.

Practical limitations, such as dynamic interchannel time displacement errors of the data acquisition system and temporal trends in the experimental boundary conditions, provide a lower limit for the smallest signal that can be retrieved. The continued development of piecewise correlation techniques fortunately shows promise for the partial elimination of the variations of boundary conditions in uncontrolled environments [9]. Environmental variations have been partially eliminated through piecewise modification of the signal time histories [10].

OPTICAL APPROXIMATION OF POINT-AREA CORRELATIONS

The common signals, which remain after the digital cross-correlation computations, are produced only by those vortices which passed the beam intersection. All beam modulations by other vortices and by light source and detector noise should cancel each other [11]. The physical interpretation of the common signals thus needs to account for only those vortices which passed through the beam intersection point. Analytical studies of the optical integration along those beam elements which intersect the "common" vortices now indicate that this optical integration may be arranged to provide the desired point-area correlation [6]. The main results of these and more recent analytical studies are summarized in Figure 4 and in the following equation:

$$\frac{<i_A(t)\ i_B(t)>}{<I_A>\ <I_B>} = \int\limits_{\substack{\text{vortex cross}\\\text{section}}} <K'(x;y;z;t)\ K'(x;y+\eta;\ z+\zeta;t)>\ d\eta\ d\zeta. \quad (11)$$

The left-hand side of equation (11) is an experimentally accessible quantity and will be denoted by the term "two-beam product mean value." The numerator is calculated by adding the instantaneous product of the ac coupled photometer outputs, i_A and i_B. The denominator is given by the mean value of the dc coupled photometer records, I_A and I_B. The

time average, $<\ >$, has been obtained by integrating over a record length, T, which was sufficient to reduce all remaining variations of the two-beam product mean value below a desired error margin $(\text{noise}/<I> \leq 10^{-4})$.

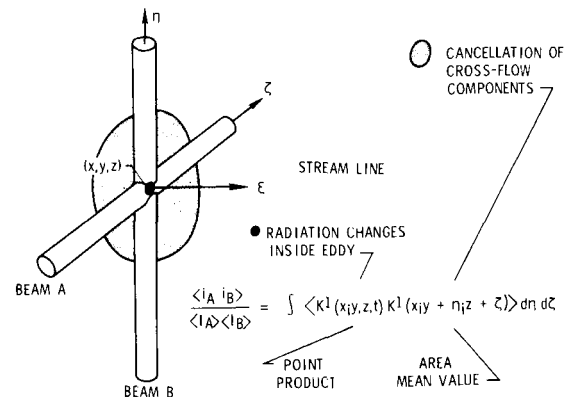$$\frac{<i_A\ i_B>}{<I_A><I_B>} = \int <K^1(x_iy,z,t)\ K^1(x_iy + \eta_iz + \zeta)>\,d\eta\,d\zeta$$

FIGURE 4. OPTICAL AREA INTEGRATION

The right-hand side of equation (11) is identical to the desired point area integration. The point is selected by the beam intersection. The area is generated by moving one beam parallel to the other. The integral may thus be described as a "point area product mean value." The correlation refers, however, to the local changes of radiative power, which are caused by the changes of opacity or transparency between passing vortices and the surrounding gas. The scalar K' is thus given by the local variation of light extinction or light emission coefficients. Two-beam product mean values, equation (11), would therefore give the desired point area integration of density variations, equation (5), only if the local variations in radiative power, K', can be related to density variations, ρ'.

The optical approximation of point-area approximation can be extended to points and areas which are separated along a streamline. Let the beams A and B intersect the common streamline at the positions x and $x + \xi$. The optical point-area correlation would then be given by:

$$G(T;x;y;z;\xi;\ \ldots) = \frac{<i_A(t)\ i_B(t)>}{<I_A>\ <I_B>}$$

$$= \int\limits_{\substack{\text{vortex cross}\\\text{section}}} <K'(x;y;z;t)\ K'(x+\xi;\ y+\eta;\ z+\zeta;\ t)>\,d\eta\,d\zeta. \quad (12)$$

The claim of point-area correlation, equation (12), cannot be verified with point probes, since such a test would require a large number of phase-matched probes, which possess a linear and time-invariant frequency response and which do not interfere with the flow. However, the point-area correlation does lead to two important conclusions on spatial resolution and spectral characteristics, which can be verified rather easily. The first conclusion is obtained by considering the isolation of individual streamlines through the location of the outside point. Thus, we should be able to distinguish between individual streamlines which are separated by no more than a beam diameter. In flows with a dominant direction, the spatial resolution of streamlines should thus be possible inside a typical vortex. The spatial resolution of flow traverses should therefore approach the resolution of point probes.

The second conclusion is reached by considering cross-flow components. Any directional fluctuation will displace a vortex only inside the beam front. The area integral across the vortex is not changed by such a displacement, and the associated two-beam product mean value will therefore not depend on cross-flow components. This discrimination against cross-flow components is the essential difference between one- and three-dimensional wave number spectra. Crossed-beam spectra should approximate the three-dimensional spectrum function and not the one-dimensional spectrum that is given by point probes.

EXPERIMENTAL VERIFICATIONS

The first crossed-beam tests were designed to check the optical approximation of point-area correlations by verifying the above conclusions. All tests were conducted in the initial portion of two supersonic jet shear layers, which were generated by expanding highly dried and unheated air through two nozzles. These nozzles produce shock-free jets of the same thrust at Mach number 2.42 ($D = 4.57$ cm) and 3.34 ($D = 5.47$ cm).

The shadowgraph of Figure 1 illustrated the jet from the M = 3.34 nozzle at off-design conditions. Typical sound pressure levels exceed 150 dB in the area where most of the crossed-beam instrumentation was located. All measurements were thus made under extremely adverse noise and vibration environments.

Most crossed-beam measurements used focused ultraviolet beams generated by projecting the image of a hydrogen discharge on the desired points of minimum beam separation [12]. The beams were mounted on a lathe bed in such a manner that the points of minimum beam separation would always be parallel to the jet axis, i.e., to the dominant direction of the streamlines. This point pair could traverse the jet axially and radially, and the separation could be varied in an axial direction. The light was extinguished in the flow by using the ultraviolet absorption of oxygen at an optical wavelength of 1850 Å inside a spectroscopic bandpass of 50 Å. Additional light extinction occurred by scattering from natural tracers which are generated by condensation of entrained wet ambient air, and from air liquefaction at high chamber pressures. Crossed-beam tests with collimated helium-neon laser beams of approximately 2 mm in diameter were performed more recently to obtain additional information on scattering without simultaneous absorption.

The modulations of the ultraviolet beam were recorded with two photomultiplyer tubes, EMR Model N 541A-05-14. The output signals from the two phototubes were amplified by specially built amplifiers and stored on an FM tape recorder, CEC, Model VR-3600, at a speed of 305 cm/sec (120 ips). Special multiplex equipment was integrated into the FM tape recorder so that any dynamic interchannel time displacement errors could be avoided by using two center frequencies (450 kHz and 825 kHz) on the same tape track. This multiplexing technique led to a flat frequency response from 500 Hz to 50 kHz and relative phase distortions of less than 3 degrees. The analog tapes were then converted to digital tapes by running them through the A/D conversion systems of MSFC's Computation Laboratory at the reduced speed of 38 cm/sec (15 ips). Because of this stretching of the time scale, the effective sampling rate was 160,000 samples/sec. The digital tapes were then processed on an IBM 7094 computer using the piecewise correlation program.

The cancellation of cross-flow components by optical area integration may be judged from the spectral measurements summarized in Figure 5. The ordinate displays crossed-beam spectra which have been calculated by including a time delay in the cross-correlation calculations.

$$S(f) = \frac{1}{2\pi} \int_{\tau = -0.003 \text{ sec.}}^{\tau = 0.003 \text{ sec.}} \frac{\langle i_A(t)\, i_B(t+\tau)\rangle}{\langle i_A^2 \rangle^{1/2} \langle i_B^2 \rangle^{1/2}}\, ws(2\pi f\tau)\, d\tau. \quad (13)$$

105

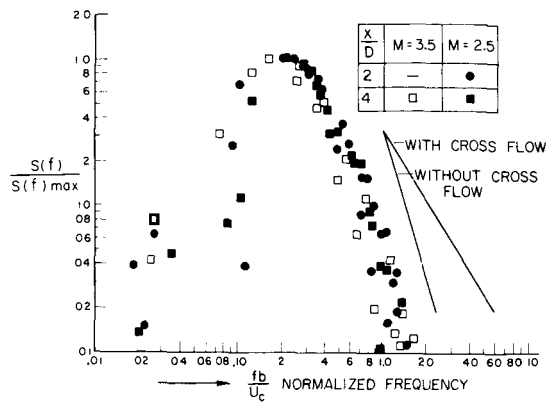| X/D	M = 3.5	M = 2.5
2	—	●
4	□	■

FIGURE 5. CROSSED-BEAM SPECTRA IN
JET-SHEAR LAYER

These spectral estimates were then normalized
with the maximum value so that the peak of the
spectrum is always equal to one. The abscissa gives
a normalized frequency which was based on the shear
layer width, b, and the turbulent convection speed,
U_c, (Fig. 6). This normalization has been successful
in collapsing hot-wire spectra in subsonic jet shear
layers on a universal curve.

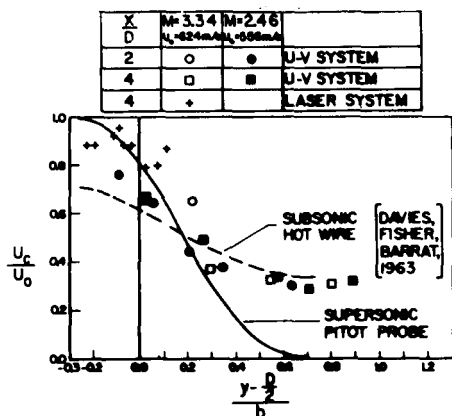| X/D	M=3.34 U_e=624m/s	M=2.46 U_e=806m/s	
2	○	●	U-V SYSTEM
4	□	■	U-V SYSTEM
4	✦		LASER SYSTEM

FIGURE 6. CONVECTION SPEED MEASUREMENTS
IN JET-SHEAR LAYER

The points in Figure 5 represent crossed-beam
spectra for six different locations in both the sub-
sonic and the supersonic portions of the two jet shear
layers. These points do approach a "universal"
spectrum shape for the high frequencies. Thus, the
local beam modulations in the supersonic flow
seem to have the same length and velocity scales as
the modulations in the subsonic flow.

The two solid lines in Figure 5 represent the
one-dimensional and three-dimensional spectra,
which the Heisenberg-Kolmogoroff theory would
predict for locally isotropic turbulence. The position
of these lines is immaterial; only the slope of the
lines is important. One-dimensional spectra, which
include cross flow components, should follow a -5/3
power law and are thus indicated by a -5/3 slope.
Three-dimensional spectra, which do not include
cross-flow components, should follow a -11/3
power law. The measured spectra obviously
approximate this -11/3 slope. This approximation of
a three-dimensional spectrum function gives confi-
dence in the optical approximation of point-area
product mean values.

The location of local sound sources may be
judged from the crossed-beam intensity measurements
summarized in Figure 7.

MACH 3.34 JET
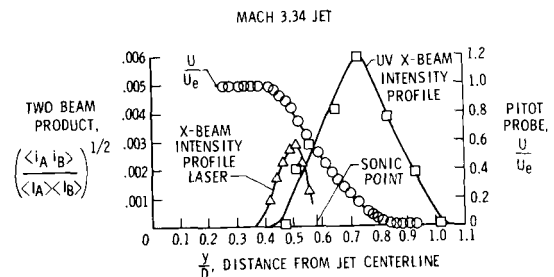
FIGURE 7. CROSSED-BEAM RESOLUTIONS OF
POINT-AREA CORRELATIONS

Intersecting light beams measured point area
correlations, and a pitot probe measured velocities
at several traverses in the two jets. The results
in Figure 7 refer to one traverse of the M = 3.34 jet.
The inner and outer edges of the shear layer are
indicated by the velocity profile and are located at
y/D = 0.4 and 0.8. The shear layer thickness is
thus b = (0.8 - 0.4) 5.47 = 2.2 cm. A typical vortex
cross section would extend over approximately 1/3
of this width.

Inspection of the two-beam product mean values
indicates that both the ultraviolet and the laser
systems clearly resolve common beam modulations
of less than 0.1 percent of the mean radiative power
in the beam. These common modulations show a
clear structure. In the outer edge of the shear layer,
the ultraviolet system produces a peak correlation,
which is probably associated with the condensation of

the wet ambient air that was entrained by the jet. The laser system produces a peak correlation at the inner edge of the shear layer, which could probably be associated with the condensation of the natural CO_2 content of air.

The radial resolution of the two-beam product mean values may be judged by comparing the width of the intensity peaks with the anticipated vortex diameter, $L_y \approx b/3$. Both peaks have clearly been resolved inside a vortex. The beam diameter was approximately 2 mm; some of the experimental points show a clear and consistent variation of two-beam product mean value along a 2 mm interval. The claim that the spatial resolution should approach the beam diameter seems therefore to be verified for this initial portion of a supersonic shear layer. We have thus every reason to believe that crossed beams do integrate over correlation areas as predicted by the analytical formulation in the section "Optical Approximation of Point-Area Correlations."

The successful approximation of point area correlations would allow us to locate sound sources in jet shear layers if the local beam modulations are proportional to density variations. The laser beams show a peak intensity at the supersonic edge of the shear layer, and the ultraviolet beams show a peak intensity at the subsonic edge of the shear layer. However, the theory of Mach wave emission would predict the maximum sound source intensities in the center of the shear layer. It is therefore unlikely that the two systems have located sound sources; i.e., the local beam modulations are not density related. Density-related beam modulations might be achieved by suppressing light scattering.

The local emission and absorption processes that remain after scattering has been reduced are uniquely determined by concentration, temperature, and density fluctuations [13]. Furthermore, most jet noise theories assume that all thermodynamic variations in supersonic shear layers occur isentropically and do not change the composition of the gas. Small disturbances of densities and temperatures are then inversely proportional to each other, and a relation to density is justified. However, chemical reactions in actual rocket exhausts will change the gas composition in an irreversible manner. Fortunately, the radiative power contributions caused by temperature variations may then be suppressed by special settings of the wavelength λ and the spectroscopic bandpass $\Delta\lambda$ [14]. We therefore believe that local infrared beam modulations which are

directly proportional to density fluctuations might be found in many jet noise investigations of practical interest.

Scattering will be reduced in future noise investigations by using infrared beams in heated flows. Heating should reduce the production of natural tracers by wet air entrainment or air liquefaction in the jet. The few remaining natural tracer particles should scatter the infrared light much less than the visible and ultraviolet beams now in use. Contamination by solid tracer particles might, however, present problems in some applications.

To study such problems, a special optical calibration cell, which can be resonated like an organ pipe, is being built. Wall pressure measurements in the cell should then provide a direct estimate of the local density fluctuations. The relation between beam modulation and density variation could thus be studied for various settings of the spectroscopic band pass and various gas samples.

VELOCITY MEASUREMENTS WITH STREAMWISE SEPARATED BEAMS

Streamwise separated beams may still contain a considerable amount of common signals, even if the separation exceeds several vortex diameters. Such commonality is a consequence of the flow, which transports the same emitting, absorbing, or scattering centers from the upstream to the downstream beam. A finite correlation might be expected if the signal of the downstream beam is delayed by the approximate transit time between the beams before the product mean value is calculated. Conversely, variable time delays might be introduced into the data reduction to analyze the motion along the streamline which has been selected by the beam triangulation. Without such time delays, widely separated beams could not contain common signals.

CONCEPTUAL VELOCITY MEASUREMENTS

Consider the conceptual crossed-beam experiment illustrated in Figure 8. Two mutually perpendicular beams have been separated along a streamline by the distance, ξ. The ac coupled signal from the downstream beam is delayed by the time interval, τ, and the delayed and the undelayed signals, $i_B(t - \tau)$ and $i_A(t)$, are then fed into a digital

cross-correlation program. The output of this program will reach a maximum when the time delay is equal to the transit time, which the average vortex needs to travel from the upstream to the downstream beam. The peak of the correlation curve may thus be used to identify the most probable velocity, as indicated in Figure 8.
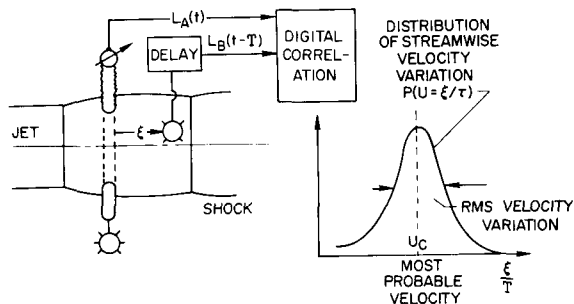

FIGURE 8. MEASUREMENT OF STREAMWISE VELOCITY VARIATIONS

The digital correlation computations may be so arranged that the shape of the correlation curve indicates streamwise velocity components other than the most probable value. Our analytical studies indicate that the following correlation of the signal time derivatives should approximate the probability, P, that the streamwise velocities, U, had the value ξ/τ.

$$P\left(U = \frac{\xi}{\tau}\right) = \frac{\tau}{\xi} \frac{< \frac{\partial}{\partial t} i_A(t) \frac{\partial}{\partial t} i_B(t - \tau)>}{\int_{-\infty}^{\infty} \frac{< \frac{\partial}{\partial t} i_A(t) \frac{\partial}{\partial t} i_B(t - \tau)>}{\tau} d\tau}$$

(14)

Equation (14) is thus the key to the desired measurement of streamwise velocity variations. The rms value, $< U'^2 >^{1/2}$, which is required for sound generation studies in shock-turbulence inter- action zones, could be read directly from the width of the correlation curves.

The approximation of the streamwise velocity distribution function, P, with crossed-beam measurements may be understood physically by identifying the time derivative of the common signal components with the slope of a passing vortex sur- face. A large oscillation is expected only if the head or the tail of a vortex traverses the beam. The correlation calculation of equation (14) represents,

then, the correlation of traveling interfaces instead of the entire vortex. An interface will need only a very short time interval to travel its own length, and the correlation curve $P(\xi/\tau)$ should therefore resemble a very sharp peak if all interfaces would travel at the same transit time. Conversely, the spread of the correlation curve will give the distri- bution of interface transit time or speeds. The correlation of time derivatives is thus quite different from the usual correlation of the signal fluctuations, where the width of the curve is identified with the time a vortex needs to travel its own length, and not with the spread of transit times.

MEASUREMENTS OF CONVECTION SPEED PROFILES

Crossed-beam measurements of convection velocities have been made in several radial and axial positions in both of the supersonic jets using the ultraviolet and the laser systems. The main results are plotted on Figure 6 in a nondimensional form with the width of the shear layer as the length scale and the nozzle exit speed as the velocity scale. Pitot tube traverses of subsonic and supersonic jets suggest that this particular normalization should give a "universal" velocity profile that is valid for both subsonic and supersonic jets [15]. A similar result is predicted by identifying the turbulent velocity field with the random walk of a single fluid particle. The velocity measurements with pitot probes did collapse on the universal curve shown in Figure 6. The dashed curve represents subsonic convection speed measure- ments with a pair of hot wires that were also sepa- rated along streamlines [16].

Inspection of the crossed-beam results leads to the following observations:

1. In the underlined subsonic portion of supersonic shear layers, crossed-beam measurements agree with scaled group velocity profiles from subsonic hot-wire measurements. The same agreement with hot-wire group velocities was found in our previous investi- gations of subsonic shear layers [17, 18].

2. In the underlined supersonic portion of the jet shear layers, laser crossed-beam measurements tend to follow the mass average speed indicated by pitot tubes. Convection velocities from ultraviolet measurements also tend to be higher than those predicted from hot-wire measurements in subsonic flows. Unfortunately, the scatter of the velocity points

is still too large for any detailed analysis. This lack of resolution is probably caused by the electronic and computational problems associated with retrieving very small signals out of noise. We believe that the experience from these first crossed-beam tests in supersonic shear layers will allow us to improve our data acquisition and reduction so that the spatial resolution of velocity profiles will be considerably better in future tests.

3. Both laser and ultraviolet beams give approximately the same velocity profile although each beam responds to different light extinction processes.

Apparently, velocity measurements are independent of the type of local extinction phenomena to which the beams respond. This independence of the local extinction process suggests that velocity and length scale measurements can be conducted whether or not the beams respond to density variations. Scaling studies between subsonic and supersonic jets, between cold and hot jets, and between model jets and the prototype engine exhaust are thus within the capability of existing crossed-beam technology.

The measurement of streamwise velocity fluctuations and length scales requires the correlation of time derivatives. In our digital program, a time derivative is replaced with the moving central difference between three adjacent data samples. These differences are so small that quantization errors are relatively large. Quantization errors can be reduced by sample reduction techniques whenever the sampling frequency exceeds the data frequency by one or two orders of magnitude. Adding many samples to obtain one data point reduces quantization errors since the average is more accurate than any of the original samples. Appropriate time scale stretching, sample reduction, and digital filtering techniques for correlation of time derivatives will be finished soon. Preliminary checks of these techniques

are encouraging, and have led us to believe that the measurement of streamwise rms velocity will be experimentally feasible.

CONCLUSIONS

Theoretical and experimental studies of crossed-beam test arrangements indicate that the statistical correlation of optical signals has the potential to provide many of the measurements which are required for jet noise investigations at the source. Remote, or inaccessible, source areas are studied optically without the probe interference problems that plague present hot-wire investigations.

The intensity and spectra of jet noise may be related mathematically to the point-area correlation of density fluctuations in jet shear layers and to streamwise velocity fluctuations in shock turbulence interaction zones.

The optical integration along the beams has been used to obtain point-area correlations that are not accessible to any point probe.

Sound sources may be located by varying the position of the beam intersection point in the jet. The two-beam product mean value should provide direct estimates of sound source intensities and spectra, if an optical wavelength region can be found that provides density-related light extinction or emission processes.

The distribution of streamwise velocity variations could conceivably be measured in subsonic and supersonic jets with streamwise separated and delayed beams.

Our velocity and length scale measurements in subsonic and supersonic jets show that present crossed-beam technology could be used for scaling studies between cold and hot jets and between model engines and the prototype.
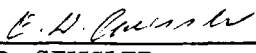
REFERENCES

1. Fisher, M. J.; and Damkevala, R. J.: Shock Wave Shear Layer Interaction on Clustered Rocket Exhausts. Final Report on Contract NAS8-20408, October 9, 1967.

2. Lighthill, M. J.: On Sound Generated Aerodynamically, Part I. Proc. Roy. Soc. (London) A, vol. 211, 1952, pp. 564-587

3. Lighthill, M. J.: On Sound Generated Aerodynamically, Part II. Proc. Roy. Soc. (London) A, vol. 222, 1954, pp. 1-32.

4. Powell, Alan: Vortex Sound. University of Calif., Los Angeles, Dept. of Engr., Rep. No. 61-70, October 1961.

5. Ffowcs-Williams, J. E.; and Maidanik, G.: The Mach Wave Field Radiated by Supersonic Turbulent Shear Flows. J. Fluid Mechanics, vol. 21, 1965, p. 641.

6. Krause, F. R.; and Fisher, M. J.: Optical Integration over Correlation Areas in Turbulent Flows. Proceedings, Fifth Int. Congr. Acoustics, paper K65, Liege, Belgium, 1965.

7. Ribner, H. S.: Acoustic Energy Flux from Shock Turbulence Interaction. UTIAS Techn. Note No. 108, AFOSR 67-0221, July 1967.

8. Ribner, H. S.: Shock Turbulence Interaction and the Generation of Noise. NACA Rep. 1233, 1955.

9. Krause, F. R.; and Hablutzel, B. C.: Noise Elimination by Piecewise Correlation of Photometer Outputs. Proceedings, National Academy of Sciences, Committee for Atmospheric Sciences, Panel on Remote Atmospheric Probing, Chicago, May 17, 1968.

10. Jayroe, R. R.; and Su, M. Y.: Optimum Averaging Times of Meteorological Data with Time-Dependent Means. Proceedings of AIAA Conference on Aerospace Meteorology, New Orleans, La., May 5-9, 1968.

11. Krause, F. R.; and Fisher, M. J.: Remote Sensing of Local Flow Instabilities and Turbulence. ASME Flow Measurement Symposium, Pittsburg, Pa., September, 1966, pp. 171-194.

12. Cann, M. W. P.: Light Sources for Remote Sensing Systems. NASA CR-854, August 1967.

13. Krause, F. R.; Davies, W. O.; and Cann, M. W. P.: The Determination of Thermodynamic Properties with Optical Cross-Correlation Methods. NASA TM X-53647, 1967.

14. Krause, R. R.; and Stephens, J. B.: Remote Detection of Local Temperatures and Local Partial Pressures with Crossed-Beam Spectroscopy. Specialist Conference on Molecular Radiation, Huntsville, Ala., NASA TM X-53711, October 1967, pp. 297-326.

15. Nash, J. F.: An Analysis of Two-Dimensional Turbulent Base Flow Including the Effect of the Approaching Boundary Layer. NPL AERO Rep. 1036, July 1962.

16. Fisher, M. J.; Davies, P. O. A. L.; and Barrat, M. J.: The Characteristics of the Turbulence in the Mixing Region of a Sound Jet. J. Fluid Mech., vol. 15, 1963, pp. 337-367.

17. Fisher, M. J.; and Krause, F. R.: The Crossed-Beam Correlation Technique. J. Fluid Mech., vol 28, 1967, p. 705.

18. Fisher, M. J.; and Damkevala, R. J.: Optical Measurements with High Temporal and Spatial Resolution. Final Report on Contract NAS8-11258, September 5, 1967.

RESEARCH ACHIEVEMENTS REVIEW
VOLUME III   REPORT NO. 4

The information in these reports has been reviewed for security classification. Review of any information concerning Department of Defense or Atomic Energy Commission programs has been made by the MSFC Security Classification Officer. These reports, in their entirety, have been determined to be unclassified.

These reports have also been reviewed and approved for technical accuracy.

E. D. GEISSLER
Director, Aero-Astrodynamics Laboratory

UNITS OF MEASURE

In a prepared statement presented on August 5, 1965, to the U. S. House of Representatives Science and Astronautics Committee (chaired by George P. Miller of California), the position of the National Aeronautics and Space Administration on Units of Measure was stated by Dr. Alfred J. Eggers, Deputy Associate Administrator, Office of Advanced Research and Technology:

"In January of this year NASA directed that the international system of units should be considered the preferred system of units, and should be employed by the research centers as the primary system in all reports and publications of a technical nature, except where such use would reduce the usefulness of the report to the primary recipients. During the conversion period the use of customary units in parentheses following the SI units is permissible, but the parenthetical usage of conventional units will be discontinued as soon as it is judged that the normal users of the reports would not be particularly inconvenienced by the exclusive use of SI units."

The International System of Units (SI Units) has been adopted by the U. S. National Bureau of Standards (see NBS Technical News Bulletin, Vol. 48, No. 4, April 1964).

The International System of Units is defined in NASA SP-7012, "The International System of Units, Physical Constants, and Conversion Factors," which is available from the U. S. Government Printing Office, Washington, D. C. 20402.

SI Units are used preferentially in this series of research reports in accordance with NASA policy and following the practice of the National Bureau of Standards.

CALENDAR OF REVIEWS

FIRST SERIES (VOLUME I)

REVIEW	DATE	RESEARCH AREA	REVIEW	DATE	RESEARCH AREA
1	2/25/65	RADIATION PHYSICS	12	9/16/65	AERODYNAMICS
2	2/25/65	THERMOPHYSICS	13	9/30/65	INSTRUMENTATION
3	3/25/65	CRYOGENIC TECHNOLOGY	14	9/30/65	POWER SYSTEMS
			15	10/28/65	GUIDANCE CONCEPTS
4*	3/25/65	CHEMICAL PROPULSION	16	10/28/65	ASTRODYNAMICS
5	4/29/65	ELECTRONICS	17	1/27/66	ADVANCED TRACKING SYSTEMS
6	4/29/65	CONTROL SYSTEMS			
7	5/27/65	MATERIALS	18	1/27/66	COMMUNICATIONS SYSTEMS
8	5/27/65	MANUFACTURING	19	1/6/66	STRUCTURES
9	6/24/65	GROUND TESTING	20	1/6/66	MATHEMATICS AND COMPUTATION
10	6/24/65	QUALITY ASSURANCE AND CHECKOUT	21	2/24/66	ADVANCED PROPULSION
11	9/16/65	TERRESTRIAL AND SPACE ENVIRONMENT	22	2/24/66	LUNAR AND METEOROID PHYSICS

SECOND SERIES (VOLUME II)

REVIEW	DATE	RESEARCH AREA	REVIEW	DATE	RESEARCH AREA
1	3/31/66	RADIATION PHYSICS	7	3/30/67	CRYOGENIC TECHNOLOGY
2	3/31/66	THERMOPHYSICS	8**	5/25/67	COMPUTATION
3	5/26/66	ELECTRONICS	9	7/27/67	POWER SYSTEMS
4	7/28/66	MATERIALS	10	9/28/67	TERRESTRIAL AND SPACE ENVIRONMENT
5	9/29/66	QUALITY AND RELIABILITY ASSURANCE	11	11/30/67	MANUFACTURING
6	1/26/67	CHEMICAL PROPULSION	12	1/25/68	INSTRUMENTATION RESEARCH FOR GROUND TESTING

THIRD SERIES (VOLUME III)

REVIEW	DATE	RESEARCH AREA	REVIEW	DATE	RESEARCH AREA
1	3/28/68	AIRBORNE INSTRUMENTATION AND DATA TRANSMISSION	5	11/21/68	COMMUNICATION AND TRACKING
2	5/22/68	ASTRODYNAMICS, GUIDANCE AND OPTIMIZATION	6	1/30/69	THERMOPHYSICS
			7	3/27/69	RADIATION PHYSICS
3	7/25/68	CONTROL SYSTEMS			
4	9/26/68	AEROPHYSICS			

* Classified. Proceedings not published.

** Proceedings summarized only.